LBL-31534

Lawrence Berkeley Laboratory
UNIVERSITY OF CALIFORNIA

EARTH SCIENCES DIVISION

Fault Zone Structure Determined through the Analysis of Earthquake Arrival Times

A. Michelini
(Ph.D. Thesis)

October 1991

Prepared for the U.S. Department of Energy under Contract Number DE-AC03-76SF00098

DISCLAIMER

LBL--31534

DE92 010322

Fault Zone Structure Determined through the Analysis of Earthquake Arrival Times

Alberto Michelini

(Ph.D. Thesis)

Department of Geology and Geophysics
University of California

and

Earth Sciences Division
Lawrence Berkeley Laboratory
University of California
Berkeley, California 94720

October 1991

This work was supported by the Director, Office of Energy Research, Office of Basic Energy Sciences, Engineering and Geosciences Division, of the U.S. Department of Energy under Contract No. DE-AC03-76SF00098.

Fault Zone Structure Determined Through
the Analysis of Earthquake Arrival Times

by

Alberto Michelini

Abstract

This thesis develops and applies a technique for the simultaneous determination of P and S wave velocity models and hypocenters from a set of arrival times. The velocity models are parameterized in terms of cubic B-splines basis functions which permit the retrieval of smooth models that can be used directly for generation of synthetic seismograms using the ray method. In addition, this type of smoothing limits the rise of instabilities related to the poor resolving power of the data. V_P/V_S ratios calculated from P and S models display generally instabilities related to the different ray-coverages of compressional and shear waves. However, V_P/V_S ratios are important for correct identification of rock types and this study introduces a new methodology based on adding some coupling (i.e., proportionality) between P and S models which stabilizes the V_P/V_S models around some average preset value determined from the data. Tests of the technique with synthetic data show that this additional coupling regularizes effectively the resulting models.

The method has been applied to two data sets recorded at the northern and southern ends of the creeping zone in California—Loma Prieta and Parkfield. The results of both analyses indicate that relatively high-velocity bodies appear to control the mode of deformation, the seismicity pattern and the extent of rupture in larger events.

At Parkfield the anomalous body ($V_P \approx 6.5$ km/sec) extends on the southwest side of the San Andreas fault, deeper than 5 km. Its velocity appears to be too high for the granitic composition of the Salinian block. A V_P/V_S anomaly ($V_P/V_S \approx 1.9$)

characterizes the hypocentral zone of the 1966 Parkfield mainshock and it is suggested to be produced by high fluid-pore pressures.

The anomalous high-velocity body at Loma Prieta ($V_P \approx 7.0$ km/sec) extends deeper than 8 km on the southwest side of the San Andreas fault. The October 18, 1989, mainshock hypocenter occurred at the northern termination of this anomalous body and ruptured through it.

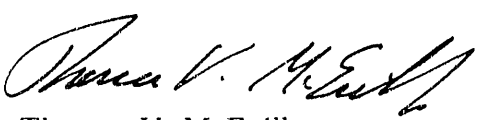

Thomas V. McEvilly

Dissertation Committee Chair

Ai miei genitori

(To my parents)

Acknowledgements

Berkeley represents an important stage of my life- -I received a scientific education, I met wonderful friends and I met my wife Luisa.

I came to Berkeley for the first time in September 1984 to spend a period of 8 months as a visiting scholar at the Seismographic Station. When I arrived they used to call me doctor until I decided to apply to graduate school[1].

Soon I met my contemporaneous graduate students with whom I have spent and appreciated these years in school. Some of them have become very close friends of mine and I will spend a few words on some of the peculiarities that have made them unique. The first person I became close after my arrival was Anthony with whom I have shared the "joy of fractals" as applied to the rims of the Grand Canyon. Although I have always tried avoiding other Italians at Berkeley, I could not elude the "Renaissance Group" of Walter Alvarez and Sandro Montanari. Caffè was the ingredient and often the pretext for widely different conversations. I became some kind of outside member (membership was only opened to geologists !). Sandro is a very atypical Italian and this is probably the reason we have become close friends through the years. His house was (and is) always an "attractor" for people, conversations and discussions blended with "great" music and food. It was at their house that I was first introduced to Luisa. During the early years of this "Cal adventure", Vicki and I shared good times and we supported each other through the difficult ones. In part, I owe to her if I am now writing this. Jay the "easterner" ? Jay started a year ahead of me and has been like my "constant" in this tenure. Although on different scales, our thesis topics were similar and we both benefited from that. Since he graduated, I felt compelled to do the same ! What about Michael, Joel and Don ? They are very different but they all share a very precious quality—generosity. I met Bill when we were both taking courses, the so called "informal" curriculum that, whether you like it or not, you were advised to take (I am glad I took it !). Bill and I have spent these years sharing the same data and working on complementary projects. Of course, the approach was different—the British versus the Italian ! In a nice way he has often ridiculed my Mediterranean heritage while I mocked his strictly British stubbornness. Bill and Mary (his wife) have become through the years some of my closest friends and the time we have spent together is filled with little unforgettable anecdotes. They used to live on a sailing boat and one day we nearly went aground close to the Golden Gate because the boat would not tack easily—it had not been designed for Bay but for "proper" ocean sailing, Bill remarked later ! I am grateful to Tom McEvilly for picking me up after my "orals" in a time when I was drifting aimlessly. After some testing we tuned onto the same frequency and his enthusiasm, understanding, and advice have contributed to these years. I feel that Tom, Bill and

[1] *The title "dottore" is awarded in Italian universities after a curriculum that falls between a bachelor and a master, rarely a Ph.D..*

I formed a "team" whose strength was based on our diversity and on our close and generous collaboration. On the other hand, Lane Johnson has been always the person to ask questions. He has always given his time freely and his answers have provided many insights.

LBL people, environment and facilities have had an important influx in the development of this thesis. In particular, Ali, Eleni and I were brought closer together by our common Mediterranean origins and background. In conversations with Eleni, it often surfaced a blend of criticism, appreciation and nostalgia for our countries that, afterall, made us feeling closer to "home" and strengthened our friendship. Tom Daley has been most helpful too many times to be mentioned here and I feel grateful to have received his altruism. Conversations with Shimon have helped to enlighten problems in inverse theory and data processing whereas Ernie, for the computer facilities, and Rich, for the data acquisition, were instrumental for this thesis. Ivan introduced me to the use of cubic splines whose smoothness, however, is in contrast with his sharp and self-derisory Czech humour. Valeri, the theoretician always submerged by obscure Cyrillic equations, taught me, in practice, the Russian way of drinking vodka—I nearly got arrested !

Through the years, I have shared my apartment with different people. Bob has been a wonderful and discreet roommate, office mate and friend. Carolina brought her Caribbean touch and "order" into the apartment and Peter, in long, diverse, and wonderful conversations has been a companion and friend for the last years. Together, we came to realize that graduate school can be best described as a form of "priesthood initiation" in which working hard for 12-14 hours a day is the tribute to "faith" !

The complex interaction of these people and the demands of the Berkeley program have made these years of my life hard but most enjoyable. Last but not the least, I wish to thank my wife Luisa for giving me this last "push" to finish what I had started several years ago and my parents to whom I am dedicating this dissertation. It was their education that infused in my character the willingness to pursue independent thinking and follow unexplored paths.

Contents

Chapter 1

Introduction

In the recent years, major efforts have been put into obtaining a better understanding of the failure process involved in the earthquake process. To this purpose, high-resolution geophysical networks have been installed in zones where the earthquake cycle has been recognized. The aim is to obtain more accurate estimates of the physical quantities that play a major role in the failure process and to monitor their variations.

Failure occurs when the medium is unable to sustain the applied stresses. Similarly, an earthquake occurs in the Earth when the applied stress field has deformed the rocks to a point that their shear strength is reached. Although failure in laboratory experiments is a relatively well understood process, the inability of earth scientists to predict the occurrence times of earthquakes appears to demonstrate that earthquake failure is a complex physical phenomenum that involves superposition and interaction among several physical processes. Seismogenic depths are not directly accessible and earth scientists have to rely for their inferences on surface manifestation of the processes ongoing at depth.

This thesis focuses on the determination of the geologic structure and the material properties at seismogenic depths. I have used earthquake arrival-times to determine simultaneously hypocenters and velocity structure in two seismically active zones on the San Andreas fault in Central California.

This problem is intrinsically coupled because accuracy in earthquake locations depends significantly on the adopted velocity model used for their location. Solution of this problem is important because, besides providing an improved understanding of the geologic structure at depth, the results can be used as platform for more sophisticated analysis. For example, determination of hypocenters, focal mechanisms, source moment tensors, attenuation, anisotropy and any other calculations relying on the geometry of seismic wave raypaths within or near the fault zone, all depend critically on a realistic three-dimensional velocity model for P and S waves. Additionally, inference on the variations in physical properties within and along the fault zone to a scale of a few kilometers may provide valuable details on the segmentation of the fault zone, on the nature and distribution of fault zone materials, and on the locations and extent of possible asperities or nucleation zones.

In this thesis, I have developed a technique that solves the joint earthquake location/velocity structure problem using arrival times of local earthquakes. A parameterization in terms of cubic B-splines basis functions of the velocity model permits use of the determined model directly as input for more complete waveform analysis. A procedure is developed to fully exploit P- and S-arrival time data in the determination of accurate and reliable V_P/V_S models. In this respect, the developed technique appears to fill an analysis gap of other similar methods.

In chapter 2, I describe the mathematical development of the model parameterization and the inverse procedure is described in detail. In chapter 3, some tests with synthetic data are presented and compared with another modeling technique. The analysis of the data recorded at Parkfield by the High Resolution Seismic Network are discussed in chapter 4, and, in chapter 5, those relative to the aftershocks of the Loma Prieta Earthquake of October 18, 1989, ($M_L \approx 7.0$) and the background seismicity as recorded by the USGS-CALNET network. In chapter 6, I summarize the main results and provide recommendations for further developments of the methodology.

Chapter 2

Method

In this chapter, I describe the joint hypocenter/velocity inversion technique developed in this study. First, an introduction to the topic will be given by providing a short account on the relevant previous investigations. Secondly, I will formalize the adopted type of parameterization of the velocity model and finally, the description of the inversion technique used throughout is provided.

2.1 Introduction

In recent years, the method of simultaneous inversion of seismic-wave arrival times for earthquake locations and velocity structure has been developed as a promising technique. This method minimizes travel-time residuals for the coupled elastic velocity model and hypocenter determination problem. Because the problem is non-linear, solutions are found by linearizing the problem locally and solving iteratively.

Initial developments of the simultaneous inversion technique were due to Crosson (1976) and Aki and Lee (1976). The approach taken in these early studies was later modified in applications by numerous investigators. The principal differences among these methods lie in the parameterization of the velocity model, a choice often dictated by the type and speed of the ray-tracing technique adopted for the forward problem and by the specific geometry imposed by station distribution and the geologic setting of the area under investigation. From a general standpoint, two different approaches

toward parameterization can be adopted, one is global and the other is local (e.g., Sambridge, 1990). In the global parameterization, the discrete model parameters consist of the coefficients of the expansion of a basis function which attains non-zero values over the entire volume of the model under investigation. Each order of the expansion corresponds to a different spatial wavelength of the model. For example, Woodhouse and Dziewonski (1984), used as basis functions the normalized spherical harmonics. Conversely, in local parameterizations the basis functions attain non-zero values only in restricted parts of the volume. For example, Crosson (1976) used homogeneous constant velocity layers and Aki and Lee (1976) parameterized their model by subdividing the volume into constant velocity cells. The Backus-Gilbert formalism which approaches the problem as under-determined was instead followed by Pavlis and Booker (1980) who solved for a vertical, one-dimensional velocity model and by Chou and Booker (1979) that solved for a three dimensional velocity structure. Pavlis and Booker (1980) also introduced, together with Rodi et al. (1980) and Spencer and Gubbins (1980), the *parameter-separation* technique to reduce the joint problem to a tractable size and proposed the progressive inversion scheme developed by Roecker (1982). The Pavlis-Booker method was extended to the joint inversion for P- and S-velocity models and station corrections by O'Connell (1986). Thurber (1983) also adopted progressive inversion, attacking the true three-dimensionality of most inversion problems by using a three-dimensional (3-D) ray-tracer on a model parameterized in terms of linear interpolating functions in a three-dimensional grid of node points having assigned velocities. Eberhart-Philips (1989) extended Thurber's formulation to include in the simultaneous inversion the S-velocity model.

An inherent difficulty with the velocity inversion problem is the often poor ray coverage of the volume to be imaged due to the limited source-receiver distribution. For example, earthquake sources are often located on planar faults, and receivers are on the earth's surface. As a result, the medium is sampled unevenly and preferentially

along certain directions. Given this non-optimal ray-coverage, the inverse problem is generally of a mixed over- and under-determined type (Menke, 1984), and some *a priori* information must be added in order to make the problem solvable and stable (i.e., regularization). Furthermore, the problem is non-linear because ray paths depend on the velocity model and simply finding a solution to the problem does not insure its uniqueness. In fact, since the problem is non-linear and a solution is found by linearizing the problem locally, solving for parameter adjustments using some norm minimization criterion given an initial model and then iterating, non-uniqueness and local minima may well be the unavoidable practical burdens of the technique. The most common way to circumvent partially these problems is to regularize the inversion by, for example, constraining the resulting model to be smooth.

Smoothing can be introduced on three different levels in the computation of tomographic models. On the first level, smoothing can be introduced directly in the order of the local basis function which is used to parameterize the model. For example, tri-linear, -quadratic and -cubic B-splines functions are defined over 8, 27 and 64 knots of the local grid mesh adopted for the parameterization. At each grid point within the subset, the degree of continuity imposed by the order of the adopted B-splines function holds. Furthermore and implicitly, smoothing also occurs because use of higher degree basis functions affects the accumulation of the partial derivatives which are needed to determine the velocity perturbations, i.e., the higher the degree of the basis function, the larger is the distance (i.e., the number of knots) over which each ray path contributes in the accumulation of the partial derivatives. This can be visualized as if each ray looses its line-connotation and instead it appears as a beam-like form peaked at its actual position and fading out over a distance defined by the order of the employed basis function and the grid sampling. It follows that this type of smoothing acts at the accumulation stage of the partial derivatives and, because of its nature, it has an averaging effect on neighbouring nodes which results

in overall smoothing.

The second level on which smoothing can be introduced is after the matrix of partial derivatives has been accumulated regardless of the employed type of parameterization. In this case, the degree of continuity of the model is still dictated by the order of the selected basis function but the resulting model will be smoother in the sense that velocity differences between adjacent nodes will be reduced according to the applied conditioning.

Finally, *a posteriori* smoothing can be applied on the third level, which is, after the model has been determined. In this last case, the smoothed model loses the character given by the adopted minimization criterion (Spakman and Nolet, 1988).

In this thesis, smoothing has been applied at the first and second levels described above. There are two main reasons to do so. First, as it was stated above, we require the final model to be the smoothest satisfying the data (Sambridge, 1990; Michelini and McEvilly, 1991). Secondly, we seek models that permit ray-theoretical calculation of Green's functions for the medium, for which the second spatial derivatives of the velocities are needed. In this respect, Cerveny, (1987), remarked that in ray amplitude calculations the requirements on the smoothness of the model are strict and at least two approaches can be followed. The first involves velocity models having first and second order discontinuities and smoothing is applied to the results of the computations (e.g., Gaussian beams). The second approach consists of applying the *ray method* to smooth models and this is one of the motivations of this study.

Selection of any parameterization scheme is to some extent arbitrary and deficient. Our "view-angle" of the Earth is generally quite limited and selection of the smoothest model that fits the data is, at present, the most reasonable assumption we can make. Unfortunately, the Earth is by no means as smooth as seismologists' models require it to be, and we can argue that imposing the same degree of smoothing via the parameterization to all parts of the volume to be imaged is a rather strict and strong

a priori assumption. We hint that a possible solution to this problem consists of using *adaptive griauing* and *adaptive parameterization* techniques, already in use in fluid-dynamic modelling, that would act on the best resolved parts of the model and through the non-linear inversion iteration scheme. These methodologies are still to be introduced and tested for inverse problems and could represent a major advancement toward limiting the effects of *a priori* selection of gridding and parameterization. This topic has not been addressed in this thesis where I have instead focused on resolving smooth models for the conceptual reasons previously stated, but it will be included and appraised in future work.

Use of cubic B-splines basis functions in seismic tomographic reconstructions was initiated by Firbas (1987) to model data from two-dimensional seismic refraction lines. Farra and Madariaga (1988) used cubic B-splines in modelling seismic reflection data, for the parameterization of both the velocity field and the position of discontinuities in a two-dimensional model. Thomson and Gubbins (1982), were first to use cubic cardinal splines to determine the 3-D velocity structure beneath the NORSAR seismic array using teleseismic observations. Sambridge (1990), used non-locally supported cardinal splines of degree 3, modified from Thomson and Gubbins (1982), to invert for hypocenters, P-, S-velocity and position of the Moho discontinuity in the Australian shield. In his study, which is most similar to the present one, he approached the inversion problem as fully underdetermined by adopting approximately 5000 ray paths and solving for $\sim$ 65000 parameters.

For a fixed grid geometry, the cubic B-splines method yields a degree of smoothing not attainable by any other local basis-function approach presently in use (Firbas, 1987), and exploits the advantages of a more accurate interpolation scheme to limit the bias introduced by the parameterization (Sambridge, 1990). In this study, we have selected tri-cubic B-splines basis functions that result in models everywhere continuous up to the second spatial derivative and, in some cases, we have experimented

with smoothing conditions to regularize the solution.

Uncertainty estimation for the calculated velocity models is another difficulty in the simultaneous inversion techniques. Mapping of all the errors introduced by non-linearity, data, type of parameterization, starting-velocity model, the ray-tracing technique and sparse ray coverage leads to a smeared final velocity model and to hypocenter mislocations. No straightforward method exists to estimate the uncertainties caused by all these factors. If the tomographic problem is large, calculation of the resolution and covariance matrices is prohibitively costly or impossible. To circumvent this problem several researchers have provided estimates of errors and resolution by performing sensitivity tests with synthetic data (e.g., Spakman and Nolet, 1988). However, if the tomographic problem has a tractable size, the resolution matrix can still be calculated but there is no obvious way to display its values.

In the following sections of this chapter, I develop the formulation of the technique. In the following chapters, the technique is applied to synthetic cases and to recorded data. We will also compare our results with those obtained using the method of Thurber (1983).

2.2 Method of Parameterization

The inversion technique adopted for joint determination of velocity structure and hypocentral locations derives from the one proposed by Thurber (1983). The fundamental difference lies in the parameterization of the velocity model. Thurber's method specifies the velocities at a discrete number of grid points (nodes or knots). Velocities within a cell delimited by eight nodes in the three-dimensional grid are calculated by linear interpolation (tri-linear B-splines) and the resulting velocity-model is piecewise continuous, having first derivatives discontinuous at each grid point and constant otherwise. The method adopted in this study parameterizes the velocity model in terms of tri-cubic B-splines, which results in a velocity model that is continuous everywhere

up to and including the second derivative. Each tri-cubic B-spline basis function is defined on a total of 64 nodes. Hereafter we refer to the linear and cubic B-splines parameterization methods as LS and CS, respectively. The basic differences between Thurber's LS technique and the CS method of this study can be illustrated in the formulation of the problem for the one-dimensional case. For completeness, extension to three dimensions is presented in section 2.2.3. The terms linear and cubic are appropriate in the 1-D case which is used here to illustrate the method. In 2-D and 3-D the approximations are not cubic but contain also mixed terms in x, y and z. For this reason, terms like bilinear, bicubic and trilinear, tricubic (our method) should be used in the 2-D and 3-D case respectively.

2.2.1 Linear B-splines basis functions

The LS methodology is represented in terms of a cardinal basis. Following Lancaster and Salkauskas (1986), the cardinal basis consists of a set of functions taken from the vector space of piecewise linear functions of dimension $N+1$, where $N+1$ is the total number of knots or grid points, x_k $(k = 0, 1, \ldots, N)$ positioned on the x-axis. These functions satisfy the condition

$$l_i(x_k) = \delta_{ik} = \begin{cases} 1 & \text{if } i = k \\ 0 & \text{if } i \neq k \end{cases} \tag{2.1}$$

and have been named differently by various authors (e.g. tent-, pyramid-, hat-functions). We use here the term "linear B-splines" (Bartels et al., 1987). They are defined as follows:

$$l_0(x) = \begin{cases} \dfrac{x - x_1}{x_0 - x_1}, & x_0 \leq x \leq x_1; \\ 0, & x_1 \leq x \leq x_N; \end{cases} \tag{2.2}$$

$$l_j(x) = \begin{cases} 0, & x_0 \leq x \leq x_{j-1}; \\ \dfrac{x - x_{j-1}}{x_j - x_{j-1}}, & x_{j-1} \leq x \leq x_j; \\ \dfrac{x - x_{j+1}}{x_j - x_{j+1}}, & x_j \leq x \leq x_{j+1}; \\ 0, & x_{j+1} \leq x \leq x_N; \end{cases} \tag{2.3}$$

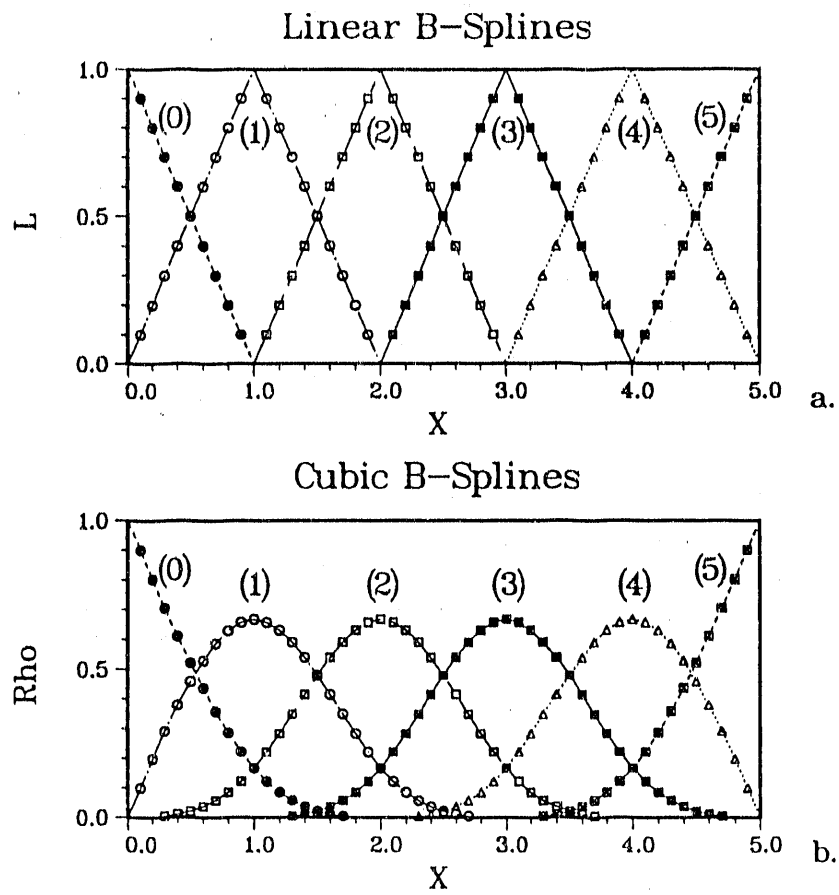

Figure 2.1: Example showing the basis functions with six equally spaced knots. (a) Linear and (b) cubic basis functions having zero value of the second spatial derivatives at the first and last knot.

$$l_N(x) = \begin{cases} 0, & x_0 \le x \le x_{N-1}; \\ \dfrac{x - x_{N-1}}{x_N - x_{N-1}}, & x_{N-1} \le x \le x_N. \end{cases} \tag{2.4}$$

An example of these functions is shown in Figure 2.1a.

In terms of these basis functions, or linear B-splines, the interpolated function $V(x)$ (velocity in our case) can be calculated at any x as

$$\begin{aligned} V(x) &= l_0 V_0 + \cdots + l_N V_N \\ &= \sum_{i=0}^{N} l_i(x) V_i. \end{aligned} \tag{2.5}$$

2.2.2 Cubic B-splines basis functions

The cubic B-spline formulation is completely analogous to the linear case. Cubic B-splines are a set of basis functions ρ_k taken from the vector space S_N of piecewise cubic functions which has dimension $N+3$. To determine uniquely a cubic spline function through a set of $N+1$ knots we need two additional constraints. We have adopted as constraints that the second spatial derivatives of the interpolated function are both equal to zero at the boundary knots ($i = 0, N$). These basis functions are shown in Figure 2.1b. A basic difference between LS and CS is the number of intervals which contribute to the interpolation. The support in LS is two intervals for interior knots and one for the boundaries (Equations 2.2 to 2.4 and Figure 2.1a), whereas the smoothness in CS (continuity up to second derivative) demands the support of four consecutive intervals for internal knots and three or two intervals at the boundaries (Equations 2.6 to 2.10 and Figure 2.1b). In principle we can define the cubic B-splines on unequally spaced intervals. For computational simplicity and speed, however, we use equal spacing on each of the three spatial coordinates. The normalized cubic B-splines functions satisfying the boundary conditions are defined as follows:

$$\rho_0(x) = \begin{cases} \frac{1}{4}h^{-3}(x-x_0)^3 - \frac{6}{4}h^{-1}(x-x_0) + \frac{6}{4}, & x_0 \le x \le x_1; \\ -\frac{1}{4}h^{-3}(x-x_1)^3 + \frac{3}{4}h^{-2}(x-x_1)^2 + \\ -\frac{3}{4}h^{-1}(x-x_1) + \frac{1}{4}, & x_1 \le x \le x_2; \\ 0, & x_2 \le x \le x_N; \end{cases} \tag{2.6}$$

$$\rho_1(x) = \begin{cases} -\frac{1}{2}h^{-3}(x-x_0)^3 + \frac{3}{2}h^{-1}(x-x_0), & x_0 \le x \le x_1; \\ \frac{3}{4}h^{-3}(x-x_1)^3 + \frac{6}{4}h^{-2}(x-x_1)^2 + 1, & x_1 \le x \le x_2; \\ -\frac{1}{4}h^{-3}(x-x_2)^3 + \frac{3}{4}h^{-2}(x-x_2)^2 + \\ -\frac{3}{4}h^{-1}(x-x_2) + \frac{1}{4}, & x_2 \le x \le x_3; \\ 0, & x_3 \le x \le x_N; \end{cases} \tag{2.7}$$

$$\rho_i(x) = \begin{cases} 0, & x_0 \le x \le x_{i-2}; \\ \frac{1}{4}h^{-3}(x-x_{i-2})^3, & x_{i-2} \le x \le x_{i-1}; \\ -\frac{3}{4}h^{-3}(x-x_{i-1})^3 + \frac{3}{4}h^{-2}(x-x_{i-1})^2 & \\ +\frac{3}{4}h^{-1}(x-x_{i-1}) + \frac{1}{4}, & x_{i-1} \le x \le x_i; \\ \frac{3}{4}h^{-3}(x-x_i)^3 - \frac{6}{4}h^{-2}(x-x_i)^2 + 1, & x_i \le x \le x_{i+1}; \\ -\frac{1}{4}h^{-3}(x-x_{i+1})^3 + \frac{3}{4}h^{-2}(x-x_{i+1})^2 + & \\ -\frac{3}{4}h^{-1}(x-x_{i+1}) + \frac{1}{4}, & x_{i+1} \le x \le x_{i+2}; \\ 0, & x_{i+2} \le x \le x_N; \end{cases} \tag{2.8}$$

$$\rho_{N-1}(x) = \begin{cases} 0, & x_0 \le x \le x_{N-3}; \\ \frac{1}{4}h^{-3}(x-x_{N-3})^3, & x_{N-3} \le x \le x_{N-2}; \\ -\frac{3}{4}h^{-3}(x-x_{N-2})^3 + \frac{3}{4}h^{-2}(x-x_{N-2})^2 & \\ +\frac{3}{4}h^{-1}(x-x_{N-2}) + \frac{1}{4}, & x_{N-2} \le x \le x_{N-1}; \\ \frac{1}{2}h^{-3}(x-x_{N-1})^3 - \frac{3}{2}h^{-2}(x-x_{N-1})^2 + & \\ +1, & x_{N-1} \le x \le x_N; \end{cases} \tag{2.9}$$

$$\rho_N(x) = \begin{cases} 0, & x_0 \le x \le x_{N-2}; \\ \frac{1}{4}h^{-3}(x-x_{N-2})^3, & x_{N-2} \le x \le x_{N-1}; \\ -\frac{1}{4}h^{-3}(x-x_{N-1})^3 + \frac{3}{4}h^{-2}(x-x_{N-1})^2 + & \\ \frac{3}{4}h^{-1}(x-x_{N-1}) + \frac{1}{4}, & x_{N-1} \le x \le x_N; \end{cases} \tag{2.10}$$

where h is the knot spacing. As in the case of linear B-splines the velocity at any x is computed as

$$\begin{aligned} V(x) &= \rho_0 a_0 + \cdots + \rho_N a_N \\ &= \sum_{i=0}^{N} \rho_i(x) a_i \end{aligned} \tag{2.11}$$

where a_i is the velocity (or CS) coefficient at knot i .

In practice, the CS coefficients are calculated at the first iteration of the inversion from the initial velocity values specified at the knots of the grid.

$$\begin{aligned} v_i &= \sum_{j=0}^{N} P_{ij} a_j \quad i,j = 0,1,\ldots,N; \\ \mathbf{v} &= \mathbf{P}\mathbf{a}, \end{aligned} \tag{2.12}$$

where $v_i = V(x_i)$ and $P_{ij} = \rho_j(x_i)$. The a_i coefficients are easily calculated by taking the inverse of the square matrix $\mathbf{P}$

$$\mathbf{a} = \mathbf{P}^{-1}\mathbf{v}. \tag{2.13}$$

It should be noted that parameterization in terms of basis splines is completely general in terms of the order of the polynomial and any kind of spline can be adopted. For example, parameterization with "step-function" B-splines (Bartels et al., 1987) would result in velocity models having constant velocities in each knot-interval — the most common parameterization in tomographic reconstructions.

2.2.3 Tricubic B-splines basis functions

In the preceding sections, we have presented two schemes for interpolation of a curve which were both based on the concept of basis functions. These functions are also needed when the interpolation is extended to more dimensions. We now extend the cubic B-splines interpolation scheme to three dimensions.

The data points lie on three perpendicular cartesian axes, x, y and z having $I+1$, $J+1$ and $K+1$ equally spaced knots. The sampling interval is constant on each axis but may differ from one axis to another. From section 2.2.2, there are three sets of cubic B-splines basis functions, ρ_i^x, ρ_j^y and ρ_k^z having dimensions $I+3$, $J+3$ and $K+3$, respectively. Because of the boundary conditions at the end points of the grid, the dimensions decrease to $I+1$, $J+1$ and $K+1$. We can now form the product of these basis functions to obtain a total of $(I+1)(J+1)(K+1)$ functions of the form

$$c_{ijk}(x,y,z) = \rho_i^x(x)\rho_j^y(y)\rho_k^z(z) \tag{2.14}$$

$$i = 0,1,\ldots,I; \quad j = 0,1,\ldots,J; \quad k = 0,1,\ldots,K.$$

It follows that any data taking value V_{ijk} at (x_i, y_j, z_k) can be interpolated to

$$V(x,y,z) = \sum_{k=0}^{K}\sum_{j=0}^{J}\sum_{i=0}^{I} c_{ijk}(x,y,z)a_{ijk} \tag{2.15}$$

which is analogous to equations 2.5 and 2.11 but in the three-dimensional formulation.

In practice, we are given the values of some function whose values are specified at the knots of a three dimensional grid, e.g., a velocity structure V_{ijk}, and we want first

to determine the a_{ijk} tricubic B-splines coefficients needed in 2.15 to determine the interpolated data values at any x, y, z. The procedure is similar to the one described in equations 2.12 and 2.13. We define:

$$c_{ijk}(x_l, y_m, z_n) = c_{ijklmn} \tag{2.16}$$

and

$$V_{ijk} = \sum_{n=0}^{K} \sum_{m=0}^{J} \sum_{l=0}^{I} c_{ijklmn} a_{lmn} \tag{2.17}$$

$i, l = 0, 1, \ldots, I-1, I;$
$j, m = 0, 1, \ldots, J-1, J;$
$k, n = 0, 1, \ldots, K-1, K.$

In equation 2.2.3, the variation on the indices ijk and lmn can be condensed into single ones, $\alpha, \beta = 1, \ldots, (I+1) \times (J+1) \times (K+1)$, to obtain:

$$V_\alpha = \sum_{\beta=1}^{(I+1)\times(J+1)\times(K+1)} c_{\alpha\beta}\ a_\beta \tag{2.18}$$

and the solution for the a_β coefficients is found using 2.13.

2.3 Inversion technique

We follow Pavlis and Booker (1980) and O'Connell (1986) in the formulation of the linearized and iterative inversion scheme.

2.3.1 Problem definition

The data of this problem consist of measured arrival times from a set of earthquakes. We define $(t_i)_j$ the i^{th} measured arrival time of a body wave phase from the j^{th} earthquake and recorded at the k^{th} station. These data are nonlinear functionals of compressional or shear wave-velocity structure and the coordinates of the hypocenters in space and time. $(t_i)_j$ can be expressed as

$$(t_i)_j = \tau_j + T_i(\mathbf{x}_k^r, \mathbf{x}_j^e, v(\mathbf{x})) + (\epsilon_i)_j, \tag{2.19}$$

$$\begin{aligned} i &= 1, 2, \ldots, n_j; \\ j &= 1, 2, \ldots, n_e; \\ k &= 1, 2, \ldots, n_s; \end{aligned}$$

where

n_j $(n_j > 4)$	number of measured arrival times for the j^{th} earthquake;
n_e	number of earthquakes;
n_s	number of recording stations;
τ_j	Origin time of the j^{th} earthquake;
$T_i(\mathbf{x}_k^r, \mathbf{x}_j^e, v(\mathbf{x}))$	i^{th} travel time between earthquake hypocenter $\mathbf{x}_j^e$ and the receiver station $\mathbf{x}_k^r$ as calculated through the *true* compressional or shear velocity model $v(\mathbf{x})$);
$(\epsilon_i)_j$	phase onset reading error for the i^{th} arrival time of the j^{th} earthquake.

The travel time can be calculated by integrating along the ray path between source and receiver

$$T_i(\mathbf{x}_k^r, \mathbf{x}_j^e, v(\mathbf{x})) \equiv (T_i)_j = \int_{\mathbf{x}_j^e}^{\mathbf{x}_k^r} \frac{1}{v(\mathbf{x})} ds \tag{2.20}$$

where for the purposes of the formulation that follows, we can drop the station index k. ds is an infinitesimal segment along the ray path; $v(\mathbf{x})$ is the velocity model which, as seen in section 2.2, can be parameterized using the basis splines formulation as

$$v(\mathbf{x}) = \sum_{k=0}^{K}\sum_{j=0}^{J}\sum_{i=0}^{I} c_{ijk}(\mathbf{x})a_{ijk} = \sum_{\alpha=0}^{m_n} c_\alpha(\mathbf{x})a_\alpha \tag{2.21}$$

$$\alpha = 1, 2, \cdots, m_n; \qquad m_n = (I+1)(J+1)(K+1).$$

Given n_e earthquakes and a total of $N = \sum_{j=1}^{n_e} n_j$ measured arrival times, the goal is to estimate the origin time τ_j, hypocenter location $\mathbf{x}_j^e$ and the velocity structure $v(\mathbf{x})$ through its parameterization in terms of m_n basis splines coefficients, a_α, that best model the observed data $(t_i)_j$.

To solve the problem, we rely on the linearization of equation 2.19

$$(t_i)_j = \hat{\tau}_j + \delta\tau_j + \hat{T}_i(\mathbf{x}_k^r, \hat{\mathbf{x}}_j^e, \hat{v}(\mathbf{x})) + \delta T_i(\mathbf{x}_k^r, \hat{\mathbf{x}}_j^e, \hat{v}(\mathbf{x})) + (\epsilon_i)_j \tag{2.22}$$

where $\hat{\tau}_j$, $\hat{\mathbf{x}}_j^e$ and $\hat{v}(\mathbf{x})$ are the current estimates of origin time, hypocentral location and velocity structure. $\hat{T}(\cdot)$ is the calculated travel time with the latter estimates. $\delta\tau_j$ and $\delta T_i(\cdot)$ are the first order perturbation terms to be applied to the current estimates.

We can define the i^{th} residual time from the j^{th} earthquake as

$$(\delta t_i)_j = (t_i)_j - (\hat{\tau}_j + (\hat{T}_i)_j) \tag{2.23}$$

and rewrite equation 2.22 in expanded form as

$$\begin{aligned}(\delta t_i)_j = \; & \delta\tau_j + \sum_{q=1}^{3} \left.\frac{\partial(\hat{T}_i)_j}{\partial x_q}\right|_{\hat{\mathbf{x}}_j^e, \hat{v}(\mathbf{x})} (\delta x_q)_j + \\ & \sum_{n=0}^{K}\sum_{m=0}^{J}\sum_{l=0}^{I} \left.\frac{\partial(\hat{T}_i)_j}{\partial a_{lmn}}\right|_{\hat{\mathbf{x}}_j^e, \hat{v}(\mathbf{x})} \delta a_{lmn} \quad + (\epsilon_i)_j\end{aligned} \tag{2.24}$$

$$q = 1, 2, 3; \qquad l = 0, 1, \cdots, I; \qquad m = 0, 1, \cdots, J; \qquad n = 0, 1, \cdots, K;$$

where

x_q spatial coordinates $(x_1, x_2, x_3) \equiv (x, y, z)$;

$I+1, J+1, K+1$ total number of grid nodes along the spatial coordinates;

$(\delta x_q)_j$ first order hypocentral perturbation of the q^{th} component of the j^{th} earthquake;

δa_{lmn} first order perturbation of the velocity basis spline coefficient for node (l, m, n) of the three dimensional grid on nodes;

$\left.\frac{\partial(\hat{T}_i)_j}{\partial x_q}\right|_{\hat{\mathbf{x}}_j^e, \hat{v}(\mathbf{x})} = -\frac{1}{V(\hat{\mathbf{x}}_j^e)} dx_q/ds$ partial derivatives of the i^{th} travel time with respect to (*wrt*) the hypocentral location of the j^{th} earthquake calculated at the current location of the focus determined with the model $\hat{v}(\mathbf{x})$;

$\left.\frac{\partial(\hat{T}_i)_j}{\partial a_{lmn}}\right|_{\hat{\mathbf{x}}_j^e, \hat{v}(\mathbf{x})} = -\int_{\hat{\mathbf{x}}_j^e}^{\mathbf{x}_k^r} \left(\frac{1}{\hat{v}(\mathbf{x})}\right)^2 \frac{\partial \hat{v}(\mathbf{x})}{\partial a_{lmn}} ds$ partial derivatives of the i^{th} travel time from the j^{th} earthquake *wrt* the velocity basis splines coefficient a_{lmn}. Current estimates of hypocentral location and velocity structure are assigned in the estimation of the partial derivatives value. It is also assumed that, to the first order, the ray path is independent of source coordinates and velocity perturbations — small changes in travel time are caused by small changes in the model (Pavlis and Booker, 1980).

Having defined the local linearization of the non linear problem described in equation 2.19, we can now take advantage of the more compact matrix notation. In the following, matrices and vectors are represented by bold, upper and lower case letters, respectively. We express equation 2.24 as

$$\begin{bmatrix} \delta\mathbf{t}_1 \\ \delta\mathbf{t}_2 \\ \vdots \\ \delta\mathbf{t}_{n_e} \end{bmatrix} \cong \begin{bmatrix} \mathbf{H}_1 & 0 & \cdots & 0 & \mathbf{M}_1 \\ 0 & \mathbf{H}_2 & \cdots & 0 & \mathbf{M}_2 \\ \vdots & \vdots & \ddots & \vdots & \vdots \\ 0 & 0 & \cdots & \mathbf{H}_{n_e} & \mathbf{M}_{n_e} \end{bmatrix} \begin{bmatrix} \delta\mathbf{h}_1 \\ \delta\mathbf{h}_2 \\ \vdots \\ \delta\mathbf{h}_{n_e} \\ \delta\mathbf{m} \end{bmatrix} \tag{2.25}$$

where

$\delta\mathbf{t}_j \in \mathcal{R}^{n_j}$ vector of residual times. $\mathcal{R}^{n_j}$ indicates the vector space of real numbers having dimension n_j;

$\mathbf{H}_j \in \mathcal{R}^{n_j \times 4}$ matrix of space-time hypocenter partial derivatives

$$(H_{iq})_j = \left.\frac{\partial(\hat{T}_i)_j}{\partial x_q}\right|_{\hat{\mathbf{x}}_j^s, \hat{v}(\mathbf{x})} \qquad q = 1,2,3; \quad (H_{i4})_j = 1;$$

$\delta\mathbf{h}_j \in \mathcal{R}^4$ vector of space-time hypocentral perturbations;

$\mathbf{M}_j \in \mathcal{R}^{n_j \times m_n}$ matrix of velocity model partial derivatives defined as

$$(M_{i\beta})_j = \left.\frac{\partial(\hat{T}_i)_j}{\partial a_\beta}\right|_{\hat{\mathbf{x}}_j^s, \hat{v}(\mathbf{x})} \qquad \beta = 1,2,\cdots,m_n$$

where $m_n = (I+1) \times (J+1) \times (K+1)$;

$\delta\mathbf{m} \in \mathcal{R}^{m_n}$ vector of basis splines coefficient perturbations $\delta m_1 = \delta a_{111}, \cdots, \delta m_{m_n} = \delta a_{(I+1)(J+1)(K+1)}$.

If we drop the index j, we can furtherly compact equation 2.25

$$\delta\mathbf{t} \cong [\mathbf{H}|\mathbf{M}] \begin{bmatrix} \delta\mathbf{h} \\ \delta\mathbf{m} \end{bmatrix} \tag{2.26}$$

where

$\delta\mathbf{t} \in \mathcal{R}^N$,

$\mathbf{H} \in \mathcal{R}^{N \times 4n_e}$,

$\mathbf{M} \in \mathcal{R}^{N \times m_n}$,

$\delta\mathbf{h} \in \mathcal{R}^{4n_e}$,

$\delta \mathbf{m} \in \mathcal{R}^{m_n}$.

The unknown reading error term $(\epsilon_i)_j$ has been assumed to be gaussian distributed with a known standard deviation $(\sigma_i)_j$ and applied as weighting term $f(\sigma_i)_j$ to the individual equations (see section 2.3.3.3).

Equation 2.26 represents a classic inverse problem of the kind

$$\mathbf{b} \cong \mathbf{A}\mathbf{x} \tag{2.27}$$

where

$$\mathbf{b} = \delta \mathbf{t} \qquad \mathbf{A} = [\mathbf{H}|\mathbf{M}] \qquad \mathbf{x} = \begin{bmatrix} \delta \mathbf{h} \\ \delta \mathbf{m} \end{bmatrix} \tag{2.28}$$

and

$\mathbf{b} \in \mathcal{R}^N$,

$\mathbf{A} \in \mathcal{R}^{N \times M}$,

$\mathbf{x} \in \mathcal{R}^M$,

$M = 4n_e + m_n$ total number of solution parameters,

$N > M$

and can be solved in various ways according to the residual norm minimization criterion that is adopted. We have selected an $\mathcal{L}^2$ norm criterion and minimized the sum of the squares of the residual arrival times

$$\min\left[\Psi(\mathbf{x})\right] = \min\left|(\mathbf{A}\mathbf{x} - \mathbf{b})\right|^2 = \min\left[(\mathbf{A}\mathbf{x} - \mathbf{b})^T(\mathbf{A}\mathbf{x} - \mathbf{b})\right]$$

Selection of an $\mathcal{L}^2$ norm will become apparent from the following considerations. It should be noticed that matrix $\mathbf{A}$ of equation 2.27 consists of two submatrices, $\mathbf{H}$ and $\mathbf{M}$. $\mathbf{H}$ increases its size of approximately a factor of $(n_e + 1)^2/n_e^2$ whenever an additional earthquake is added into the problem to the existent n_e ones. Hence, storage of its elements soon becomes intractable in terms of computer core memory

required. We find ourselves in the undesirable position that, in order to sharpen the results and improve the resolution, it would require the use of a large data set composed of several earthquakes but it soon becomes computationally impossible.

To obviate this problem, three groups of researchers (Spencer and Gubbins, 1980; Pavlis and Booker, 1980; Rodi et al., 1980) independently developed and applied a new technique to the joint problem of seismic wave velocity/hypocenter determination. This technique is known as *parameter-separation* technique and is discussed in the next section.

2.3.2 Separation of parameters

2.3.2.1 Basis

The basis of the technique lies in the application of an orthogonal transformation to equation 2.27 and use the properties of the null space of matrix $\mathbf{A}$.

In general, we are given the following problem

$$\mathbf{b} \cong \mathbf{A}\mathbf{x} \tag{2.29}$$

where

$\mathbf{b} \in \mathcal{R}^n$ data vector;

$\mathbf{A} \in \mathcal{R}^{n \times m}$ matrix defining the linear transformation;

$\mathbf{x} \in \mathcal{R}^m$ solution vector;

$n > m$.

Matrix $\mathbf{A}$ has $0 \leq rank(\mathbf{A}) \leq m$. For our purposes however, we will concentrate in the following formulation on the case in which $rank(\mathbf{A}) = m$. The general case has been discussed by various authors (e.g., Pavlis and Booker, 1980; Spencer, 1985).

We can solve equation 2.29 by adopting a least squares minimum norm criterion and define the pseudoinverse matrix $\mathbf{A}^\dagger$ in terms of some orthogonal decomposition (Lawson and Hanson, 1974)

$$\begin{aligned} \mathbf{A} &= \mathbf{H}\mathbf{R}\mathbf{K}^T \\ \mathbf{A}^\dagger &= \mathbf{K}\mathbf{R}^{-1}\mathbf{H}^T \end{aligned} \tag{2.30}$$

where

$\mathbf{H} \in \mathcal{R}^{n \times n}$ orthogonal matrix,

$\mathbf{R} \in \mathcal{R}^{n \times m}$,

$\mathbf{K} \in \mathcal{R}^{m \times m}$ orthogonal matrix

and

$$\mathbf{R} = \begin{bmatrix} \mathbf{R}_1 \\ 0 \end{bmatrix} \tag{2.31}$$

$\mathbf{R}_1 \in \mathcal{R}^{m \times m}$ non-singular triangular matrix or non-negative diagonal matrix.

It can be shown that if we define

$$\mathbf{H}^T\mathbf{b} = \begin{bmatrix} (\mathbf{b})_1 \\ (\mathbf{b})_0 \end{bmatrix} = \begin{bmatrix} (\mathbf{R})_1 \\ 0 \end{bmatrix} \mathbf{K}^T\mathbf{x} \tag{2.32}$$

where

$(\mathbf{b})_1 \in \mathcal{R}^m$,

$(\mathbf{b})_0 \in \mathcal{R}^{n-m}$,

the solution vector $\mathbf{x}$ is dependent solely on the transformed data vector $(\mathbf{b})_1$ of dimension m. This is the most important result and it is basic to the separation of parameters technique. It shows that by applying an orthogonal transformation we have decomposed the data vector $\mathbf{b}$ into two perpendicular components having m and $(n-m)$ elements. The vector $(\mathbf{b})_1$ uniquely defines the vector estimate $\hat{\mathbf{x}}$ whereas the remaining transformed data vector $(\mathbf{b})_0$ having dimension $(n-m)$ is completely independent and maps solely the residual vector. It can be shown that the residual vector can be expressed solely as function of the $(n-m)$ components of $(\mathbf{b})_0$

$$(\mathbf{b} - \mathbf{A}\hat{\mathbf{x}}) = \mathbf{H} \begin{bmatrix} 0 \\ (\mathbf{b})_0 \end{bmatrix} \tag{2.33}$$

(see Lawson and Hanson, 1974, for details)

2.3.2.2 Application

The basic result that was described in the previous section is of great importance for our needs. Equation 2.26 can be rewritten as

$$\delta \mathbf{t} \cong \mathbf{H}\delta\mathbf{h} + \mathbf{M}\delta\mathbf{m} \tag{2.34}$$

and we can apply the orthogonal decomposition previously described to the matrix of the j^{th} hypocenter partial derivatives. For our purposes, we have chosen the singular value decomposition (SVD)

$$\mathbf{H}_j = \mathbf{U}_j \mathbf{\Lambda}_j \mathbf{V}_j^T \tag{2.35}$$

where

$\mathbf{H}_j \in \mathcal{R}^{(n_j \times 4)}$,

$\mathbf{U}_j \in \mathcal{R}^{(n_j \times n_j)}$,

$\mathbf{\Lambda}_j \in \mathcal{R}^{(n_j \times 4)}$,

$\mathbf{V}_j \in \mathcal{R}^{(4 \times 4)}$,

to orthogonally decompose the matrix of the hypocenter partial derivatives $\mathbf{H}_j$ calculated from the j^{th} earthquake. Thus, we left multiply equation 2.34 by

$$\mathbf{U}_j^T = \begin{bmatrix} (\mathbf{U}_j)_1^T \\ (\mathbf{U}_j)_0^T \end{bmatrix}$$

where

$(\mathbf{U}_j)_1^T \in \mathcal{R}^{4 \times n_j}$,

$(\mathbf{U}_j)_0^T \in \mathcal{R}^{(n_j - 4) \times n_j}$,

to obtain

$$\begin{bmatrix} (\delta\mathbf{t}_j)_1 \\ (\delta\mathbf{t}_j)_0 \end{bmatrix} \cong \begin{bmatrix} (\mathbf{H}_j)_1 \\ 0 \end{bmatrix} [\delta\mathbf{h}_j] + \begin{bmatrix} (\mathbf{M}_j)_1 \\ (\mathbf{M}_j)_0 \end{bmatrix} [\delta\mathbf{m}] \tag{2.36}$$

where

$$(\delta \mathbf{t}_j)_1 = (\mathbf{U}_j)_1^T \delta \mathbf{t}_j \in \mathcal{R}^4,$$

$$(\delta \mathbf{t}_j)_0 = (\mathbf{U}_j)_0^T \delta \mathbf{t}_j \in \mathcal{R}^{n_j-4},$$

$$(\mathbf{H}_j)_1 = (\mathbf{U}_j)_1^T \mathbf{H}_j \in \mathcal{R}^{4\times 4},$$

$$\delta \mathbf{h}_j \in \mathcal{R}^4,$$

$$(\mathbf{M}_j)_1 = (\mathbf{U}_j)_1^T \mathbf{M}_j \in \mathcal{R}^{4\times m_n},$$

$$(\mathbf{M}_j)_0 = (\mathbf{U}_j)_0^T \mathbf{M}_j \in \mathcal{R}^{(n_j-4)\times m_n},$$

$$\delta \mathbf{m} \in \mathcal{R}^{m_n},$$

If we follow Pavlis and Booker (1980) terminology, matrix $(\mathbf{U}_j)_0^T$ has annihilated $\mathbf{H}_j$ and we are left with $(n_j - 4)$ linear equations that depend only on the annulled data set

$$(\delta \mathbf{t}_j)_0 \cong (\mathbf{M}_j)_0 \delta \mathbf{m} \tag{2.37}$$

which is independent of the time and space hypocentral coordinates of the j^{th} earthquake.

The computational advantage of the separation of variables technique becomes clear in what follows. Matrix $\mathbf{H}$ has a diagonal block structure and the single hypocenters are coupled only through the velocity terms. The SVD of matrix $\mathbf{H}$ in equation 2.34 preserves the the diagonal block structure

$$\mathbf{U} = \begin{bmatrix} \mathbf{U}_1 & 0 & \cdots & 0 \\ 0 & \mathbf{U}_2 & \cdots & 0 \\ \vdots & \vdots & \ddots & \vdots \\ 0 & 0 & \cdots & \mathbf{U}_{n_e} \end{bmatrix} \tag{2.38}$$

and its transpose $\mathbf{U}^T$, can be rearranged for our purposes as

$$\mathbf{U}^T = \begin{bmatrix} (\mathbf{U}_1)_1 & 0 & \cdots & 0 \\ 0 & (\mathbf{U}_2)_1 & \cdots & 0 \\ \vdots & \vdots & \ddots & \vdots \\ 0 & 0 & \cdots & (\mathbf{U}_{n_e})_1 \\ --- & --- & --- & --- \\ (\mathbf{U}_1)_0 & 0 & \cdots & 0 \\ 0 & (\mathbf{U}_2)_0 & \cdots & 0 \\ \vdots & \vdots & \ddots & \vdots \\ 0 & 0 & \cdots & (\mathbf{U}_{n_e})_0 \end{bmatrix} \tag{2.39}$$

and used to leftmultiply equation 2.34

$$\begin{bmatrix} (\delta\mathbf{t}_1)_1 \\ (\delta\mathbf{t}_2)_1 \\ \vdots \\ (\delta\mathbf{t}_{n_e})_1 \\ -- \\ (\delta\mathbf{t}_1)_0 \\ (\delta\mathbf{t}_2)_0 \\ \vdots \\ (\delta\mathbf{t}_{n_e})_0 \end{bmatrix} \cong \begin{bmatrix} (\mathbf{H}_1)_1 & 0 & \cdots & 0 \\ 0 & (\mathbf{H}_2)_1 & \cdots & 0 \\ \vdots & \vdots & \ddots & \vdots \\ 0 & 0 & \cdots & (\mathbf{H}_{n_e})_1 \\ --- & --- & --- & --- \\ 0 & 0 & \cdots & 0 \\ 0 & 0 & \cdots & 0 \\ \vdots & \vdots & \ddots & \vdots \\ 0 & 0 & \cdots & 0 \end{bmatrix} \begin{bmatrix} \delta\mathbf{h}_1 \\ \delta\mathbf{h}_2 \\ \vdots \\ \delta\mathbf{h}_{n_e} \end{bmatrix} + \begin{bmatrix} (\mathbf{M}_1)_1 \\ (\mathbf{M}_2)_1 \\ \vdots \\ (\mathbf{M}_{n_e})_1 \\ -- \\ (\mathbf{M}_1)_0 \\ (\mathbf{M}_2)_0 \\ \vdots \\ (\mathbf{M}_{n_e})_0 \end{bmatrix} [\delta\mathbf{m}] \tag{2.40}$$

where the dimensions of the individual matrix elements have been defined in equation 2.36. In analogy with equation 2.37, it results that the annulled data set to be used is

$$(\delta\mathbf{t})_0 = (\mathbf{M})_0 \delta\mathbf{m} \tag{2.41}$$

which is solved for the velocity basis spline coefficient perturbations $\delta\mathbf{m}$ using an $\mathcal{L}^2$ norm criterion which will be described in the following sections.

We notice that

I . The singular value decomposition is calculated individually for each earthquake which is very advantageous because it is not necessary to store and compute the decomposition of $\mathbf{H} \in \mathcal{R}^{N \times 4n_e}$ at once.

II . The annulled matrices $(\mathbf{M}_j)_0 \in \mathcal{R}^{(n_j-4)\times m_n}$ which are used to determine the velocity basis spline coefficient perturbations using least squares can be accumulated earthquake by earthquake as $(\mathbf{M}_j)_0^T(\mathbf{M}_j)_0 \in \mathcal{R}^{m_n \times m_n}$ without having to store in the computer core memory the large sparse matrix $(\mathbf{M})_0 \in \mathcal{R}^{N \times m_n}$.

III . In principle, the annulled equations can be solved by using any minimization criterion.

2.3.2.3 Extension to S-waves

Inclusion of S-wave measured arrival times and correspondent inversion for the S-velocity model does not introduce further complications. We define:

n_j^P	number of measured P-wave arrival times from the j^{th} earthquake;
n_j^S	number of measured S-wave arrival times from the j^{th} earthquake;
m_n^P	number of P-wave velocity basis spline coefficients;
m_n^S	number of S-wave velocity basis spline coefficients.

Following O'Connell (1986), we can express equation 2.34 for the j^{th} earthquake as

$$\begin{bmatrix} \delta \mathbf{t}_j^P \\ \delta \mathbf{t}_j^S \end{bmatrix} \cong \mathbf{H}_j \delta \mathbf{h}_j + \begin{bmatrix} \mathbf{M}_j^P & 0 \\ 0 & \mathbf{M}_j^S \end{bmatrix} \begin{bmatrix} \delta \mathbf{m}^P \\ \delta \mathbf{m}^S \end{bmatrix} \tag{2.42}$$

where

$$\delta \mathbf{t}_j^P \in \mathcal{R}^{n_j^P},$$

$$\delta \mathbf{t}_j^S \in \mathcal{R}^{n_j^S},$$

$$\mathbf{H}_j \in \mathcal{R}^{(n_j^P + n_j^S) \times 4},$$

$$\delta \mathbf{h}_j \in \mathcal{R}^4,$$

$$\mathbf{M}_j^P \in \mathcal{R}^{n_j^P \times m_n^P},$$

$$\mathbf{M}_j^S \in \mathcal{R}^{n_j^S \times m_n^S},$$

$$\delta \mathbf{m}^P \in \mathcal{R}^{m_n^P},$$

$$\delta \mathbf{m}^S \in \mathcal{R}^{m_n^S}.$$

We can equally apply the annulling transformation to equation 2.42 as was previously done for the P velocity case to obtain

$$\begin{bmatrix} (\delta \mathbf{t}_j)_1 \\ (\delta \mathbf{t}_j)_0 \end{bmatrix} \cong \begin{bmatrix} (\mathbf{H}_j)_1 \\ 0 \end{bmatrix} [\delta \mathbf{h}_j] + \begin{bmatrix} (\mathbf{S}_j^P)_1 & (\mathbf{S}_j^S)_1 \\ (\mathbf{T}_j^P)_0 & (\mathbf{T}_j^S)_0 \end{bmatrix} \begin{bmatrix} \delta \mathbf{m}^P \\ \delta \mathbf{m}^S \end{bmatrix} \tag{2.43}$$

where

$$(\delta \mathbf{t}_j)_1 \in \mathcal{R}^4,$$

$$(\delta \mathbf{t}_j)_0 \in \mathcal{R}^{(n_j^P + n_j^S) - 4},$$

$$(\mathbf{H}_j)_1 = (\mathbf{U}_j)_1^T \mathbf{H}_j \in \mathcal{R}^{4 \times 4},$$

$$\delta \mathbf{h}_j \in \mathcal{R}^4,$$

$$(\mathbf{S}_j^P)_1 \in \mathcal{R}^{4 \times m_n^P},$$

$$(\mathbf{S}_j^S)_1 \in \mathcal{R}^{4 \times m_n^S},$$

$$(\mathbf{T}_j^P)_0 \in \mathcal{R}^{(n_j^P + n_j^S - 4) \times m_n^P},$$

$$(\mathbf{T}_j^S)_0 \in \mathcal{R}^{(n_j^P + n_j^S - 4) \times m_n^S},$$

$$\delta \mathbf{m}^P \in \mathcal{R}^{m_n^P},$$

$$\delta \mathbf{m}^S \in \mathcal{R}^{m_n^S}.$$

Equation 2.43 is analogous to 2.36 and the method of solution follows analogous steps. The annulled data set used for the velocity model determination is

$$(\delta \mathbf{t}_j)_0 \cong \left[\; (\mathbf{T}_j^P)_0 \quad (\mathbf{T}_j^S)_0 \; \right] \left[\begin{array}{c} \delta \mathbf{m}^P \\ \delta \mathbf{m}^S \end{array} \right] \tag{2.44}$$

As noted by O'Connell (1986), application of the orthogonal matrix $\mathbf{U}_j$, calculated from the SVD of the matrix of hypocenter partial derivatives from both P- and S-arrival times, results in an annulled data set of mixed P and S type though, as with P-arrivals only, completely independent of the estimated hypocentral location. However, after application of the orthogonal transformation the block structure of the velocity term of equation 2.42 is no longer present in equation 2.43, and simultaneous inversion for both $\delta \mathbf{m}^P$ and $\delta \mathbf{m}^S$ adjustments is needed and to some extent P and S models are now coupled. As in the case with P- arrival times only, we accumulate the matrix product

$$\left[(\mathbf{T}_j^P)_0 (\mathbf{T}_j^S)_0 \right]^T \left[(\mathbf{T}_j^P)_0 (\mathbf{T}_j^S)_0 \right]$$

at each iteration.

2.3.3 Least squares solution

2.3.3.1 Introduction

In general, we seek a solution of equation 2.26 or, when separation of parameters is applied of equation 2.41. The separation of parameters method yields two independent data sets. The first, $(\delta \mathbf{t}_j)_1$, is used to solve for the earthquake location of the j^{th} event whereas the second, $(\delta \mathbf{t}_j)_0$, is used in the estimation of the velocity model through the calculation of some first order perturbations to the coefficients of the B-splines basis functions parameterization. In both cases we have adopted an $\mathcal{L}^2$ norm criterion, or the minimization of an objective functional consisting of the sum of the squares of the residuals (least squares). Use of this norm in the hypocenter problem permits application of the separation of parameters technique.

A fundamental difference distinguishes the matrices of partial derivatives $\mathbf{H}$ and $\mathbf{M}$ in equation 2.26: the $\mathbf{H}_j$, $j = 1, \cdots, n_e$ submatrix of $\mathbf{H}$ has always $rank(\mathbf{H}_j) = 4$ which is equal to the number of hypocenter parameters to be determined whereas matrix $\mathbf{M}$ has generally $rank(\mathbf{M}) \ll m_n$ where m_n is the total number of velocity parameters.

The reason for having matrix $\mathbf{H}_j$ of rank 4 is the nature of the earthquake location problem. For example, although the earthquake location problem is non-linear, it is generally found that, regardless what trial initial location is used, the final location is quite robust if the earthquake locates inside the network array and both P- and S-wave arrival phases are available. This implies that convergence can be achieved and the final solution is uniquely resolved.

Conversely, the reason for having $rank(\mathbf{M}) \ll m_n$ is the generally limited ray coverage provided by the source- receiver geometry and our inexact knowledge of the true ray-paths (Berryman, 1990). The elements of matrix $\mathbf{M}$ are the travel time partial derivatives with respect to the velocity coefficients calculated along the ray-path, so that $\mathbf{M}$ is sparse and ill-conditioned. It follows that the estimated model

is not unique. To partially obviate this problem, some *a priori* information on the estimates of the model parameter adjustments $\delta\mathbf{m}$ needs to be included to stabilize the solution. This process of adding *a priori* information is also known as *regularization*.

Another aspect that should be included when solving an inverse problem is provided by the errors in the recorded data. For example, P- arrival times determined from an impulsive P- waveform are more accurate than an emergent arrival of the same phase. S- arrival phases are always much more difficult to measure because their first break is in the coda of the P- arrival and because their frequency content is peaked at lower frequencies. These errors affect the solution vector and it is desirable to weight the linear equations according to some estimated measure of the unknown error of the data.

In summary, it should be reminded that the solution of our problem is based on the local linearization of a non-linear problem. A solution is found by iterating from an initial velocity model until some minimum of the objective functional is determined. In general, different initial models will be the departure points for different descent paths in the minimization, and it is to be expected that nonuniqueness is one of the inevitable burdens of the estimated solution.

2.3.3.2 Basis

We now focus on the different operations that can be performed on the general inverse problem stated in equation 2.29 where we now suppose that $rank(\mathbf{A}) < m$,

$$\mathbf{b} \cong \mathbf{A}\mathbf{x}$$

where

$\mathbf{b} \in \mathcal{R}^n$ data vector,

$\mathbf{A} \in \mathcal{R}^{n \times m}$ matrix defining the linear transformation,

$\mathbf{x} \in \mathcal{R}^m$ solution vector,

$$n \gg m,$$

$$rank(\mathbf{A}) < m,$$

and whose $\mathcal{L}^2$ solution $\hat{\mathbf{x}}$, can be found through the minimization of the objective functional

$$\Psi(\mathbf{x}) = |(\mathbf{Ax} - \mathbf{b})|^2 = \left[(\mathbf{Ax} - \mathbf{b})^T(\mathbf{Ax} - \mathbf{b})\right] \tag{2.45}$$

as

$$\begin{aligned} \hat{\mathbf{x}} &= \left(\mathbf{A}^T\mathbf{A}\right)^{-1}\mathbf{A}^T\mathbf{b} \\ &= \mathbf{A}^\dagger\mathbf{b} \end{aligned} \tag{2.46}$$

where

$$\mathbf{A}^\dagger = \left(\mathbf{A}^T\mathbf{A}\right)^{-1}\mathbf{A}^T$$

is the Penrose pseudoinverse[1] of $\mathbf{A}$ (Lawson and Hanson, 1974).

From the arguments in section 2.3.3.1, we need to stabilize the solution vector $\hat{\mathbf{x}}$ by adding some *a priori* information. We follow Lawson and Hanson to outline the four basic operations that can be applied to equation 2.29:

1 . Left multiplication of $\mathbf{A}$ and $\mathbf{b}$ by an $(n \times n)$ matrix $\mathbf{G}$;

2 . Append additional rows to $\mathbf{A}$ and $\mathbf{b}$;

3 . Right multiplication of $\mathbf{A}$ by a matrix $\mathbf{H}$ and change of variables $\mathbf{x} = \mathbf{H}\tilde{\mathbf{x}} + \xi$;

4 . Assign zero values to some components of the solution vector $\mathbf{x}$.

In the following, we will describe in detail the first two operations of Lawson and Hanson, because only those have been applied to our problem.

[1] $\mathbf{A}^\dagger$ is also called the Moore-Penrose inverse or more commonly the *generalized inverse* of $\mathbf{A}$ (Strang, 1976).

Left multiplication of A and b: It consists of left multiplying the matrix of coefficients $\mathbf{A}$ and the data vector $\mathbf{b}$ by a matrix $\mathbf{G}$

$$\mathbf{Gb} \cong \mathbf{GAx} \tag{2.47}$$

where

$$\mathbf{G} \in \mathcal{R}^{n \times n}$$

and it corresponds to minimization of the objective functional

$$\Psi^{\mathbf{G}}(\mathbf{x}) = (\mathbf{b} - \mathbf{Ax})^T \left(\mathbf{G}^T\mathbf{G}\right)(\mathbf{b} - \mathbf{Ax}).$$

Left multiplication is commonly done using a diagonal matrix $\mathbf{G}$ and, in this case, it can be interpreted as a row scaling operation in which each i^{th} row of $\mathbf{A}$ and $\mathbf{b}$ is multiplied by a real non-negative number g_{ii}. Assigning a large value to g_{ii} corresponds to weighting more the i^{th} equation which will cause the correspondent residual to be smaller. This procedure is generally referred as weighted least squares and the weights are commonly chosen to be some function of the standard deviations of the uncertainty of the i^{th} datum b_i. Overall, this operation constitutes conditioning the data space.

Appending rows to A and b: The second operation consists of appending rows to the original problem defined in equation 2.29.

$$\begin{bmatrix} \mathbf{A} \\ \mu\mathbf{F} \end{bmatrix} \mathbf{x} \cong \begin{bmatrix} \mathbf{b} \\ \mathbf{d} \end{bmatrix} \tag{2.48}$$

where

$$\mathbf{F} \in \mathcal{R}^{l \times m},$$

$$\mathbf{d} \in \mathcal{R}^{l},$$

$$\mu \in \mathcal{R}^{+}.$$

This operation can be illustrated more clearly by supposing the following special case. We would like to obtain a solution $\hat{\mathbf{x}}$ closer to a known vector ξ. To this purpose we set $\mathbf{F} = \mathbf{I}_m$, $\mathbf{I}_m \in \mathcal{R}^{m \times m}$ being the identity matrix, and $\mathbf{d} = \xi$. μ is a non-negative parameter that weights the preference toward an estimate of this kind. In a more general case, when one has sufficient *a priori* statistical information or there are physical constraints about the expected value ξ of the solution vector $\mathbf{x}$ and the interdependencies among the various components ξ_i, it is possible to incorporate this information in the matrix $\mathbf{F}$ which will no longer be an identity matrix. Overall, when appending rows to equation 2.29, we minimize the following objective functional

$$\Psi^{\mu}(\mathbf{x}) = (\mathbf{b} - \mathbf{A}\mathbf{x})^T (\mathbf{b} - \mathbf{A}\mathbf{x}) + \mu^2 (\mathbf{x} - \xi)^T \left(\mathbf{F}^T\mathbf{F}\right) (\mathbf{x} - \xi).$$

This minimization can be assessed by assigning extreme values to the parameter μ which is also called the damping parameter. It is easy to verify that when $\mu = 0$, we minimize the original objective function $\Psi(\mathbf{x})$ of equation 2.45, whereas when μ is large, and large is intended if $\mu \gg \lambda_1$ where λ_1 is the largest eigenvalue of the SVD of $\mathbf{A}$, the solution $\hat{\mathbf{x}}$ attains the *a priori* expected value which was set as $\xi = \mathbf{F}^{-1}\mathbf{d}$. Minimization of $\Psi^{\mu}(\mathbf{x})$ as function of μ is also commonly referred as *ridge regression* or *damped least squares* and it is usually solved by adopting the Marquardt technique (Marquardt, 1963, 1970).

For completeness, we also discuss briefly the remaining two operations listed by Lawson and Hanson (1974) and explain the practical reasons why they have not been included in our problem. The third operation consists of right multiplying $\mathbf{A}$ by a matrix $\mathbf{H}$ and changing the solution vector $\mathbf{x}$ to $\mathbf{x} = \mathbf{H}\tilde{\mathbf{x}}$. This operation can be visualized as a column scaling operation which alters in the parameter space the weight of the individual parameters. This operation has been applied in tomographic problems to scale well and poorly sampled parts of the model and also to scale for different knot spacing on the same axis (Nolet, 1987). We note that the same effect can

be obtained by the operation of appending rows using a suitable matrix $\mathbf{F}$. Overall, application of right multiplication constitutes conditioning the parameter space.

The fourth and last operation that Lawson and Hanson describe consists of deleting some of the variables of the solution vector $\mathbf{x}$. Although various schemes have been envisaged to properly delete some variables without altering the solution, it remains unclear the amount that one variable x_j $(j = 1, \cdots, m)$ of $\mathbf{x}$ contributes to the minimization. As stated by Lawson and Hanson, one way to circumvent this problem is by applying a linear transformation to obtain a new set of variables whose individual effects on the transformed residual vector are mutually independent. A clear description of the methodology is provided by Lawson and Hanson (p. 196). This linear transformation is analogous to the process previously described in the basis for separation of variables, i.e., each new variable is function of the corresponding eigenvalue of the SVD of $\mathbf{A}$. It follows that either a cut-off criterion which preserves the largest eigenvalues or a non-negative damping parameter can be selected to this purpose.

Summary: Application of the first two operations to equation 2.29 can be expressed as

$$\begin{bmatrix} \tilde{\mathbf{A}} \\ \mu\mathbf{F} \end{bmatrix} \mathbf{x} \cong \begin{bmatrix} \tilde{\mathbf{b}} \\ \mu\mathbf{d} \end{bmatrix} \tag{2.49}$$

where

$\tilde{\mathbf{A}} = \mathbf{GA} \in \mathcal{R}^{n \times m}$,

$\mathbf{G} \in \mathcal{R}^{n \times n}$,

$\mathbf{F} \in \mathcal{R}^{l \times m}$,

$\mu \in \mathcal{R}^{+}$,

$$\tilde{\mathbf{b}} = \mathbf{G}\mathbf{b} \in \mathcal{R}^n,$$

$$\mathbf{d} = \mathbf{F}\xi \in \mathcal{R}^l,$$

$$\xi \in \mathcal{R}^n,$$

and corresponds to the minimization of

$$\Psi_\mu^{\mathbf{G}}(\mathbf{x}) = (\mathbf{b} - \mathbf{A}\mathbf{x})^T \left(\mathbf{G}^T\mathbf{G}\right)(\mathbf{b} - \mathbf{A}\mathbf{x}) + \mu^2 (\mathbf{x} - \xi)^T \left(\mathbf{F}^T\mathbf{F}\right)(\mathbf{x} - \xi).$$

We now analyze the way the first two operations have been implemented in our specific problem of non-linear inversion of travel time data for velocity and hypocenters described in equation 2.26.

2.3.3.3 Conditioning the *data* space

This case corresponds to the first operation, row scaling, which was previously reviewed. For the j^{th} earthquake, we have selected a diagonal matrix $\mathbf{G}_j \in \mathcal{R}^{n_j \times n_j}$, $(j = 1, \cdots, n_e)$, whose elements g_{ii}^j, $(i = 1, \cdots, n_j)$ are functions of the estimated standard deviation of the reading error of the i^{th} observation (i.e., arrival time) and of the source-receiver distance. The source-receiver distance weighting term accounts for the diminished accuracy of the ray tracer at larger distances.

$$g_{ii}^j = f_d\left((\sigma_i)_j\right) f_h\left(\left|\mathbf{x}_i^r - \mathbf{x}_j^e\right|\right) \tag{2.50}$$

where

$f_d\left((\sigma_i)_j\right)$	weighting scheme defined in table 2.1;
$\mathbf{x}_i^r$	location of the receiver recording the i^{th} phase from the j^{th} earthquake;
$\mathbf{x}_j^e$	location of the j^{th} earthquake;

and

$$f_h\left(\left|\mathbf{x}_i^r - \mathbf{x}_j^e\right|\right) = \begin{cases} 1, & \left|\mathbf{x}_i^r - \mathbf{x}_j^e\right| \leq X_1; \\ 1 - \frac{\left|\mathbf{x}_i^r - \mathbf{x}_j^e\right| - X_1}{X_2 - X_1}, & X_1 < \left|\mathbf{x}_i^r - \mathbf{x}_j^e\right| < X_2; \\ 0, & \left|\mathbf{x}_i^r - \mathbf{x}_j^e\right| \geq X_2; \end{cases} \tag{2.51}$$

where X_1 and X_2 ($X_1 \leq X_2$) are distance thresholds to be defined according to the ray-tracer accuracy.

Reading errors of individual phases in our input files are given in terms of the USGS quality designators which are listed in table 2.1. The last two columns of this table list the corresponding standard error criterion adopted to assign the individual quality values for the Parkfield and Loma Prieta data sets which are analyzed in chapter 4 and 5, respectively.

PHASE WEIGHTING			
USGS quality	$f_d(\cdot)$	σ^a	σ^b
0	1.0	0.002	0.020
1	0.5	0.005	0.040
2	0.25	0.010	0.080
3	0.125	0.025	0.160
4	0.0		

[a] Estimated standard deviation of the onset reading error for the Parkfield data set (values are in seconds).
[b] Same as above but for the Loma Prieta data set.

Table 2.1: This table summarizes the reading error weighting scheme adopted for the row scaling operation.

This row scaling does not affect the structure of the matrix operations in equations 2.42 and 2.43, where, each row was assigned a unit weight. In the following, we will assume that weighting has been applied and will introduce a tilde symbol above vectors and matrices, e.g., $\tilde{\delta\mathbf{t}} = \mathbf{G}\delta\mathbf{t}$.

2.3.3.4 Conditioning the *parameter* space

It consists of appending some additional rows to equation 2.44

$$\begin{bmatrix} (\tilde{\delta \mathbf{t}})_0 \\ \mu \mathbf{d} \end{bmatrix} \cong \begin{bmatrix} (\tilde{\mathbf{T}}^P)_0 & (\tilde{\mathbf{T}}^P)_0 \\ & \mu \mathbf{F} \end{bmatrix} \begin{bmatrix} \delta \mathbf{m}^P \\ \delta \mathbf{m}^S \end{bmatrix} \tag{2.52}$$

where

$$(\tilde{\delta \mathbf{t}})_0 \in \mathcal{R}^{N-4n_e},$$

$$\mathbf{d} = \mathbf{F}\xi \in \mathcal{R}^l,$$

$$\mu \in \mathcal{R}^+,$$

$$(\tilde{\mathbf{T}}^P)_0 \in \mathcal{R}^{(N-4n_e)\times m_n^P},$$

$$(\tilde{\mathbf{T}}^S)_0 \in \mathcal{R}^{(N-4n_e)\times m_n^S},$$

$$\mathbf{F} \in \mathcal{R}^{l\times(m_n^P+m_n^S)},$$

$$\xi^P \in \mathcal{R}^{m_n^P},$$

$$\xi^S \in \mathcal{R}^{m_n^S}.$$

Matrix $\mathbf{F}$ and vector $\mathbf{d}$ permit to incorporate some *a priori* information into the solution vector. Jackson (1979) names these additional rows the *a priori* data. To find the solution to our problem we have to minimize the following objective functional

$$\tilde{\Psi}_\mu \left(\delta \mathbf{m}^P, \delta \mathbf{m}^S\right) =$$

$$= \left(\left[(\tilde{\mathbf{T}}^P)_0 (\tilde{\mathbf{T}}^S)_0\right] \begin{bmatrix} \delta \mathbf{m}^P \\ \delta \mathbf{m}^S \end{bmatrix} - (\tilde{\delta \mathbf{t}})_0 \right)^T \left(\left[(\tilde{\mathbf{T}}^P)_0 (\tilde{\mathbf{T}}^S)_0\right] \begin{bmatrix} \delta \mathbf{m}^P \\ \delta \mathbf{m}^S \end{bmatrix} - (\tilde{\delta \mathbf{t}})_0 \right) +$$

$$+\mu^2 \left(\begin{bmatrix} \delta \mathbf{m}^P \\ \delta \mathbf{m}^S \end{bmatrix} - \begin{bmatrix} \xi^P \\ \xi^S \end{bmatrix} \right)^T \left(\mathbf{F}^T \mathbf{F}\right) \left(\begin{bmatrix} \delta \mathbf{m}^P \\ \delta \mathbf{m}^S \end{bmatrix} - \begin{bmatrix} \xi^P \\ \xi^S \end{bmatrix} \right)$$

For our purposes, however, we can simplify in part the problem by setting equal the number of P- and S- velocity parameters.

We have used the following considerations in setting up the rows of matrix $\mathbf{F}$.

1 . The solution vector in our linearized inversion consists of perturbations needed to augment a current model. We would like to determine the smallest perturbations which are needed in order to obtain the largest decrease of the objective functional and at the same time prevent the descent path from falling into a local minimum. With this in mind, we can condition the parameter space by adding the following set of linear equations to (2.44)

$$\begin{bmatrix} \mu_P \mathbf{I}_m & 0 \\ 0 & \mu_S \mathbf{I}_m \end{bmatrix} \begin{bmatrix} \delta \mathbf{m}^P \\ \delta \mathbf{m}^S \end{bmatrix} = [\mathbf{0}] \tag{2.53}$$

where

$m_n^P = m_n^S = m$ equal number of P- and S- velocity coefficients (i.e., nodes);

$\mathbf{I}_m \in \mathcal{R}^{m \times m}$ Identity matrix;

$\mu_\chi \ (\chi \equiv P, S) \in \mathcal{R}^+$ P- and S-velocity damping parameter;

$\mathbf{0} = \mathbf{d} \in \mathcal{R}^{2m}$ vector of zeros

μ_P and μ_S should be set as $\mu_P/\mu_S = V_S/V_P$ because they act on the P- and S- velocity model respectively (O'Connell, 1986; Eberhart-Phillips, 1989). Determination of the proper values to be assigned to these constants will be addressed in section 2.3.5.2

2 . Reliable estimates of V_P/V_S ratios are important because they impose strong constraints in the identification of rock types. Unfortunately, P- and S-ray coverage generally differs through the volume to be imaged because fewer S-waves are read. This different ray coverage when combined to other factors such as discretization and parameterization

of the velocity model and onset reading errors, can cause fictitious relatively large or small values of V_P/V_S ratios. This will result in misidentification of rock types and biased interpretation. Our aim is to limit as much as possible these wrong diagnostics but also to be able to identify possible V_P/V_S anomalies. To this end, we can try to direct the solution, at least in the first iterations of the non-linear inversion, toward some preselected average value of V_P/V_S which was previously determined from the data. Eventually, this preference can be released in the later iterations. To achieve this goal, the following set of linear equations that condition the V_P/V_S ratios can be appended to equation 2.44

$$\left[\begin{array}{cc} \eta_{PS}\mathbf{I}_m & -\eta_{PS}\kappa\mathbf{I}_m \end{array} \right] \left[\begin{array}{c} \delta\mathbf{m}^P \\ \delta\mathbf{m}^S \end{array} \right] = [\mathbf{0}] \tag{2.54}$$

where

$\eta_{PS} \in \mathcal{R}^+$ is a preselected constant whose value defines the preference toward a pre-assigned value of the ratio $\kappa = V_P/V_S$.

3. Individual nodes of the three-dimensional grid are sampled unevenly and preferentially along certain directions. We can correct this problem to some degree by adding the following conditions to equation (2.44)

$$\left[\begin{array}{cc} \eta_P^D\mathbf{J}_m^P & 0 \\ 0 & \eta_S^D\mathbf{J}_m^S \end{array} \right] \left[\begin{array}{c} \delta\mathbf{m}^P \\ \delta\mathbf{m}^S \end{array} \right] = [\mathbf{0}] \tag{2.55}$$

where

$\chi \equiv P, S;$

$\eta_\chi^D, \in \mathcal{R}^+$ preselected constants whose value defines the preference toward enhancing and damping the perturbations for poorly and well sampled nodes respectively;

$\mathbf{J}_m^\chi \in \mathcal{R}^{m \times m}$ ray density diagonal matrix having elements

$$j_{ii}^\chi = \frac{\sum_{j=1}^{N^\chi} \sum_{k=1}^{j_k} c_{ij}(\mathbf{x}_k^\chi)}{\sum_{i=1}^{m_n^\chi} \sum_{j=1}^{N^\chi} \sum_{k=1}^{j_k} c_{ij}(\mathbf{x}_k^\chi)}$$

where

N^χ total number of ray-paths for the χ-model;

$c_{ij}^\chi(\mathbf{x}_k)$ value attained by the i^{th} B-spline basis function from the j^{th} ray path. $\mathbf{x}_k^\chi$ indicates the mid point of the k^{th} segment along the j^{th} ray path. Each ray path is discretized in j_k segments.

4 . Finally, it is desirable to determine models which are inherently simple. In part this is already achieved by means of the velocity parameterization specified in terms of tricubic B-splines basis functions but also it can be obtained explicitly by conditioning the velocity parameter space so that the spatial derivatives of the B-splines perturbations are minimized. Like others (e.g., Lees and Crosson, 1989; Sambridge, 1990; Pulliam, 1991) we can condition the models to be laterally homogeneous by adding either a first or a second derivative (Laplacian) and equate it to zero. The following linear equations can be added to equation 2.44

$$\begin{bmatrix} \eta_P^{\partial}\partial & 0 \\ 0 & \eta_S^{\partial}\partial \end{bmatrix} \begin{bmatrix} \delta\mathbf{m}^P \\ \delta\mathbf{m}^S \end{bmatrix} = [\mathbf{0}] \tag{2.56}$$

where

$\partial \in \mathcal{R}^{[(K+1)(2IJ+I+J)]\times m}$ condition matrix of first derivatives;

η_χ^{∂}, $(\chi = P, S) \in \mathcal{R}^+$ preselected constant whose value defines the preference toward minimizing the first spatial derivatives of the in-layer velocity coefficient perturbations;

$I+1$, $J+1$, $K+1$ total number of nodes along the 3-D cartesian axes

and analogously for the second derivatives

$$\begin{bmatrix} \eta_P^{\nabla^2}\partial^2 & 0 \\ 0 & \eta_S^{\nabla^2}\partial^2 \end{bmatrix} \begin{bmatrix} \delta\mathbf{m}^P \\ \delta\mathbf{m}^S \end{bmatrix} = [\mathbf{0}] \tag{2.57}$$

where

$\partial^2 \in \mathcal{R}^{[2(K+1)(IJ-1)]\times m}$ condition matrix of second derivatives,

$\eta_\chi^{\nabla^2}$, $(\chi = P, S) \in \mathcal{R}^+$ preselected constant whose value define the preference toward minimizing the second spatial derivatives of the in-layer velocity coefficient perturbations

If we now implement the *a priori* information, we can write the following system of equations

$$\left[(\hat{\delta\mathbf{t}})_0\right] \cong \begin{bmatrix} (\hat{\mathbf{T}}^P)_0 & (\hat{\mathbf{T}}^S)_0 \\ \mu_P \mathbf{I}_m & 0 \\ 0 & \mu_S \mathbf{I}_m \\ \eta_{PS}\mathbf{I}_m & -\eta_{PS}\kappa\mathbf{I}_m \\ \eta_P^D \mathbf{J}_m^P & 0 \\ 0 & \eta_S^D \mathbf{J}_m^S \\ \eta_P^D \mathbf{J}_m^P & 0 \\ 0 & \eta_S^D \mathbf{J}_m^S \\ \eta_P^\partial \partial & 0 \\ 0 & \eta_S^\partial \partial \\ \eta_P^{\nabla^2} \partial^2 & 0 \\ 0 & \eta_S^{\nabla^2} \partial^2 \end{bmatrix} \begin{bmatrix} \delta\mathbf{m}^P \\ \delta\mathbf{m}^S \end{bmatrix} \tag{2.58}$$

and the least squares solution of equation 2.58 is

$$\begin{aligned} \begin{bmatrix} \delta\hat{\mathbf{m}}^P \\ \delta\hat{\mathbf{m}}^S \end{bmatrix} = \Bigg(& \begin{bmatrix} (\hat{\mathbf{T}}^P)_0^T(\hat{\mathbf{T}}^P)_0 & (\hat{\mathbf{T}}^P)_0^T(\hat{\mathbf{T}}^S)_0 \\ (\hat{\mathbf{T}}^S)_0^T(\hat{\mathbf{T}}^P)_0 & (\hat{\mathbf{T}}^S)_0^T(\hat{\mathbf{T}}^S)_0 \end{bmatrix} + \begin{bmatrix} \mu_P^2\mathbf{I}_m & 0 \\ 0 & \mu_S^2\mathbf{I}_m \end{bmatrix} + \\ & + \eta_{PS}^2 \begin{bmatrix} \mathbf{I}_m & -\kappa\mathbf{I}_m \\ -\kappa\mathbf{I}_m & \kappa^2\mathbf{I}_m \end{bmatrix} + \begin{bmatrix} \eta_P^{D\,2}\mathbf{J}_m^{P\,2} & 0 \\ 0 & \eta_S^{D\,2}\mathbf{J}_m^{S\,2} \end{bmatrix} + \\ & + \begin{bmatrix} \eta_P^{\partial\,2}\partial^T\partial & 0 \\ 0 & \eta_S^{\partial\,2}\partial^T\partial \end{bmatrix} + \begin{bmatrix} \eta_P^{\nabla^2\,2}\partial^{2T}\partial^2 & 0 \\ 0 & \eta_S^{\nabla^2\,2}\partial^{2T}\partial^2 \end{bmatrix} \Bigg)^{-1} \cdot \\ & \cdot \begin{bmatrix} (\hat{\mathbf{T}}^P)_0^T \\ (\hat{\mathbf{T}}^S)_0^T \end{bmatrix} (\hat{\delta\mathbf{t}})_0 \end{aligned} \tag{2.59}$$

In practice, we have partitioned $\mathbf{F}$ in 22 submatrices of which only 12 contain non-zero elements.

If only the first matrix term within the parenthesis on the *rhs* of equation 2.59 were used, we would solve using the Penrose pseudoinverse with no conditioning applied. However to stabilize the inversion, we would have to apply some cut-off criterion to eliminate the small eigenvalues from the solution vector. The following matrix terms in the *rhs* of 2.59 indicate the preferences toward some solution vector and reflect our *a priori* conditioning.

The values of μ and η each weight some *a priori* information term in the final solution. However in this formulation, there is a difference between μ and η constants. μ's are recalculated at each iteration according to a criterion which is described in

section 2.3.5.2 whereas all the η's are set at the beginning of the iterative procedure and maintained constant. In chapter 3 where we present a series of tests with synthetic data, we will throughly address the effects that each *a priori* information term has on the final model.

2.3.4 Resolution and errors

Having determined some estimates of the model parameters, we now turn into the assessment of their errors. To this purpose, two matrices, resolution and covariance of the model parameters, are needed to appraise the results. Resolution shows to what degree each parameter is independently resolved by the data whereas the covariance provides an estimate of how errors in the data are mapped into the model parameter estimates.

2.3.4.1 Resolution

Before describing the calculation of the resolution matrix, we emphasize that the configuration of the experiment in which the data are collected is of fundamental importance in attaining good resolution because it is the geometry of an experiment and the measured physical phenomenum (with its relative functional form, e.g. gravity, magnetics or seismic waves) that define the number of independent parameters that can be resolved with the available data set.

In a general case, following Jackson (1979), an estimate of the solution vector of the inverse problem

$$\delta \mathbf{t} \cong \mathbf{T}\delta \mathbf{m} \tag{2.60}$$

can be found from the formulation given in the previous sections as

$$\delta \hat{\mathbf{m}} = \mathbf{T}^{+}\delta \mathbf{t} \tag{2.61}$$

where

$\delta \hat{\mathbf{m}} = \in \mathcal{R}^{m_n^P + m_n^S}$ estimated solution vector;

$\mathbf{T}^{+} \in \mathcal{R}^{(m_n^P + m_n^S)\times(N-4n_e)}$ linear estimator which corresponds to the term on the *rhs* that left multiplies $(\tilde{\delta \mathbf{t}})_0$ in equation 2.59;

$\delta \mathbf{t} \equiv (\tilde{\delta \mathbf{t}})_0 \in \mathcal{R}^{N-4n_e}$ data vector;

and

$$\mathbf{T} \equiv \left[(\tilde{\mathbf{T}}^P)_0 (\tilde{\mathbf{T}}^S)_0\right] \in \mathcal{R}^{(N-4n_e)\times(m_n^P+m_n^S)}.$$

Equation 2.61 can be written as

$$\delta\hat{\mathbf{m}} = \mathbf{R}\delta\mathbf{m} \tag{2.62}$$

where

$$\mathbf{R} = \mathbf{T}^+\mathbf{T} \in \mathcal{R}^{(m_n^P+m_n^S)\times(m_n^P+m_n^S)} \tag{2.63}$$

is the resolution matrix. In the interpretation given by Jackson (1979), the rows of $\mathbf{R}$ are a set of filters through which we see the true model vector.

2.3.4.2 Spread function

One problem in displaying tomographic reconstructions is the difficulty of simultaneously representing both model and resolution, i.e., defining which parts of the model are well resolved. When a large problem is solved, formal calculations of resolution are impossible because of the computer core memory that would be required. For smaller problems such as ours, formal calculation of the resolution matrix is possible, raising the problem of some visual display for the information contained in this matrix. Given that each row of the resolution matrix is a vector and that graphical representation of a multi-dimensional vector is difficult, we must condense the information contained in each row into a single scalar value for each parameter. We chose to calculate the *spread function* of Backus and Gilbert, (Menke, 1984, Toomey and Foulger, 1989), for each row of the resolution matrix which, in a general case, is

$$spread(\mathbf{r}_i) = \sum_{j=1}^{m} D_{ij} R_{ij}^2$$

where

$\mathbf{r}_i \in \mathcal{R}^m$ $\quad$ i^{th} row of the resolution matrix $\mathbf{R}$;

D_{ij} ij element of the *penalty matrix* $\mathbf{D}$ which can be conveniently chosen as some distance between the i^{th} and j^{th} parameter;

m size of the solution vector.

The scalar value $spread(\mathbf{r}_i)$ determines how much the i^{th} row differs from a delta function. A zero value indicates an exact delta function. Matrix $\mathbf{D}$ penalizes cases in which the rows of $\mathbf{R}$ differ significantly from the delta function. For example in a 3-D geometry, D_{ij} is usually defined as the distance between the i^{th} and j^{th} node of the grid.

It should now be noted that in our formulation matrix $\mathbf{R}$ is of mixed type because we solve simultaneously for P- and S-velocity adjustments. This causes some problems in defining the penalty matrix $\mathbf{D}$ because it is difficult to chose a criterion that permits to penalize properly the amount of coupling between P- and S-models.

To circumvent this problem, we partition the resolution matrix as follows

$$\mathbf{R} = \begin{bmatrix} \mathbf{R}^{PP} & \mathbf{R}^{PS} \\ \mathbf{R}^{SP} & \mathbf{R}^{SS} \end{bmatrix}$$

where

$\mathbf{R}^{PP} \in \mathcal{R}^{m_n^P \times m_n^P}$ mapping of the P-parameter resolution onto the P-parameter subspace;

$\mathbf{R}^{PS} \in \mathcal{R}^{m_n^P \times m_n^S}$ mapping of the P-parameter resolution onto the S-parameter subspace;

$\mathbf{R}^{SP} \in \mathcal{R}^{m_n^S \times m_n^P}$ mapping of the S-parameter resolution onto the P-parameter subspace;

$\mathbf{R}^{SS} \in \mathcal{R}^{m_n^S \times m_n^S}$ mapping of the S-parameter resolution onto the S-parameter subspace.

We define also the vector $\mathbf{r}_j^{PP}$ as the j^{th} row of the partitioned matrix $\mathbf{R}^{PP}$ and analogously $\mathbf{r}_j^{PS}$, $\mathbf{r}_j^{SP}$ and $\mathbf{r}_j^{SS}$ for $\mathbf{R}^{PS}$, $\mathbf{R}^{SP}$ and $\mathbf{R}^{SS}$, respectively.

We determine two scalar quantities from the resolution matrix for each parameter. The first quantity is the spread function for each parameter, which is calculated using only the corresponding part of the resolution matrix, i.e., for the j^{th} P parameter the correspondent row of $\mathbf{R}^{PP}$, $\mathbf{r}_j^{PP}$. The second instead, that we can name the *coupling function*, evaluates the amount of coupling between P and S (or S and P) for a given parameter as defined by the corresponding rows of $\mathbf{R}^{PP}$ and $\mathbf{R}^{PS}$ (or $\mathbf{R}^{SS}$ and $\mathbf{R}^{SP}$). In the analysis, the *spread function* was defined as follows:

$$s_i^{\chi} = \log\left(|\mathbf{r}_i^{\chi\chi}|^{-1} \sum_{j=1}^{m_n^{\chi}} \left(\frac{R_{ij}^{\chi\chi}}{|\mathbf{r}_i^{\chi\chi}|}\right)^2 D_{ij}^{\chi}\right) \qquad (2.64)$$

$$i, j = 1, \cdots, m_n^{\chi};$$

where

$\chi \equiv P, S;$

$\mathbf{s}^{\chi} \in \mathcal{R}^{m_n^{\chi}}$ spread function vector relative to χ velocity model;

$\mathbf{r}_i^{\chi\chi} \in \mathcal{R}^{m_n^{\chi}};$

$|\mathbf{r}_i^{\chi\chi}| \in \mathcal{R}^{m_n^{\chi}}$ i^{th} row normalizing factor calculated as

$$|\mathbf{r}_i^{\chi\chi}| = \sqrt{\sum_{j=1}^{m_n^{\chi}} R_{ij}^2} \quad ;$$

R_{ij} ij^{th} element of the resolution matrix $\mathbf{R}$;

$\mathbf{D} \in \mathcal{R}^{m_n^{\chi} \times m_n^{\chi}}$ penalty matrix having as elements the distances in kilometers between pairs of nodes.

The *coupling function* is defined as

$$z_i^{\chi\Phi} = \log\left(\frac{\sum_{j=1}^{m_n^\chi}\left|R_{ij}^{\chi\chi}\right|}{\sum_{k=1}^{m_n^\Phi}\left|R_{ik}^{\chi\Phi}\right|}\right) \tag{2.65}$$

where

$$\chi, \Phi \equiv P, S \quad (\chi \neq \Phi);$$

In the analysis of the spread function according to our formulation, a perfectly resolved parameter has a value that tends to $-\infty$ whereas large values correspond to parameters having broad kernel shapes and small overall values of $\mathbf{R}$. In practice, the spread function provides a scalar value for the amount of smearing in each row of the resolution matrix. This analysis makes it possible to display both the estimated model and its resolution in a single display (see figure 3.3 for an example). More critical interpretations of the results can be achieved because the well-resolved parts of the model can be promptly visualized.

Large values of the coupling function will indicate limited coupling between the two velocity model parameters[2] and analogously, we can display the resolved P-model and the amount of coupling with the S-model (or viceversa) on the same display (see figure 3.3 for an example)[3].

2.3.4.3 Covariance

The covariance matrix indicates how the errors of the data map into the solution vector. Here, we follow the definitions given by Jackson (1979) and Tarantola and Valette (1982). The *a posteriori* covariance matrix is given by

$$\mathbf{C} = (\mathbf{A}^T\mathbf{C}_e^{-1}\mathbf{A} + \mathbf{C}_x^{-1})^{-1}. \tag{2.66}$$

Comparing this definition with our formulation, yields

[2]Perhaps a more appropriate denomination for the coupling function would be *decoupling function*, i.e., larger values and less coupling.

[3]In the actual calculations of the spread and coupling functions, some instabilities can arise because $\mathbf{R}$ can attain very small values. To prevent this problem, some small value ($\approx 10^{-3}$) should be added to all elements of $\mathbf{R}$.

$$\mathbf{C}_e^{-1} = \mathbf{G}^T\mathbf{G}$$

and

$$\mathbf{C}_x^{-1} = \begin{bmatrix} \mu_P^2\mathbf{I}_m & 0 \\ 0 & \mu_S^2\mathbf{I}_m \end{bmatrix} + \cdots + \begin{bmatrix} \eta_P^{\nabla^2 2}\partial^{2T}\partial^2 & 0 \\ 0 & \eta_S^{\nabla^2 2}\partial^{2T}\partial^2 \end{bmatrix}$$

where $\mathbf{C}_x^{-1}$ is the *a priori* covariance matrix of the solution vector. In this estimate it is assumed that the solution vector is linearly close to the true solution. Berryman (1990) has pointed out that equation 2.66 takes into account only the statistical errors of the data but it does not consider that, in our estimate of the solution vector, errors are in large part caused by our inexact knowledge of the raypaths through the unknown structure and only to a lesser extent by the observational statistical errors which are a small percentage of the total error. This topic will be addressed more throughly in the discussion on the choice of the damping parameter.

A topic which has not been addressed analytically in this thesis is the covariance on the hypocenter location estimates as function of both statistical errors in the observations and non uniqueness of the velocity model adopted for their locations. Pavlis and Booker (1980), O'Connell (1986), and O'Connell and Johnson (1991) are among the few authors that have addressed this topic, relying on the formulation of errors given by Backus (1970). We have addressed this topic with synthetic tests for various structures.

2.3.5 Progressive inversion

2.3.5.1 Procedure

The progressive inversion is summarized in figure 2.2. After selection of the earthquakes and relative arrival phases to be used in the inversion, a best estimate of the velocity model is made. This initial estimate could be determined by solving first the reduced problem for a one-dimensional velocity structure or by incorporating independent geophysical information. The first step in the inversion scheme is to locate

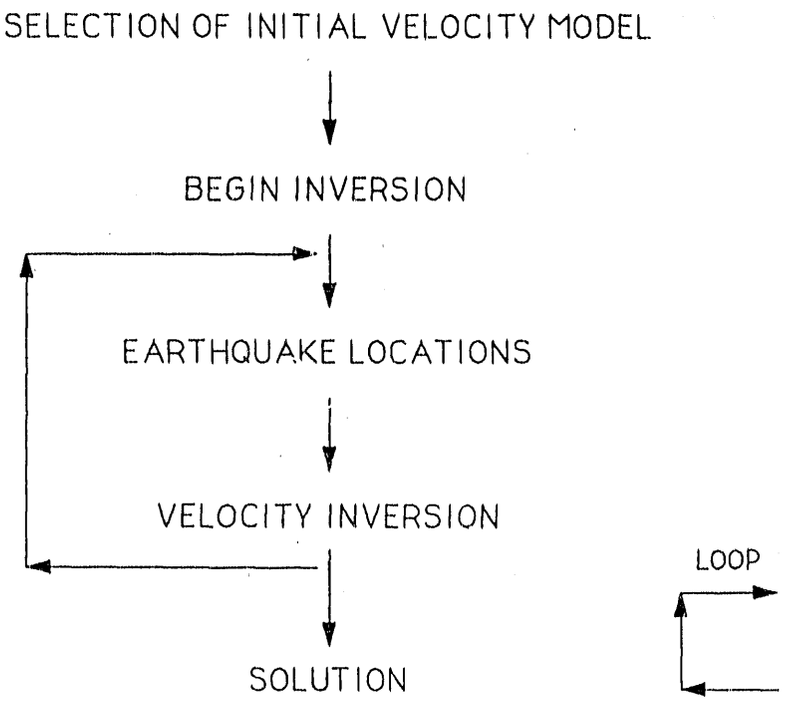

Figure 2.2: Flow diagram of the progressive inversion.

the earthquakes and accumulate the annulled data set according to the method described in the previous sections. At the end of this process the annulled data set is inverted for the velocity parameter adjustments. These adjustments are applied to the existing velocity model and all the earthquakes are relocated by ray tracing again through the new structure. A new annulled data set is determined in this way. At each iteration after the earthquakes have been relocated with the updated velocity model, an F-test is performed to verify if the adjusted model is meaningful when compared to that of the previous iteration. Iterations are stopped when the variance reduction according to the F-test is not meaningful at the 95% confidence level, when the variance increases or when a preassigned threshold of the weighted root mean square of the travel time residuals has been reached.

2.3.5.2 Step size

Throughout the iterative inversion, one of the most critical parameters to be set is the non-negative damping constant μ_P (both μ_P and μ_S when the inversion is performed for both P- and S-model). The value of this parameter determines both the direction and the size of the adjustments in the velocity coefficients. It stabilizes the solution by limiting the effect of small eigenvalues of the matrix of the travel time partial derivatives of the annulled data set. These small eigenvalues produce large perturbations of the velocity model, deteriorating and often reversing the descent path toward the minimum of the objective functional.

Selection of an appropriate value for the damping parameter has been addressed in different ways. In general, the aim is to obtain the smallest perturbation of the solution vector that permits the maximum decrease of the objective functional and, at the same time, avoids local minima. The burden in our problem is that the most costly part of the inversion algorithm is in the forward modelling, i.e., ray tracing part through the three-dimensional structure. It is thus impractical and computationally

intensive to explore the tradeoff between the perturbation vector and the objective functional directly by forward modelling. To solve this problem, we can either select an initial value of damping and keep it fixed throughout the iterations (e.g., Eberhart-Phillips, 1989) or we can adopt some criterion to determine a self-adjusting damping parameter at each iteration. One possibility is to determine the norm of the vector perturbations to the velocity model and analyze its variations as function of the applied damping (e.g., O'Connell, 1986). Another approach toward determination of the proper damping value, is to use some estimate of the current model misfit combined with some measure of the model perturbations errors. We used this second approach.

At each iteration step, we can determine the variance, σ^2, of the current model

$$\sigma^2 = \frac{\sum_{i=1}^{n_e} \sum_{j=1}^{n_j} (\delta t_j)_i}{N - 4n_e} \tag{2.67}$$

and the covariance matrix of the model perturbations, $\mathbf{C}$, (see section 2.3.4.3). Estimation of proper values of damping can be made by defining what I name the modified covariance matrix as

$$\tilde{\mathbf{C}} = \sigma^2 \mathbf{C} \tag{2.68}$$

and the criterion is to select the damping value to satisfy

$$\sigma_{max} = \max_i \left\{ \left(\tilde{\mathbf{C}}_{ii} \right)^{1/2} \right\} \leq \sigma_t \tag{2.69}$$

where σ_t is a preassigned threshold value. When solving for both P- and S-models simultaneously, σ_{max}, σ_t and μ are replaced by σ^{χ}_{max}, σ^{χ}_t and μ_{χ} ($\chi \equiv P, S$). Determination of the damping value μ can be made by applying the root bisection method to equation 2.69. The properties of the criterion stated in equation 2.69 can be summarized as follows. At the beginning of the inversion, the matrix of model partial derivatives, which is calculated along the ray paths and it is used to determine the velocity perturbations, is partly inconsistent with the true model (Berryman, 1990)

and this is evidenced by the large residuals and corresponding large variance. It follows that in order to attain the preset value, σ_t, of the modified standard error estimate of the perturbations, the damping parameter will have to be set to a relatively large value which will insure the elimination through damping of the ruinously large perturbations caused by the small values of the eigenvalues of the matrix of partial derivatives. As iterations proceed, the calculated variance decreases in value and smaller values of damping will be needed. In the limiting case in which the variance of the solution is equal to zero, convergence is achieved and no damping is needed. The use of the covariance matrix is a sophistication motivated by the need for having some control on the errors in the perturbations in various parts of the model and scale the amount of damping accordingly.

In our formulation, the various a priori types of conditioning introduce different amounts of damping. We have chosen to fix through the iterations the values of the ηs parameters and to determine only the values of the μs using equation 2.69.

2.4 Summary

I have introduced a parameterization of the velocity structure in terms of cubic B-splines basis functions into a general three-dimensional joint P-, S-velocity/hypocenter inversion algorithm (Thurber, 1983). This type of parameterization has the advantage of producing smooth models that retain the principal features of the velocity field and, in addition, they can be used for generation of synthetic seismograms by adopting the ray-method (e.g., Cerveny, 1987). In order to regularize the inversion and avoid artifacts due to limited sampling of the volume to be imaged, various types of *a priori* conditioning terms can be included through the setting of the correspondent constants that indicate the preference toward some preferred solution. In this respect, introduction of V_P/V_S *a priori* conditioning is new. It is designed to limit the V_P/V_S ratio instabilities that can arise in the inversion and permits more critical

interpretations of the resolved models.

The perturbations of the velocity model at each iteration are found by selecting the damping parameter as function of some predefined maximum value of a modified model covariance matrix that, in my interpretation, takes more into account the errors due to inexact ray-tracing through the structure.

Appraisal of the results through calculation of the spread and coupling functions permits more critical interpretations of the results.

Chapter 3

Synthetic data tests

In this chapter we apply the method to two synthetic data sets which were designed to test effectively the method presented in chapter 2. The velocity structures that were analyzed in detail were named *spike* and *fault* model after their main features.

Throughout these tests I adopt the same source-receiver geometry of the Parkfield data set which will be thoroughly analyzed in chapter 4.

The aim of these two tests is to address the following main questions.

1 . What is the resolving power of the data set ?

2 . What kind of instabilities can be attributed to the ray coverage ?

3 . To what extent is the non-linear iterative inversion scheme capable of convergence toward the correct model when the latter is complex ?

4 . Can the method, when applied to the given data set, image a low velocity fault zone with anomalous values of V_P/V_S ratio ?

5 . What are the effects of discrete meshing and parameterization ?

3.1 Model percent difference function

Throughout the following tests, we will compare the results of the inversion with the given *true* model which was used to generate the synthetic travel times used in the inversion. To this purpose, we introduce the *model percent difference function*, MPDF, as the percent difference between the true and the resolved model. Some weighting can also be applied in the calculation of this function if we want to determine the percent difference between true and estimated models in parts of the resolved model having better resolution. In this case, the weighting can be chosen to be the spread function which was defined in chapter 2. In general, weighting by the resolution is motivated by the need to determine how well our technique performs in the well-resolved parts of the model. In a general case with arbitrary weighting, the MPDF is defined as follows

$$\Phi_w(v^\chi_{inv}) = \int_{volume} w^\chi(\mathbf{x}) \frac{|v^\chi_{inv}(\mathbf{x}) - v^\chi_{true}(\mathbf{x})|}{v^\chi_{true}(\mathbf{x})} d\mathbf{x} \tag{3.1}$$

where

$|\cdot|$ indicates absolute value,

$\chi \equiv P, S,$

$w^\chi(\mathbf{x})$ weighting function for the χ model,

$v^\chi_{inv}(\mathbf{x})$ resolved χ-velocity model at position $\mathbf{x}$,

$v^\chi_{true}(\mathbf{x})$ true χ-velocity model at position $\mathbf{x}$.

In the discrete case, equation 3.1 can be rewritten as

$$\Phi_w(v^\chi_{inv}) = \sum_{\omega=1}^{\Omega} w^\chi(\mathbf{x}_\omega) \frac{|v^\chi_{inv}(\mathbf{x}_\omega) - v^\chi_{true}(\mathbf{x}_\omega)|}{v^\chi_{true}(\mathbf{x}_\omega)} \tag{3.2}$$

where

Ω total number of discretized points in the volume resolved by the inversion. Because we adopt cubic B-splines basis functions in the interpolation between the m_n^χ nodes of the grid mesh and we do not solve analytically, it is necessary to adopt a denser grid in order to obtain reliable estimates of the true differences between the true model, $v_{true}^\chi(\mathbf{x}_\omega)$, and the inverted model, $v_{inv}^\chi(\mathbf{x}_\omega)$. In principle, we should remesh the grid at infinitesimal spacing between nodes however, in the following, we adopt $\Omega \gg m_n^\chi$.

We have selected two different types of weighting function in equation 3.2. The first consists of applying equal weight to all points of the volume, that is,

$$w^\chi(\mathbf{x}_\omega) = \frac{1}{\Omega} \tag{3.3}$$

whereas the second consists of applying larger weights to parts of the model which are better resolved (i.e., according to the values attained by the spread function)

$$w^\chi(\mathbf{x}_\omega) = (s_{max}^\chi - s_\omega^\chi) \left(\sum_{\omega=1}^{\Omega} (s_{max}^\chi - s_\omega^\chi) \right)^{-1} \tag{3.4}$$

where s_{max}^χ is the maximum value of the spread function for a given resolved model. For both weighting schemes

$$\sum_{\omega=1}^{\Omega} w^\chi(\mathbf{x}_\omega) = 1 \quad . \tag{3.5}$$

The first weighting scheme is *global* because it permits direct comparison of the different resolved models. The second weighting is *local* because for each model, we apply a normalized weight which depends on the maximum value of the determined spread function, s_{max}^χ . This second weighting scheme tests whether the relatively better resolved parts of the model display also an improved fit to the true model.

In summary, adoption of the model percent difference function together with the data misfit as measured by the weighted root mean square (WRMS) of the residual times provides a quantitative estimate of the *goodness* of the fit between true and

inverted models. We will make extensive use of this function because it effectively summarizes the results of the tests. In the tables that list the values of the MPDF (tables 3.1, 3.3 and 3.4), $\Phi_1(v^{\chi}_{inv})$ adopts the equal weight of equation 3.3 and $\Phi_s(v^{\chi}_{inv})$ uses the weighting given by equation 3.4.

3.2 Statistics of the earthquake mislocations

A second approach that we have used in these tests in order to assess the accuracy of the inversion scheme is provided by the analysis of the earthquake mislocations. The term mislocation is used to define the distance between the earthquake location adopted in the calculation of the synthetic arrival times and the location obtained in the joint inversion.

In practice, we choose to determine some statistical estimates of the mislocations derived from the ensemble of earthquakes. Three measures are of interest for our purposes. The first consists of calculating the mean mislocation along the three Cartesian coordinates. This measure tests whether the locations determined with the resolved model have some inherent bias, i.e., the locations tend to be shifted along some particular direction. This measure is defined by

$$\bar{x} = \frac{1}{n_e} \sum_{j=1}^{n_e} (x^e_j - \bar{x^e_j}) \tag{3.6}$$

where

n_e — total number of earthquakes;

x^e_j — x-coordinate of the j^{th} earthquake determined from the resolved model $v_{inv}(\mathbf{x})$;

$\bar{x^e_j}$ — x-coordinate of the *true* earthquake location used to generate the travel times in the synthetic test.

Identical relationships hold for the estimates $\bar{y}$ and $\bar{z}$ for the y and z coordinates, respectively.

The second measure provides instead an estimate of the absolute mean mislocation along each coordinate axis. It is defined as

$$|\bar{x}| = \frac{1}{n_e} \sum_{j=1}^{n_e} \left| x_j^e - \bar{x_j^e} \right| \quad , \tag{3.7}$$

with analogous estimates for $|\bar{y}|$ and $|\bar{z}|$.

Finally, the third measure consists of calculating the mean distance, $|\bar{s}|$, between the true and the determined earthquake location

$$|\bar{s}| = \frac{1}{n_e} \sum_{j=1}^{n_e} \left((x_j^e - \bar{x_j^e})^2 + (y_j^e - \bar{y_j^e})^2 + (z_j^e - \bar{z_j^e})^2) \right)^{1/2} . \tag{3.8}$$

3.3 Ray-tracing

Two ray-tracers have been used in these tests and in the application of the technique to the observed data in chapter 4 and 5. Both are approximate ray-tracers and are based on bending an initial circular arc-path between source and receiver. The first one is the 3-D ray-tracer developed by Prothero et al. (1988) that adopts the simplex method of function minimization to find the path of minimum time. The second is the Um and Thurber (1987) pseudobending ray-tracer which iteratively perturbs the initial ray-path in the direction of maximum velocity gradient, i.e., toward higher velocities. The Prothero et al. ray-tracer is more accurate, although more computing intensive, and has been used to generate the travel-times through the "true" models of these tests. The Um and Thurber ray-tracer is considerably faster and has been used throughout this thesis for the inversions. In a test designed to test the differences in the resolved model as function of these two ray-tracers (not shown in this thesis), it was found that minor differences distinguished the resolved models. This result indicates that when thousands of ray paths are used in a tomographic inversion,

second order errors in the travel-time calculations tend to be averaged out and do not introduce bias.

Um and Thurber introduced the use of two parameters in setting the accuracy of the ray-tracer, the *Travel Time Improvement Parameter* and the *Enhancement Factor*. We have set the first parameter equal to 0.001 (0.01 in the initial iterations of the non-linear inversion), and the second to 1.2. Um and Thurber have shown in testing their ray tracer against an exact one that this parameter setting would produce errors in the travel time calculations in the range 0.1 to 0.7 % of the total travel time for different velocity structures and in the range of distances of the present study.

3.4 Source-receiver geometry

The source-receiver geometry adopted in all the synthetic test is shown in figures 3.1 and 3.2 for the spike test and in figures 3.18 and 3.19 for the fault model. The source-receiver geometry refers to the Parkfield data set. A total of 24 receiver sites, 110 earthquakes and 8 vibration locations were used for the spike test. In the fault test, we added 59 earthquakes.

In the inversion, we have included 35 P and 25 S travel times from the surface vibrator sources for shallow velocity control (Figure 3.1 and figure 3.18). The earthquakes were selected to satisfy the joint criteria of well-timed onsets and a spatially uniform sampling of the region to be analyzed. We include the CALNET data in order to constrain the gross features of the three-dimensional model on a larger scale. We selected 396 P phases from 36 earthquakes in this subset (no CALNET data S-times were included). Each CALNET source had P readings at ten stations or more. We used 522 P times and 263 S times from 74 selected microearthquakes (about 10 per cent of the available events) recorded by the HRSN in the spike test. In the fault test and in the inversion with observed data, we added 59 earthquakes recorded by

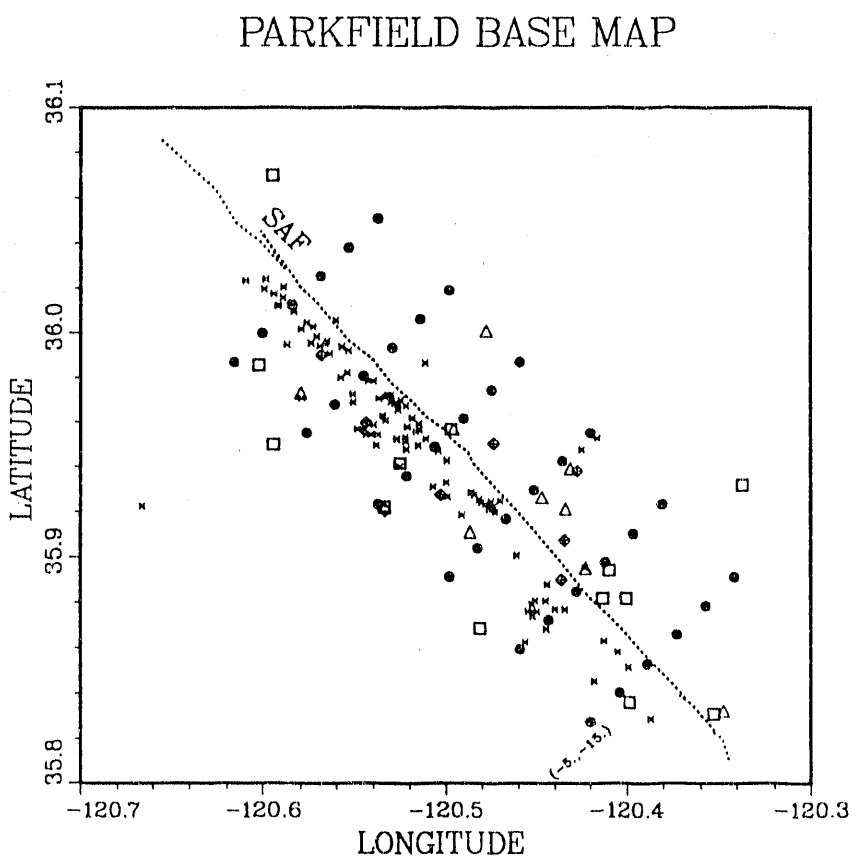

Figure 3.1: Parkfield base map showing locations of the HRSN stations (open triangles), the CALNET-USGS stations (open squares), the grid nodes used in the inversion (solid circles), the vibration points of the controlled source experiment (diamonds with inner cross), the 110 earthquakes used for the joint inversion in the spike test (crosses), and the trace of the San Andreas Fault (SAF) (dashed line). The grid mesh is centered at the 1966 main shock ($35°57.3'N$, $120°29.7'W$) and rotated $45°$ counterclockwise. For reference, the coordinates of the southernmost-column of the grid mesh are shown. Node interval is 2 and 5 km across and along the SAF, respectively.

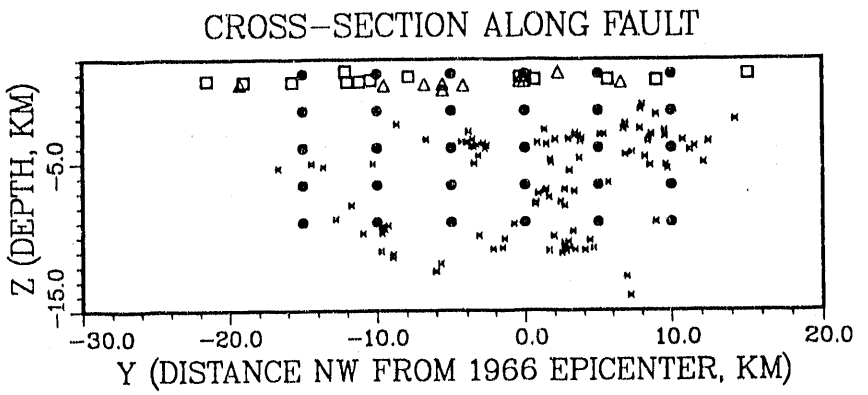

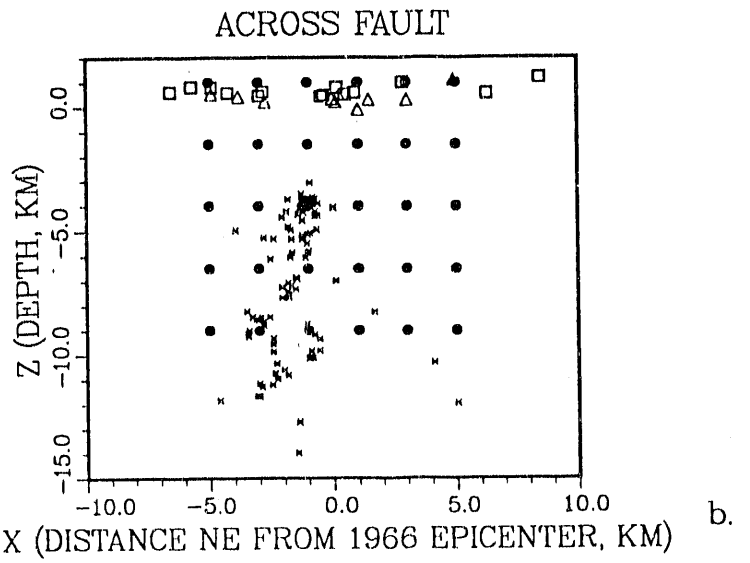

Figure 3.2: The 110 earthquakes used for the inversion and the position of the nodes in the local reference system defined by the grid mesh. a) vertical cross-section along fault (southeast-northwest, $y - z$); b) vertical cross-section across the fault (southwest-northeast, $x - z$). Grid mesh, stations and earthquakes are plotted with the same symbols of figure 3.1.

the HRSN to the 74 previously selected and a total of 1380 P and 435 S phases were used. Each earthquake recorded by the HRSN has a minimum of eight recorded P or S phases. For common events, the CALNET and HRSN times were treated separately because the HRSN clock was not synchronized accurately to UTC, and time corrections could not be determined to the millisecond accuracy required to merge the data sets. For the synthetic tests described below, the entire data set (HRSN, CALNET-USGS and Vibroseis) was included in all the iterations.

The three-dimensional velocity model is parameterized within a Cartesian coordinate system having its origin at the 1966 main shock epicenter (35°57.3′N 120°29.9′W, see McEvilly et al., 1967). The coordinate system is rotated 45° counterclockwise. The x- and y-axes lie in the horizontal plane and are oriented northeast and northwest, or across and along strike of the San Andreas Fault (SAF), respectively (Figure 3.1 and 3.18), z is negative down, $z = 0$ being mean sea level.

3.5 Spike model

The spike model consists of adjacent high- and low-velocity "spikes" within the same horizon and intercalated with horizons having constant background velocity. The spikes anomalies are 15 to 20 per cent of the background velocity. Spike horizons were set at $z = 0$, $z = 4$ and $z = 6$ km depth. The $z = 2$ and $z = 10$ km horizons have constant velocity. The $z = 8$ horizon does not vary in the y direction, along the fault, and is characterized by a low velocity (5 km/sec) zone at $x = -3$ km and a high velocity (7 km/sec) at $x = 1$ km. S velocities were calculated from the P-model by imposing a V_P/V_S ratio of 1.75 throughout. The model is parameterized in terms of cubic B-splines basis functions.

Grid spacing for the inversion differs intentionally from the one used in the construction of the forward model in that, we used six layers of nodes in depth for the true model (layer to layer spacing of 2.0 km) and only five in the inversion (layer

spacing of 2.5 km). This introduces some undersampling (aliasing) of the structure to be determined but it is motivated by the expectation that the inversion with real data will be also undersampled given our inexact knowledge of the geologic structure. In this respect, this synthetic data test provides some evaluation of the effects of undersampling on the resolved model. Furthermore, this particular choice of velocity structure is attractive because of its complexity. As stated at the beginning of this chapter, one of the main objectives of these tests is to verify to what extent the iterative inversion is capable of reproducing the true model. For example, when there is a large degree of complexity of the velocity model, such as in this test, and when iterations are started from a laterally homogeneous model, the matrix of partial derivatives, especially at the beginning of the iterative procedure, will be affected by the inexact knowledge of the ray paths determined through the structure (Berryman, 1990) and this can have ruinous effects on the resolved model, i.e., convergence to a local minimum.

3.5.1 Inversions

The inversion grid is shown in figures 3.1 and 3.2. It consists of 180 nodes ($6 \times 6 \times 5$) for a total of 360 velocity parameters to be determined when both P and S models are calculated. Node spacing is 2 km ($\times 6$ nodes), 5 km ($\times 6$ nodes) and 2.5 km ($\times 5$ nodes) along the x, y and z coordinates, respectively (see section 2.3.5.2).

In the following subsections we show the results obtained by applying various *a priori* conditioning. The subsections are named for the applied conditioning.

In all these tests we have adopted values of σ_t^P and σ_t^S of 0.20 and 0.15, respectively. Larger and smaller values of these threshold values were also tested but we found that with larger values the resulting model was underdamped, i.e., it displayed more oscillatory features and its final value of the weighted root mean square of the residuals was larger. Conversely, smaller values of the thresholds produced models

which were overdamped, had a larger average weighted WRMS value and the model features were strongly degraded. When some *a priori* conditioning was applied, a variable amount of P and S damping, μ_P and μ_S, was applied in order to adjust the values of the modified covariance, $\tilde{\mathbf{C}}$, to the preset values of σ_i^P and σ_i^S as explained in section 2.3.5.2 while the *a priori* conditioning which is regulated by the η-constant(s) was maintained constant throughout the iterative inversion. The initial model consisted of the background velocity model on which the spikes were superimposed.

We adopt a standard format for the figures throughout all tests. It consists of a top row showing the true model of the test case, a middle row showing the resolved model using contour lines and with superimposed as shading the spread function which features darker shading in the poorly resolved zones. The bottom row is similar to the middle one but it has the spread function replaced by the coupling function and, similarly, darker shading was assigned to parts of the model with larger amount of coupling. The panels are vertically aligned according to where the cross-section has been taken, i.e., $y = -15$ is a cross-section of the 3-D model perpendicular to the y-axis at -15 *km* from the origin of the Cartesian coordinate system.

3.5.1.1 P- and S-damping

No explicit *a priori* conditioning was applied in the first inversion for the spike model, that is, only the μ_P and μ_S damping values were determined at each iteration according to the formulation given in section 2.3.5.2. The resolved P-model is shown in figure 3.3 where in the inner cross-sections ($y = -10$ to $y = 5$ km, panels *b.* to *e.*) it appears as a smoothed version of the true one shown in the top row.

At the boundaries the ray coverage is not adequate to resolve the details of the structure. The estimated model either misses the fit to the true model due to introduction of some fictitious anomalous inhomogeneity (see section *f.* at $y = 10$ km) or it remains at values close the initial model (see section *a.* at $y = -15$ km). The

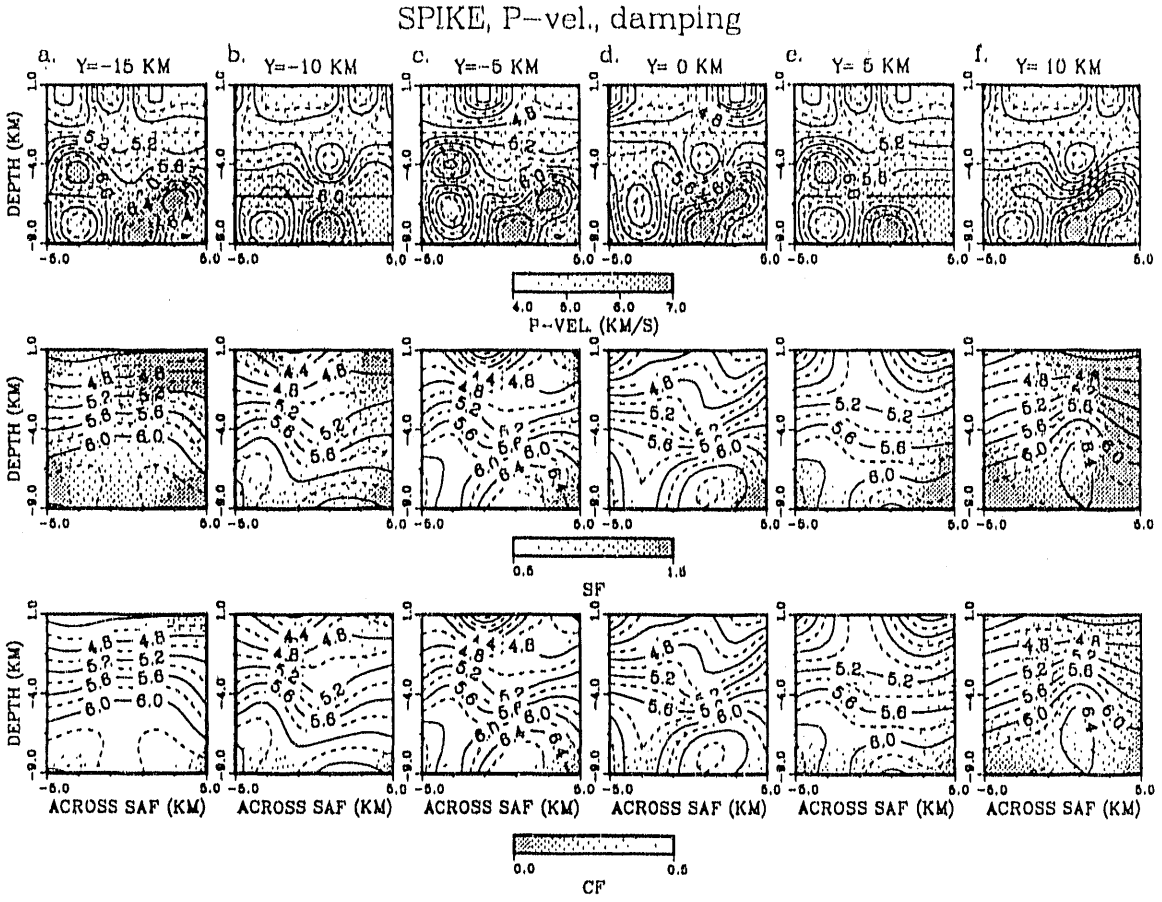

Figure 3.3: Spike P-model: true velocity model used to generate the synthetic arrival times (both contouring and shading are used to indicate the velocity values) (top); resolved velocity model plotted using contour lines, shading is used to plot the spread function (SF), darker areas are more poorly resolved (middle); same resolved velocity model as in the middle row but shading is used to represent the coupling function (CF), darker areas indicate larger amounts of coupling (bottom).

spread function warns us about these fictitious features by attaining in these parts of the model relatively larger values. In general, it is found that a closer fit to the true model is obtained at shallow depths whereas the deeper parts, which are relatively less sampled and have a ray coverage which is more concentrated along the vertical direction, differ more from the correct values.

The resolved S model which is shown in figure 3.4, is to large extent, a scaled version of the P models although it lacks of the same resolving power because of the

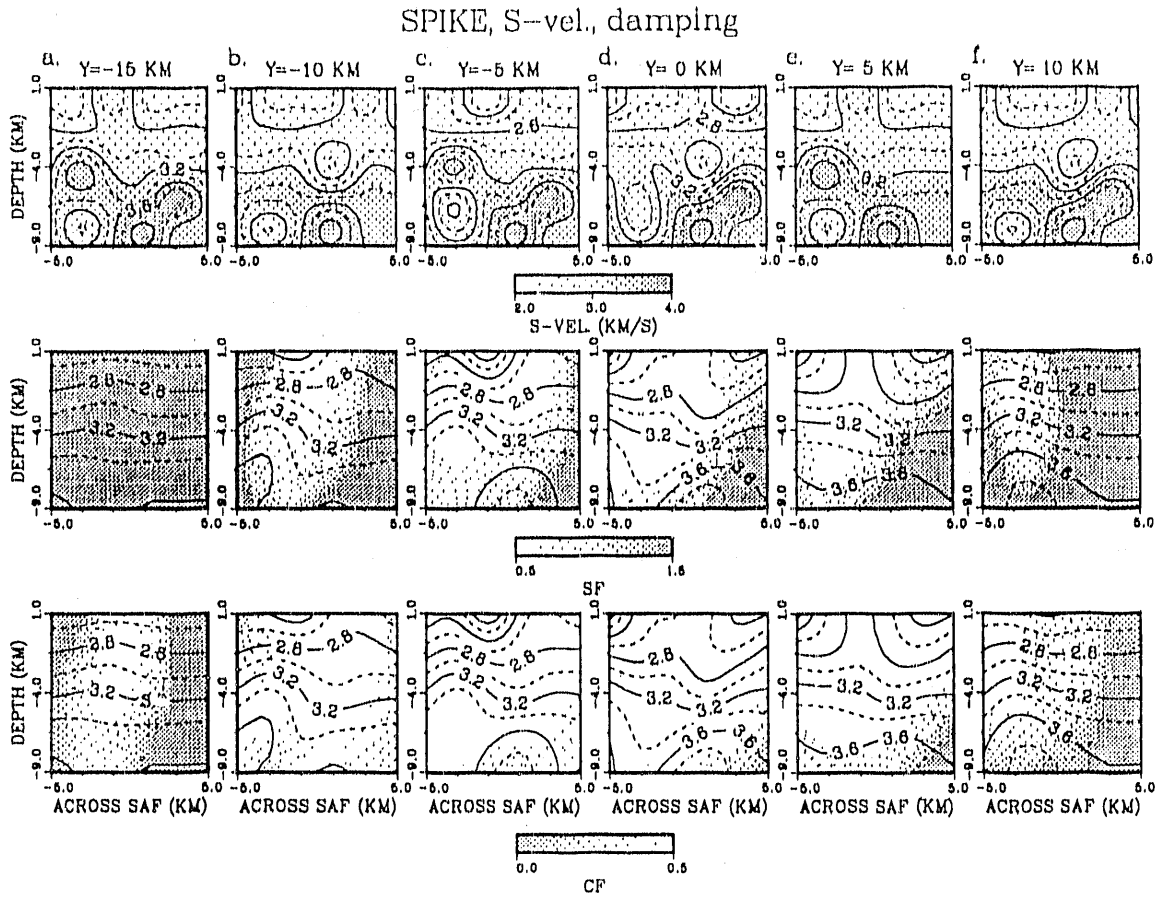

Figure 3.4: Spike S-model: same format as in figure 3.3.

sparser ray coverage. The V_P/V_S which is shown in figure 3.5 displays some fluctuations around the true value of 1.75 in the inner well resolved sections. These fluctuations are mainly caused by the different P and S ray coverages. At the boundaries, the V_P/V_S model suffers of the instabilities observed for the P- and S-models. Specifically, it is observed that in the inner sections (*b.* to *e.* in figure 3.5), the V_P/V_S values range between 1.65 and 1.80. In table 3.1, we summarize the results of this test inversion by listing the values of the MPDF. It is found that the model with equal weight MPDF, $\Phi_1(v_{inv})$, is equal to 4.41 and 4.48 per cent for the P and S models, respectively. The spread function weighted percent difference, $\Phi_s(v_{inv})$, which is a local estimate for the resolved model, attains values that are slightly larger

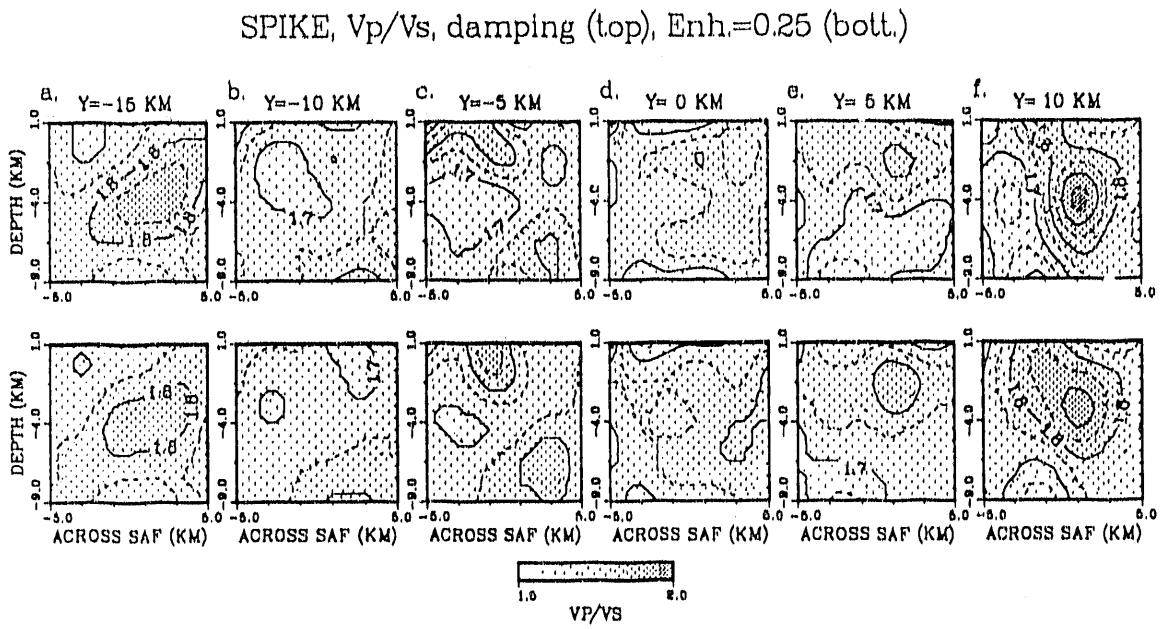

Figure 3.5: Spike V_P/V_S model: P and S damping applied only (top); P and S ray-density condition (bottom). Contour interval is 0.1 for solid lines whereas dashed lines indicate half-interval.

than the equal weight MPDF difference (4.58 and 5.00 for P- and S-models, respectively). Although this difference in value between the MPDF calculated with the two types of weighting is rather small, this result is important and it is contrary to what expected. It can be explained by observing that low values of the spread function at the boundaries of the model are only indicative of the amount of resolution there and not of the actual model misfit, i.e., the resolved model might have fallen into a local minimum even if it attains good resolution there. This result should be taken into account when interpreting models obtained from observed data because it advises the interpreter to be critical of regions in the resolved model that have good resolution but whose adjacent parts are considerably more poorly resolved. The final weighted RMS residual value is 10.0 msec.

To summarize the results obtained by applying P and S damping only, we found that the main features of both P and S models can be retrieved from the available source receiver geometry in the inner parts of the model (sections ranging from $y = -10$ to $y = 5$). At the boundaries of the model ($y = -15$ and $y = 10$) the resolved models are ill-determined and diverge locally from the true one. The V_P/V_S ratio ranges in value from 1.65 to 1.8 in the inner sections whereas it diverges and has larger fluctuations at the boundaries. In the next sections, we apply some *a priori* conditioning to compensate for the observed instabilities.

3.5.1.2 P and S ray-density conditioning

This *a priori* conditioning is designed to compensate for the sparse ray coverage. It consists of applying different damping values to well- and poorly-sampled nodes of the 3-D grid mesh (i.e., ray-density). Figure 3.6 and 3.7 display the P and S models, respectively, for a preset value of ray-density conditioning, η_P^D and η_S^D, of 0.25. The principal effect that can be observed on the resulting models is smoothing especially at the boundaries of the model. There, part of the instabilities that characterized the previous test have been damped out. The inner sections (*b.* to *e.*) are also slightly smoother. The V_P/V_S ratio shown in figure 3.5 does not show any significant improvement in terms of instabilities when it is compared to the previous case. Overall, the observed greater amount of smoothness at the boundaries is rewarded by the values of Φ_1^P and Φ_1^S listed in table 3.1. These values are slightly smaller than in the P and S damping-only case. The value of the final weighted RMS is instead slightly larger than that observed in the previous case, 12.0 msec. At first glance this seems a rather inconsistent result which, however, can be explained in the following way. Minimization of the time residuals in parts of the model that have good ray-coverage (i.e., innermost parts in our case) can be achieved only by convergence toward the true model or a smeared version of it. Conversely, at the boundaries, the ray-coverage

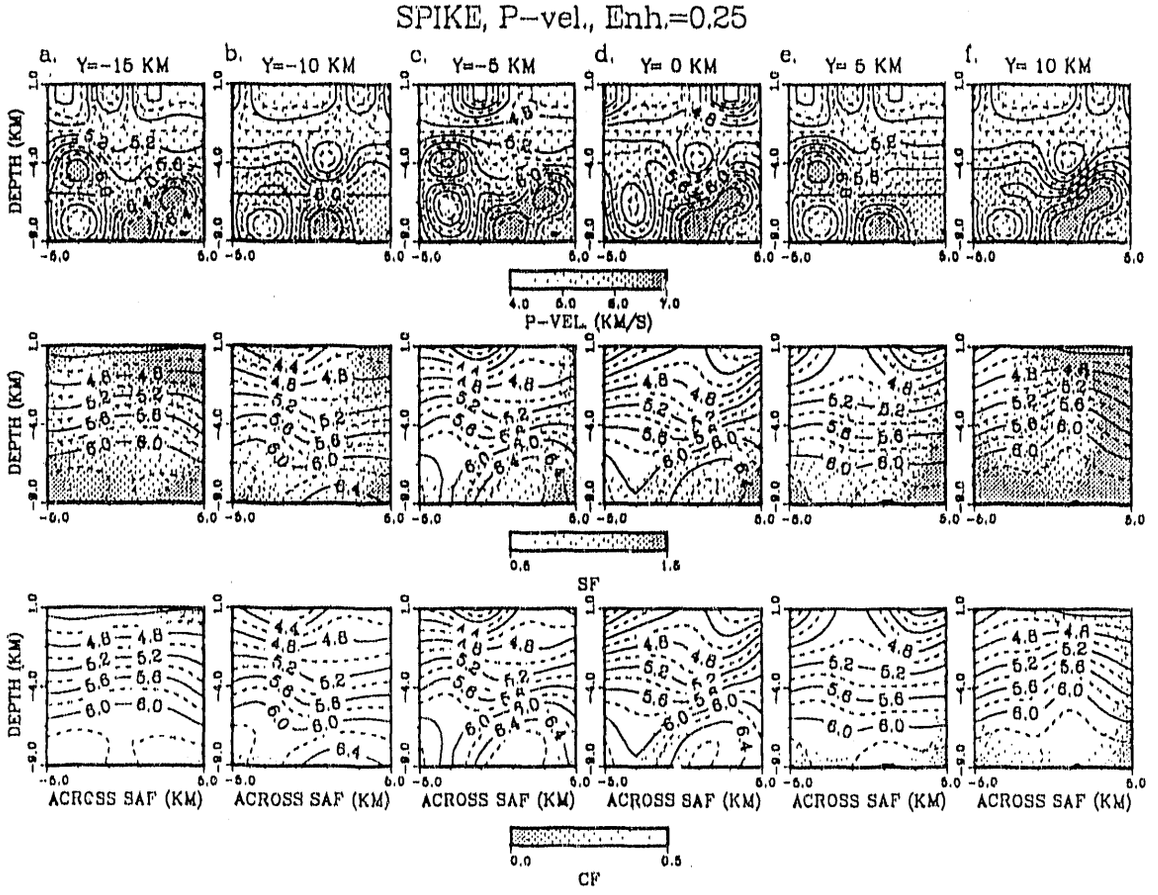

Figure 3.6: Spike P-model: P and S ray-density condition (same format as in figure 3.3).

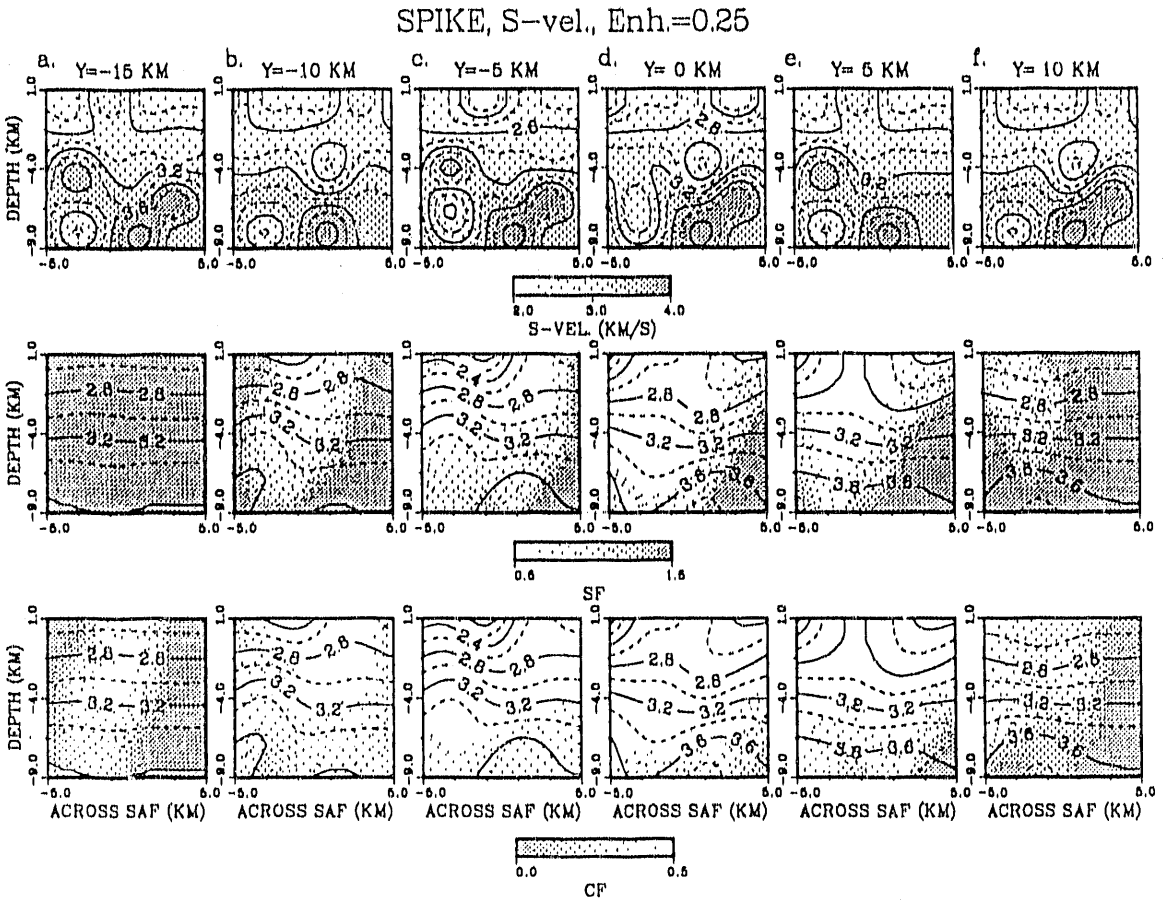

Figure 3.7: Spike S-model: P and S ray-density condition (same format as in figure 3.3).

is poorer and along some preferential directions so that the residuals are minimized but the resolved model can easyly fall into a local minimum (i.e., non-uniqueness). The ray-density conditioning prevents the model from falling into a local minimum at the boundaries which results into improved fits to the true model (i.e., lower values of $\Phi_1(v_{inv})$) but inhibits local residual minimization (i.e., larger values of WRMS). In the previous test the model was falling into a local minimum at the boundaries (i.e., larger values of $\Phi_1(v_{inv})$) but local minimization was achieved (i.e., lower values of WRMS).

3.5.1.3 Smoothing conditions

Another way to limit instabilities in poorly-resolved parts of the structure is by explicitly applying some smoothing condition. In the formulation described in section 2.3.3.4, it was shown that two in-layer smoothing constants, first and second derivative minimization, can be applied to the problem. The models resolved with this *a priori* conditioning are shown in figures 3.8 to 3.12. A smoothing value of 0.1 was selected for the parameters η_P^{∂}, η_S^{∂}, $\eta_P^{\nabla^2}$ and $\eta_S^{\nabla^2}$. The effects of this *a priori* information are evident in the figures.

Examination of the values listed in table 3.1 reveals that for both types of smoothing the final weighted RMS has increased to 13.7 and 15.2 msec, for the first and second derivatives smoothing, respectively. This combined with the model fit as indicated by the values of $\Phi_1(v_{inv})$ and $\Phi_s(v_{inv})$ suggests that caution must be observed in applying explicit smoothing conditions especially in cases like the present one where the wavelength of the model anomalies is comparable to the grid spacing. Furthermore, at the boundaries of the model where the solution is most unstable, it is not possible to see any sensible improvement when compared to the damping-only case. Eventually, some sensible improvement could be obtained by increasing the values of the smoothing constant but, as a tradeoff, this would degrade the fit in the

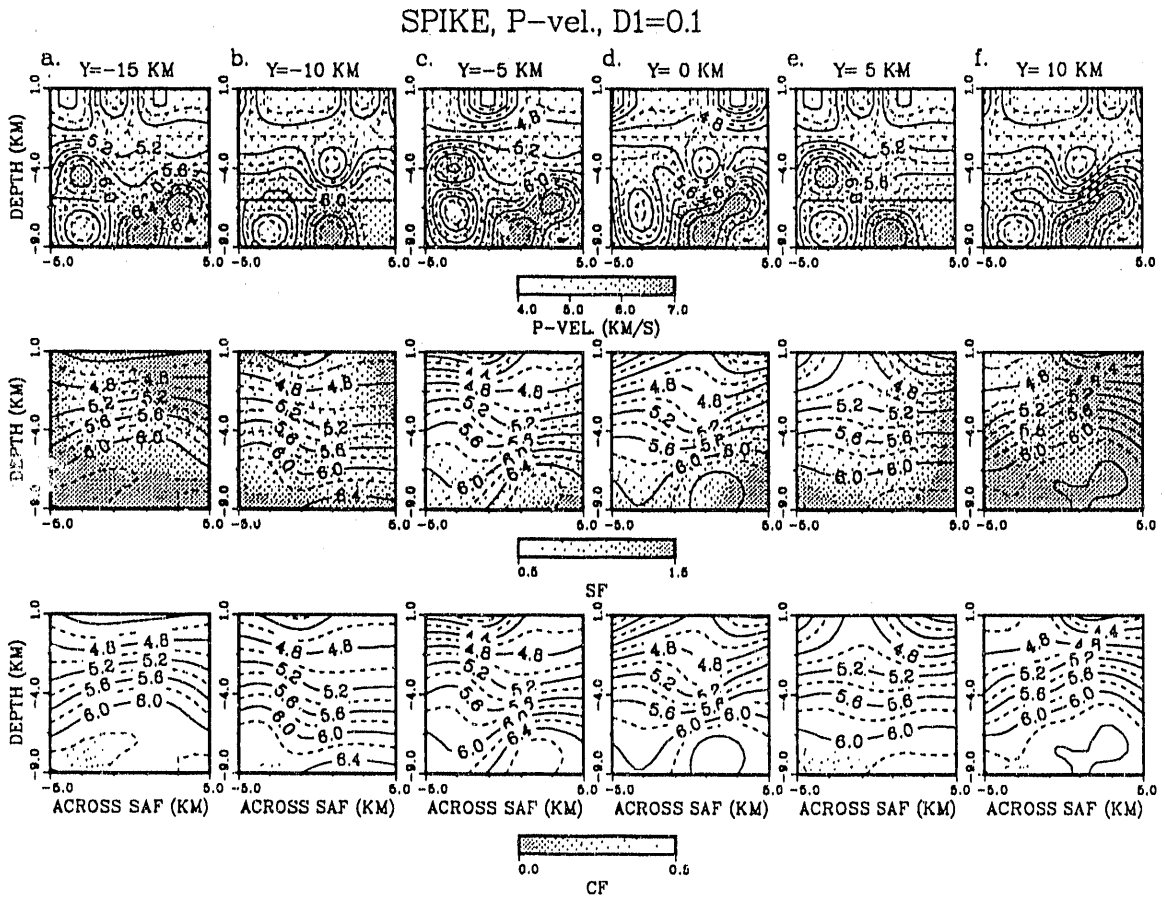

Figure 3.8: Spike P-model: first derivative conditioning (same format as in figure 3.3).

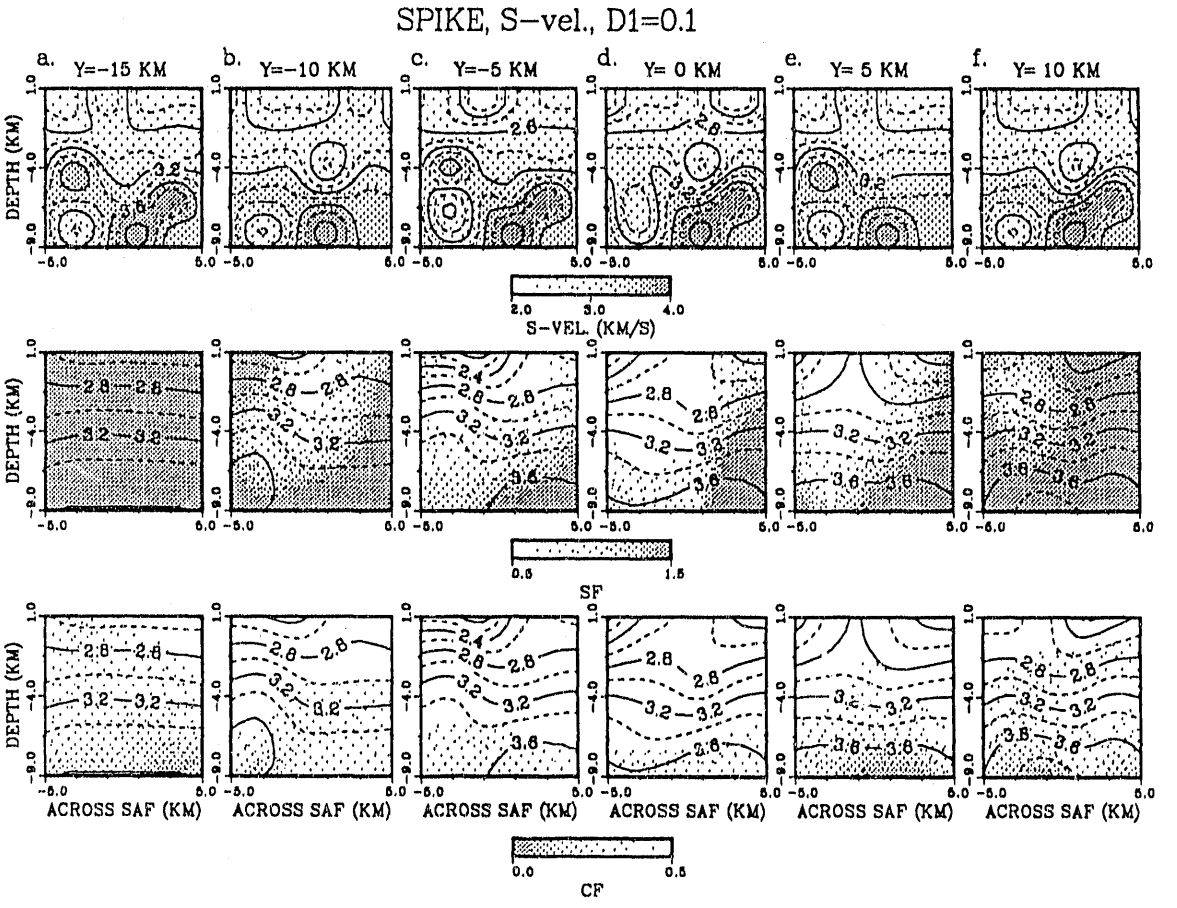

Figure 3.9: Spike S-model: first derivative conditioning (same format as in figure 3.3).

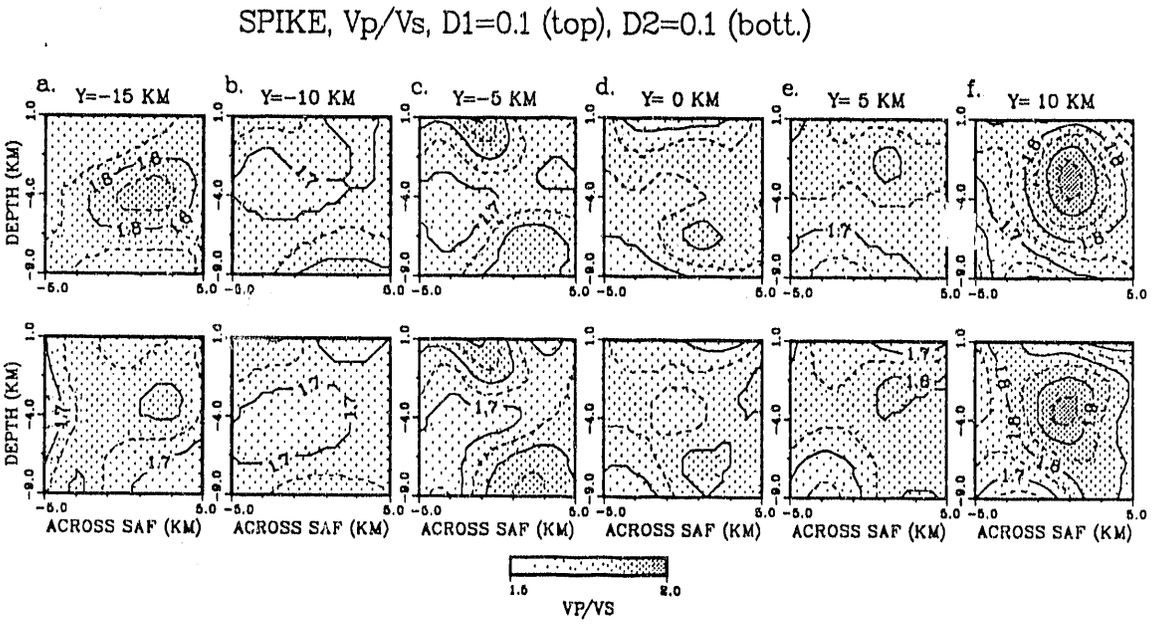

Figure 3.10: Spike V_P/V_S model: first derivative conditioning (top); second derivative conditioning (bottom), (see figure 3.5 for details).

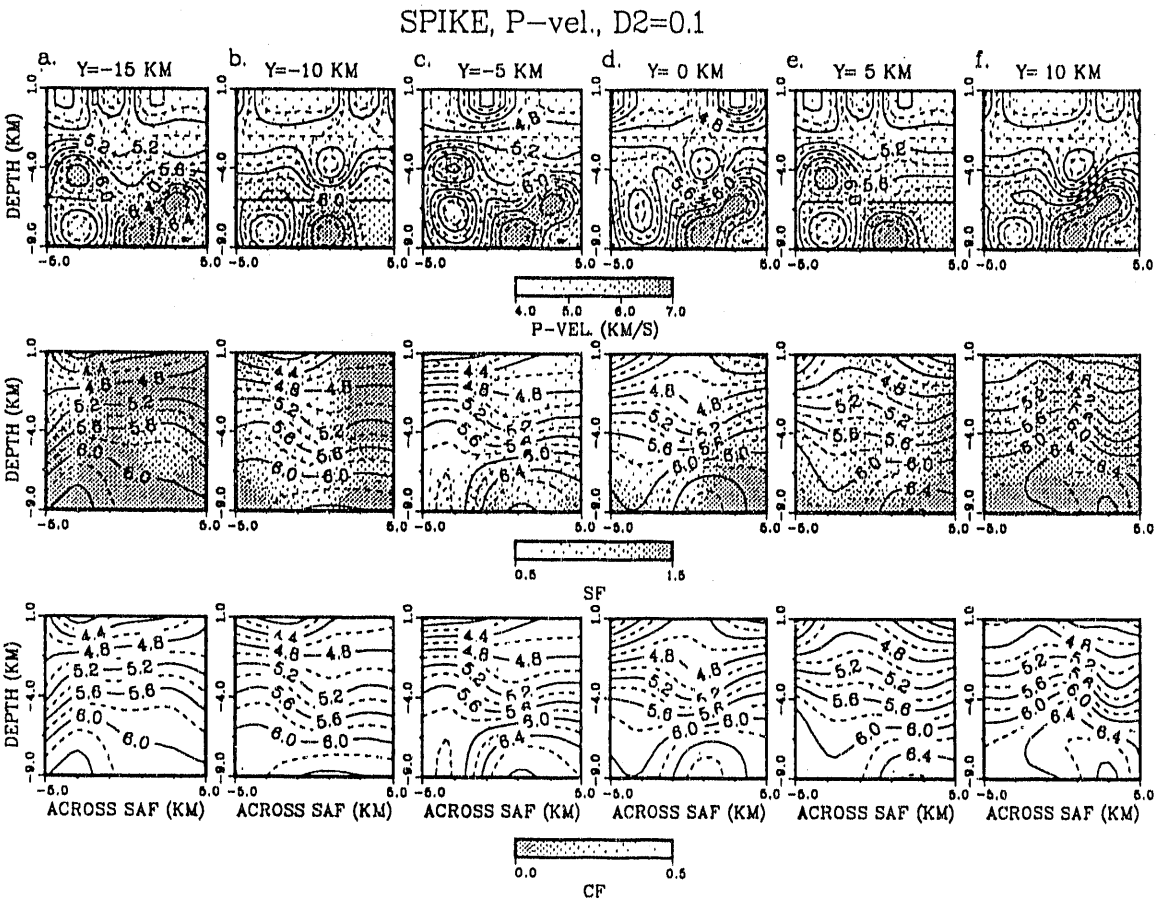

Figure 3.11: Spike P-model: second derivative conditioning (same format as in figure 3.3).

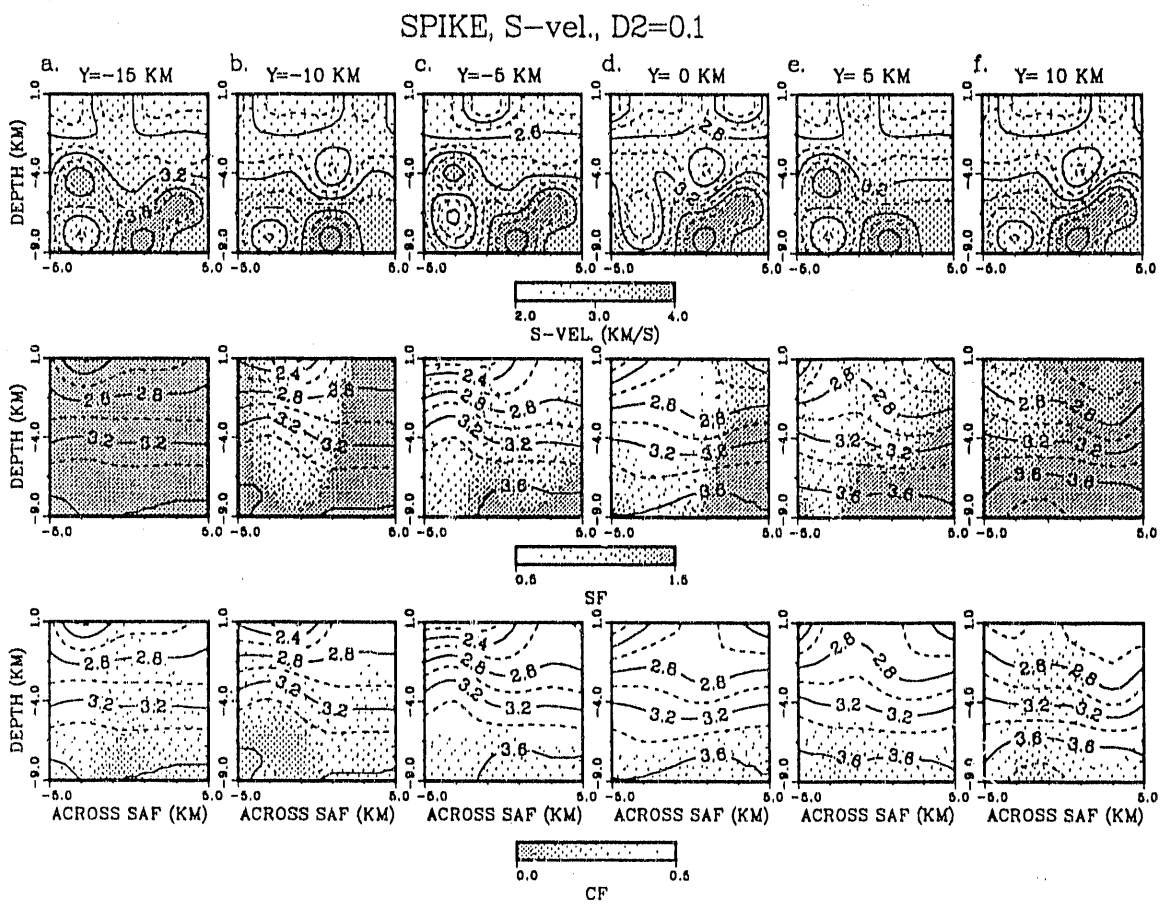

Figure 3.12: Spike S-model: second derivative conditioning (same format as in figure 3.3).

inner parts of the model and slow the rate of convergence in the minimization procedure. To avoid this problem, a possible alternative would consist of applying different smoothing values to well- and poorly-resolved parts or sampled parts of the model, i.e., larger values in the poorly sampled areas (this approach was not tested in this study). The V_P/V_S models shown in figure 3.10 suffer the most with this conditioning because smoothing acts evenly on an unevenly sampled grid, i.e., velocity nodes having different P and S ray coverage. This has the effect of enhancing fictitious V_P/V_S anomalies.

3.5.1.4 V_P/V_S conditioning

In the formulation described in chapter 2 it was shown that some amount of extra coupling between P and S models can be introduced by assigning some non-zero value to η_{PS} and by setting the V_P/V_S equal to some constant κ. In the formulation of section 2.3.3.4 this coupling is not introduced as a fixed constraint on the given ratio κ, but rather a preferred value toward which the V_P/V_S model will tend. The intensity of this coupling is governed by the value of η_{PS}. A more enlightening example of this type of conditioning is presented in the fault model test, but here for the sake of completeness, application to the spike test is presented. In figures 3.13 to 3.15, we have plotted the results obtained by setting $V_P/V_S = \kappa = 1.75$ and $\eta_{PS} = 0.25$. The P model is essentially similar to the one resolved only with P and S damping and it suffers of the same maladies. However because of the extra coupling, the S model is now sharper in the inner sections, than that resolved without any coupling applied. At the boundaries, it resembles the P model and it suffers of the same instabilities. The amount of coupling is given by the values of the coupling function in figures 3.13 and 3.14. The V_P/V_S ratio in figure 3.15 (top) is now nearly constant and the anomalies at the boundaries are no longer present. Examination of table 3.1 shows that the MPDF with equal weight for the P model is slightly better than in the

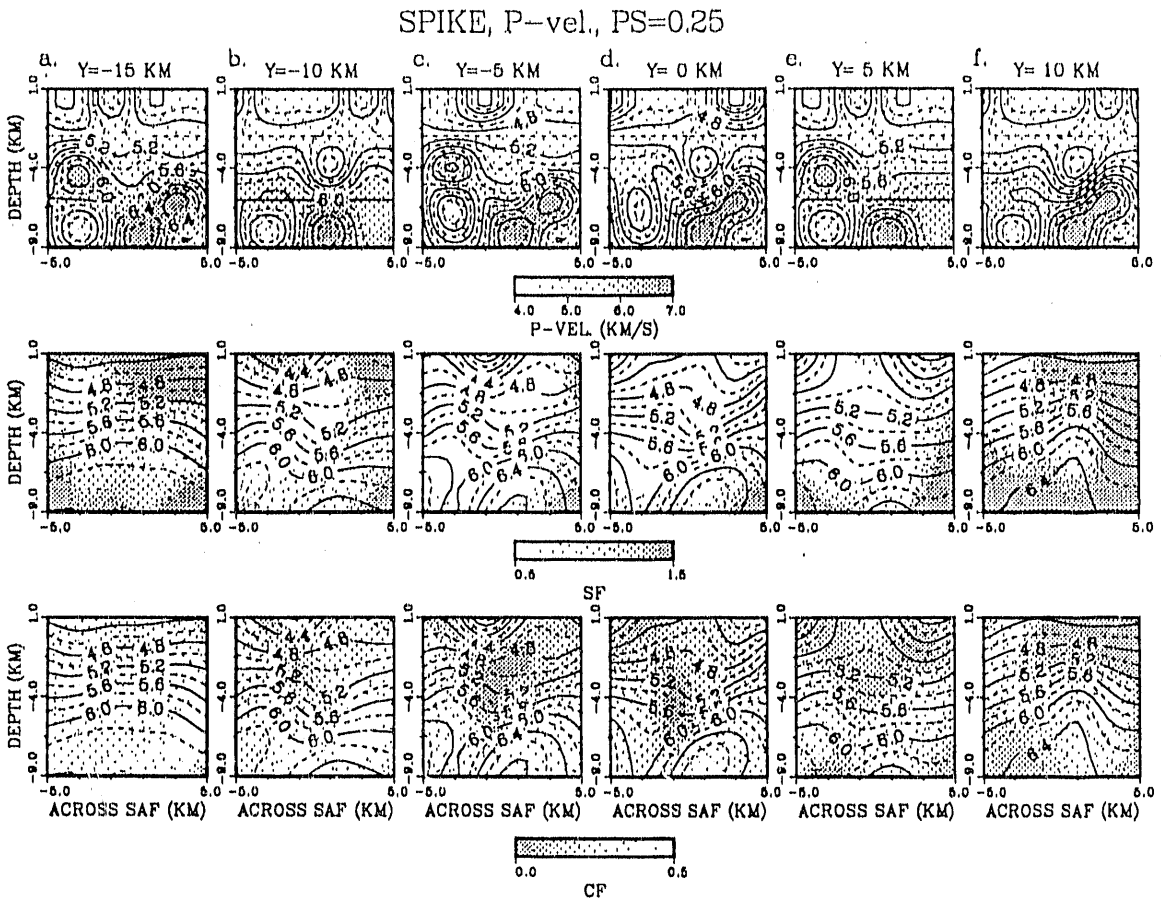

Figure 3.13: Spike P-model: V_P/V_S conditioning (same format as in figure 3.3).

case where only P and S damping were applied. Conversely, because of the introduced coupling and, especially, because of the border instabilities, the S model MPDF shows some degradation of the fit to the true model. In practice, by explicitly introducing some coupling we have gained a slightly sharper S model in the inner, better-resolved sections, and a value of V_P/V_S which is now stable throughout the model but this conditioning has biased the resulting S model at the boundaries.

3.5.1.5 P, S ray-density and V_P/V_S conditioning

From the previous test cases performed with different *a priori* conditioning, we have found that P and S ray-density conditioning decreases the instabilities at the model

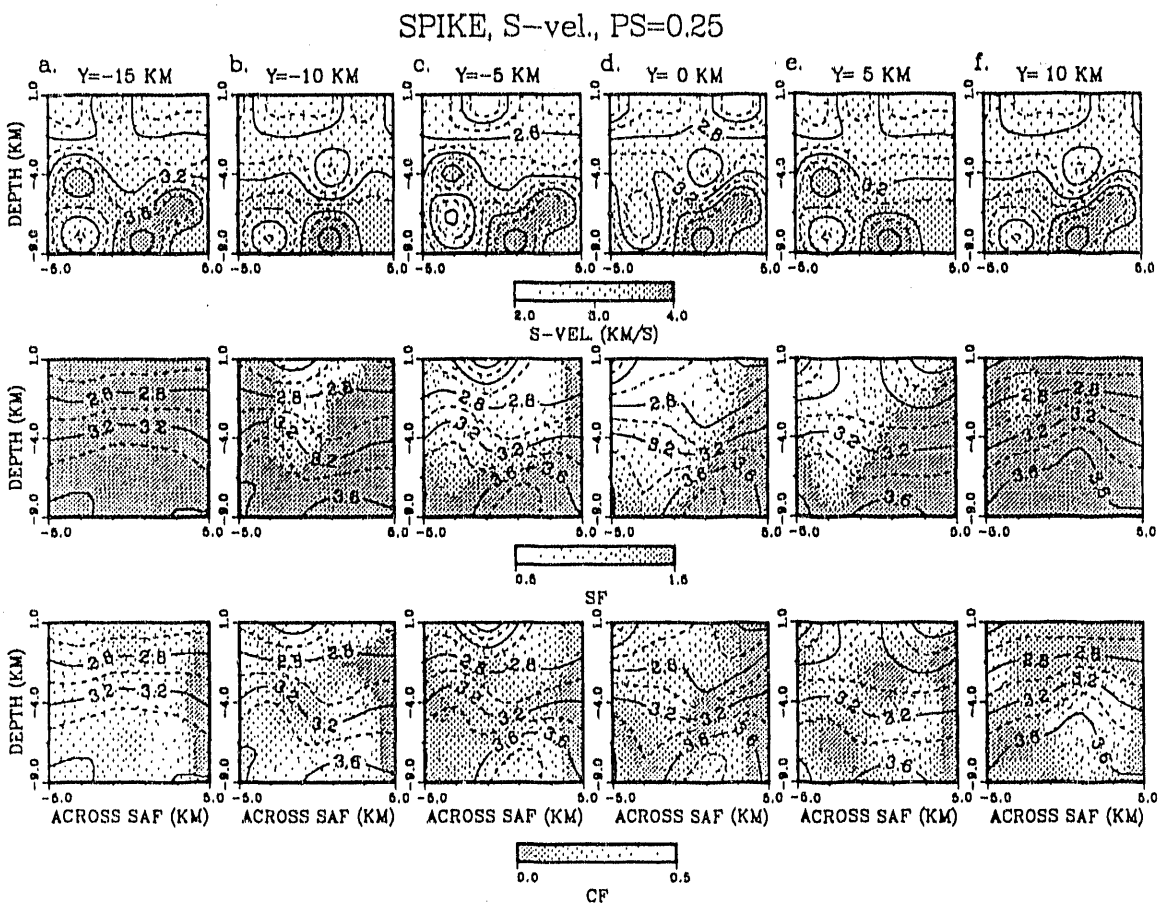

Figure 3.14: Spike S-model: V_P/V_S conditioning (same format as in figure 3.3).

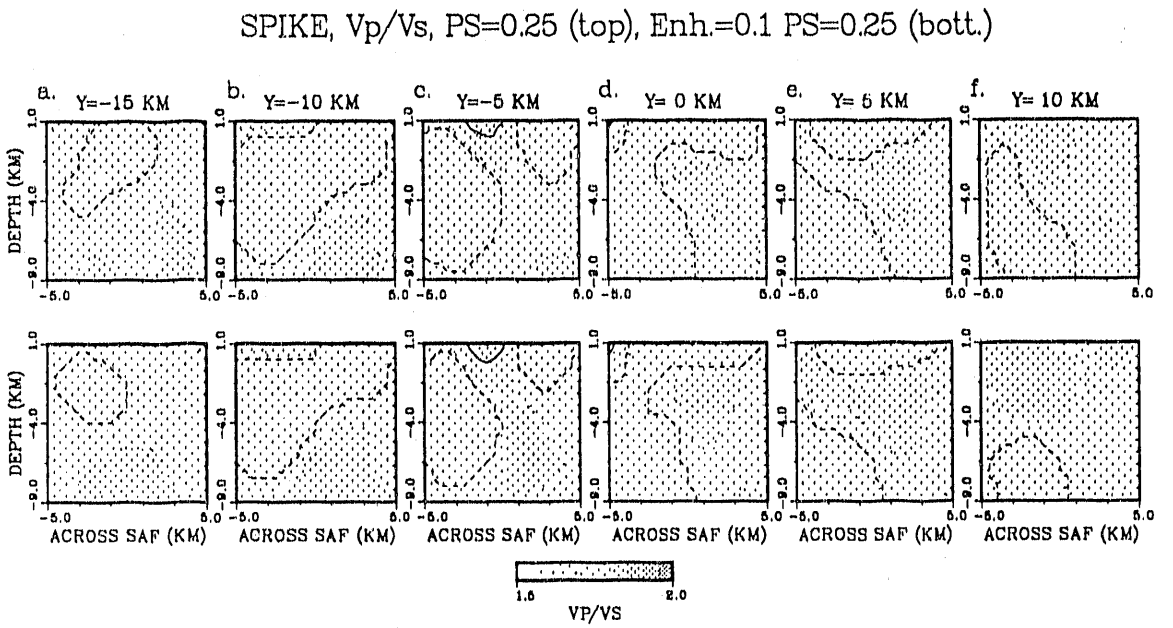

Figure 3.15: Spike V_P/V_S model: V_P/V_S conditioning (top); P, S ray-density and V_P/V_S conditioning (bottom), (see figure 3.5 for details).

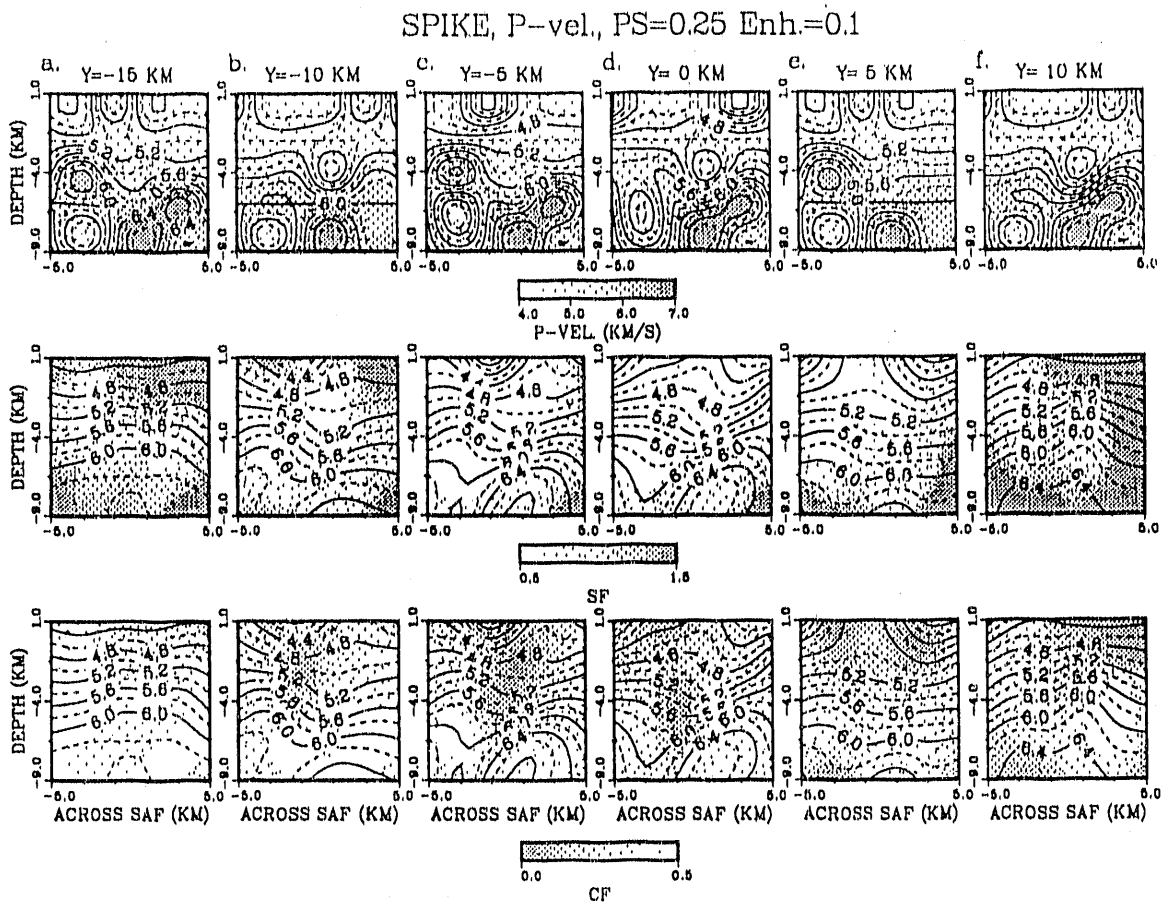

Figure 3.16: Spike P-model: P, S ray-density and V_P/V_S conditioning (same format as in figure 3.3).

boundaries where the ray coverage is sparse and that some amount of coupling between P and S models stabilizes the V_P/V_S ratio throughout the structure. We now follow the pragmatic approach of combining these two *a priori* conditioning. The resolved models are shown in figures 3.16, 3.17 and 3.15 (bottom) for P, S and V_P/V_S models, respectively. Besides some minor effects at the borders of the P and S models, use of both conditioning simultaneously does not seem to improve the fit significantly. Examination of table 3.1 suggests that more ray-density enhancement and less V_P/V_S conditioning may improve the results. However this modified conditioning was not tested.

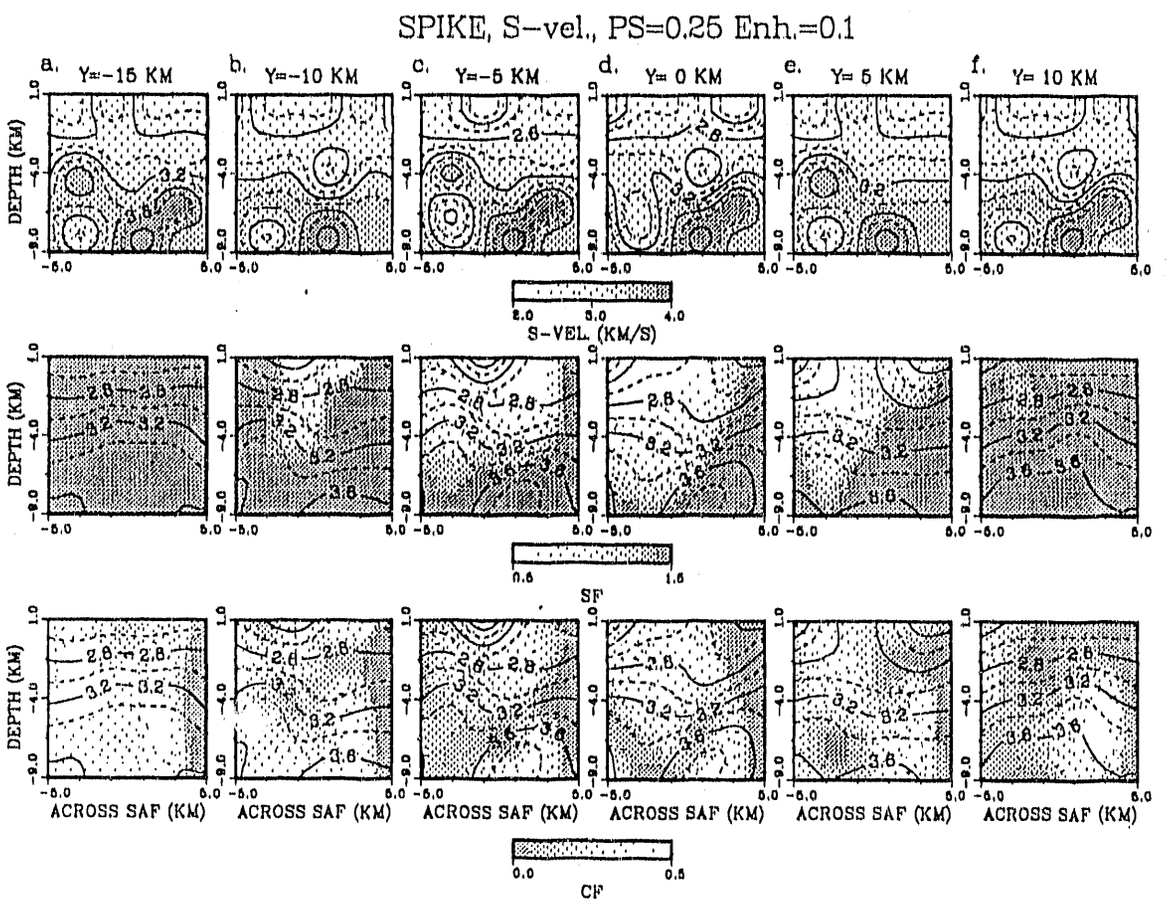

Figure 3.17: Spike S-model: P, S ray-density and V_P/V_S conditioning (same format as in figure 3.3).

3.5.2 Earthquake mislocations

Another measure that permits a critical assessment of the resolved models is provided by the statistics of the mislocations (section 3.2) summarized in table 3.2. The first three columns indicate the mean shift of the locations with respect to the true ones along the three Cartesian axes (equation 3.6). The next three columns instead provide an estimate of the absolute mean mislocation (equation 3.7) and the last one is the mean absolute mislocation distance, $|\bar{s}|$.

All these values represent global estimates that do not take into account local trends in parts of the model. A more local approach will be followed in the fault test. In the present synthetic test, it is found that the significant bias of the hypocenters occurs in depth where the estimated locations tend to be deeper. Overall, the model constructed with both the ray-density and V_P/V_S conditioning performs slightly better than the other cases (see table 3.2). The values of the estimates' two standard deviations (2σ) and the values of the absolute average mislocation, $|\bar{s}|$, indicate that mislocations of the order of several hundred meters have occurred. However, apart from this bias along depth, it appears that the mislocations are rather uniformly distributed along the x- and y-axis. We suspect that this is partly due to the nature of the spike model, i.e., high and low velocity spikes approximately evenly distributed, and that in the fault model test the mislocations will attain some definite bias when the entire model is analyzed.

SPIKE MODEL PERFORMANCE[a]						
method[b]	*WRMS*[c]	*iterations*	$\Phi_1(v^P_{inv})$	$\Phi_1(v^S_{inv})$	$\Phi_s(v^P_{inv})$	$\Phi_s(v^S_{inv})$
$\mu_P,\ \mu_S$	0.0100	4	4.41	4.48	4.58	5.00
$\eta_{PS} = 0.25$	0.0110	4	4.39	4.55	4.55	4.85
$\eta^{\partial}_P = 0.10$ $\eta^{\partial}_S = 0.10$	0.0137	4	4.54	4.74	4.55	5.05
$\eta^{\nabla^2}_P = 0.10$ $\eta^{\nabla^2}_S = 0.10$	0.0152	4	5.14	4.93	4.94	5.24
$\eta^{D}_P = 0.10$ $\eta^{D}_S = 0.10$	0.0102	4	4.47	4.38	4.69	4.91
$\eta^{D}_P = 0.25$ $\eta^{D}_S = 0.25$	0.0120	4	4.28	4.40	4.47	5.00
$\eta^{D}_P = 0.10$ $\eta^{D}_S = 0.10$ $\eta_{PS} = 0.25$	0.0110	4	4.46	4.57	4.63	4.89

[a]Values of Φ were multiplied by 100 to express percentages and each value is determined from a discretization of the model in 68921 points, i.e., $\Omega = 68921$, see equation 3.2.

[b]$\sigma^P_i = 0.20$, $\sigma^S_i = 0.15$. See section 2.3.3.4 for notation.

[c]The initial weighted root mean square residual (WRMS) was 0.037 sec. Values are in seconds.

Table 3.1: Spike model. This table summarizes the results of the inversion for the same starting model but with different *a priori* conditions applied.

SPIKE MODEL MISLOCATIONS[a]							
method	$\overline{x}$	$\overline{y}$	$\overline{z}$	$\lvert\overline{x}\rvert$	$\lvert\overline{y}\rvert$	$\lvert\overline{z}\rvert$	$\lvert\overline{s}\rvert$
μ_P, μ_S	0.003	0.092	-0.386	0.282	0.233	0.483	0.652
	0.748	*0.723*	*1.037*	*0.488*	*0.582*	*0.858*	*1.038*
$\eta_{PS} = 0.25$	0.049	0.071	-0.215	0.287	0.176	0.331	0.520
	0.780	*0.539*	*0.732*	*0.534*	*0.430*	*0.529*	*0.748*
$\eta_P^\partial = 0.10$ $\eta_S^\partial = 0.10$	0.129	0.055	-0.323	0.267	0.232	0.408	0.583
	0.736	*0.666*	*0.911*	*0.566*	*0.489*	*0.762*	*0.972*
$\eta_P^{\nabla^2} = 0.10$ $\eta_S^{\nabla^2} = 0.10$	0.113	0.042	-0.287	0.278	0.253	0.431	0.627
	0.774	*0.744*	*1.011*	*0.582*	*0.549*	*0.776*	*0.988*
$\eta_P^D = 0.10$ $\eta_S^D = 0.10$	0.065	0.075	-0.279	0.274	0.213	0.404	0.571
	0.728	*0.649*	*0.924*	*0.494*	*0.511*	*0.714*	*0.919*
$\eta_P^D = 0.25$ $\eta_S^D = 0.25$	0.077	0.031	-0.246	0.260	0.220	0.359	0.538
	0.724	*0.676*	*0.803*	*0.524*	*0.514*	*0.607*	*0.851*
$\eta_P^D = 0.10$ $\eta_S^D = 0.10$ $\eta_{PS} = 0.25$	0.110	0.059	-0.158	0.283	0.173	0.290	0.486
	0.764	*0.511*	*0.656*	*0.556*	*0.393*	*0.437*	*0.699*

[a] Estimates determined from a total of 110 earthquakes.

Table 3.2: Spike model: this table summarizes the statistics of the mislocations for the various inversions with different *a priori* conditioning applied. All values are expressed in kilometers, (calculated–true) distances. The lower value in each entry is the 2σ of the given estimate (see section 3.2 for details).

3.6 Fault model

This second test with synthetic data was designed expressly to verify whether the method is capable of imaging a relatively narrow fault zone such as the one which has been proposed for the San Andreas fault. Imaging of fault zones is important to assess the mechanical properties of the medium which reveal the earthquake nucleation processes acting there. Much debate is presently underway on this topic and various techniques have been proposed to retrieve properly the fault zone structure. The two main approaches used are travel-time and waveform modeling. The limitation of the first approach is the lack of resolving power at scale lengths of the same order as the fault width. The second approach models the waveform data for wave propagation in the fault zone but relies on simplifications of the velocity structure (e.g., Ben-Zion and Aki, 1990; Li and Leary, 1990). In this thesis, we address the fault zone problem by using the first approach. We follow the pragmatic approach of investigating via synthetic data tests the degree with which an idealized fault zone can be imaged properly, and what kind of *a priori* conditioning should be adopted.

The true fault model which was adopted in this test is shown as a vertical section across the fault in the top row panels of all the figures showing the results. It consists of a two-sided velocity model having a low-velocity zone in the middle. The two sides of the fault have different overall velocity values. Larger velocities were set for $x < 2$ km, in the southwest block, and smaller velocities were assigned for $x > 1$ km, in the northeast block. The central low velocity zone has a constant width of 1 km and is flanked by zones with widths of 1.2 km in which the velocity values vary linearly from the fault zone value to the two side values. Selection of this model was motivated by the need to simulate realistically the characteristic lithologies that have been inferred on either side of the San Andreas fault at Parkfield; the Salinian block to the southwest and the Franciscan formation to the northeast. V_P/V_S is 2.0 near the surface, values of 1.80 and 1.75 in the northeast and southwest blocks, respectively.

SPIKE MODEL MISLOCATIONS[a]							
method	$\overline{x}$	$\overline{y}$	$\overline{z}$	$\lvert\overline{x}\rvert$	$\lvert\overline{y}\rvert$	$\lvert\overline{z}\rvert$	$\lvert\overline{s}\rvert$
μ_P, μ_S	0.003	0.092	-0.386	0.282	0.233	0.483	0.652
	0.748	*0.723*	*1.037*	*0.488*	*0.582*	*0.858*	*1.038*
$\eta_{PS} = 0.25$	0.049	0.071	-0.215	0.287	0.176	0.331	0.520
	0.780	*0.539*	*0.732*	*0.534*	*0.430*	*0.529*	*0.748*
$\eta_P^{\partial} = 0.10$ $\eta_S^{\partial} = 0.10$	0.129	0.055	-0.323	0.267	0.232	0.408	0.583
	0.736	*0.666*	*0.911*	*0.586*	*0.489*	*0.762*	*0.972*
$\eta_P^{\nabla^2} = 0.10$ $\eta_S^{\nabla^2} = 0.10$	0.113	0.042	-0.287	0.278	0.253	0.431	0.627
	0.774	*0.744*	*1.011*	*0.582*	*0.549*	*0.776*	*0.988*
$\eta_P^D = 0.10$ $\eta_S^D = 0.10$	0.065	0.075	-0.279	0.274	0.213	0.404	0.571
	0.728	*0.649*	*0.924*	*0.494*	*0.511*	*0.714*	*0.919*
$\eta_P^D = 0.25$ $\eta_S^D = 0.25$	0.077	0.031	-0.246	0.260	0.220	0.359	0.538
	0.724	*0.676*	*0.803*	*0.524*	*0.514*	*0.607*	*0.851*
$\eta_P^D = 0.10$ $\eta_S^D = 0.10$ $\eta_{PS} = 0.25$	0.110	0.059	-0.158	0.283	0.173	0.290	0.486
	0.764	*0.511*	*0.656*	*0.556*	*0.393*	*0.437*	*0.699*

[a]Estimates determined from a total of 110 earthquakes.

Table 3.2: Spike model: this table summarizes the statistics of the mislocations for the various inversions with different *a priori* conditioning applied. All values are expressed in kilometers, (calculated-true) distances. The lower value in each entry is the 2σ of the given estimate (see section 3.2 for details).

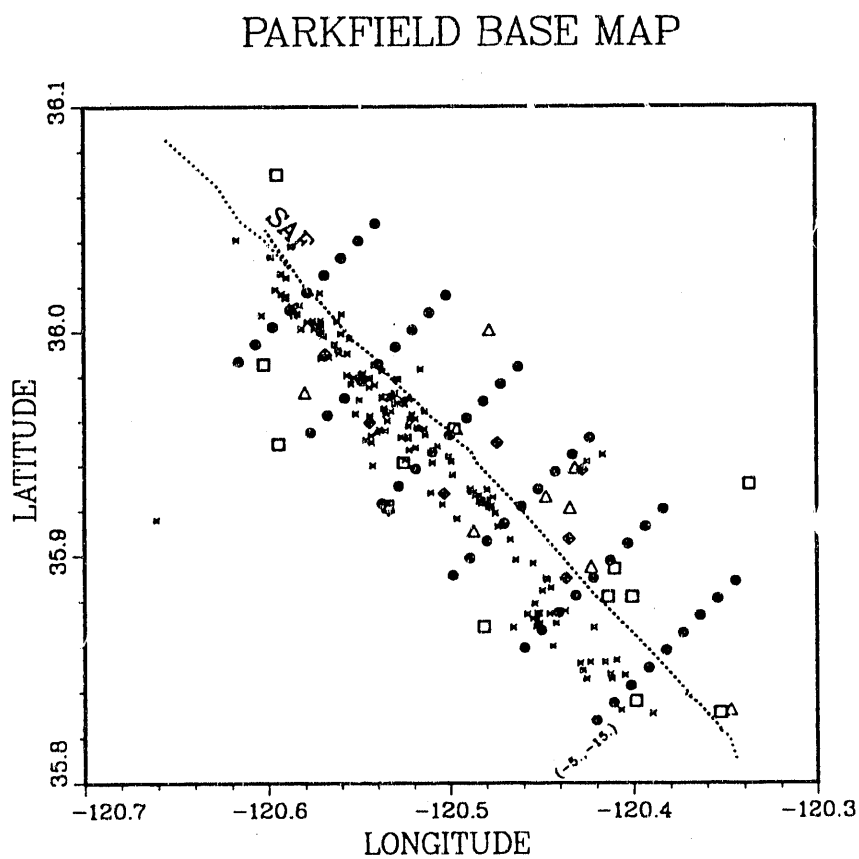

Figure 3.18: Parkfield base map showing locations of the HRSN stations (open triangles), the CALNET-USGS stations (open squares), the grid nodes used in the inversion (solid circles), the vibration points of the controlled source experiment (diamonds with inner cross), the 169 earthquakes used for the joint inversion in the fault test (crosses), and the surface trace of the San Andreas Fault (SAF) (dashed line). The grid mesh is centered at the 1966 main shock ($35°57.3'N, 120°29.7'W$) and rotated 45° counterclockwise. For reference, the coordinates of the southernmost knot-column of the grid mesh are shown. Node interval is 1.2 and 5.0 km across and along the SAF, respectively.

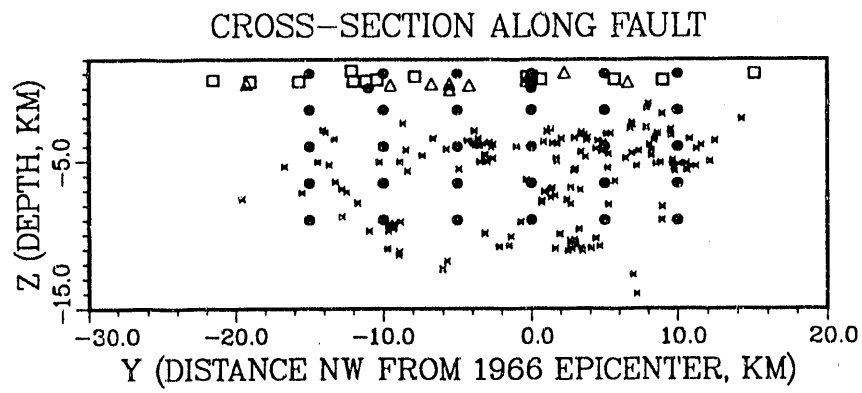

a.

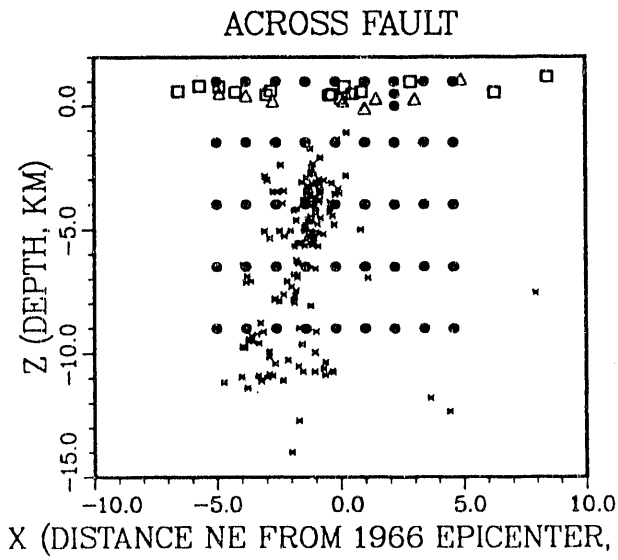

b.

Figure 3.19: The 169 earthquakes used for the inversion and the position of the nodes in the local reference system defined by the grid mesh. a) vertical cross-section along fault (southeast-northwest, $y - z$); b) vertical cross-section across the fault (southwest-northeast, $x - z$). Grid mesh, stations and earthquakes are plotted with the same symbols of figure 3.18.

In the fault zone at depth of 6.5 km, a V_P/V_S value of 2.1 is assigned. This relatively large value of the V_P/V_S ratio implies that the S model has a more accentuated low velocity zone than the P-model. The synthetic travel times were calculated using the Prothero et al. (1988) ray tracer with linear B-splines velocity interpolation.

Two grids were used for the inversions. The first is similar to the one used for the spike test shown in figures 3.1 and 3.2. The second has a more dense grid mesh along the x-axis (1.2 km interval), increasing the total number of nodes to 270 ($9 \times 6 \times 5$ along x, y and z, respectively) The total number of velocity parameters when both P and S models are determined is 540.

3.6.1 Inversions

In general, there are two different philosophies that can be followed when performing tomographic reconstructions.

The first consists of solving initially with a coarse grid spacing. The resulting velocity model is interpolated and used as starting model for the final inversion with a more dense grid.

The second philosophy begins with a dense grid and adopts it throughout the inversion. As I will show in what follows, there seem to be advantages and disadvantages in both procedures. In general, researchers who advocate the second philosophy remark that the first one can suffer of some structure spatial aliasing whereas those that favor the first remark that the second approach can generate numerical instabilities because too many velocity parameters are used. In the following, I will show application of both procedures.

3.6.1.1 Inversion performance

The results of the inversion with different initial discretization grids and different *a priori* conditioning are summarized in tables 3.3 and 3.4. The values of $\Phi_1(v_{inv})$ and

$\Phi_s(v_{inv})$ are calculated from a total of 68921 points (i.e., $41 \times 41 \times 41$, along x, y and z, respectively) within the imaged volume.

Table 3.3 lists the values of the final weighted RMS, the total number of iterations required for final convergence and the values of the MPDF calculated with equa weighting, $\Phi_1(v_{inv})$, and spread function weighting, $\Phi_s(v_{inv})$. In table 3.3 the values of the MPDF are calculated for the entire volume target of the inversion. In table 3.4 the results obtained from a subset of three inversions are listed for the inner and better resolved parts of the model ($-5 \leq x \leq 5$, $-10 \leq y \leq 5$ km) and for different depth ranges.

We proceed by analyzing first tables 3.3 and 3.4. Description and discussion of some selected velocity models is given in individual subsections.

The inversion results listed in table 3.3 can be roughly subdivided into two groups according to their performance measured in terms of WRMS and MPDF. The first group performs better and includes inversions with coarse and fine initial gridding, damping-only, ray-density and V_P/V_S conditioning. The second group includes inversions in which some smoothing conditions have been applied.

Among the inversions of the first group, the model resolved with an initial coarse grid interval along the x-axis (2.0 km across the fault) produces the minimum residual misfit (WRMS=0.014 sec), and the best fit to the true P model ($\Phi_1^P(v_{inv}) = 5.32$ %). The best fit to the true S model is obtained with some V_P/V_S conditioning and a fine initial gridding ($\eta_{PS} = 0.25$, $\kappa = 1.8$, $\Phi_1^S(v_{inv}) = 7.67$ %). The other inversions of the first group display WRMS, Φ_1^P and Φ_1^S ranging within 1.6 msec and within 1 % from the best values listed above, respectively. With one exception that will be discussed shortly, the spread function weighted MPDF for the P model, Φ_s^P, displays values similar or slightly higher than the equal weight case, Φ_1^P. In contrast, for the S model, Φ_s^S is generally smaller than Φ_1^S.

The relatively higher values observed for Φ_s^P in this test suggest that the better

resolved parts of the model are not necessarily closer to the true ones. This might result, in part, from overdiscretization of the velocity model and it is suggested by the lower values of Φ_s^P for the inversion performed with an initial coarse grid and finer discretization in the last iterations of the inversion —the previously mentioned exception. However, this line of reasoning does not appear to apply for the S model. Φ_s^S is always less than the Φ_1^S implying that the better resolved parts of the S model have also improved fit to the true model. While it is difficult to provide an explanation for the different behaviours of Φ_s^P and Φ_s^S, we can speculate that relatively poorer fits of the P model in well-resolved volumes might be caused by underdamping in the iterative inversion (i.e., the selected threshold value, σ_t^P, of the modified covariance is too large which results in smaller values of μ_P, see section 2.3.5.2). This underdamping combined with overparameterization would produce short-wavelength fluctuations in well-resolved parts of the model.

The best fit to the true S-velocity is obtained with some small amount of V_P/V_S conditioning. This result confirms the validity of this type conditioning when the iterative simultaneous inversion is performed for both P and S models. In practice, the introduced additional coupling has the effect of "spilling" P into S ray-coverage, and vice versa, while stabilizing the inversion. This effect is exemplified in table 3.3 by the lower values attained by the MPDF when, in identical grid parameterizations, only some coupling is added (i.e., $\eta_{PS} = 0.25$ vs. μ_P, μ_S). The overall degraded fit as indicated by the MPDF for the S models can be explained instead by the poorer resolving power of the S data set.

The inversion with linear B-splines basis functions (Thurber, 1983) resulted in values of the MPDF lower than its analogous with cubic B-splines, although a larger number of iterations (13) were needed to avoid short wavelength instabilities. This result was expected and follows from the more local parameterization of the linear B-splines (i.e., 8 vs. 64 nodes needed to interpolate the velocities) and from the nature

of the selected true model which features large linear gradients.

In the second group of inversions in table 3.3, first and second derivatives smoothing conditions were applied. The poorer fit in terms of both WRMS and MPDF confirms the results obtained in the spike test, that is, this type of smoothing can severely degrade the fit to the true model.

We now focus the discussion to the results listed in table 3.4 for the inner part of the model and for different depth ranges. In this table we compare the values of the equal weight MPDF calculated from the inversions with 1) initial coarse grid with damping-only (μ_P, μ_S), 2) initial fine grid with damping-only (μ_P, μ_S) and 3) initial fine grid with some V_P/V_S conditioning applied ($\eta_{PS} = 0.25,\ \kappa = 1.8$).

The listed values in table 3.4 suggest an apparent duality between velocity models resolved with initial coarse and initial fine grids.

The coarse initial grid displays improved fits to the true P model in the entire depth range ($-9 \leq z \leq 1$) km and at shallow depths ($-5 \leq z \leq 1$) for both P and S models. Conversely, improved fits to the deep P model are obtained only when the fine discretization grid is selected throughout the inversions. With regards to the S model, the initial fine discretization grids appear to perform better in the entire depth range ($-9 \leq z \leq 1$) and again in the deeper parts ($-9 \leq z \leq -4$). It appears that both these trends, i.e., better fits of P and S models in the shallow parts with initial coarse gridding and improved fits to the S model overall and to the deeper parts of P and S models with fine discretization, have a common origin — partial lack of resolving power in the data set.

In fact, when the inversion is performed with coarse grids in the initial iterations, the data set in the final series of iterations does not have enough resolving power where the coverage is sparse (i.e., at depth) and is not capable to sharpen the previously resolved features. Similar arguments apply to the S model which, as well, suffers of sparse ray-coverage.

The need for a detailed model at depth has lead us to use initial fine gridding across the SAF for the inversions with the Parkfield data set presented in chapter 4.

A brief description of the features of some of the selected models now follow.

3.6.1.2 P and S damping, initial coarse mesh

In this test, inversion was performed first with a coarse, 2 km grid along the x-coordinate followed by interpolation and inversion with a 1.2 km grid. Figures 3.20, 3.21 and 3.22 illustrate the resolved P, S and V_P/V_S models. Examination of the P model shows that the use of a coarse grid has inhibited the retrieval of the low velocity zone. In fact, it is found that it can be retrieved only in the shallow 4 kilometers in the inner, well-resolved sections (panels *c.* and *d.* in figure 3.20).

The S model in figure 3.21 shows a more marked fault zone anomaly which derives from the marked low-velocity imposed in the true S model. The V_P/V_S value is highly unstable at the boundary cross-sections whereas in the inner, better-resolved ones at $y = -5$ and $y = 0$, true anomalies at the surface and at depth are grossly reproduced.

From this test, it appears that, once an initial model with a coarse grid is obtained, lack of resolving power prevents the determination of the necessary adjustments to correct the long wavelength features impressed by the meshing and resolve the details of the given model, although the values of $\Phi_1(v_{inv})$ and $\Phi_s(v_{inv})$ listed in table 3.3 show that this inversion attained the best fit to the true P model.

3.6.1.3 P and S damping

The results obtained from the inversion with only P and S damping and a dense grid mesh adopted throughout the entire inversion are shown in figures 3.23, 3.24 and 3.22. Both P and S models display much sharper boundaries for the fault but, unfortunately, they also show a larger number of instabilities. The fault low velocity zone is reasonably well-imaged by both P and S models down to depths of 9 km in

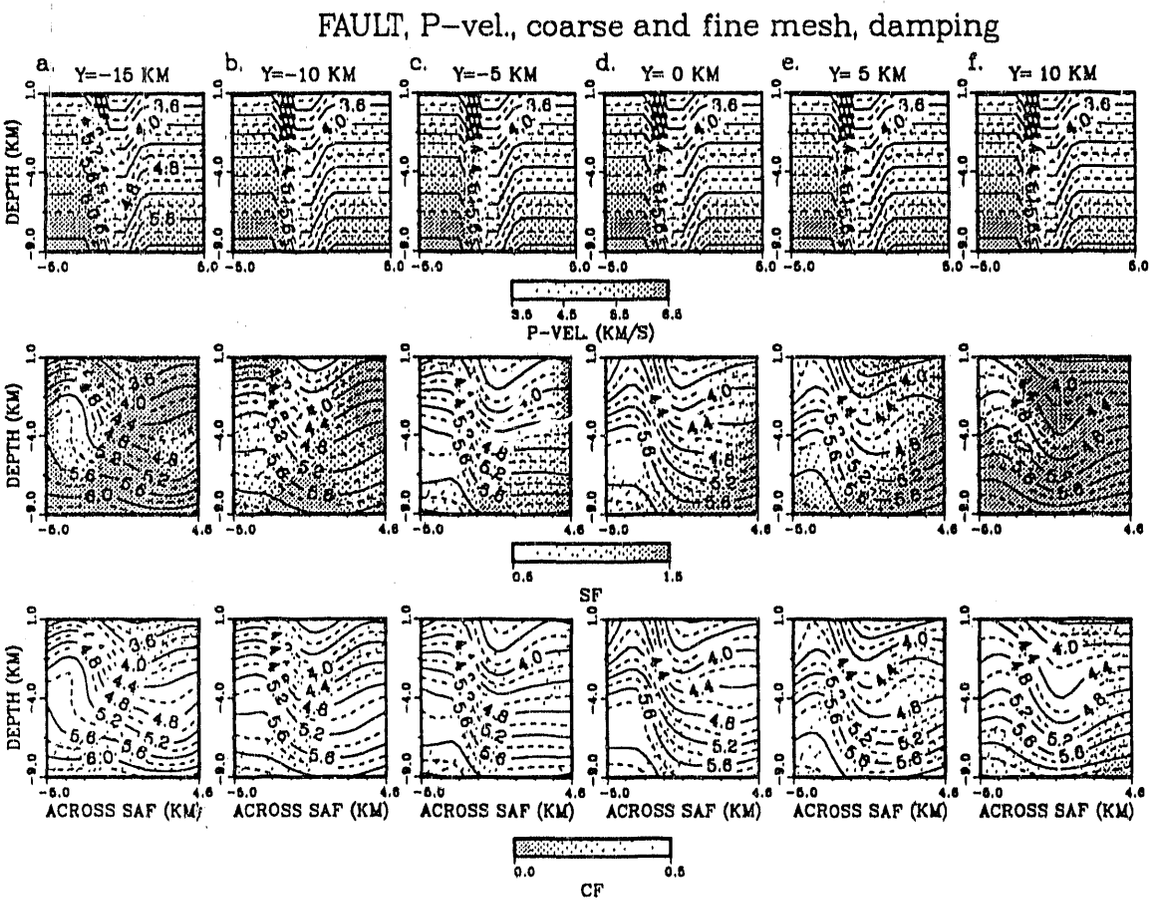

Figure 3.20: Fault P-model: P and S damping with coarse gridded model in the first iterations (same format as in figure 3.3).

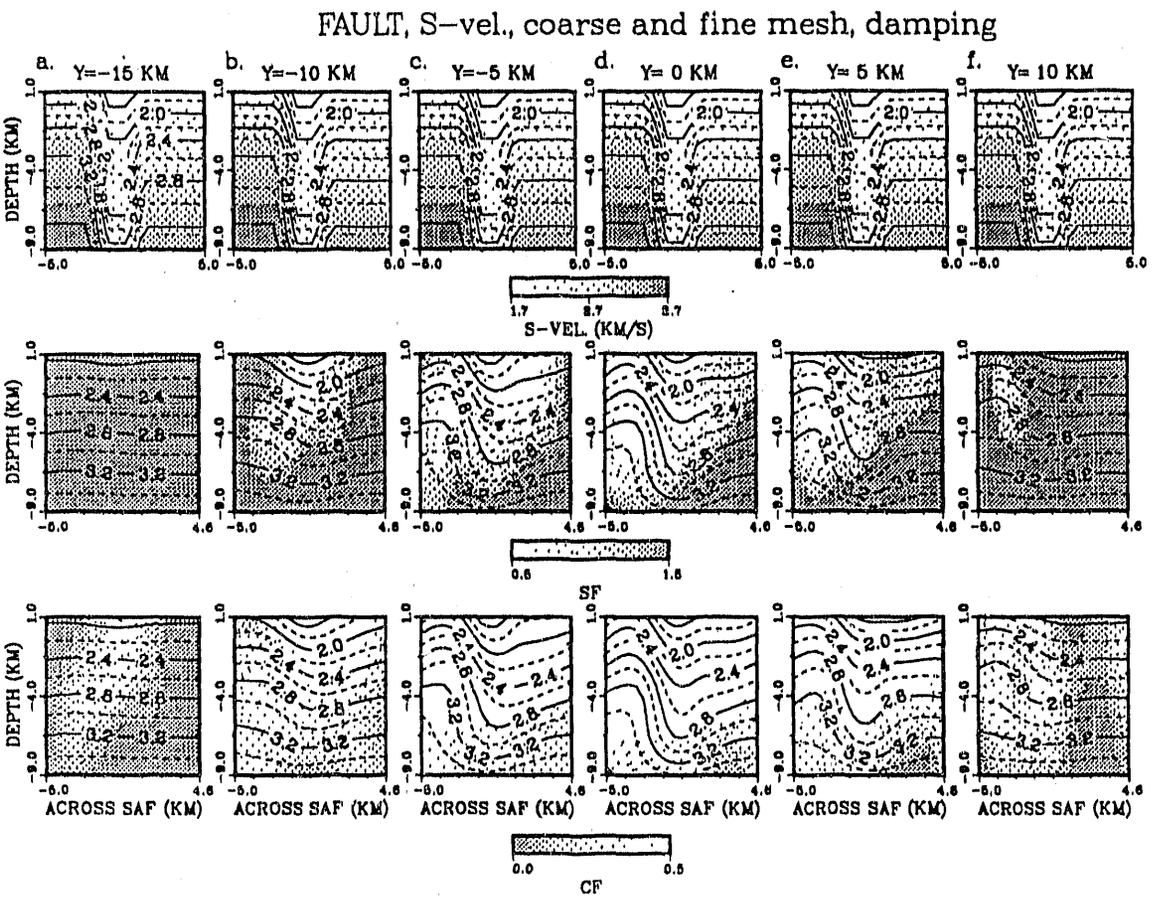

Figure 3.21: Fault S-model: P and S damping with coarse gridded model in the first iterations (same format as in figure 3.3).

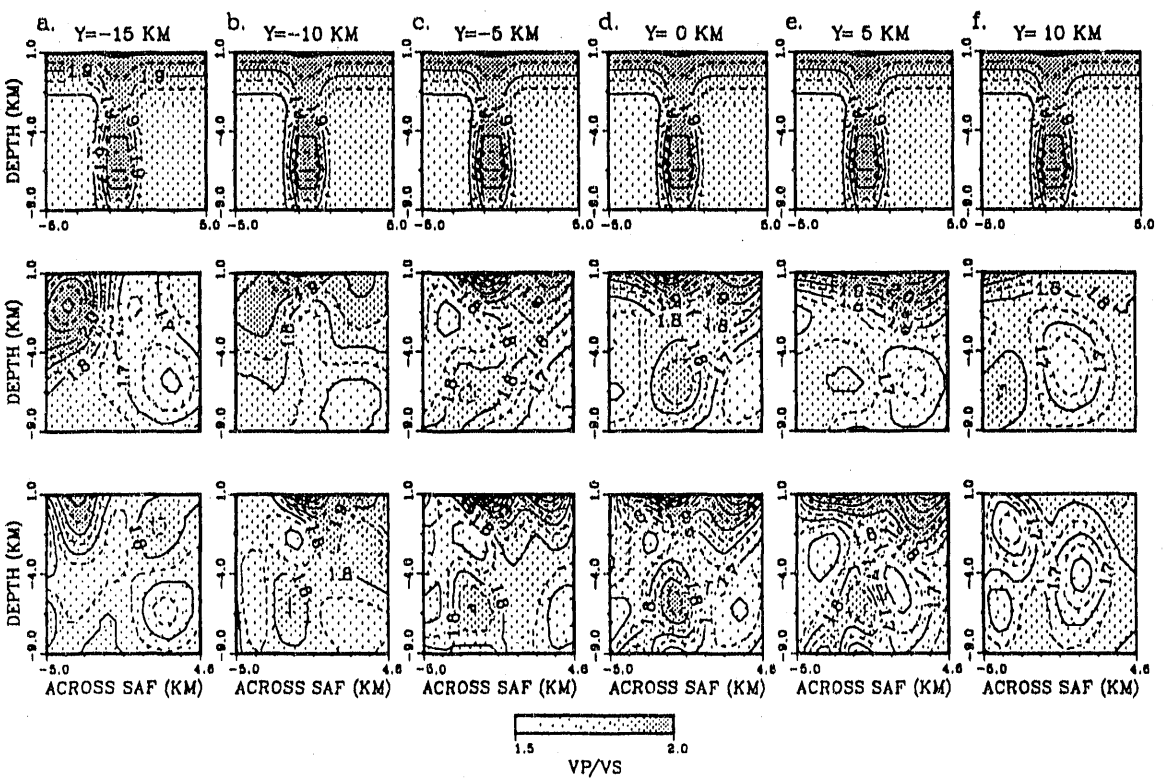

Figure 3.22: Fault V_P/V_S model: true model (top); P and S damping with initial coarse grid mesh (middle); P and S damping (bottom).

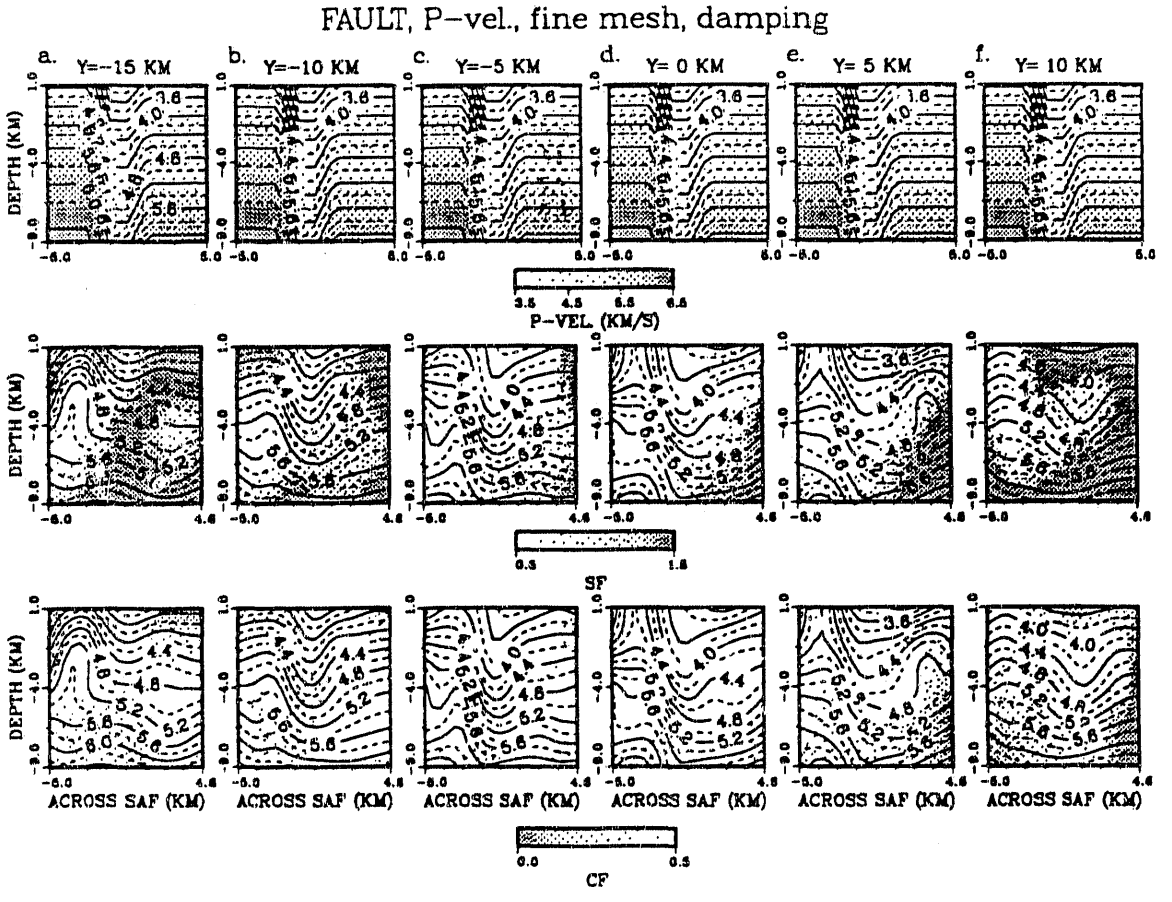

Figure 3.23: Fault P-model: P and S damping (same format as in figure 3.3).

the inner cross sections (panels *c.* and *d.* in figures 3.23 and 3.24). The V_P/V_S ratio in the fault zone displays a value of 1.95 in the inner cross-sections at $y = 0$ at the location of the true anomaly. However in the same section, some instabilities can be noticed around the fault zone having values as low as 1.6.

Although the fit to the true P model is poorer (see table 3.3), comparing figures 3.23 and 3.20 shows that resemblance to the true model is better when the dense grid is adopted from the beginning of the inversion. This follows from the improved fits in the deeper parts of the model (see table 3.4) and from the fine discretization that allows to model large gradients.

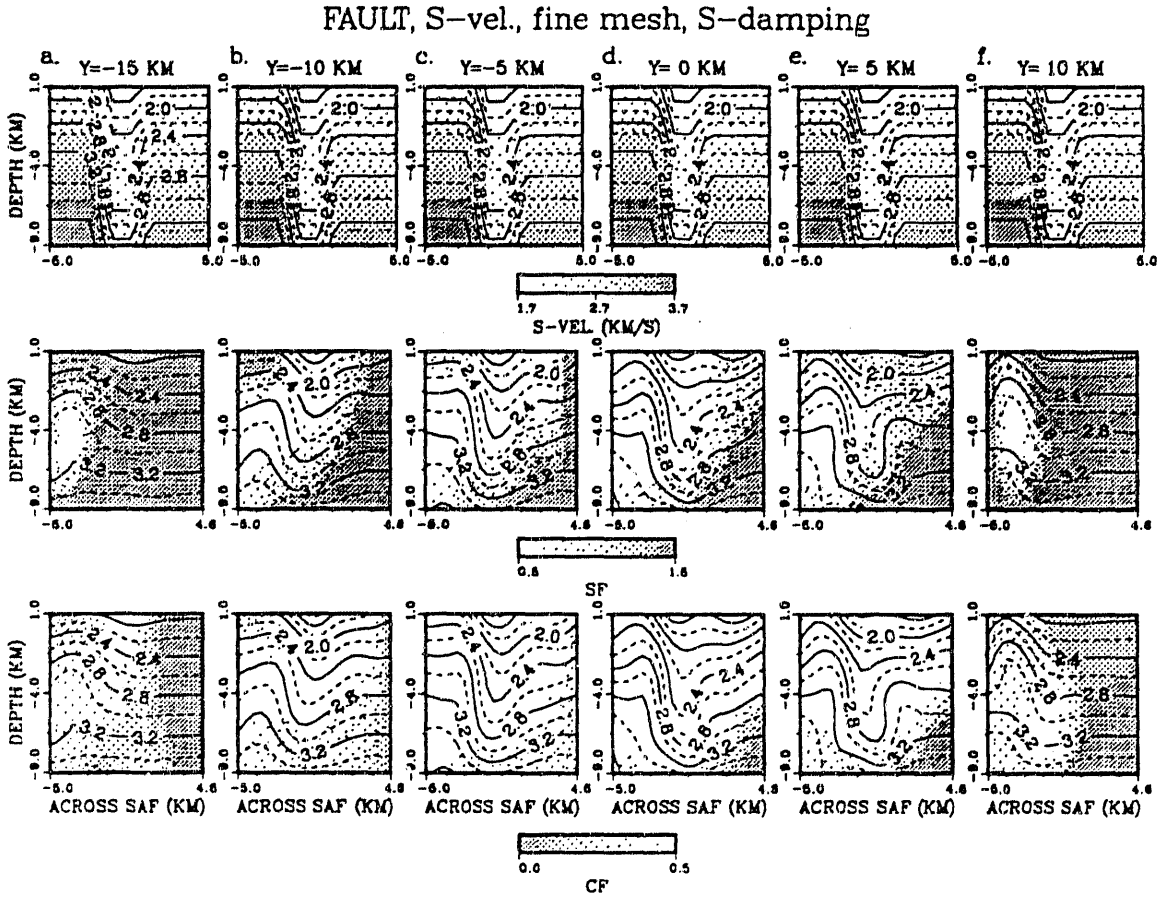

Figure 3.24: Fault S-model: P and S damping (same format as in figure 3.3).

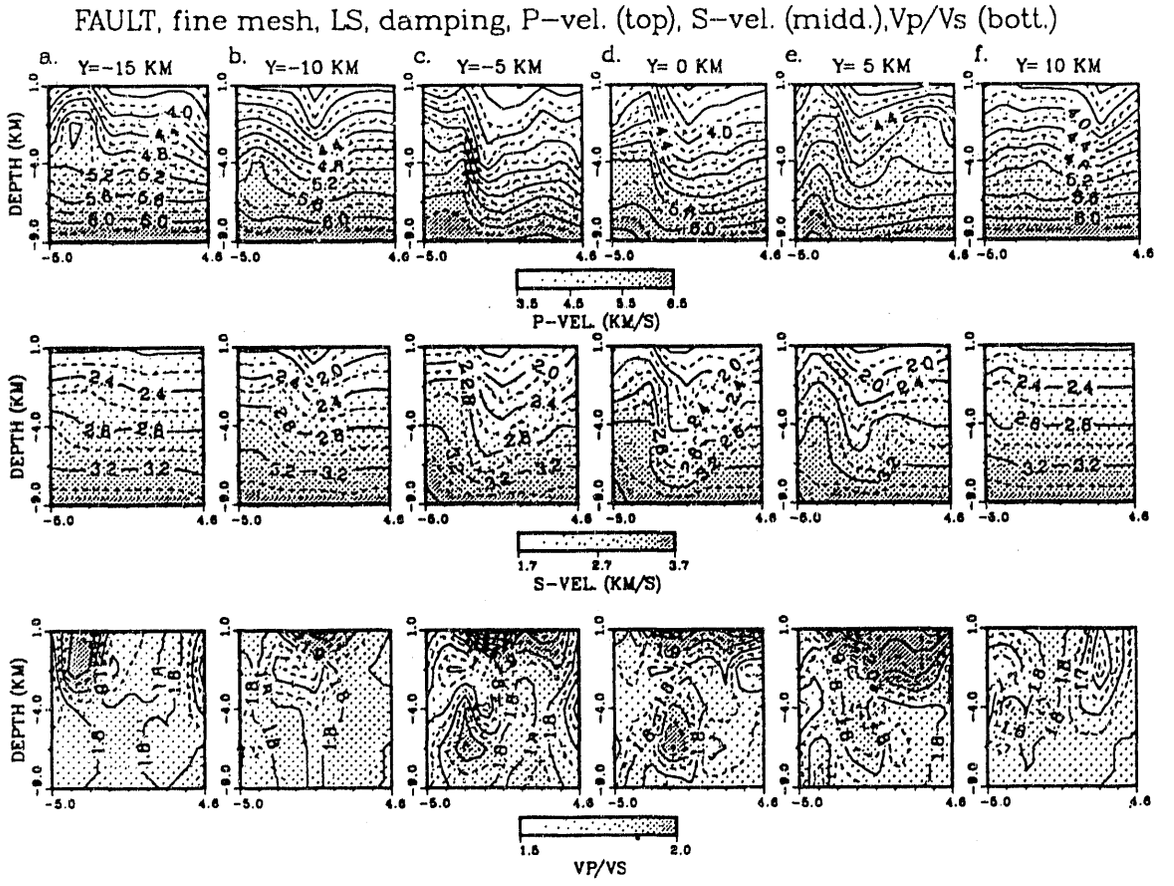

Figure 3.25: Fault models obtained using linear B-splines parameterization: P-model (top); S-model (middle) and V_P/V_S (bottom).

3.6.1.4 P and S damping with linear B-splines

This test compares the results obtained with a lower degree basis function such as the one introduced by Thurber (1983). The model obtained using the same synthetic data of the previous tests is shown in figure 3.25. Comparison of the resolved P models obtained using cubic and linear B-splines basis functions parameterization shows that there are not significant differences among them (see figures 3.23 and 3.25) besides the inherent degree of smoothness that results from the different choice of basis functions.

Examination of the tabulated values of $\Phi_1(v_{inv})$ in table 3.4 shows that the fit of the model obtained using linear basis functions is slightly better than the others

resolved with cubic B-splines. This applies to the P model and in most cases to the S model and it is due the more *local* nature of the parameterization which can produce velocity values which are closer to true ones. The obvious shortcoming of this improved but more local fit is the rise of more abrupt instabilities in the V_P/V_S models. Finally and anticipating a topic that will be addressed later, the linear splines parameterization consistently produces earthquake locations which are more biased than those obtained using cubic basis functions (see tables 3.5 and 3.6).

3.6.1.5 Smoothing condition

When damping only and a fine discretization are used as in the previous test, some instabilities arise in the resolved models. As seen in the spike model test, two types of *a priori* conditioning can be applied to control this problem to some degree: smoothing using first or second derivatives, and ray-density weighting. In figures 3.26 to 3.28, we show the results obtained by adding some first derivative conditioning. A value of 0.25 was assigned to both η_P^∂ and η_S^∂. As expected, this amount of conditioning produces the desired smoothing by considerably reducing the sharpness of the resolved model. Incidentally, the final resolved model resembles the one resolved by using a coarse grid in the initial iterations. However, it should be noticed that the values of the MPDF and of the weighted RMS listed in table 3.3 indicate that this smoothing condition has substantially degraded the fit to the true model. This is opposite to what was observed when the initial iterations were made using the coarse grid, producing a smooth model having also an good fit.

Another feature of the resolved model is its difficulty in imaging the low-velocity zone. In general, ray paths bend toward zones of high-velocity, leaving zones with relatively low velocities poorly sampled. It follows that when some *a priori* smoothing is applied and no attempt is made to account for poorly sampled nodes, the model will be smoother in parts which are sparsely sampled. Eventually, this feature can

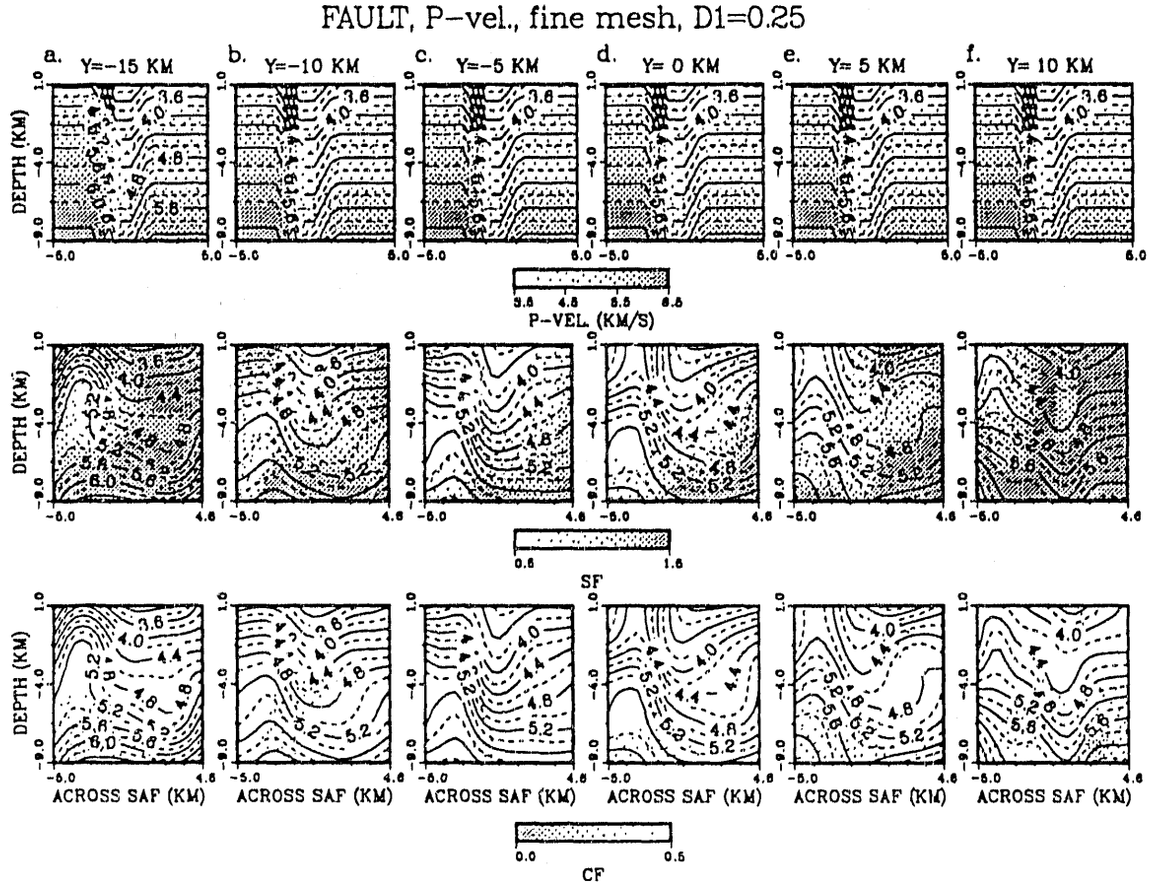

Figure 3.26: Fault P-model: first derivative conditioning (same format as in figure 3.3).

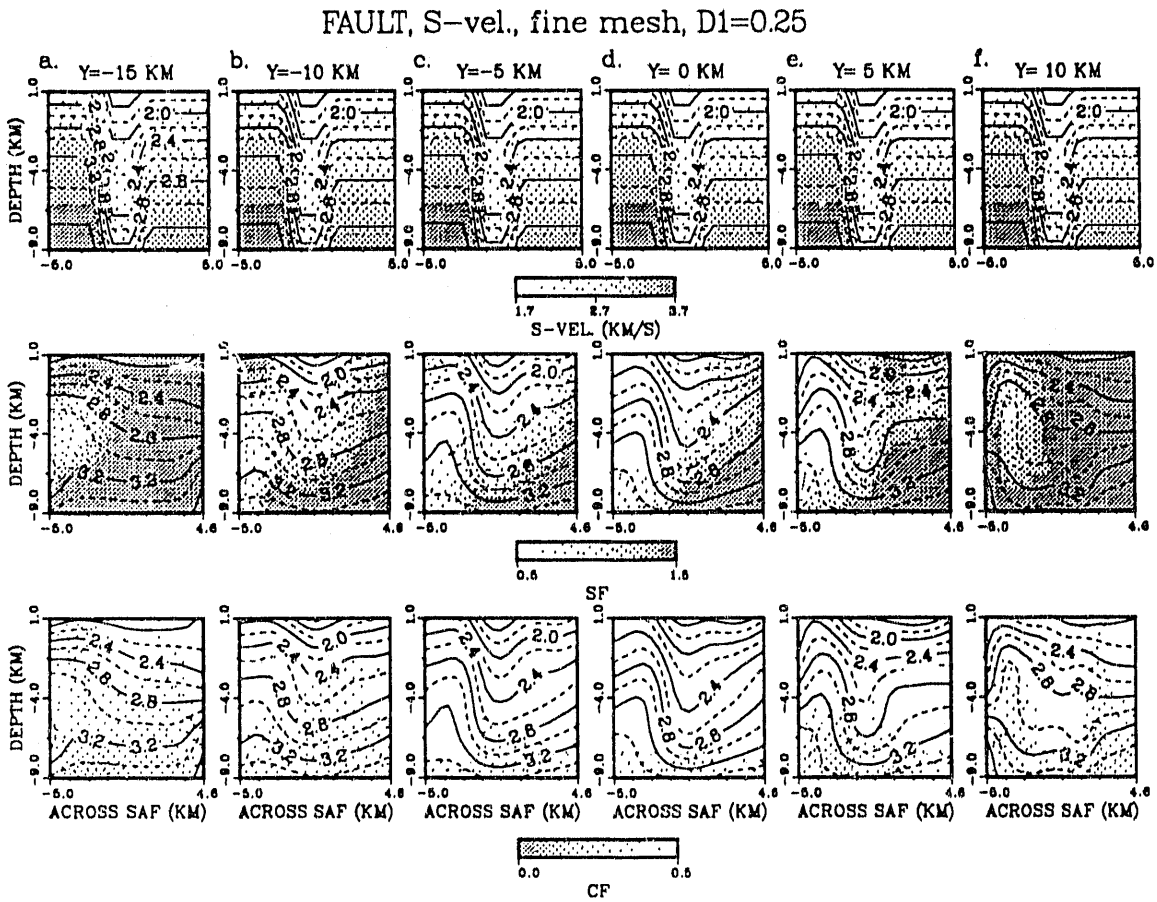

Figure 3.27: Fault S-model: first derivative conditioning (same format as in figure 3.3).

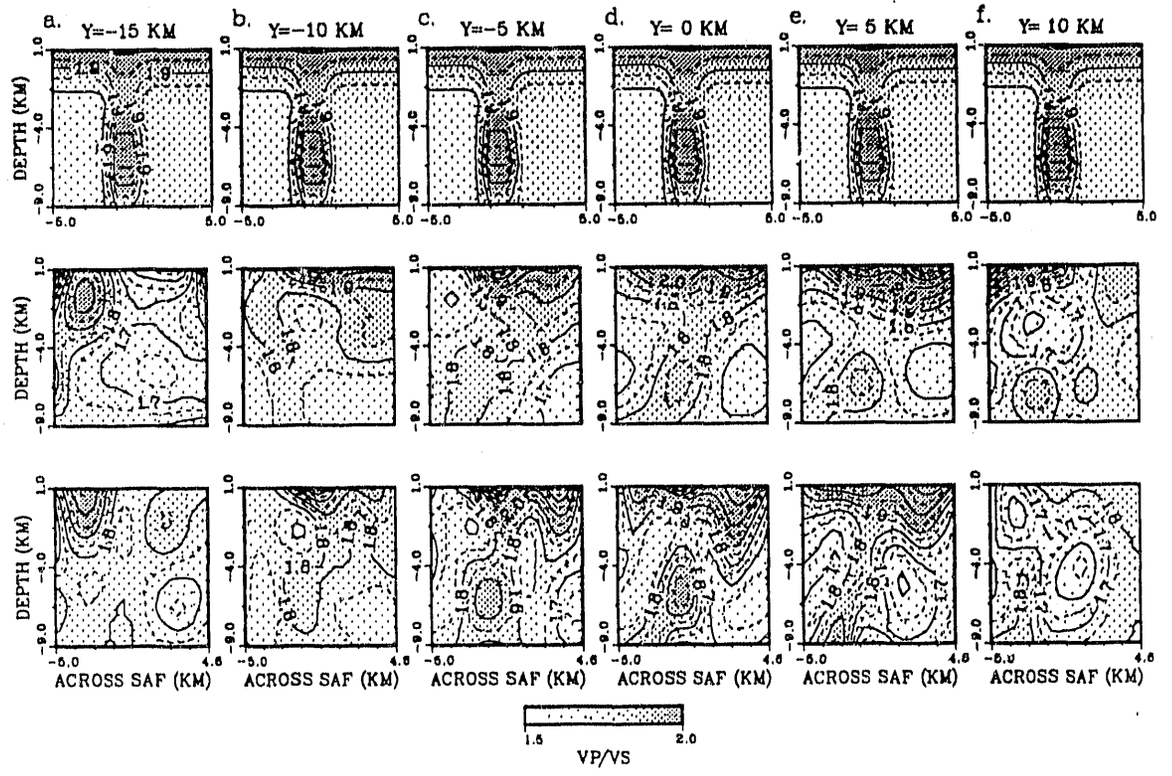

Figure 3.28: Fault V_P/V_S model: true model (top); first derivative conditioning (middle); ray-density conditioning (bottom).

be corrected but, in some cases, it may be desirable to have smoother models where the coverage is sparse. Finally, the V_P/V_S ratio shown in figure 3.28 defines the anomalous zones having large values in the inner parts of the model, but it contains large instabilities at the boundary cross sections.

3.6.1.6 Ray-density conditioning

It was shown in the spike test that this type of conditioning compensates for the different ray-coverages and tends to smooth the resolved model. In the spike test it was also found that the resulting model had the best fit to the true one. In this test, we have assigned a value of ray-density conditioning of 0.1 to both η_P^D and η_S^D and the resolved models are shown in figures 3.29, 3.30 and 3.28. These do not differ significantly from our first case in which we applied only damping although, the final weighted RMS value has now slightly decreased and the MPDF, $\Phi_1(v_{inv})$, has also a smaller value (5.95 % versus 6.33%) for the P model whereas the S model performs slightly worse. The V_P/V_S model is shown in figure 3.28 and it is also very similar to the one obtained by applying P and S damping only.

3.6.1.7 V_P/V_S conditioning

This conditioning was applied in the spike test, resulting in coupled P and S models. Where the P model diverged from the true one in poorly sampled zones, the S model suffered of the same fate. Conversely, in well-sampled areas for P, the coupling produced a better defined S model. In any event, the spike test was a highly idealized case because the V_P/V_S was equal to 1.75 throughout the model. The fault test instead has varying V_P/V_S ratio and the aim of this section is to verify whether some amount of extra coupling can be introduced to limit instabilities and preserve the true anomalies without severely biasing the results. The results of this conditioning for a value of $\eta_{PS} = 0.25$ and a value of $V_P/V_S = 1.80$ are shown in figures 3.31, 3.32

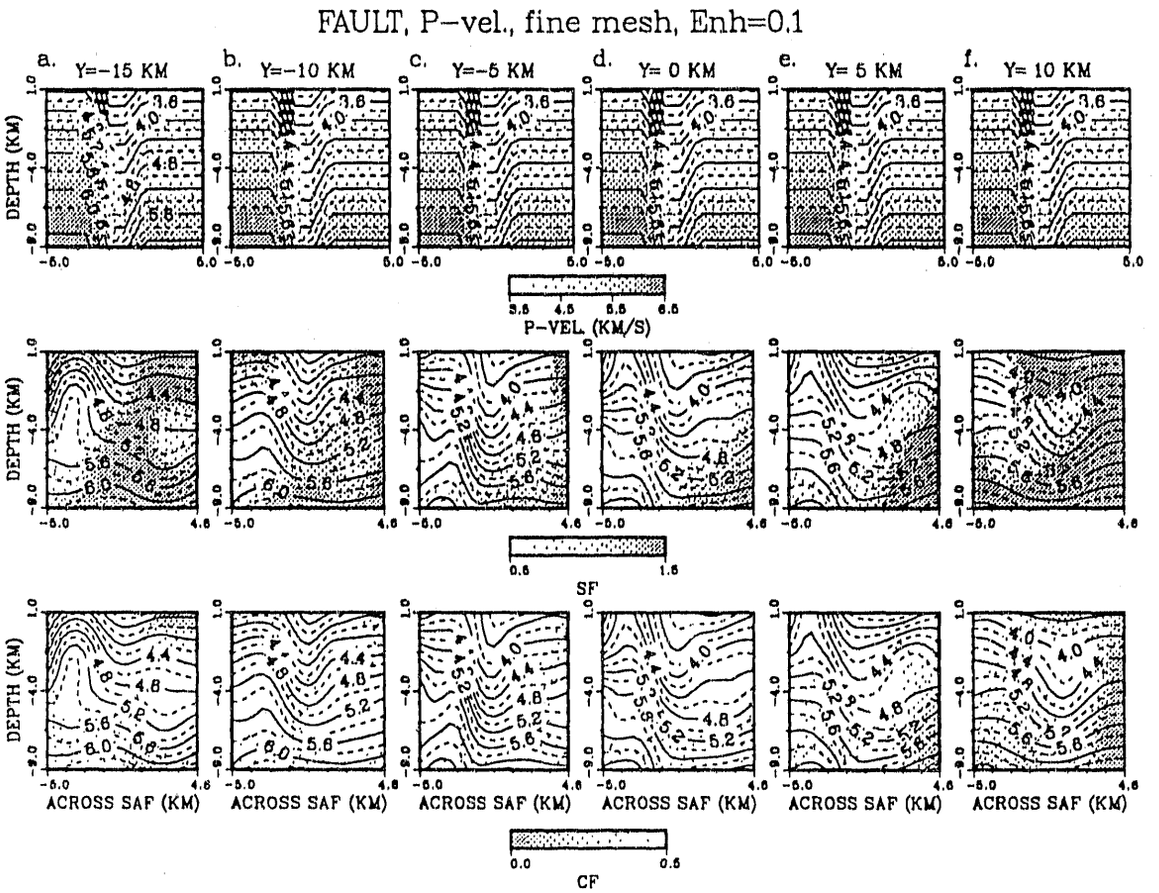

Figure 3.29: Fault P-model: ray-density conditioning (same format as in figure 3.3).

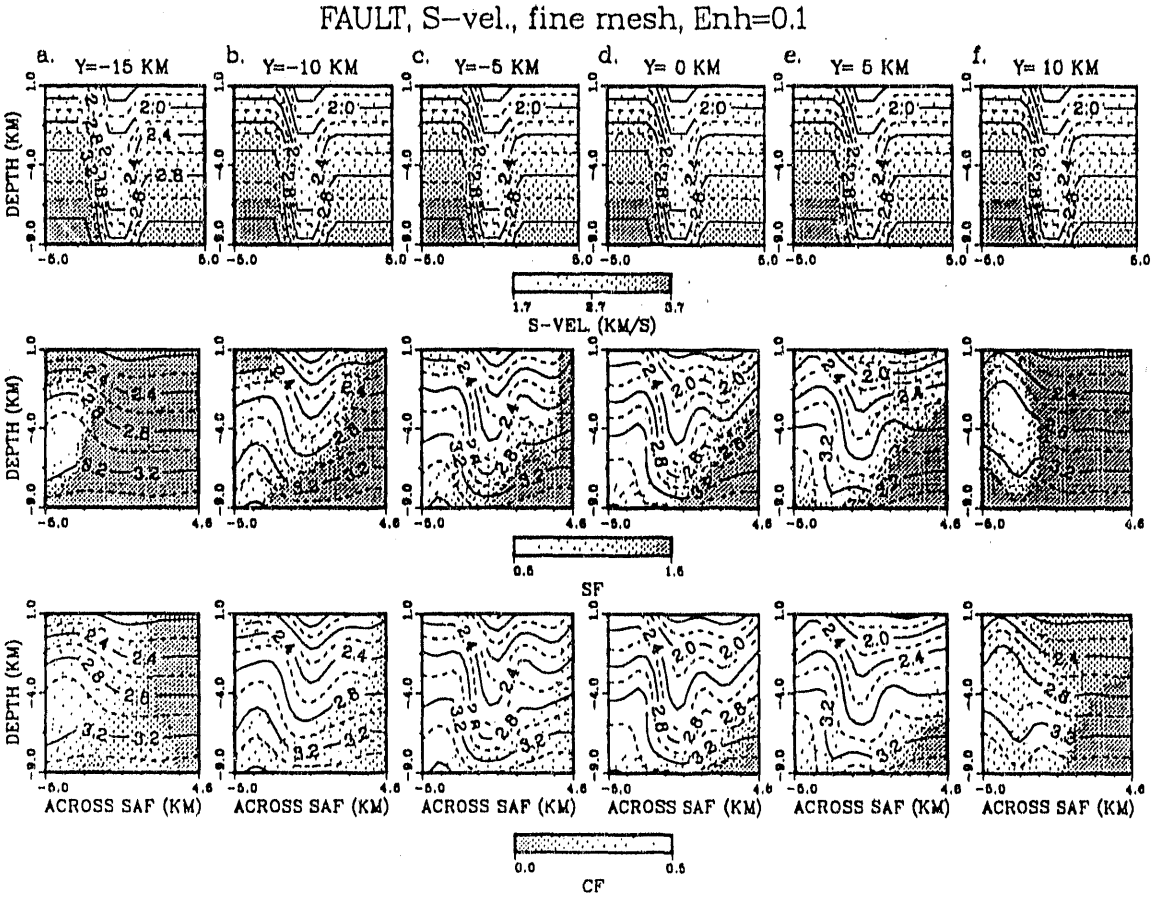

Figure 3.30: Fault S-model: ray-density conditioning (same format as in figure 3.3).

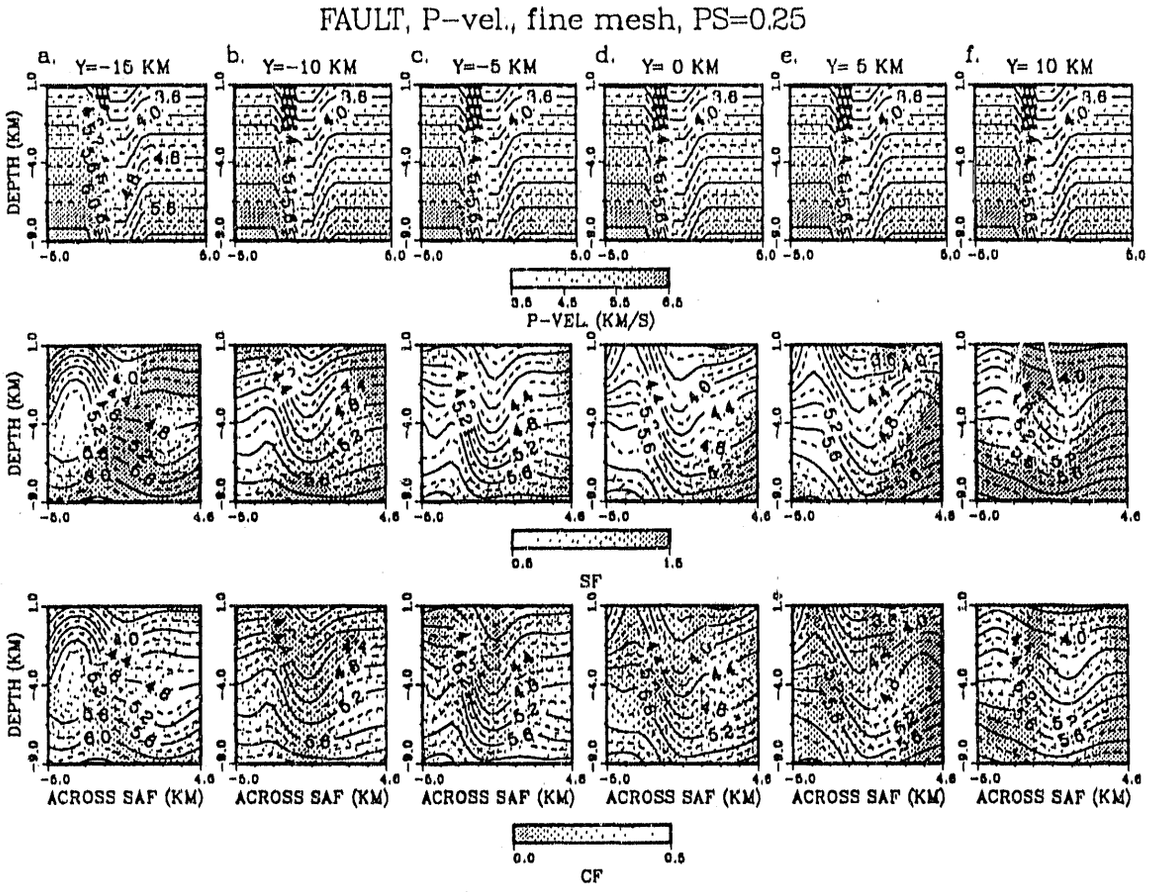

Figure 3.31: Fault P-model: V_P/V_S conditioning (same format as in figure 3.3).

and 3.33. Although it is difficult to discern any real improvement for the P model (compare with figure 3.23), there is some slight improvement in the fit as indicated by the values in table 3.3. The S model has also improved (see table 3.3) and at the boundaries, as expected, it closely resembles the P model. The real improvement can be observed in the sections of the V_P/V_S model, where the conditioning has eliminated the instabilities while preserving the true anomalies at the surface and in the fault zone. Furthermore, in the better resolved sections, V_P/V_S converges to the true values on both sides of the fault.

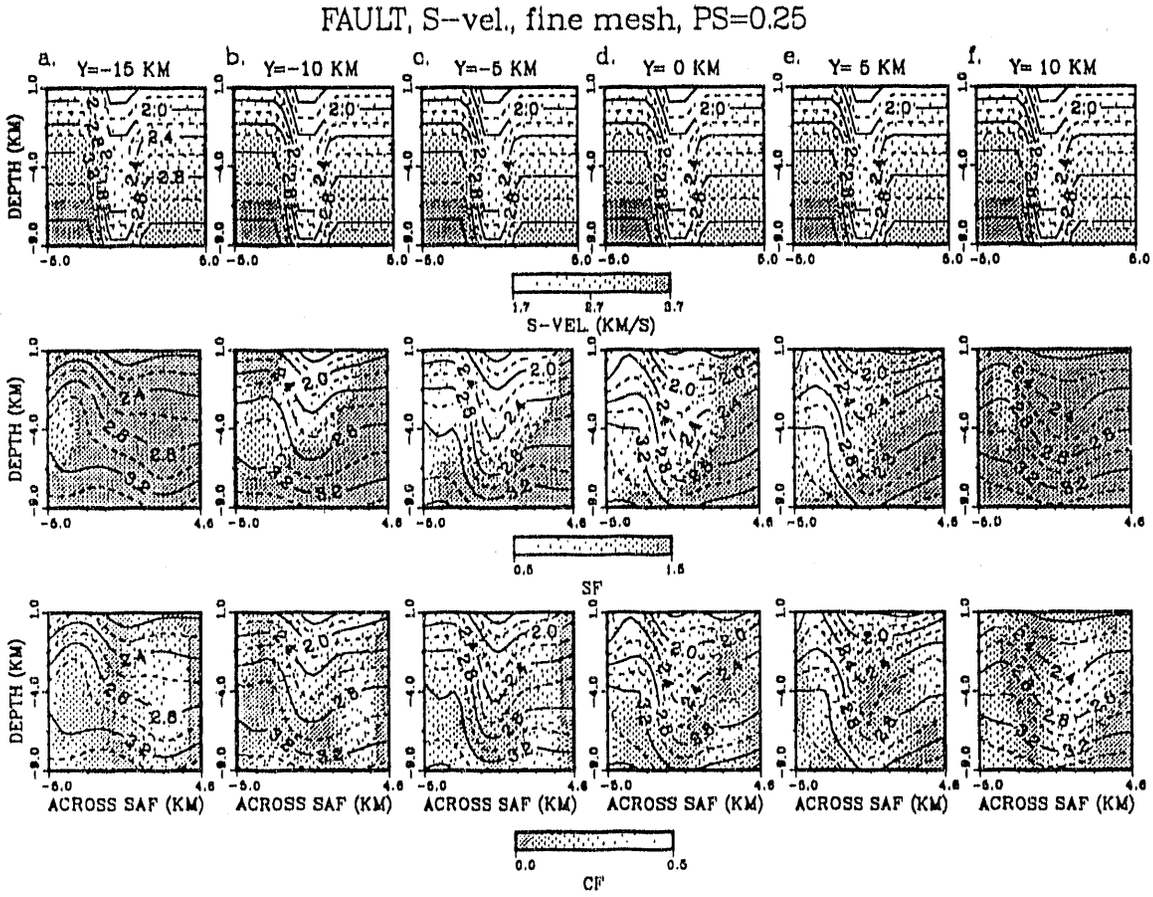

Figure 3.32: Fault S-model: V_P/V_S conditioning (same format as in figure 3.3).

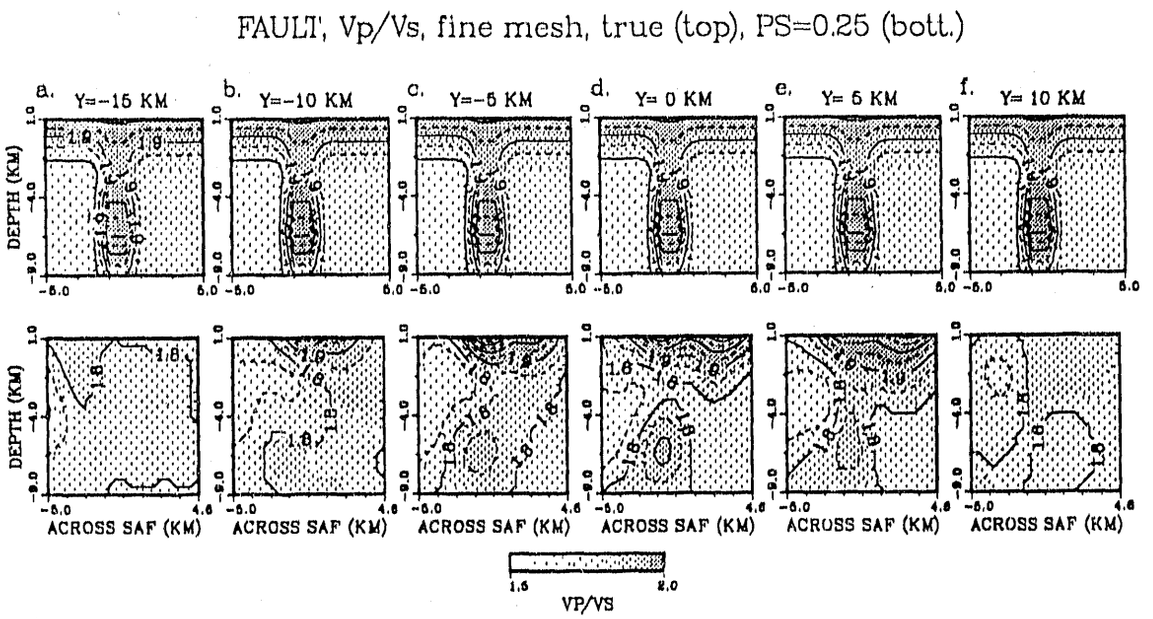

Figure 3.33: Fault V_P/V_S model: true model (top); V_P/V_S conditioning (bottom).

3.6.2 Earthquake mislocations

The statistics of the earthquake mislocation calculated using all the earthquakes in the inversion is listed in table 3.5. The first three columns show that in the fault test the earthquake locations are biased because their mean location moved to the southwest and shallower by some variable amount. The shift toward the southwest ranges between 0.6 km for the inversion with coarse grid spacing in the first iterations and about 1.4 km when the resolved model was parameterized in terms of linear B-splines basis functions. Depth is biased about 0.5 km deeper. The mean mislocation distance, $|\bar{s}|$ ranges between a minimum of approximately 1 km which was obtained with an initial coarse model to about 1.7 km obtained with linear parameterization.

In table 3.6, the values of the mislocations obtained from a subset of earthquakes which were located in the inner parts of the resolved models ($-10 \leq y \leq 5$ km) are listed. Within this range along the y-axis of the model, the earthquakes of interest

have been further subdivided into shallow, $-7 \leq z \leq 0$ km, and deep, $z < -7$ km. When earthquakes from all depths are considered in this range along the fault, it is found that the average bias toward the southwest ranges between 0.6 km for those located with a cubic, initial coarse grid model and about 1 km for those obtained with linear parameterization. Furthermore in this range along the y-axis and when deep and shallow earthquakes are analyzed separately, we observe that the shallow ones have the least amount of shift toward the southwest, ranging from 0.4 to 0.6 km in all cases, whereas the deeper ones move between approximately 0.7 km in the initial coarse mesh case, to approximately 1.6 km for the linear B-splines model. This result is relevant because it shows that apparent dips of the San Andreas fault, or any other fault that separates lithologies having overall different average velocities, can be attributed to inaccuracies of the velocity models used to locate the earthquakes, with a local network.

For this subset of earthquakes and in the y-direction, there is no apparent bias when the mean location, $\bar{y}$, is appraised by taking into account its two standard deviations confidence interval. Along depth, the earthquakes tend to be shifted deeper by varying amounts (maximum value is approximately 0.6 km). Overall, the minimum mean distance of mislocation in the entire depth range is obtained using the ray-density conditioning or the initial coarsely gridded model, with values of approximately 0.9 km along this inner part of the resolved model.

FAULT MODEL PERFORMANCE[a]						
method[b]	*rms*[c]	*iterations*	$\Phi_1(v^P_{inv})$	$\Phi_1(v^S_{inv})$	$\Phi_s(v^P_{inv})$	$\Phi_s(v^S_{inv})$
μ_P, μ_S[d]	0.0140	6	5.32	8.84	5.25	7.72
μ_P, μ_S[e]	0.0153	13	5.50	8.17		
μ_P, μ_S	0.0154	6	6.33	8.30	6.40	7.82
$\eta_{PS} = 0.25$	0.0156	6	5.94	7.67	5.99	7.11
$\eta_{PS} = 0.50$	0.0147	6	6.09	7.90	6.13	7.39
$\eta^D_P = 0.10$ $\eta^D_S = 0.10$	0.0147	6	5.95	8.54	5.97	8.09
$\eta^\partial_P = 0.25$ $\eta^\partial_S = 0.25$	0.0173	6	7.46	9.22	7.52	8.81
$\eta^\partial_P = 1.0$ $\eta^\partial_S = 1.0$	0.0196	6	7.94	10.06	7.94	9.53
$\eta^{\nabla^2}_P = 1.0$ $\eta^{\nabla^2}_S = 1.0$	0.0201	6	7.44	8.75	7.53	8.48
$\eta_{PS} = 0.50$ $\eta^\partial_P = 1.0$ $\eta^\partial_S = 1.0$	0.0230	6	7.86	10.39	7.86	9.96
$\eta_{PS} = 0.25$ $\eta^\partial_P = 0.25$ $\eta^\partial_S = 0.25$	0.0163	6	7.25	8.86	7.29	8.46

[a] Values of Φ were multiplied by 100 to express precentages and each value is determined from a discretization of the model in $\Omega = 68921$ points (see equation 3.2).
[b] $\sigma^P_t = 0.20$, $\sigma^S_t = 0.15$ (see sections 2.3.3.4 and 2.3.5.2 for details).
[c] Values are in seconds and the initial WRMS was 0.115 sec.
[d] First iterations with coarse grid mesh and 110 earthquakes used in the inversion.
[e] Linear B-splines basis functions (the spread function was not determined for this test).

Table 3.3: Fault model. This table summarizes the results of the inversion for the same starting model but with different *a priori* conditions applied.

FAULT MODEL PERFORMANCE (inner model)[a]						
	coarse initial grid μ_P, μ_S		fine initial grid μ_P, μ_S		fine initial grid $\eta_{PS} = 0.25$	
Depth range[b]	$\Phi_1(v^P_{inv})$	$\Phi_1(v^S_{inv})$	$\Phi_1(v^P_{inv})$	$\Phi_1(v^S_{inv})$	$\Phi_1(v^P_{inv})$	$\Phi_1(v^S_{inv})$
$-9 \leq z \leq 1$	4.89	6.93	5.47	6.77	5.21	6.16
$-4 \leq z \leq 1$	5.12	5.97	6.49	6.33	6.35	6.04
$-9 \leq z \leq -4$	4.37	7.65	3.98	6.75	3.53	5.80
entire model[c]	5.32	8.84	6.33	8.30	5.94	7.67

[a] Values of Φ_1 were multiplied by 100 to express precentages and each value is determined from a discretization of the inner model in $\Omega = 68921$ points (equation 3.2).

[b] $-10 \leq y \leq 5$ and $-5 \leq x \leq 5$ are the distance ranges along and across the fault, respectively. All distances are in kilometers.

[c] $-15 \leq y \leq 10$ (same values listed in table 3.3).

Table 3.4: Fault model. This table summarizes the fit of the resolved models in the inner part of the grid mesh.

FAULT MODEL MISLOCATIONS[a]							
method	$\overline{x}$	$\overline{y}$	$\overline{z}$	$\lvert\overline{x}\rvert$	$\lvert\overline{y}\rvert$	$\lvert\overline{z}\rvert$	$\lvert\overline{s}\rvert$
μ_P, μ_S[b]	-0.621	-0.061	-0.527	0.655	0.185	0.636	1.010
	0.819	*0.498*	*1.125*	*0.705*	*0.353*	*0.867*	*0.874*
μ_P, μ_S[c]	-1.393	0.101	-0.607	1.405	0.295	0.757	1.726
	1.792	*1.121*	*1.362*	*1.753*	*0.972*	*1.017*	*1.914*
μ_P, μ_S	-1.003	-0.036	-0.624	1.006	0.263	0.759	1.394
	1.334	*0.721*	*1.524*	*1.324*	*0.496*	*1.255*	*1.556*
$\eta_{PS} = 0.25$	-1.011	-0.014	-0.448	1.014	0.234	0.665	1.326
	1.159	*0.647*	*1.460*	*1.150*	*0.447*	*1.077*	*1.320*
$\eta_{PS} = 0.50$	-0.998	-0.020	-0.445	0.995	0.237	0.663	1.309
	1.221	*0.657*	*1.490*	*1.199*	*0.456*	*1.119*	*1.405*
$\eta_P^{\partial} = 0.25$ $\eta_S^{\partial} = 0.25$	-1.070	-0.012	-0.709	1.082	0.283	0.821	1.501
	1.304	*0.788*	*1.587*	*1.263*	*0.547*	*1.353*	*1.551*
$\eta_P^{\partial} = 1.0$ $\eta_S^{\partial} = 1.0$	-1.102	0.049	-0.589	1.117	0.333	0.734	1.487
	1.344	*0.918*	*1.574*	*1.295*	*0.638*	*1.306*	*1.589*
$\eta_P^{\nabla^2} = 1.0$ $\eta_S^{\nabla^2} = 1.0$	-1.130	0.007	-0.684	1.137	0.299	0.802	1.521
	1.418	*0.825*	*1.482*	*1.396*	*0.567*	*1.221*	*1.613*
$\eta_{PS} = 0.50$ $\eta_P^{\partial} = 1.0$ $\eta_S^{\partial} = 1.0$	-1.160	0.029	-0.458	1.168	0.335	0.703	1.506
	1.358	*1.045*	*1.621*	*1.330*	*0.802*	*1.217*	*1.643*
$\eta_{PS} = 0.25$ $\eta_P^{\partial} = 0.25$ $\eta_S^{\partial} = 0.25$	-0.911	-0.009	-0.567	0.923	0.273	0.715	1.290
	1.111	*0.739*	*1.497*	*1.069*	*0.496*	*1.215*	*1.402*
$\eta_P^D = 0.10$ $\eta_S^D = 0.10$	-0.884	0.020	-0.472	0.893	0.211	0.632	1.209
	1.165	*0.591*	*1.312*	*1.136*	*0.415*	*1.005*	*1.261*

[a] Values are in kilometers and were determined from a set of 169 earthquakes.
[b] First iterations with coarse grid mesh and 110 earthquakes used in the inversion.
[c] Linear B-splines basis functions.

Table 3.5: This table summarizes the mislocations for the various inversions (the format is similar to table 3.2).

3.7 Summary

The spike and fault tests have shown that the resolving power of the Parkfield data set is sufficient, in the inner parts of the model volume ($-10 \leq y \leq 5\ km$), to retrieve the main features of the true models. However, instabilities arise at the borders of the models and their form appears to be rather unpredictable. The resolved models converge toward the true model in the well-resolved parts but some fictitious features can arise at the boundaries where the ray-coverage is poor. The spread function allows assessment which parts of the model are well resolved, but good resolution implied by small spread function values in localized zones, may not guarantee that the model is close to the true one. The model may well have reached a local minimum there.

The final weighted RMS values in these two tests never decrease to values at the level of the accuracy of the ray tracer. In the spike test, the minimum RMS value was approximately 10 msec and approximately 15 msec for the fault model. This result may be attributed to the limited *view angle* provided by the ray-coverage. 10–15 msec, however, may well represent fine scale heterogeneity impossible to estimate at the scale of the experiment.

Coarse grid meshes for the initial iterations can be used, but the final model will retain the introduced smoothness, i.e., once a reasonably good fit is obtained with a coarse mesh, the algorithm is unable to superimpose the necessary shorter wavelength features of the true model. This again can be probably attributed to the limited resolving power of the data set.

Caution must be also observed in introducing explicit smoothing conditions. In the spike test which was purposely underparameterized, first- and second-derivative conditioning degraded the fit. In the fault model test which was instead overparameterized across the fault, explicit smoothing tends to smear the features of the model. Furthermore, at the boundaries where fictitious features can arise because of

the sparse ray-coverage, explicit smoothing does not introduce the desired stabilizing effect. The V_P/V_S models calculated from first and second derivative *a priori* conditioned P- and S-models exhibit larger instabilities that can lead to misinterpretations. Explicit smoothing seems to be advantageous only when the parameterized model consists of very dense meshes where some *a priori* smoothing is indispensable to stabilize the inversion (e.g., Sambridge, 1990). In our case however, the adoption of the fine grid meshing across the fault introduces some instabilities which are only partly cured by the use of first- and second-derivative conditioning. Unfortunately, the same smoothing tends to inhibit the retrieval of some true features of the model. Ray-density conditioning has to some extent also a smoothing effect and seems to effectively contribute toward improvement of the fit with the true models.

The V_P/V_S conditioning, tested with the fault model in which the ratio varies through the structure, limits instabilities and preserves the true anomalies. This feature makes the resolved V_P/V_S models more reliable for meaningful interpretations. This conditioning also improves the S fit in the inner parts of the model. For the Parkfield data set, the source-receiver geometry provides enough resolving power to image reliably anomalous V_P/V_S ratios in the fault zone.

In the fault test within the better resolved parts of the model, earthquakes tend to be shifted on the average less than 1.0 km to the southwestern high velocity side of the model. This bias increases for deeper earthquakes, and can suggest fictitious dip of the fault toward the southwest.

The general conclusion from the two test models is that some amount of V_P/V_S and ray-density conditioning can systematically improve the results of the tomographic inversion.

FAULT MODEL MISLOCATIONS (inner model) [a]				
method	$\overline{x}$	$\overline{y}$	$\overline{z}$	$\lvert\overline{s}\rvert$
$z < 0$				
μ_P, μ_S [b]	-0.591	-0.120	-0.441	0.887
	0.851	*0.280*	*0.878*	*0.806*
μ_P, μ_S	-0.769	-0.084	-0.355	0.999
	1.109	*0.331*	*0.955*	*1.069*
$\eta_{PS} = 0.25$	-0.793	-0.084	-0.212	0.971
	0.950	*0.353*	*0.944*	*0.927*
$\eta^D = 0.10$	-0.696	-0.054	-0.279	0.898
	0.998	*0.291*	*0.887*	*0.944*
μ_P, μ_S [c]	-1.041	-0.053	-0.453	1.276
	1.333	*0.388*	*1.016*	*1.266*
$-7 \leq z \leq 0$				
μ_P, μ_S [b]	-0.399	-0.106	-0.557	0.747
	0.464	*0.303*	*0.509*	*0.496*
μ_P, μ_S	-0.517	-0.067	-0.576	0.826
	0.470	*0.269*	*0.760*	*0.740*
$\eta_{PS} = 0.25$	-0.552	-0.072	-0.477	0.781
	0.458	*0.257*	*0.685*	*0.667*
$\eta^D = 0.10$	-0.466	-0.041	-0.486	0.730
	0.448	*0.353*	*0.706*	*0.671*
μ_P, μ_S [c]	-0.633	-0.047	-0.621	0.935
	0.585	*0.258*	*0.647*	*0.693*
$z < -7$				
μ_P, μ_S [b]	-0.733	-0.133	-0.332	1.018
	0.973	*0.257*	*1.083*	*0.950*
μ_P, μ_S	-1.140	-0.109	-0.029	1.254
	1.346	*0.404*	*0.838*	*1.270*
$\eta_{PS} = 0.25$	-1.147	-0.102	-0.178	1.250
	1.045	*0.460*	*0.704*	*0.981*
$\eta^D = 0.10$	-1.035	-0.072	0.027	1.147
	1.187	*0.340*	*0.768*	*1.069*
μ_P, μ_S [c]	-1.644	-0.062	-0.205	1.779
	1.206	*0.527*	*1.244*	*1.255*

[a] Values are in kilometers and were calculated from a set of 104 earthquakes (62 shallow and 42 deep earthquakes, respectively).

[b] First iterations with coarse grid mesh.

[c] Linear B-splines basis functions.

Table 3.6: This table summarizes the mislocations for selected inversions in the inner part of the resolved models.

Chapter 4

Application to Parkfield

The Parkfield segment of the San Andreas Fault (SAF) lies at the transition between the creeping part of the San Andreas Fault in Central California and the locked southern part that ruptured last in the great 1857 Fort Tejon earthquake. Bakun and McEvilly (1984) recognized that this segment ruptures in a characteristic fashion with a periodicity of 22 ± 5 years and that the last two Parkfield earthquake sequences in 1934 and 1966 were remarkably similar (Bakun and McEvilly, 1979). In addition, Sieh (1978) found that Parkfield earthquakes such as the 1966 main shock may have induced the 1857 Fort Tejon earthquake. These findings are some of the principal lines of evidence that have led to the development of the Parkfield Prediction Experiment (PPE) (Bakun and Lindh, 1985), which is currently underway. One of the principal objectives of the experiment is to monitor the details of the deformation in the final stages and during the failure of the Parkfield segment.

4.1 Data

The Parkfield area is densely instrumented with a variety of seismic and deformation detectors as part of the PPE (Bakun and Lindh, 1985). Data recorded by the two seismic networks, shown in figure 4.1, are employed in this study. The High-Resolution Seismic Network (HRSN) is a 10-station, 3-component, high-frequency, digitally-telemetered (500 16-bit samples per second per component) system installed

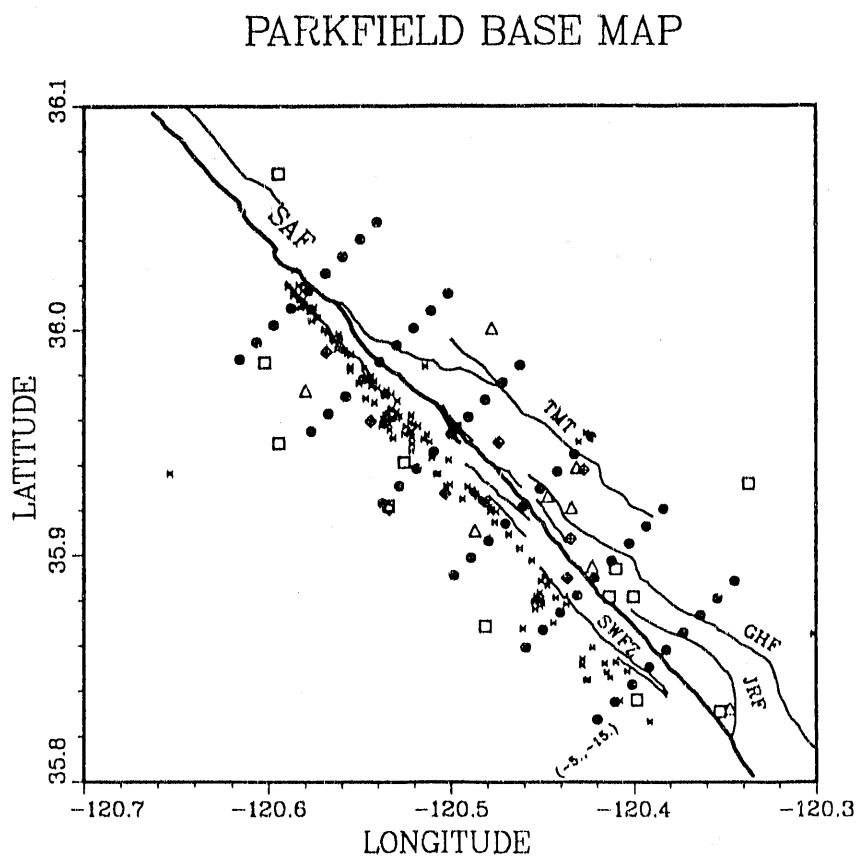

Figure 4.1: Parkfield base map showing locations of the HRSN stations (open triangles), the CALNET-USGS stations (open squares), the grid nodes used in the inversion (solid circles), the vibration points of the controlled source experiment (diamonds with inner cross), the 169 earthquakes used for the joint inversion (crosses), and the trace of the San Andreas Fault (SAF) (dashed line). The grid mesh is centered at the 1966 main shock (35°57.3′N, 120°29.7′W) and rotated 45° counterclockwise. For reference, the coordinates of the southernmost knot-column of the grid mesh are shown. See text for fault abbreviations.

in boreholes at depths of 200- 300m. The sensors for this network are 2 Hz geophones, except for one station which has a 4.5 Hz units. The HRSN monitors microearthquake activity to $M_L \approx -0.5$ throughout the study area. It also serves as the receiving array for the controlled-source (shear vibrator) search for evidence of precursory temporal changes in anisotropy, Q, and velocity of S- waves throughout the nucleation zone of the expected earthquake (Clymer et al., 1989, Karageorgi et al., 1991). The HRSN covers an area of approximately 10x15 km, centered on the town of Parkfield. The second network used in this study consists of the 14 USGS-CALNET stations in the Parkfield zone including those shown in figure 4.1. Its coverage is more regional (approximately 15 x 35 km extent) with a lower magnitude threshold around $M_L \approx 1.0$. CALNET data are transmitted by analog telemetry to Menlo Park and then sampled at 100 samples per second.

4.2 Geology

The San Andreas Fault in the Parkfield area juxtaposes two widely different geologic blocks: granitic basement rocks of the Salinian block of Mesozoic age to the southwest against Franciscan assemblage, Coast Range ophiolite and sediments of the Great Valley Sequence to the northeast (e.g., Dickinson, 1966; Brown and Vedder, 1967).

The Salinian basement in the southwestern block is unconformably overlained by a thin cover of marine and non-marine sedimentary and volcanic rocks whereas thicker sequences of Cretaceous, Tertiary and Quaternary sediments structurally overlie the Franciscan on the northeast.

The two blocks have responded differently to the acting tectonic stress field in Neogene time. The Salinian block is relatively undeformed whereas the northeast side is densely faulted and folded. The Salinian consists of more rigid crystalline granitic and metamorphic rocks that have resisted deforming stress. Conversely, the Franciscan assemblage that includes a large variety of sedimentary, metamorphic and

mafic rocks, deformed in a complex fashion. As a result, the sedimentary rocks overlying the Franciscan basement are tightly folded and faulted and display trends subparallel to the SAF (Brown and Vedder, 1967).

The major structural features in the Parkfield area can be summarized as follows. The Gold Hill Fault (GHF) and the Table Mountain Thrust (TBT) on the northeast of the SAF are the boundaries of the Parkfield syncline. These two faults are subparallel to the SAF and dip to the southwest and northeast, respectively. The Parkfield syncline is composed of Upper Cenozoic strata and in a well (Varian well) on the southwest of its axis, Franciscan basement rocks were found at depths of approximately 1500 m (Sims, 1990).

Further to the southeast in the study area and in the northeast block, the Gold Hill exotic fragment consisting of a quartz horneblende gabbro is bounded by the SAF and the Jack Ranch Fault (JRF) to the southwest and northeast, respectively.

In the southwest block and at distances ranging between 1.0 and 1.5 km from the SAF, the southwest fracture zone (SWFZ) extends subparallel to the SAF for approximately 10 km. The SWFZ ruptured in the 1966 Parkfield earthquake and a total amount of 2.2 cm was measured Brown and Vedder (1967). Furthermore, at its southeastern termination it may be connected to the western segment of the SAF in the northern part of the Cholame Valley (Sims, 1990). The Lang Canyon volcanic rocks which run subparallel to the SAF outcrop approximately 2 km southwest of the SAF near the northern end of the SWFZ and is considered a second important exotic fragment in the Parkfield area (Sims, 1990).

The SAF itself presents two large scale and significant features in the Parkfield area. The first is the one kilometer right step at the northern end of the Cholame Valley near Gold Hill and the second is the approximately 5° left bend near the hypocenter of the 1966 Parkfield earthquake at Middle Mountain.

4.3 Seismicity and deformation

Several studies have addressed the Parkfield seismicity and mode of deformation. In the following I will summarize results most relevant to the present study. I will list first the seismicity studies followed by the earthquake studies that address the role of a varying stress field in the area and, finally, the deformation studies that analyze the build up of the stress field as indicated by geodetic measurements.

A fundamental feature that characterizes the Parkfield segment is that it lies at the transition zone where the SAF changes its mode of strain release, i.e., creeping and a relatively larger number of small size earthquakes to the north versus moderate to very large earthquakes to the south. McEvilly et al. (1967) analyzed the sequence of earthquakes that preceded and followed the 1966 main shock and found some indication that the locations of the earthquakes north of the main shock tended to converge toward the focus of the main event in the months before the main sequence. In particular, they found that the two largest foreshocks which occurred a few minutes prior the main shock clustered in the vicinity and north of the main event. In contrast, the early aftershocks extended 20 km to the south of the main event.

A detailed study of the aftershocks seismicity was composed by Eaton et al. (1970). They used the aftershock data recorded by a temporary network which was installed soon after the 1966 main shock and operated for about three months, to find that the earthquakes were confined to a nearly vertical and planar zone extending down to depths of 12 to 14 km and that all the earthquakes displayed a right-lateral strike-slip mechanism.

Nishioka and Michael (1990) extracted a subset of the earthquakes analyzed by Poley et al. (1987) along a 15 km long segment centered approximately at the 1966 mainshock (Middle Mountain). They improved the accuracy of the hypocenter locations, by adding to and retiming the arrivals and by recalculating station corrections. They found that the earthquakes tended to be more tightly clustered than previously

determined and that their locations were closer to the vertical projection of the SAF. They did not detect the expected 5° bend in the seismicity at Middle Mountain because, from Middle Mountain northward, the seismicity was less tightly clustered. However, Nishioka and Michael confirmed the results of Lindh and Boore (1981) on the pattern of compressional and dilatational first arrivals as recorded at Gold Hill (i.e., approximately 20 km southeast of the 1966 mainshock) for earthquakes that lie southeast and northwest of the 1966 mainshock epicenter, respectively. This change in first-motion polarity had been interpreted by Lindh and Boore to indicate a change in strike of the focal active plane at depth associated with the surface bend of the SAF. Finally, they observed that two of their selected earthquakes displayed a thrust focal mechanism and one these earthquakes was located approximately 2 km off the main trace to the northeast. Foxall et al. (1989) used the data recorded by the HRSN and located the earthquakes using the 3-D model developed by Michelini et al. (1989), finding that the locations were significantly more clustered than previously found using a 1-D model with station corrections and CALNET recorded data. They also pointed out that about 60 % of the located earthquakes concentrated in separate clusters, a few hundred meters in size. Earthquakes belonging to each cluster consistently displayed nearly identical waveforms. Malin et al. (1989), used a 1-D model with station corrections to locate the earthquakes recorded by the HRSN. They suggest that the current background seismicity in the locked segment of the SAF at Parkfield defines the perimeter of the asperity that is expected to fail in the next M5+ Parkfield earthquake. They also found a low magnitude roll-off of the $M - \log(N_M)$ relationship which, as they remark, cannot be attributed to lack of sensitivity of the network.

Lindh and Boore (1981) studied the rupture of the 1966 mainshock and found that the focus nearly coincides with the 5° bend of the trace at Middle Mountain, and that the main rupture stopped at the right step of the SAF at Gold Hill. They

also emphasized that the aftershock activity concentrated along the perimeter of the main rupture and that some discontinuity at depth must be present and possibly causing the surface 5° bend where both stress concentration and change in background seismicity occur. This topic has been addressed in detail by Bakun and McEvilly (1981), who compared the stress drop estimates for two M5 immediate foreshocks of the 1934 and 1966 earthquake with those determined from other earthquakes. They found that the two immediate foreshocks exhibited higher stress drop sources and displayed northward unilateral rupture which is opposite to that observed in the main shock. O'Neill (1984) repeated to some extent the analysis of Bakun and McEvilly (1981) by using a different and larger data set that included background seismicity earthquakes from 1977 to 1982. She calculated stress drops and source dimensions for 37 earthquakes that span the location of the 1934 and 1966 immediate foreshocks and mainshocks. She found that a cluster of earthquakes in the vicinity of the 1966 mainshock exhibited anomalously large values of stress drop. The apparent implication of these stress drop studies is that the nucleation zone around the 1966 hypocenter is highly anomalous. More recently, Poley et al. (1987) have analyzed the background seismicity in the proximity of the nucleation of the 1966 earthquake for the time period 1975-1985. Their results suggest that this zone of the fault is particularly sensitive to changes of the local and regional stress field. They observed that changes in the regional stress field caused by moderate earthquakes that occurred within 50 km northeast of Parkfield consistently decreased the rate of seismicity in the Parkfield nucleation zone.

Various studies have addressed the stress build up in the Parkfield transition segment in terms of observed surface deformation. Tse et al. (1985) have attempted to model the stress accumulation at the transition zone between the creeping northern segment and the currently locked southern one which ruptured last in 1857. They propose the existence of a small locked zone in the Parkfield area. Stuart et al. (1985)

have proposed a forecast model which incorporates current preseismic measurements and applied it to Parkfield. In order to fit the past data (i.e., the already collected preseismic measurements such as creep measurements and trilateration lines) in their modeling, they needed a locked fault-patch having 3 km radius and located approximately at depth of 5 km, 8 km southeast of the 1966 mainshock. Harris and Segall (1987) have addressed the inverse problem of determining the slip rate at depth since the 1966 earthquake by using trilateration data and shallow fault slip data. Their solution suggests that the presently locked part of the SAF coincides with the part of the fault that ruptured last in the 1966 earthquake. In a second study, Segall and Harris (1987) estimated the time interval required to accumulate the strain energy release by the 1966 mainshock. Their results are in close agreement with the recurrence interval inferred from earthquakes alone by Bakun and McEvilly (1984).

In summary, the results of these studies suggest the existence of two anomalous zones of stress concentration. The first is located near the hypocenter of the 1966 main shock and it is revealed by the seismicity and the earthquake source studies. The second instead lies further to the south and is supported by geodetic measurements and by the lack of background seismicity.

4.4 Tomographic models

Three groups have independently attempted to determine the Parkfield 3-D structure. In their first study, Michelini et al. (1989) used Thurber's linear B-splines parameterization to jointly invert for earthquake locations, P- and S-velocity structure. They used 75 well-timed earthquakes and surface vibrator data recorded by the HRSN. Although in this initial attempt they used a rather coarsely sampled grid, they recognized the existence of higher velocities on the southwest side of the fault and a pronounced low velocity fault zone for the S-model. This initial attempt was later modified by Michelini and McEvilly (1991) with the use of cubic B-splines basis

functions to stabilize and smooth the results of the inversions. In this second study, they used a larger data set that included earthquakes recorded by the more regional CALNET stations. Michelini and McEvilly cubic B-splines models resolved nearly all the features of the models seen in the current study presented in this chapter, but in smoother fashion because the velocity grid interval across the fault was larger. The main results found in the first (1989) study were also confirmed.

Lees and Malin (1990), derived a 3-D model by using a different method. In their P-model tomographic reconstruction, they first located the earthquakes using a 1-D velocity model with station corrections and subsequently used the calculated residual times to infer velocity perturbations in a one-step inversion fashion. Given that their station corrections do not seem to correct only for local velocity anomalies near the station but reflect instead some long wavelength features of the true model (i.e., their positive and negative station correction values systematically group on either side of the SAF and exhibit values ranging between -0.43 to 0.2 sec), it can be argued that their model is biased.

Eberhart-Phillips and Michael (1989), and Michael and Eberhart-Phillips (1991), have also determined the Parkfield P-velocity structure by adopting arrival times from earthquakes, surface explosions and vibroseis recorded by CALNET and HRSN. They used Thurber's (1983) joint hypocenter and velocity inversion technique and although their model is more regional, it also reveals most of the features resolved by Michelini and McEvilly (1991) for the overlapping parts of the model.

4.5 Inversions

The results of the application of the method to the Parkfield data set for various settings of the *a priori* inversion parameters are shown in figures 4.3 to 4.5.

Table 4.1 summarizes the results obtained from all the inversion cases that were attempted. In this table we list the total number of iterations that were necessary for

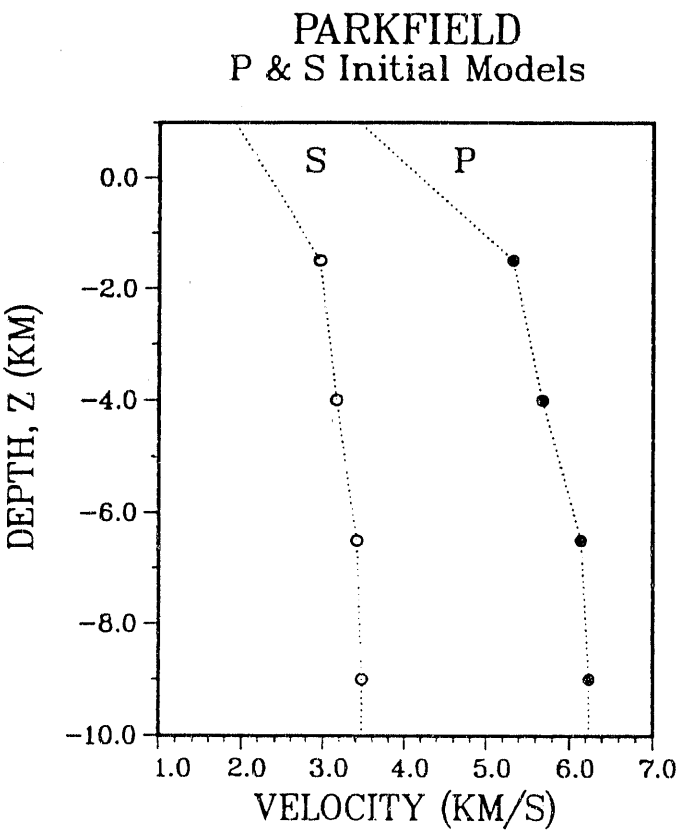

Figure 4.2: Parkfield P and S velocity 1-D initial models. Velocities attain constant value for $z \leq -9$ km.

convergence in the non-linear inversion and the final weighted RMS value. The initial model for all the inversions consisted of a 1-D model which was determined using Thurber's linear B-splines parameterization. This model is shown in figure 4.2 and produced a final weighted RMS value of 0.141 seconds. Different data sets were used at different stages of the 3-D inversion because of differing onset reading accuracy. We chose to disregard the less accurate data as iterations proceeded. In practice, we iterated until convergence using the entire data set in the first stage of the inversion. In the second stage, we eliminated the surface vibrator data and used the P- and S-velocity models determined in the first stage as the initial ones. Similarly, in the third stage, we eliminated the CALNET data. Approximately four to six iterations

PARKFIELD INVERSIONS		
method[a]	*RMS*[b]	*iterations*[c]
μ_P, μ_S	0.025	9
$\eta_{PS} = 0.25$	0.025	9
$\eta_{PS} = 0.5$	0.027	8
$\eta_P^D = 0.25$ $\eta_S^D = 0.25$ $\eta_{PS} = 0.25$	0.025	9
$\eta_{PS} = 0.25$[d]	0.026	5
$\eta_{PS} = 0.25$[e]	0.026	8

[a] $\sigma^P_{max} = 0.20$, $\sigma^S_{max} = 0.15$ unless stated.
[b] Values are in seconds and the initial RMS was 0.141 sec
[c] Sum of the iterations at all stages of the inversion.
[d] CALNET recorded earthquakes were not used and the initial rms was 0.104 sec.
[e] The inversion grid was shifted by one-half the discretization distance along the x and y-coordinates.

Table 4.1: This table summarizes the results of the Parkfield inversion with different *a priori* conditions applied.

were needed in the first series with the entire data set, and zero to two iterations in each of the last two series of iterations with fewer data. In table 4.1, the listed final weighted RMS value was calculated at final convergence with the depleted data set

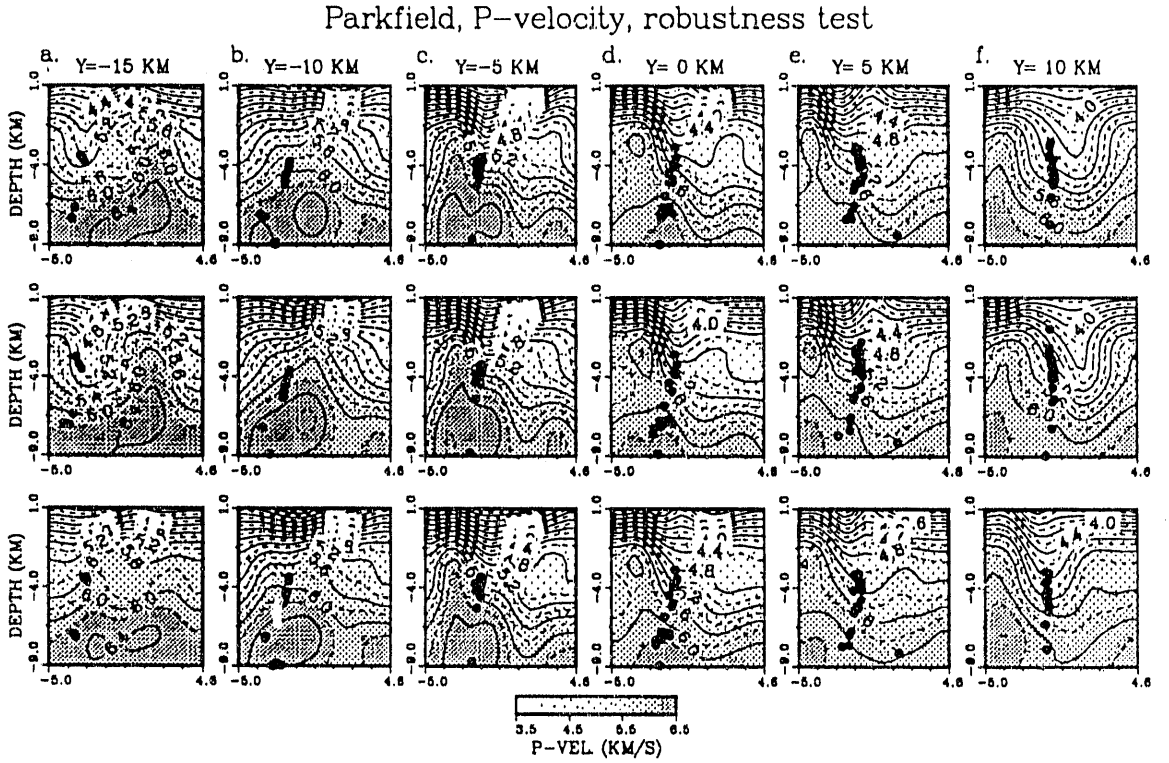

Figure 4.3: Robustness test for the Parkfield P-model (vertical cross sections across the SAF). P and S damping-only (top); P-S coupling ($\eta_{PS} = 0.5$ and $V_P/V_S = 1.8$) (middle); P-S coupling and grid mesh shifted by one-half the discretization interval along the x and y-coordinates (i.e., 0.6 and 2.5 km, respectively) (bottom).

consisting of the earthquakes recorded by the HRSN.

The pseudo-bending ray tracer of Um and Thurber (1987) was used throughout. However, to diminish the computational time needed for the inversion, a value of 0.01 for the Um and Thurber's *Travel Time Improvement Parameter*, which results in generally less accurate calculation of the travel times, was selected for the initial iterations with the entire data set. This value was decreased to 0.001 in the final iterations where more accuracy was needed.

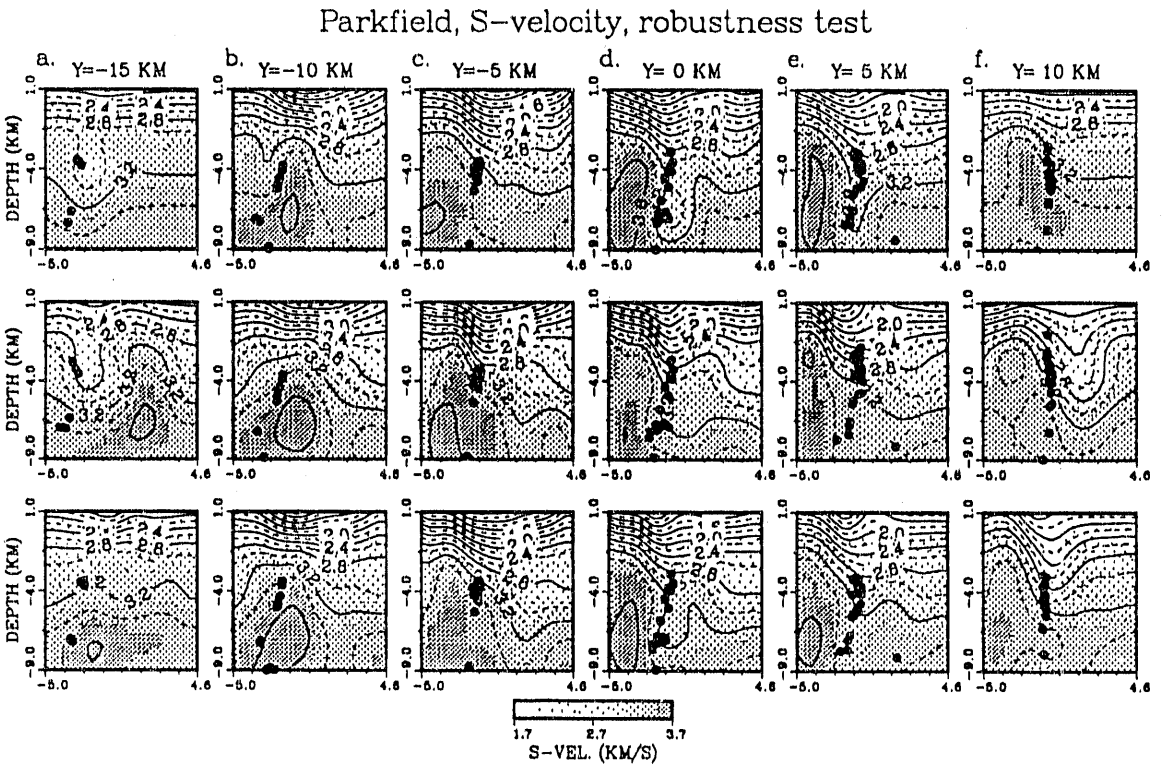

Figure 4.4: Robustness test for the Parkfield S-model (vertical cross sections across the SAF). The format is the same as in figure 4.3.

4.5.1 Robustness tests

We show first two models derived with different applied *a priori* conditioning and a third which has the nodes' grid mesh shifted along the x and y coordinates by one-half the discretization interval (figures 4.3 to 4.5). The results obtained with other *a priori* conditioning are summarized in table 4.1 and the selected P and S-models are shown in figures 4.8 to 4.16. The purpose of showing final models obtained with different *a priori* conditioning and with a shifted grid is to provide an indication of the robustness of the results.

Figures 4.3 to 4.5 display the inversion results obtained with damping-only applied

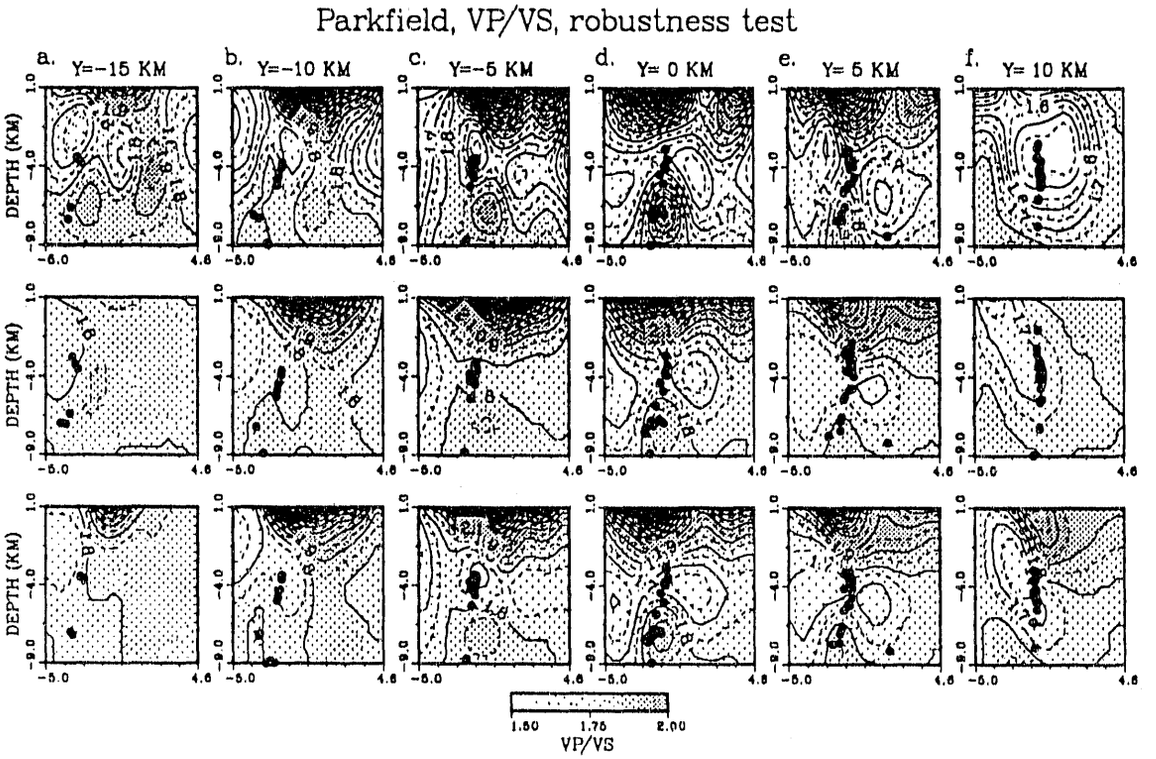

Figure 4.5: Robustness test for the Parkfield V_P/V_S model (vertical cross sections across the SAF). The format is the same as in figure 4.3.

(top row), significant P-S coupling, i.e., $\eta_{PS} = 0.5$ for an implemented V_P/V_S ratio of 1.80[1] (middle row), and a discretization grid shifted 0.6 km southwest (x-coordinate) and 2.5 km southeast (y-coordinate) with some P-S coupling ($\eta_{PS} = 0.25$, bottom row). For reasons of conciseness, the associated spread and coupling functions are shown only for the final model shown in figures 4.8 to 4.16.

Examination of the P- and S-models shown in figures 4.3 and 4.4 indicates that only minor differences distinguish the three resolved models. However, the P and S models resolved with damping-only applied (top row in figures 4.3 to 4.5) display more *structure* in the form of short wavelength features. This causes the derived V_P/V_S model to exhibit larger fluctuations (see figure 4.5). Introduction of V_P/V_S conditioning obviates the rise of V_P/V_S fluctuations (figure 4.5) but slightly increases the misfit as indicated by the weighted RMS (see table 4.1). Our selection of the final model was based on the misfit and on the addition of the minimal amount of *a priori* conditioning needed to stabilize the inversion. Inversions with larger amounts of coupling (i.e., $\eta_{PS} > 0.5$) were not tried but it is expected that stronger V_P/V_S conditioning will further increase the misfit values. In our final model, we adopted a value of $\eta_{PS} = 0.25$ which limited the development of significant V_P/V_S fluctuations and resulted in a nearly identical final value of weighted RMS as the one determined when no P-S coupling was applied (see table 4.1).

The inversion results obtained with the model grid shifted by one half the discretization interval along the x and y coordinates demonstrate the robustness of the inversion for the given data set. The only zone in the 3-D model where the shifted model-grid inversion differs from the non-shifted ones is at the southeastern border of the model. This partial lack of resolution at the southeastern boundary of the velocity model is consistent with what was previously found in the synthetic tests, and it cautions us on providing interpretations for this part of the model.

[1]This value of V_P/V_S is a gross mean average derived from P- and S-arrival times determined from the data set.

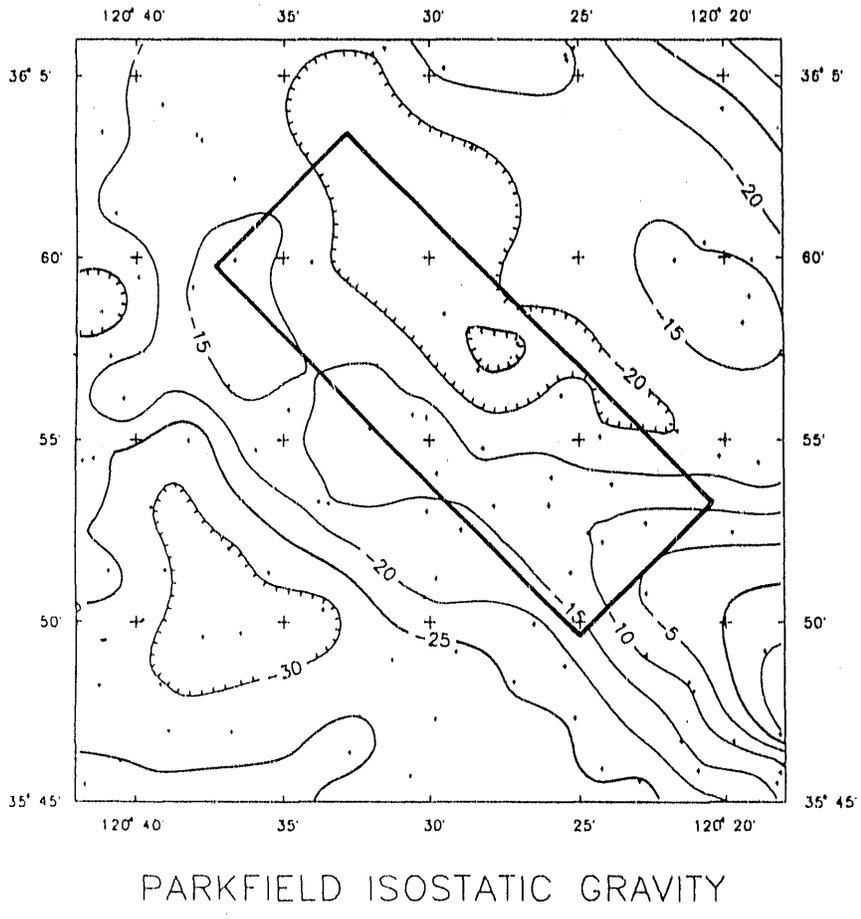

Figure 4.6: Parkfield isostatic gravity map. The inset rectangular area is the target area of the velocity inversion.

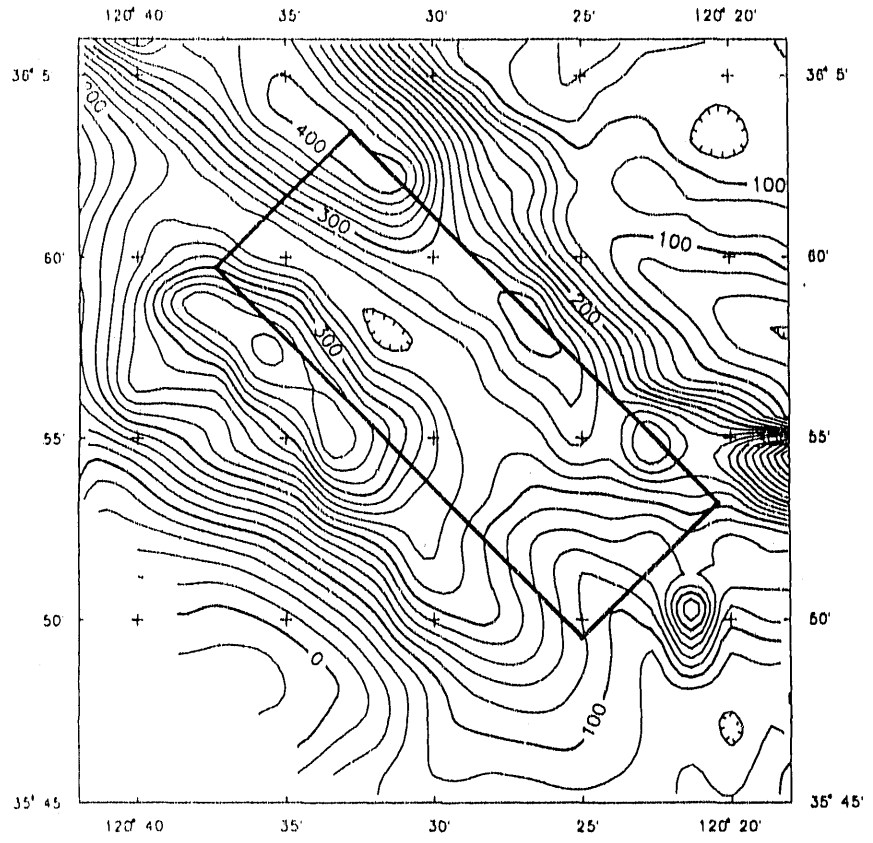

PARKFIELD AEROMAGNETIC 2 km spacing

Figure 4.7: Parkfield aeromagnetic map. The format is the same as in figure 4.6.

A final attempt to verify the robustness of the inversion was made using the data recorded by the HRSN alone throughout the inversion. We do not show the results of this test but the final model was smoother and the final weighted RMS values were not as low as for the other inversions at final convergence (see table 4.1). This result can be explained by noting that the CALNET data set adds more resolving power to the data set, permits resolution of shorter wavelength features of the model, and decreases the misfit values.

Another approach for assessing the reliability of the velocity model is through comparison with other types of geophysical data. In figures 4.6 and 4.7, we show the Parkfield isostatic gravity and aeromagnetic maps. Comparison of these maps with

the final model plan-view sections displayed in figures 4.8 and 4.9 shows that the general pattern of the contour line trends is similar. At shallow depths the velocity models resemble the aeromagnetic map whereas at larger depths the velocity models have many features of the isostatic gravity map.

4.5.2 Description of the final model

The selected final model was determined by adding some V_P/V_S conditioning, i.e., $\eta_{PS} = 0.25$, as *a priori* information. This model has both the minimum amount of explicit conditioning and preserves the minimum value of misfit as indicated by the weighted RMS value (i.e., 0.025 sec.; see table 4.1).

This final model is shown in figures 4.8 to 4.16 as different sections: across and along the fault and in plan view. In these figures we have superimposed the surface main geologic features of the Parkfield area as mapped by Sims (1988, 1990) and the earthquakes used in the inversion. We describe first the plan view sections which are displayed in figures 4.8 to 4.10 with the purpose of isolating the principal long wavelength features of the resolved models.

The overall most distinctive feature of all the plan view sections is the marked difference in velocities between the northeast and the southwest side of the SAF (i.e., approximately $x > 0$ and $x < 0$, respectively, with higher velocities found on the southwest side). By proceeding from shallow to deep and from the southwest toward the northeast in the description of the sections, we observe that a well-imaged and elongated high-velocity body (HVB) extends from northwest to southeast at approximately $x = -4$ km and for approximately 10 km between $y = 5$ to $y = -5$ at depths of about 1.5 km ($z = -1.5$). This HVB persists at depth and increases its longitudinal size at depths of 4 km (see sections at $z = -1.5$ and $z = -4$ km in figures 4.8 and 4.9). Adjacent and subparallel to this high-velocity body and toward the northeast, we find a shallow and elongated low-velocity zone (LVZ) that extends

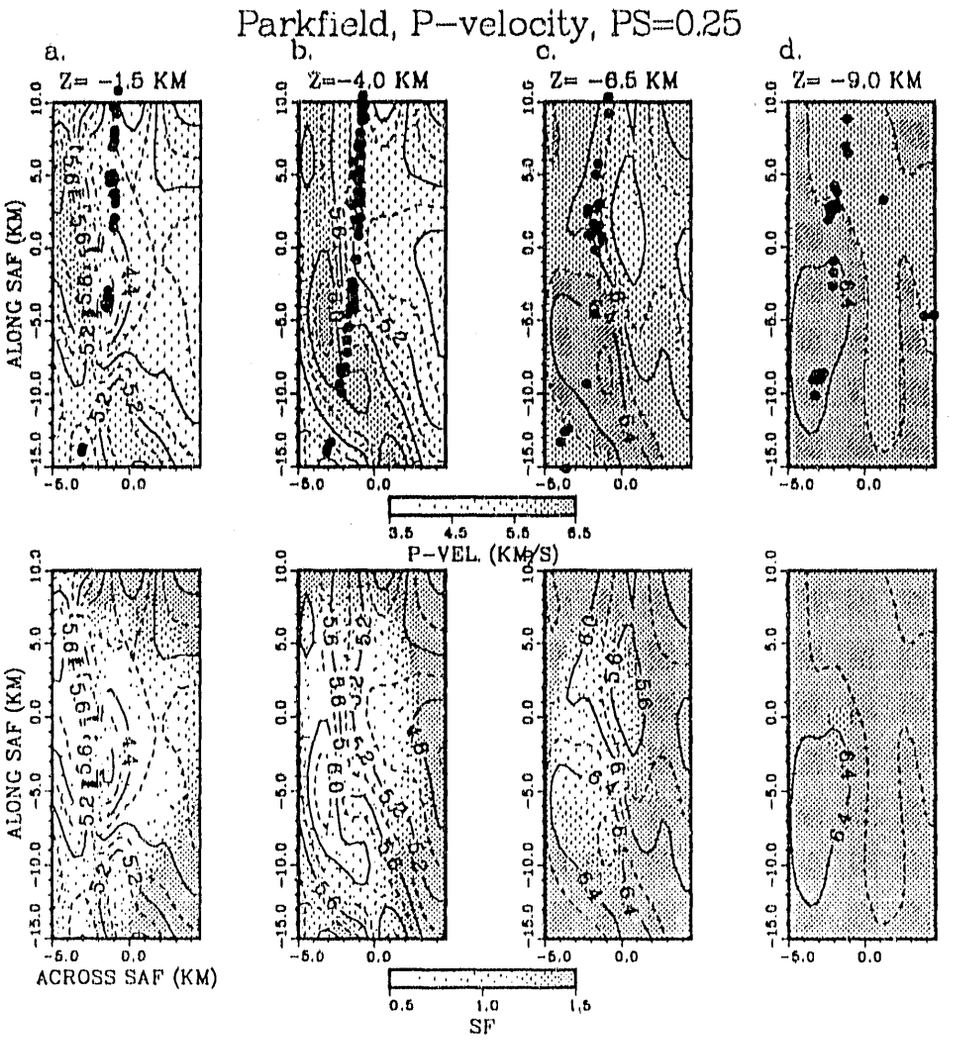

Figure 4.8: Parkfield final P-model: plan view sections. Contour lines indicate the resolved velocity values whereas the shading indicates the velocity values (top row) and the values of the associated spread function (SF) (bottom row). Larger values of the SF indicate less resolution.

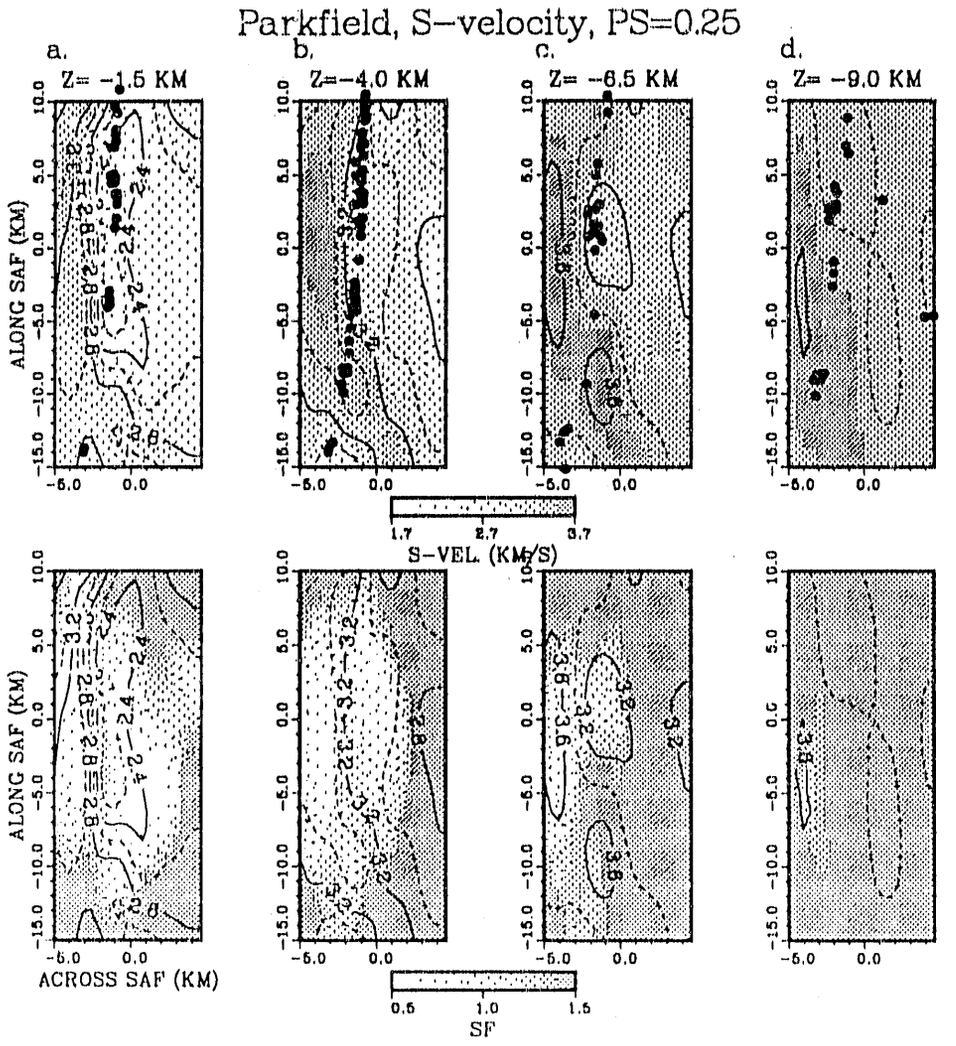

Figure 4.9: Parkfield final S-model: plan view sections (same format as figure 4.8).

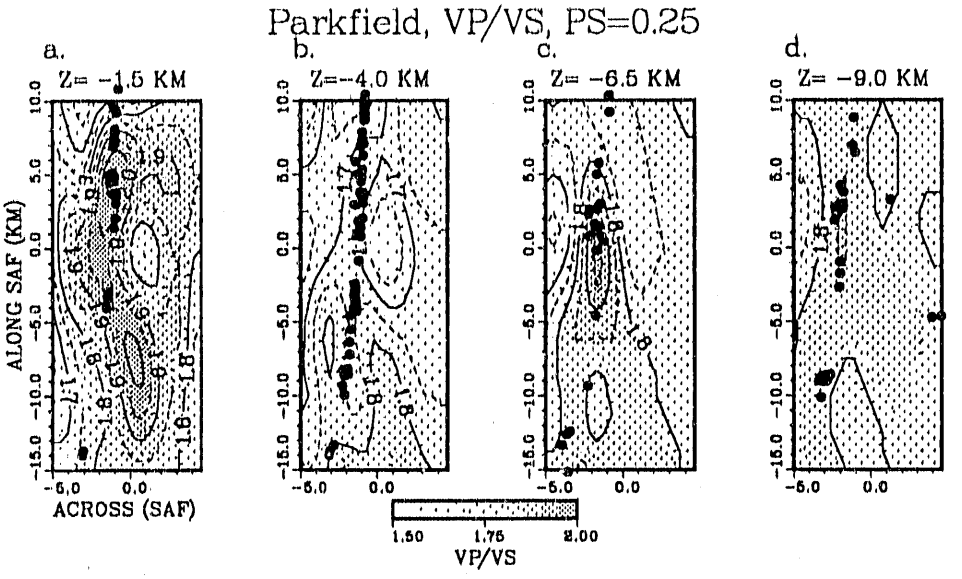

Figure 4.10: Parkfield final V_P/V_S model: plan view sections.

along the SAF. Farther to the northeast and at shallow depths between $z = -1.5$ and $z = -4$ km, P- and S-velocity values are intermediate between those found on the southwest side and in the LVZ. Another feature of these shallow plan view sections through the P- and S- models is the appearance of a relatively HVB centered at $x = 1$ km and approximately 2 km wide at the southeastern end of the resolved models. Between $y = -13$ and $y = -10$ km, this high velocity body appears to be in contact with the high-velocity body resolved on the southwest side.

At $z = -6.5$ km, the shallow and elongated high-velocity body on the southwest side appears to broaden and reaches velocities of approximately 6.4-6.6 km/sec. This body again appears to be in contact with the HVB found on the southern end of the imaged region but, because of partial lack of resolution at the boundaries of the model, the contact of the two bodies is less certain. The deepest plan view section at $z = -9$ km suffers from poor resolution but, if we restrict the model description to

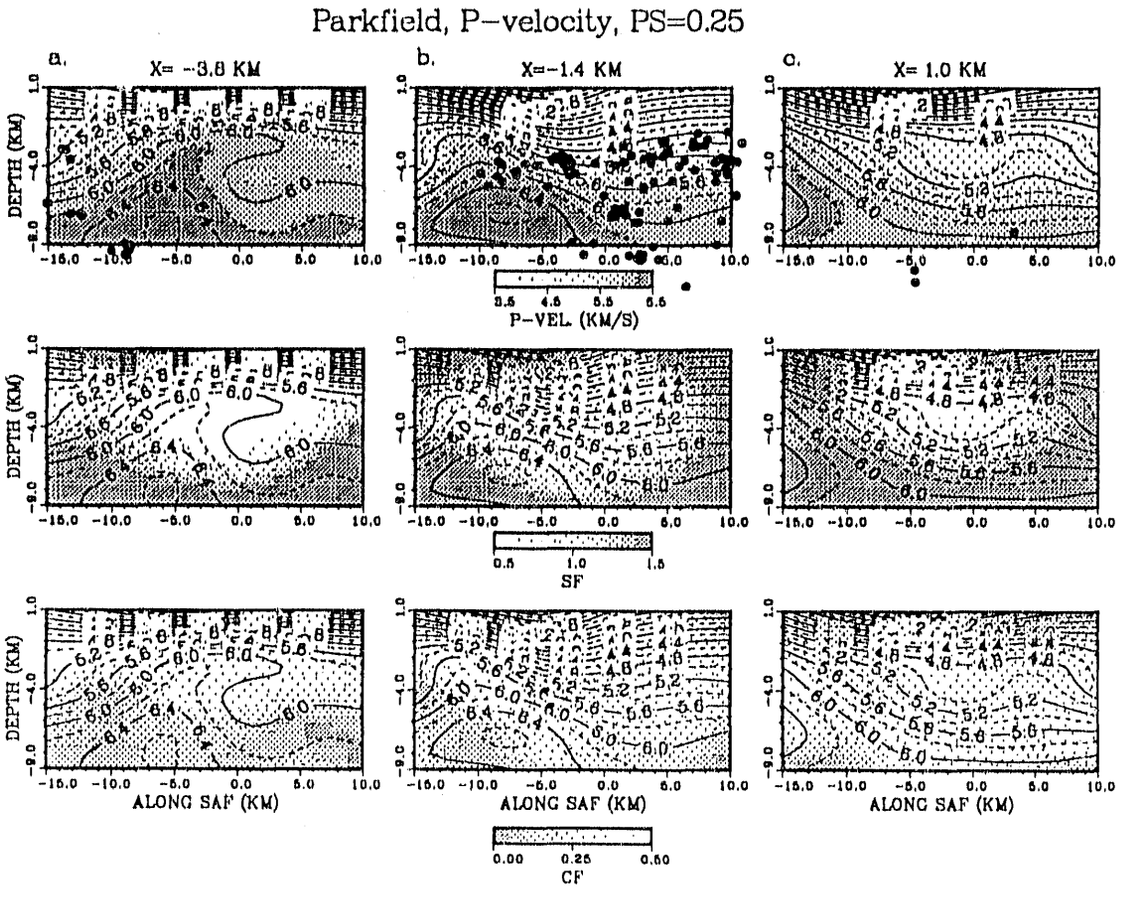

Figure 4.11: Parkfield final P-model: vertical sections along the fault (the view is from the northeast). The format of the upper two rows is the same as in figure 4.8. Shading is used for the coupling function (CF) in the bottom row. Larger values of the CF indicate less P-S coupling.

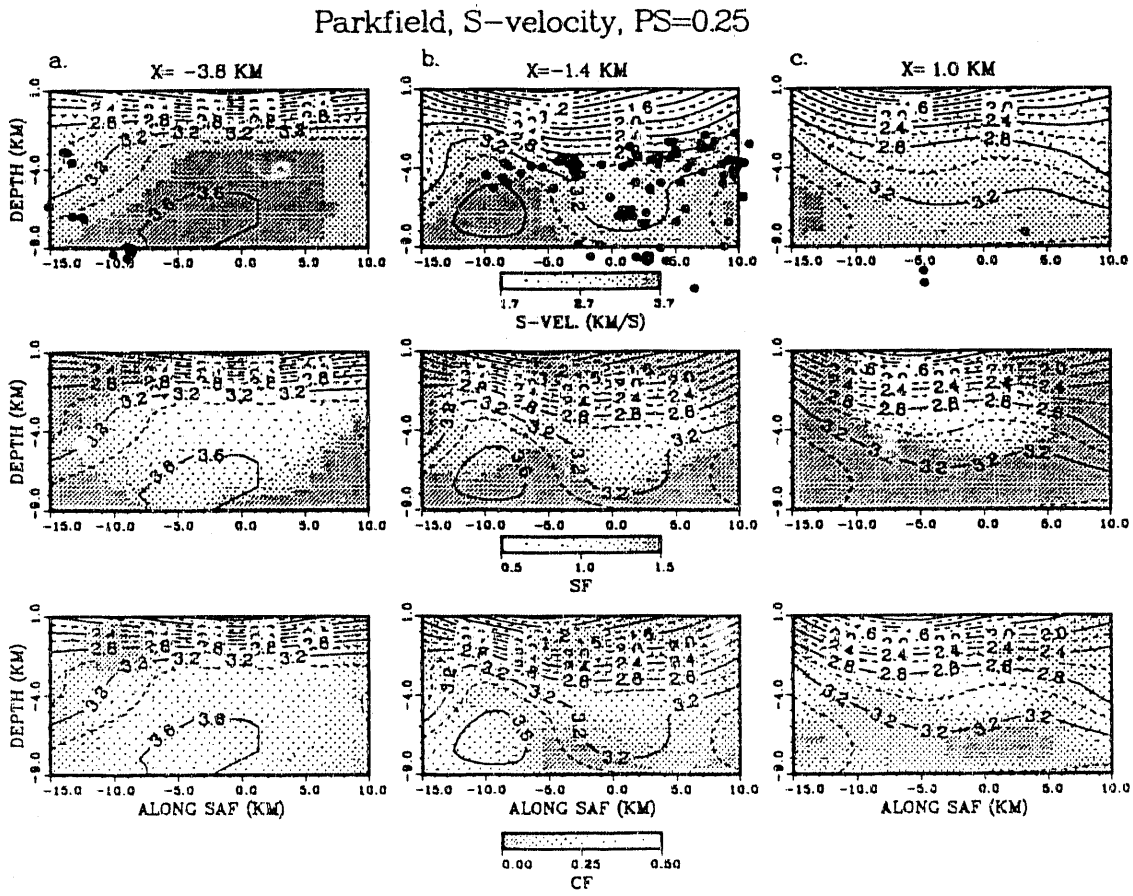

Figure 4.12: Parkfield final S-model: vertical sections along the fault (the view is from the northeast and the format is the same as in figure 4.11).

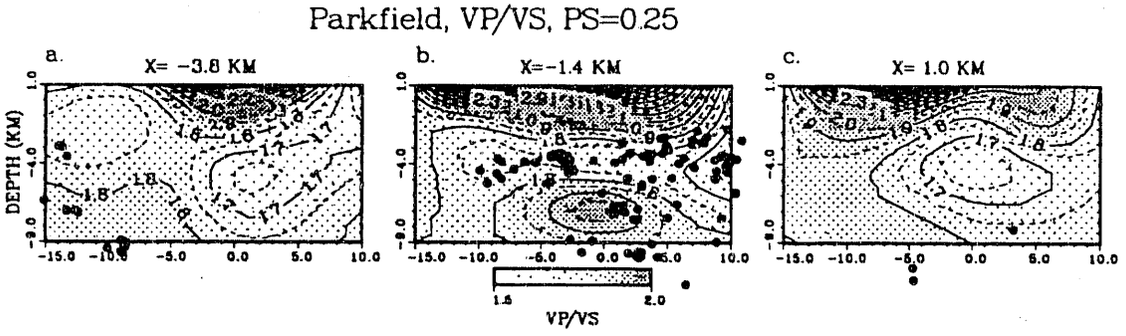

Figure 4.13: Parkfield final V_P/V_S model: vertical sections along the fault (the view is from the northeast).

the inner and better resolved parts, we find a continuation at depth of the southwest high-velocity body and the presence of a characteristic LVZ centered at $x = 1$ km and 1 to 2 km wide between $y = -10$ and $y = 0$ km. This low velocity zone widens to the north of $y = 0$ km.

The S-velocity model displays most of the features of the P-model with the notable difference that at depths ranging between $z = -6.5$ and $z = -9$ km there is a pronounced LVZ between $y = -2$ and $y = 5$ km which is 2 to 3 km wide.

The vertical cross-sections along the strike of the SAF which are displayed in figures 4.11 and 4.12 clearly show the HVB on the southwest side. The cross-sections at $x = -3.8$ and $x = -1.4$ show the HVB as a patch of the fault without background seismicity. In fact, there is an apparent correlation between the location of the earthquakes for $y < 2$ km and the 6.2 km/sec contour line.

The vertical sections across the fault permit a closer examination of the fault structure in the Parkfield nucleation zone and are shown in figures 4.14 and 4.15. Starting from the south, at $y = -15$ km (section *a.*), the HVB found on the southern end of the model is located approximately at the northern termination of the exotic

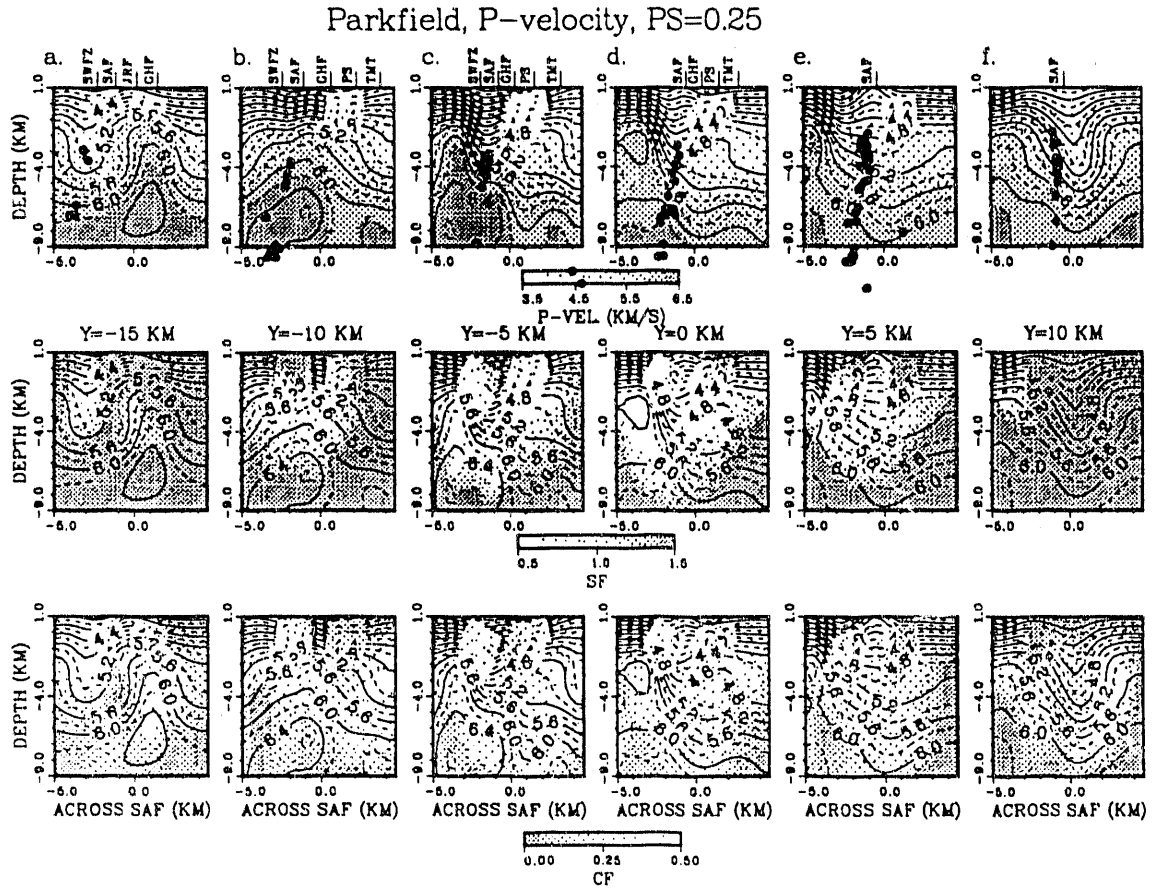

Figure 4.14: Parkfield final P-model: vertical sections across the fault (the view is from the southeast and the format is the same as in figure 4.11). The principal structural features of the area are plotted in the top row: South West Fracture Zone (SWFZ), San Andreas Fault (SAF), Jack Ranch Fault (JRF), Gold Hill Fault (GHF), Parkfield Syncline (PS) and Table Mountain Thrust (TMT).

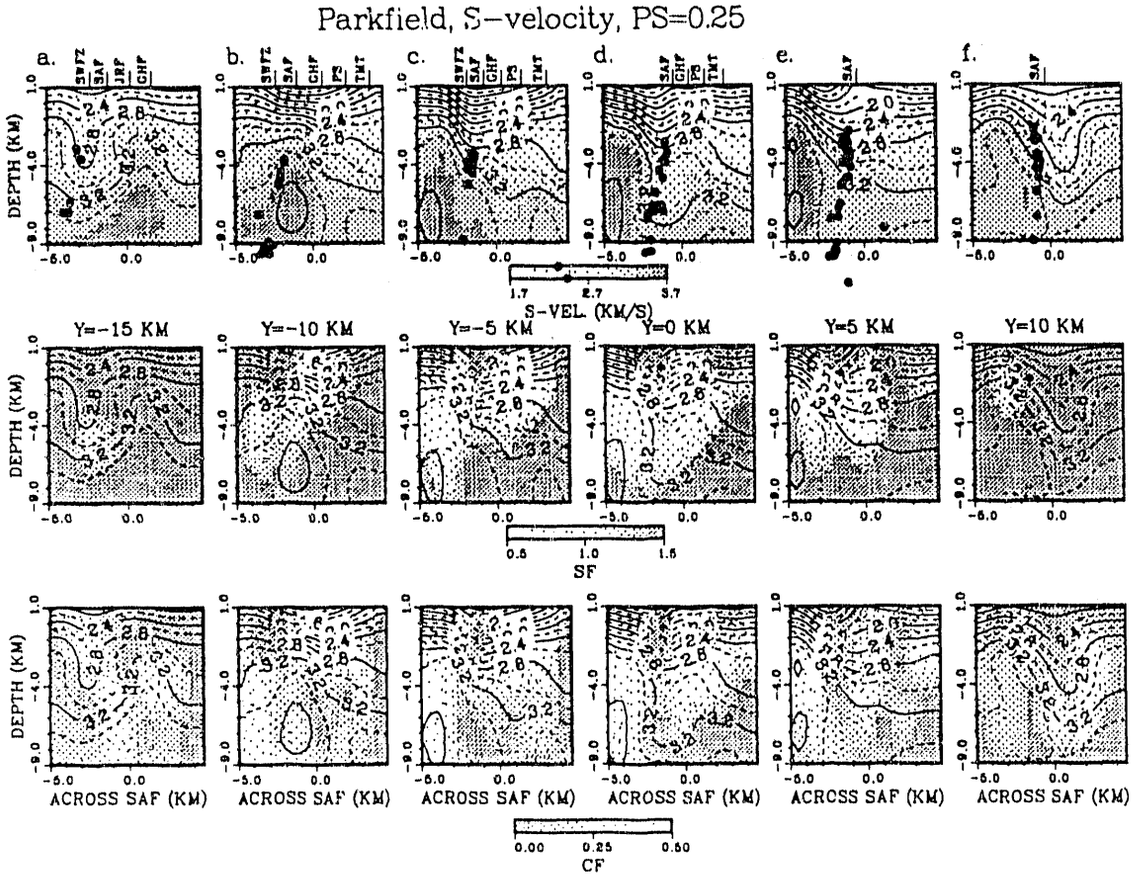

Figure 4.15: Parkfield final S-model: vertical sections across the fault (the view is from the southeast and the format is the same as in figure 4.11).

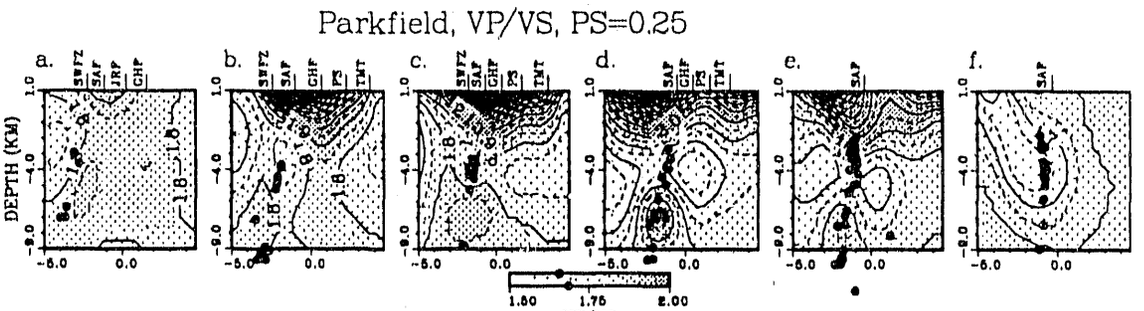

Figure 4.16: Parkfield final V_P/V_S model: vertical sections across the fault (the view is from the southeast).

gabbroic body of Gold Hill. The slight shift toward the northeast may be attributed to the loss of resolving power at the southeastern boundary. At $y = -10$ km (section *b.*), the vertical projection of the SAF cuts through the broadened high-velocity body observed on the southwest side and the deeper LVZ is found at $x \approx 1$, $z \approx -9$ km. Although, the resolution of this LVZ is low, its persistence in all the sections suggests that it is a true feature of the model. The $y = -5$ cross-section (*c.*) features the broadening with depth of the southwest HVB. A LVZ is found at more shallow depth ($z \geq -3.5$ km) and lies under the mapped trace of the South West Fracture Zone (SWFZ). The seismicity in this section is concentrated in a tight cluster at $z = -4$ km which lies below the shallow LVZ and just above the broadening of the high-velocity body. The cluster dips steeply toward the southwest and appears to be shifted by less than a kilometer to the southwest *wrt* the SAF trace. In this section, the best fitting line through the hypocenters meets the SAF trace. At shallow depths and farther to the northeast, a decrease in shallow seismic velocities at $x = 2$ km lies on the vertical projection of the Table Mountain Thrust (TMT).

The vertical cross-section at $y = 0$ (section *d.*) features the southwest HVB

at shallow depths, nearly disappearing at depths below 4 km ($z < -4$ km). The seismicity is nearly vertical to depths of approximately 5 km whereas deeper it dips steeply to the southwest. A cluster of earthquakes occurs at $z = -7.5$ km and it appears to lie at the fringes of the 6.2 km/sec isoline in the P-model. The deeper LVZ appears again as in the previous cross-sections to be shifted northeast of the SAF trace and of the seismicity. At shallow depths the model correlates again with the TMT.

The section at $y = 5$ km (section *e.*) is marked by the broadening of the low velocity zone between the two sides of the fault and by the disappearance of the southwest high velocity body. The seismicity in this section seems again to lie on two different strands. The shallow strand is nearly vertical or steeply dipping to the northeast whereas the deeper one dips steeply to the southwest.

The section at $y = 10$ km (section *f.*) is more poorly resolved and the overall features resemble those found in the $y = 5$ km section.

The S-model, plotted in figures 4.9, 4.12 and 4.15 resembles closely the P-model and this in part is caused by the imposed P-S coupling. However, it should be noted that in the well-resolved cross-sections at $y = -5$ and $y = 0$, the S-model features a wider and more sharply defined LVZ extending from $z = -9$ to $z = -3$ km. In these sections the seismicity lies on the southwest flank of the LVZ.

Finally, the V_P/V_S ratio plotted in figures 4.10, 4.13 and 4.16 shows high values near the surface and a well-defined zone of high V_P/V_S between $z = -6.5$ and $z = -9$ km depth in the inner parts of the model. This feature is emplaced within material having relatively lower values of V_P/V_S .

4.6 Discussion

In the following discussion I focus on the well-resolved features of the model.

The velocities found on the northeast side of the SAF lie in the range obtained

in laboratory experiments for Franciscan rocks (Stewart and Peselnik, 1977,1978; Lin and Wang, 1980) This observation when combined with the known local geology supports the interpretation of a northeastern block at Parkfield mainly consisting of Franciscan assemblage rocks at least down to depths resolved by the present study. The HVB resolved on the northeast side of the SAF between $y = -15$ and $y = -10$ km is probably related to the Gold Hill gabbroic exotic block.

On the southwest side of the SAF, the resolved structure is characterized by the high-velocity body south of the 1966 main shock with velocities between 6.4 and 6.6 km/sec at depths larger than 5 km ($z < -5$ km). These P-velocities appear too large for granitic compositions such as those found for the Salinian block and they may indicate the emplacement of a gneissic or an ultramafic/mafic body. These kind of compositions have been recognized elsewhere in the Central California Coast Ranges (Bailey et al., 1970). S-velocities for this HVB range between 3.5 and 3.7 km/sec, also suggestive of a gneissic or mafic composition (e.g., Kern and Richter, 1981). McBride and Brown (1986) in their study of the COCORP seismic line across the SAF at Parkfield[2] found a significant reflector at 3.4 sec which could be related to the HVB. The same COCORP seismic line was analyzed by Louie et al. (1988) with a Kirchoff migration technique. They proposed a nearly vertical reflector near the upward extension of our HVB at $y = -5$ (see figure 4.14).

Velocity values at intermediate depths between the HVB and the near-surface low-velocities, suggest the emplacement of granitic rocks of the Gabilan range. North of $y = 0$ the high-velocity body in the southwest block is not seen and the range of velocities suggests a granitic composition.

The seismicity at Parkfield appears to be strongly influenced by the high-velocity body imaged on the southwest side. The hypocenters shown in the vertical sections at $y = -10$ and $y = -5$ km in figures 4.14 and 4.15 and in the vertical longitudinal

[2]The COCORP seismic line is located between the vertical sections across the SAF at $y = -10$ and $y = -5$.

section at $x = -1.4$ km in figures 4.14 and 4.12 do not occur within the anomalous body, suggesting that the HVB may represent the asperity that ruptures in the characteristic Parkfield earthquakes (see also Michael and Eberhart-Phillips, 1991). This interpretation implies that the asperity at Parkfield involves material differing from its surroundings and, in this case, stronger if the higher velocities are associated with more competent rocks. The position of the HVB is consistent with results of deformation studies based on surface measurements. Tse et al. (1985), Stuart et al. (1985) and Harris and Segall (1987) have all proposed the existence of an asperity, or presently locked fault segment, although of different shape, in the same general location where we find the anomalous velocities. In addition, the northern termination of this HVB is near the 5° bend of the fault trace and the coincident change in the mode of deformation of the SAF. It is therefore appealing to attribute to this HVB a prominent role in the formation of the SAF bend. In the same region, the S-model displays a remarkable LVZ which is responsible for the anomalously high V_P/V_S ratio in figure 4.16d. This portion of the fault zone is also the location of the high stress drop earthquakes reported by Bakun and McEvilly (1981) and O'Neill (1984), and the zone of anomalous response to regional stress field changes observed by Poley et al. (1987). These contrasting blocks imaged by this tomographic study may provide a model for finite element modeling of the Parkfield region in an attempt to explain the complex block interactions and associated seismicity and deformation.

The shapes of the P- and S-LVZ appear even more intriguing. In the southern sections at $y = -10$ and $y = -5$ km, in both P and S models, a LVZ appears immediately northeast of the vertical projection of the SAF trace at depths greater than 7 km ($z < -7$ km). Remarkably, virtually no earthquakes occur in this LVZ. North of Middle Mountain ($y > 0$), a striking difference is observed between P and S models. The S model in sections at $y = 0$ and $y = 5$ km (figure 4.15) is characterized by a well pronounced LVZ which is wider and shifted to the southwest with respect

to the LVZ in the P model. The width of the S-LVZ is approximately 3 km, and the earthquakes tend to be located on its southwestern flank. However, the true vertical extension of this LVZ cannot be determined due to lack of resolving power at depth. The wider S-LVZ suggests differing responses of bulk and shear moduli to the continuous deformation produced by the long-term strike-slip movement of the SAF. Alternatively, the S-LVZ could be caused by non-random errors in the S-onset determinations. While we cannot exclude this cause, extremely careful attention went into reading the S waves, and only those with clear and impulsive onsets were selected. The wide S-LVZ seems to be partly inconsistent with the findings of Li and Leary (1990) on the width of the SAF at Parkfield. They modeled fault zone trapped S waves and inferred widths of the fault of the order of 100 m or less. Their result can be reconciled with ours if the SAF consists of several relatively thin and subparallel LVZ. Mooney and Ginzburg (1986) have suggested that the fault zone may consists of several subparallel zones of fault gauge. If we compare our results with other studies on the shape of the SAF, we find that the overall shape of the LVZ at $y = 5$ km closely resembles the findings of Feng and McEvilly (1983) for a seismic reflection profile crossing the creeping SAF in Bear Valley, Central California. The velocity values that Feng and McEvilly found in the fault are consistently lower than those found in this study. This can be attributed to a different local structure along their profile and/or to lack of resolving power of our data set. However, the results of Feng and McEvilly are strongly dependent on their initial model which was derived from Healy and Peake (1975) fault model. Conversely, our initial model is laterally homogeneous and there is no *a priori* assumption on the final shape of the fault zone. In sections from $y = -10$ to $y = 5$ the shape and overall width of the fault zone varies along the fault, suggesting that the "classic" fault zone structure cannot be generalized to all the active segments of an active fault such as the SAF, although there may be characteristic features common to locked and creeping fault zones.

The V_P/V_S anomaly found near the hypocenter of the 1966 mainshock appears to coincide with the zone of anomalous response to regional stress changes observed by Poley et al. (1987). This anomalous V_P/V_S ratio could be also explained by high fluid pressures in the nucleation zone of the expected M6 earthquake. Theoretical studies on interacting, saturated macrofractures by O'Connell and Budiansky (1974), the findings of Moos and Zoback (1983) in densely fractured well samples, the laboratory experiments of Nur and Simmons (1969), Christensen (1984) and Christensen and Wang (1985), among the others, for fluid-saturated rock samples, the observations along the SAF reported by Berry (1973) and Irwin and Barnes (1975) and at the bottom of the Varian well in the study area (Sims, 1990), can explain the observation, although by differing physical mechanisms.

The earthquake hypocenters located using the 3-D model tend to lie on a steeply southwest dipping plane in the southern sections at $y = -10$ and $y = -5$ km which meets the SAF trace at the surface. In the northern sections ($y = 0$ and $y = 5$), the earthquake foci appear to lie on a vertical plane at depths less than 4 km and to be steeply dipping to the southwest at greater depths. However, it was shown in the synthetic tests that some apparent dip can be introduced simply by the presence of large gradients in the velocity model, and it remains unresolved whether the observed dip is real. When epicenters are plotted in different depth ranges (figures 4.8 and 4.17), foci with $-5.5 \leq z \leq -2.5$ (section at $z = -4$) lie along two differing alignments north and south of $y = 0$ km (Middle Mountain and epicenter of the 1966 main shock). The 5° angle between these two alignments coincides with the 5° bend observed for the trace of the SAF.

4.7 Conclusions

In this chapter we have applied the joint velocity and hypocenters inversion technique formulated in chapter 2 to the Parkfield data set. Inversions performed with different

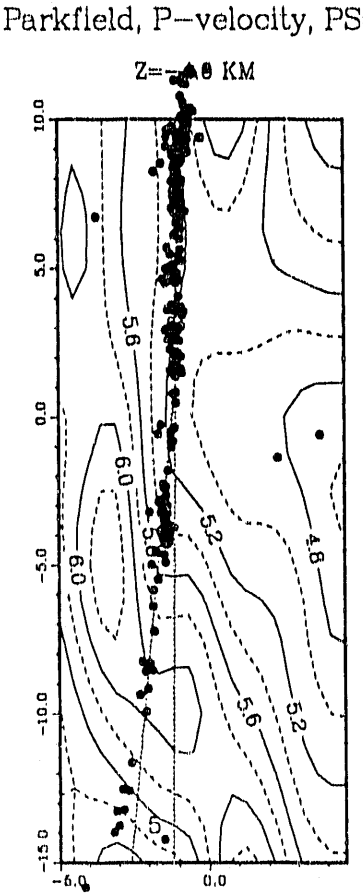

Figure 4.17: Parkfield: plan view section at $z = -4$ km with epicenters of the earthquakes located between $-5.5 \leq z \leq -2.5$ in the time period from April 1987 to December 1989. Earthquakes at the boundaries of the 3-D model have been disregarded in fitting the two dotted lines through the epicenters because the model is less resolved and the earthquakes lie outside the HRSN.

a priori conditioning, different data sets and a shifted grid mesh have demonstrated the robustness of the resolved models.

The overall P- and S- velocities in the Parkfield area reflect the presence of Franciscan rocks to the northeast of the SAF and the emplacement of a relatively high-velocity body ($V_P \approx 6.4 - 6.6$ km/sec) on the southwest side of the fault and south of the 1966 mainshock epicenter. This anomalous high-velocity body is believed to be related to the "asperity" that ruptures in the characteristic Parkfield earthquakes, and it appears to control the 5° bend of the SAF near the 1966 epicenter.

An interesting feature of the resolved P- and S- models is a deep LVZ immediately northeast of the vertical projection of the SAF and south of the 1966 main shock. Nearly all the earthquakes in this part of the fault zone lie outside this LVZ.

The S-model displays a prominent LVZ which suggests differing long-term response of the shear and bulk moduli to the continued action of the SAF and/or the existence of anomalously high pore-fluid pressure at depth.

The seismicity located using the 3-D model displays a 5° bend near Middle Mountain, nearly coinciding with the identical bend of the fault trace. All earthquake foci south of Middle Mountain lie on a steeply southwest-dipping plane and foci north of Middle Mountain lie on a nearly vertical plane in the upper 4 km and on a plane steeply dipping to the southwest at larger depths. Some apparent and unrecognizable southwest dip in the locations can be introduced by the nature of the 3-D model.

The present model suggests that the SAF fault zone structure varies along locked and creeping parts. These different fault zone structures are probably responsible for the different modes of deformation observed along the fault.

Chapter 5

Application to Loma Prieta

The Loma Prieta (LP) Earthquake of October 18, 1989, ($M_L \approx 7.0$) occurred at the southern end of the San Andreas fault (SAF) segment that ruptured last in the great 1906 San Francisco earthquake. Possible failure of this part of the SAF had been proposed by various authors (Lindh, 1983; Sykes and Nishenko, 1984; Scholz, 1985), and the Working Group on California Earthquake Probabilities (1988) had assigned a probability of occurrence of 0.2 in the next 30 years. Although this long term prediction had recognized the epicentral area, several other features of this earthquake such as the hypocentral depth, rupture extent, focal mechanism of the main shock and its aftershocks and the lack of a surface break, had only in part been predicted.

The U.S. Geological Survey operates in the epicentral area a large number of short-period seismic stations that recorded several thousands aftershocks that followed the mainshock and have provided an ideal data set for application of the simultaneous inversion technique described in chapter 2.

5.1 Geology

The following description of the geology is based on the regional description along the San Andreas fault system by Irwin (1990) and the local on the Southern Santa Cruz mountains (SCM) by Clark and Rietman (1973).

The SAF in the southern SCM juxtaposes two major tectonic blocks — a block characterized by diverse basement rocks of the Franciscan Formation to the northeast and the Salinian block of granitic and regionally metamorphosed rocks to the southwest.

The Franciscan is a heterogeneous assemblage of dismembered sequences that consists mainly of graywacke and shale with smaller amounts of mafic volcanic rocks, chert and limestone. This assemblage is characterized by serpentinite and highly metamorphosed (blue shists) melange zones that have been highly deformed along with generally separate blocks of more coherent units. The age of the Franciscan ranges between Late Jurassic and Cretaceous and, in the northern Coast Ranges, is as young as Tertiary.

The Coast Range thrust separates a lower plate consisting of Franciscan rocks from an upper plate that consists of Great Valley Sequence in depositional contact on the Coast Range Ophiolite. It is believed that the serpentinite outcropping along the faults of the SAF system is derived from the Coast Range Ophiolite.

The Great Valley sequence consists mainly of interbedded marine mudstones, sandstones and conglomerate of Late Jurassic to Cretaceous age and it has a maximum thickness of approximately 12 km. It outcrops generally as thick, monotonously layered sections that have experienced markedly less deformation than have the contemporaneous Franciscan rocks.

In the study area, northeast of the Sargent fault (SF), the Franciscan sequence contains limestone lenses and horneblende- glaucophane-bearing metamorphic rocks. At the northeastern edge of the study area, serpentinite appears to be associated with known faults.

To the southwest of the SAF, the Salinian block consists of Cretaceous plutons intruding metamorphic rocks of unknown age. The plutonic rocks consist mainly of granite and tonalite. In the study area, the plutonic rocks are exposed south

of the Vergeles fault (VF) and their composition varies between quartz-diorite and adamellite. Metamorphic rocks of the Salinian block consist of moderate- to high-grade gneiss, granofels, impure quartzite and minor amounts of schists and marble. They probably originated from a bedded sequence that consisted predominantly of siltstone and sandstone. These rocks outcrop southwest of the Vergeles fault.

Tertiary rocks outcrop extensively in the study area and consist of marine clastic sedimentary sequences ranging in age from Paleocene to Pliocene, with a total thickness of more than 7 km. End members of these clastic rocks sequences are shales and conglomerates, indicating a neritic near-shore environment for deposition. The Purisima formation of Pliocene age lies unconformably on the older Tertiary rocks. Quaternary deposits are also common in the region. In particular, tertiary and quaternary deposits outcrop extensively on the southeast part of the study area (northeast side of the SAF). The area between the SAF and the Sargent fault in the central part of the study area is characterized by imbricated southwest dipping reverse faults that juxtapose thin faulted slivers of Great Valley Sequence, Coast Range Ophiolite and Tertiary marine and non-marine sediments (McLaughlin et al., 1988). In the same area but southwest of the SAF, Tertiary sediments extend into the Watsonville valley.

Exploratory wells southwest of the Zayante-Vergeles (ZF-VF) tectonic line have shown that Tertiary sediments overlie the crystalline granitic basement, confirming the continuity at depth of the Salinian block from south of the Vergeles fault to the Ben Lomond granitic outcrops outside our study area to the northwest. Between the Zayante-Vergeles line and the SAF the Tertiary sediments are much thicker and the crystalline basement appears to be downfaulted.

In the southeastern part of the study area and on the southwest side of the San Andreas Fault a horneblende quartz gabbro which is petrologically distinct from the granite in the Salinian outcrops near Logan. Gravity data suggest that this gabbro extends southwest in the subsurface, but its relation to the rocks of the Salinian range

is uncertain.

5.2 Main shock rupture and seismicity

Several studies have addressed the LP mainshock mechanism and aftershock sequence. The mainshock mechanism has been determined by adopting a variety of data sets and techniques. The general consensus among scientists can be summarized as follows:

1. the hypocenter was located at a depth greater than 15 km within the restraining surface bend of the SAF in the Santa Cruz mountains and the rupture extended toward shallow depths;

2. a comparable amount of thrust and right-lateral strike-slip on a southwest dipping fault plane whose strike is nearly parallel to the SAF occurred during the main shock (dip $\approx 70°$, strike $\approx 130°$) (e.g., among the others Kanamori and Satake, 1990; Lisowski et al., 1990; Oppenheimer, 1990; Zhang and Lay, 1990);

3. the average value of 1.8 m of oblique slip on the entire southwest dipping plane was found by Beroza (1991) to be partitioned predominantly into two zones with large strike-slip and reverse motion to the southeast and northwest of the hypocenter, respectively;

4. no surface main-fault break could be observed in the epicentral and neighbouring areas, consistent with geodetic modeling of the mainshock which precludes ruptures more shallow than 4–5 km (e.g., Lisowski et al., 1990).

These findings differ from the generally observed pattern of right-lateral strike-slip faulting of the SAF and are probably related to the morphology of the fault in

the restraining bend of the SCM. More intriguing is, however, the nature of the LP earthquake and its relation to the 1906 San Francisco earthquake.

Sibson (1982) used the distribution of hypocentral depths in Central California to infer the depth for the transition between the brittle and ductile regime on the SAF. The hypocentral depth determined for the main shock suggests that the transition zone in the Santa Cruz Mountains segment is 3 to 5 km deeper than what previously inferred by Sibson. In fact, the hypocenter appears to be within 5 km of the base of the crust.

Dietz and Ellsworth (1990) have addressed the large component of thrust in the mainshock and have shown, by using geometrical arguments and the relative directions of plate motion, that the amount of thrust in the LP main shock can be explained by the local variation in strike of the SAF at the restraining bend in the SCM and by a 65° to 70° southwest dipping slip-surface. However, the proposed recurrence intervals which vary between 65 and 115 years for this segment of the SAF (e.g., Sykes and Nishenko, 1984), when combined with the main shock reverse component of fault motion, would produce an uplift rate of the order of 1 cm/yr if LP type earthquakes are the only mode of deformation in the SCM. In this scenario, a "spectacular" topographic relief should be present in the SCM (Kanamori and Satake, 1990) and lower crust rocks should crop out on the southwest side of the SAF (Dietz and Ellsworth, 1990). Kanamori and Satake have discussed three different hypothesis to explain the relief in the SCM. In their first hypothesis, they suggest that the geometry of fault plane motion changes on time scales of several thousand years so that coseismic uplift has not accumulated enough to produce the high topographic relief. In their second hypothesis, they recognize that the mode of deformation can be quite complex with several faults of different orientation acting through the seismic cycle. Finally in their last hypothesis, they view the LP event as a highly unusual one that might not involve the plate boundary. Schwartz et al. (1990) have noted, however, that the highest

relief in the SCM has experienced subsidence in the main shock and that the present topographic relief cannot be explained by LP type earthquakes alone. They have proposed that accommodation of deformation in the SCM involves the activation of a series of northeast and southwest dipping faults throughout the earthquake cycle.

The relationship between the LP earthquake and the great 1906 San Francisco earthquake is also difficult to assess. The 1906 rupture extended as far south as San Juan Bautista, which also defines the southernmost zone of activity in the LP aftershock sequence. However, after the 1906 earthquake, approximately 1 m of surface fault offset was observed by the Lawson's team (USGS Staff, 1990) in the Wright railway tunnel a few hundred meters beneath the crest of the SCM ridge crest but no clear fault break could be observed at the surface, indicating that either the Lawson's team missed rupture on the trace of the SAF or that no clear fault-related offset occurred in the southern SCM. Because Wright tunnel has been sealed and is currently not accessible, possible fault offsets in the tunnel caused by the LP earthquake have not been measured, but the pattern of surface deformation and breakage appears, in some places, to closely resemble that described in Lawson's report on the 1906 earthquake (USGS Staff, 1990).

Preliminary geodetic modeling of the LP mainshock appears to preclude slip on the main rupture plane at depths less than 5 km, whereas, for the 1906 rupture there has been some debate in the past on the actual fault displacement in the southern SCM. Geodetic data alone indicate that approximately 2.5 m of right-lateral strike-slip have occurred in 1906 along this section of the SAF to about 10 km southeast of Loma Prieta Peak (Thatcher and Lisowski, 1987). Conversely, surface break evidence alone (i.e., 1 m offset in Wright tunnel) would suggest reduced slip on this segment in 1906. This smaller 1906 slip along with other geologic and seismicity evidence was used by Lindh (1983), Sykes and Nishenko (1984) and Scholz (1985) to assign a relatively high long-term probability for the occurrence of a M6.5+ earthquake along

this section of the SAF.

The LP mainshock and its aftershocks filled a U-shaped seismicity gap (e.g., Olson, 1990). This gap was one of the lines of evidence that led Lindh (1983) to propose a M6.5+ earthquake at this location.

According to Dietz and Ellsworth (1990), LP aftershocks extended from approximately 20 to 25 km north of the mainshock epicenter southwestward to location about 3 km into the northern part of the creeping zone of the SAF. Aftershocks concentrated at the northern and southern perimeter of the inferred mainshock rupture surface. Fewer aftershocks occurred within the mainshock rupture zone. The aftershocks tend to lie on a 65° southwest dipping plane that intersects the vertical projection of the SAF surface trace at approximately 10 km depth. This plane, according to the seismicity plots presented by Dietz and Ellsworth appears to steepen when proceeding from north to south and, at the southern boundary of the aftershock zone, it is nearly vertical. The best fitting plane through the aftershocks deeper than 10 km strikes $N51°W \pm 2°$, dips $65°SW \pm 5°$ and coincides with the fault plane solution determined for the mainshock by Oppenheimer (1990). Aftershock mechanisms are very consistent outside the perimeter of the main rupture. Predominant reverse and right-lateral strike-slip faulting are observed in the northern and southern part of the aftershock zone, respectively.

The main rupture appears to have activated at its southern end a cluster of seismicity that connects the SAF and the Sargent fault at depth. Olson (1990) has interpreted this cluster as closing a wedge-like structure whose boundaries are the SAF and the Sargent fault to the southwest and northeast, respectively. The Lake Elsman cluster of earthquakes that became active two years before the LP mainshock lies at the intersection of the SAF and Sargent fault to the north and represents the northern end of Olson's wedge structure. The focal mechanisms of these earthquakes suggest reverse faulting on a northeast dipping plane that Olson has interpreted as a

blind fault intersecting the SAF at depth.

In summary, the LP earthquake displays several features which substantially differ from larger shocks on other segments of the SAF system. Although the LP earthquake ruptured within a segment of the SAF that ruptured last in the great 1906 San Francisco, its relationship with the latter is not clear. It appears that an improved knowledge of the velocity structure in the mainshock region combined with the known geology in the SCM might clarify some of the previously mentioned anomalous features. The determination of the velocity structure and its relationship to the local geology will be addressed in the next sections of this chapter.

5.3 Data

P-arrival times from aftershocks of the Loma Prieta earthquake and from previous background seismicity were used in this application of the technique developed in chapter 2. The data were recorded by the short period seismic stations of the USGS Central California network (CALNET) which are shown in figure 5.1. For this tomographic inversion, we have selected the handpicked CUSP (on line event detection and seismogram storage computer) P-arrivals from a total of 173 earthquakes. The selected data are digitally recorded at 100 samples per second and we estimate the accuracy for the well recorded P-onsets to be of the order of ± 0.02 seconds. Background seismicity earthquakes and aftershocks were selected to have a minimum of 30 and 25 recorded P-arrival times, respectively. A total of 5422 travel times were used in the simultaneous inversion. An initial 1-D laterally homogeneous model was determined using the linear B-splines algorithm of Thurber (1983). This initial model produced a weighted RMS residual of 0.236 seconds and was adopted as starting model in all the 3-D inversions (see Figure 5.2).

5.4 Discretization Grid

The discretization grid used in this application is shown in figures 5.1 and 5.3. It consists of $9 \times 11 \times 6 = 596$ nodes which are equally spaced, 3, 7 and 3 km, along the three cartesian coordinates, x, y and z, respectively. This grid configuration produced a final weighted RMS residual of 0.092 seconds at the end of the eighth and last iteration of the simultaneous inversion. To test the robustness of the inversion with respect to the discretization grid, we have repeated the tomographic inversion using various grid sampling intervals along the three cartesian coordinates. Because of the current dimensioning in the inversion algorithm, i.e., a maximum of 600 nodes to be inverted at one time, some tradeoff in the node sampling interval along the three coordinates had to be applied.

Table 5.1 displays the final RMS residuals obtained with different grid configurations. An unexpected result of these grid configuration tests is the sharp decrease in final RMS residual that occurs when a finer discretization was selected along the y-coordinate which runs nearly parallel to the strike of the SAF system in the area. In fact, it appears that regardless of the selected discretization interval along the x and z coordinates, a decrease in sampling interval along the y-axis from 10 to 6 km, reduced the weighted RMS residual by nearly 0.020 seconds. This result suggests the presence of substantial lateral variations at scale length < 10 km in the velocity structure along the SAF system in the SCM.

5.5 Robustness test

To select the optimal grid spacing to be adopted, the inversion has been repeated using different discretization grids. Figures 5.4 to 5.6 show a series of vertical cross-sections obtained using different grid configurations. The top row in these figures was

determined using a grid which has sampling distances of 4.0, 3.0 and 6.0 km along the x, y and z coordinates, respectively. This model has the smallest discretization interval along the y-axis, i.e., the fault strike, (dense along, DAL). The middle row was determined using the smallest sampling distance along the vertical axis, 2.5 km along z, and intervals of 3.5 and 10 km along the x and y coordinates, respectively (i.e., dense vertical, DVE). Finally, the bottom row in figures 5.4 to 5.6 displays the model determined using a sampling interval of 2.5 km along the x-axis (i.e., dense across, DAC) and 10 and 3 km sampling interval along the y and z coordinates, respectively.

These figures show that, other than the obvious smoothing introduced by larger sampling intervals, the main features of the model are remarkably stable, indicating that the resolved models are inherently robust. The final model that was selected in this thesis and by Foxall et al. (1991) trades off the discretization distance across and along the fault, i.e., 3.0 and 7.0 km along x and y, respectively. The final RMS of the selected model has a value that coincides with the one obtained using the DAL grid.

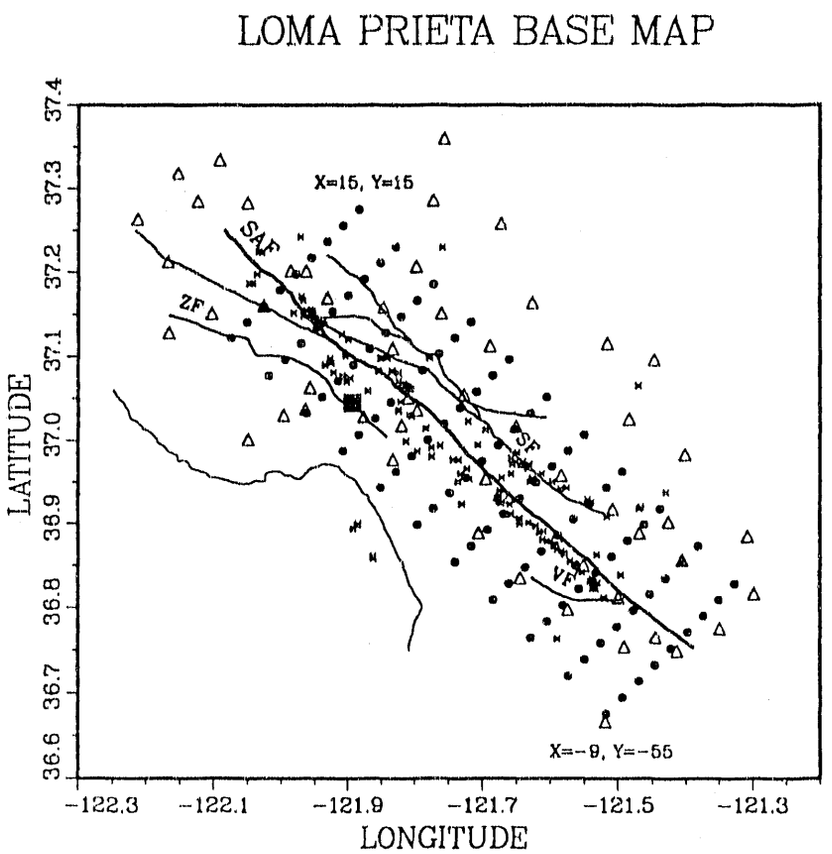

Figure 5.1: Loma Prieta base map showing locations of the CALNET-USGS stations (open triangles), the grid nodes used in the inversion (solid circles), the 173 earthquakes used for the joint inversion (crosses), and the surface trace of the San Andreas Fault (thick solid line) and the other main fault in the area (thin solid lines). The grid mesh is centered at $37°5.0'N, 121°53.0'W$ and is rotated 45° counterclockwise. For reference, the coordinates of the southernmost and northernmost knot-column of the grid mesh are shown. See text for abbreviations.

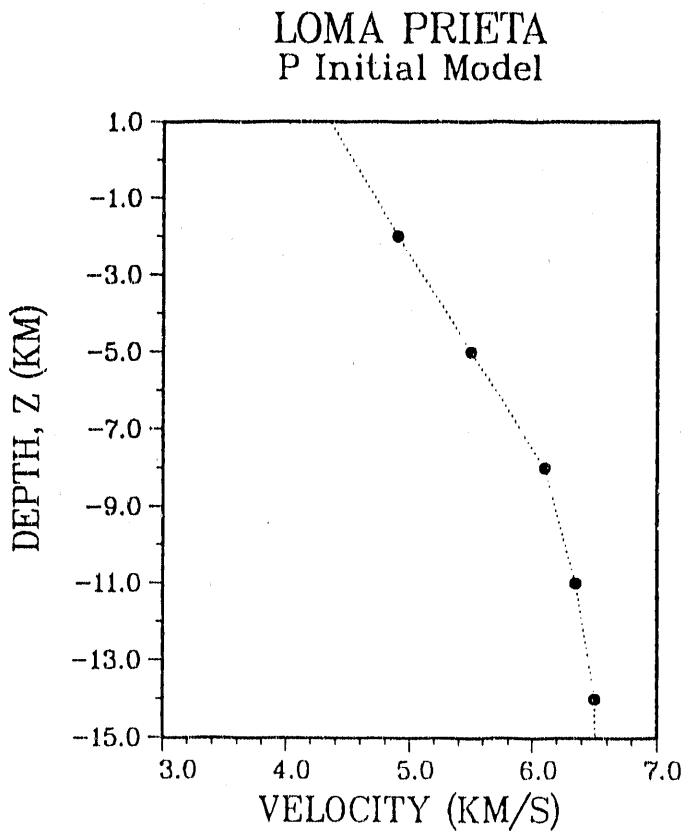

Figure 5.2: Loma Prieta P-velocity 1-D initial model. Velocities attain a constant value for $z \leq -14$ km.

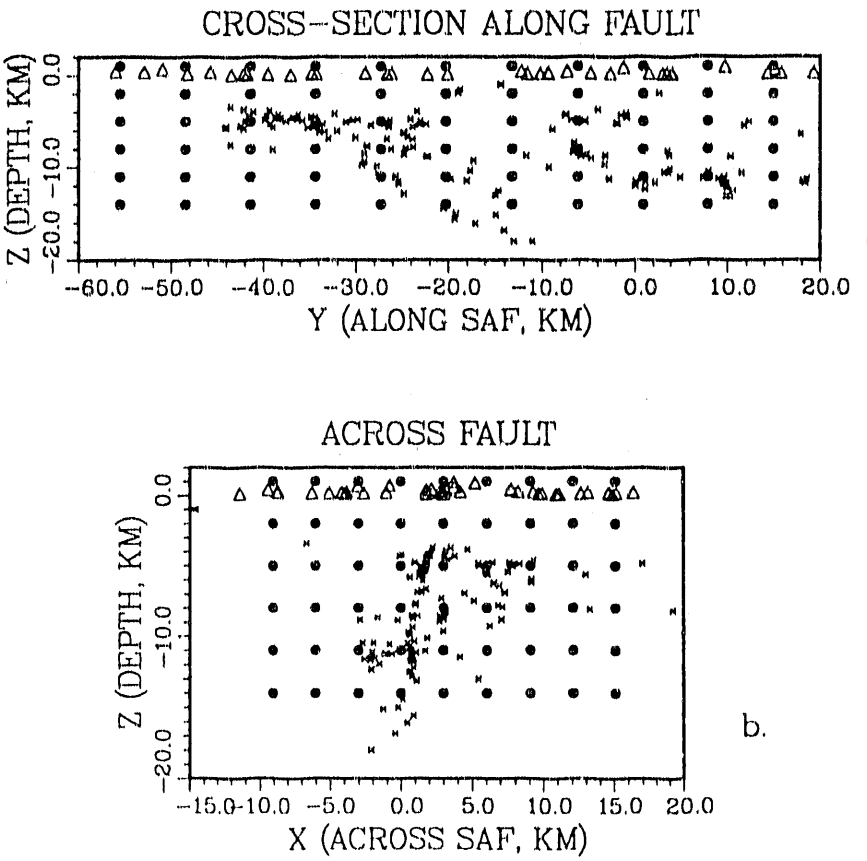

Figure 5.3: The 173 earthquakes used for the inversion and the position of the nodes in the local reference system defined by the grid mesh. a) vertical cross-section along fault (southeast-northwest, $y - z$); b) vertical cross-section across the fault (southwest-northeast, $x - z$). Grid mesh, stations and earthquakes are plotted with the same symbols of figure 5.1.

LOMA PRIETA INVERSIONS			
method[a]	*WRMS*[b]	*iterations*	*grid*[c]
μ_P	0.092	7	9, 11, 6 (3., 7., 3.) (−9., −55., −1.)
$\eta_P^D = 1.0$	0.093	7	*same as above*
μ_P	0.111	5	8, 9, 8 (3.5, 10., 2.5) (−9., −60., −1.)
μ_P	0.092	5	7, 14, 6 (4., 6., 3.) (−9., −58., −1.)
μ_P	0.094	5	9, 11, 6 (3., 7., 3.) (−9., −48., −1.)
μ_P	0.115	3	11, 9, 6 (2.5, 10., 3.) (−10., −60., −1.)

[a] $\sigma_t^P = 0.13$.
[b] Values are in seconds and the initial WRMS was 0.237 sec.
[c] Number of nodes, discretization distance (km) and position of the most shallow node of the southwest corner of the grid (km). Each line refers to values along the x, y and z coordinates, respectively.

Table 5.1: Results of the Loma Prieta inversion with different grid-configurations and *a priori* conditions applied.

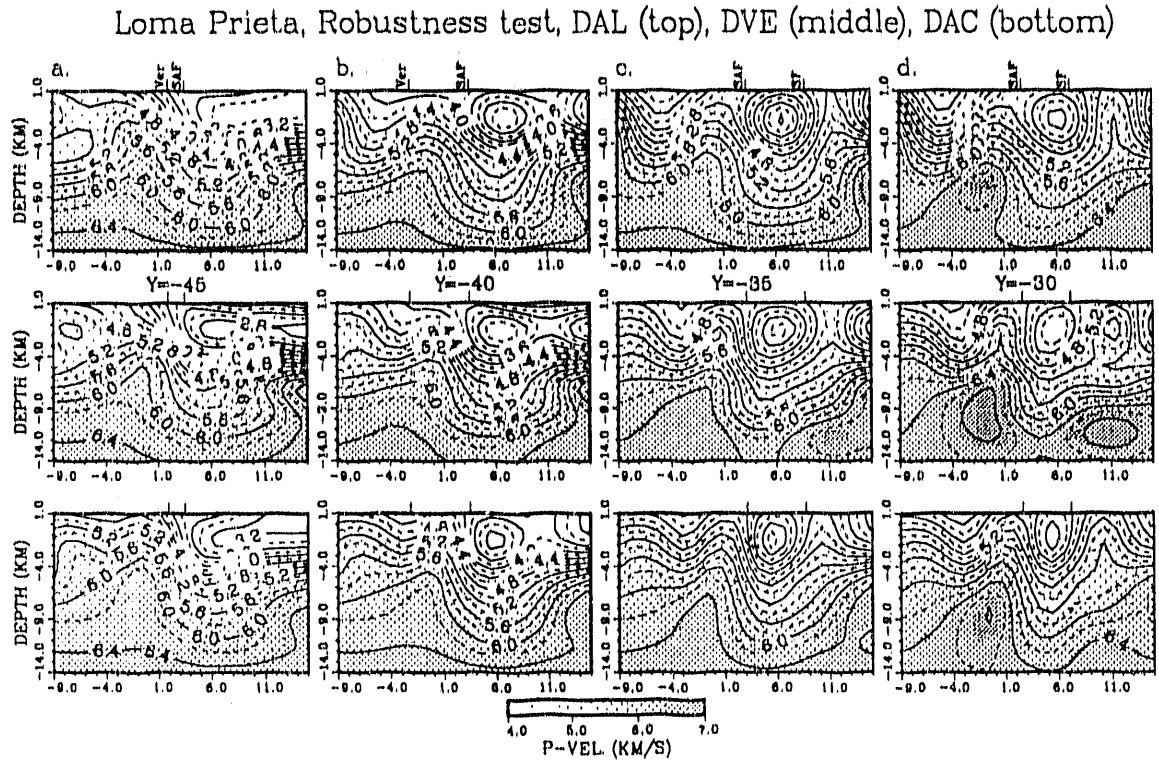

Figure 5.4: Robustness test for the Loma Prieta P-model from $y = -45$ to $y = -30$ km (vertical cross sections across the SAF, i.e, $x - z$). Denser grid along the fault, DAL (top); Denser grid in depth, DVE (middle); Denser grid across the fault, DAC (bottom). (See text and table 5.1 for details).

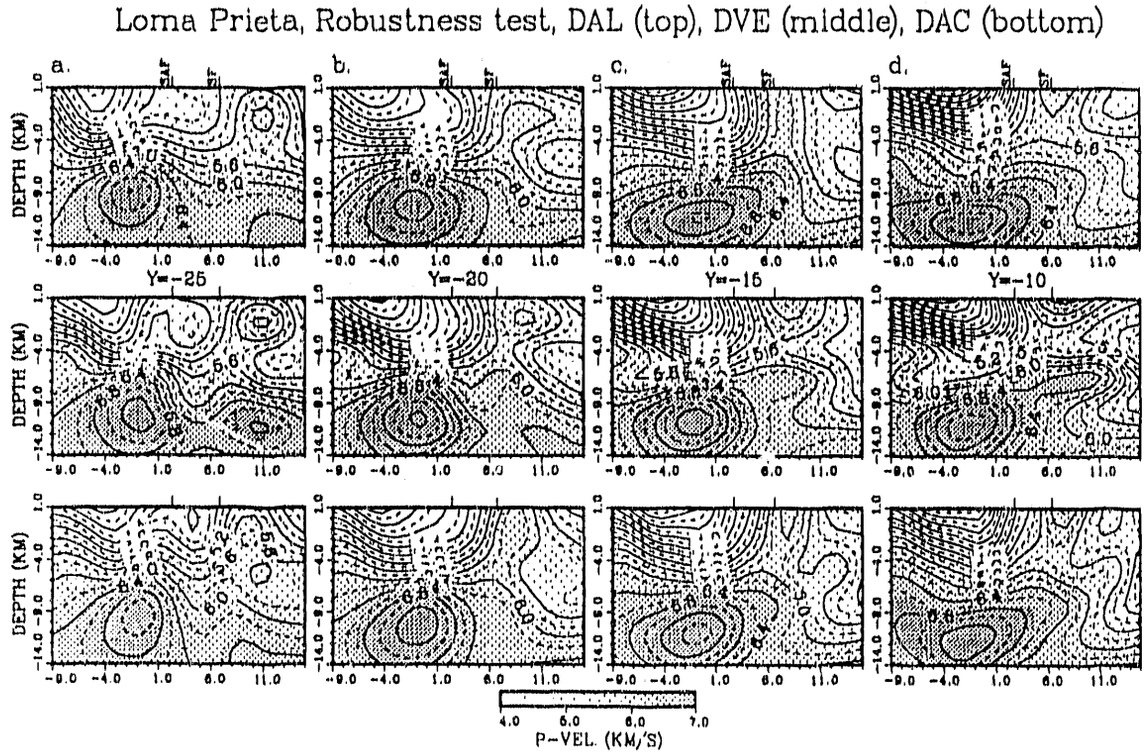

Figure 5.5: Robustness test for the Loma Prieta P-model from $y = -25$ to $y = -10$ km. (See figure 5.4 for explanations).

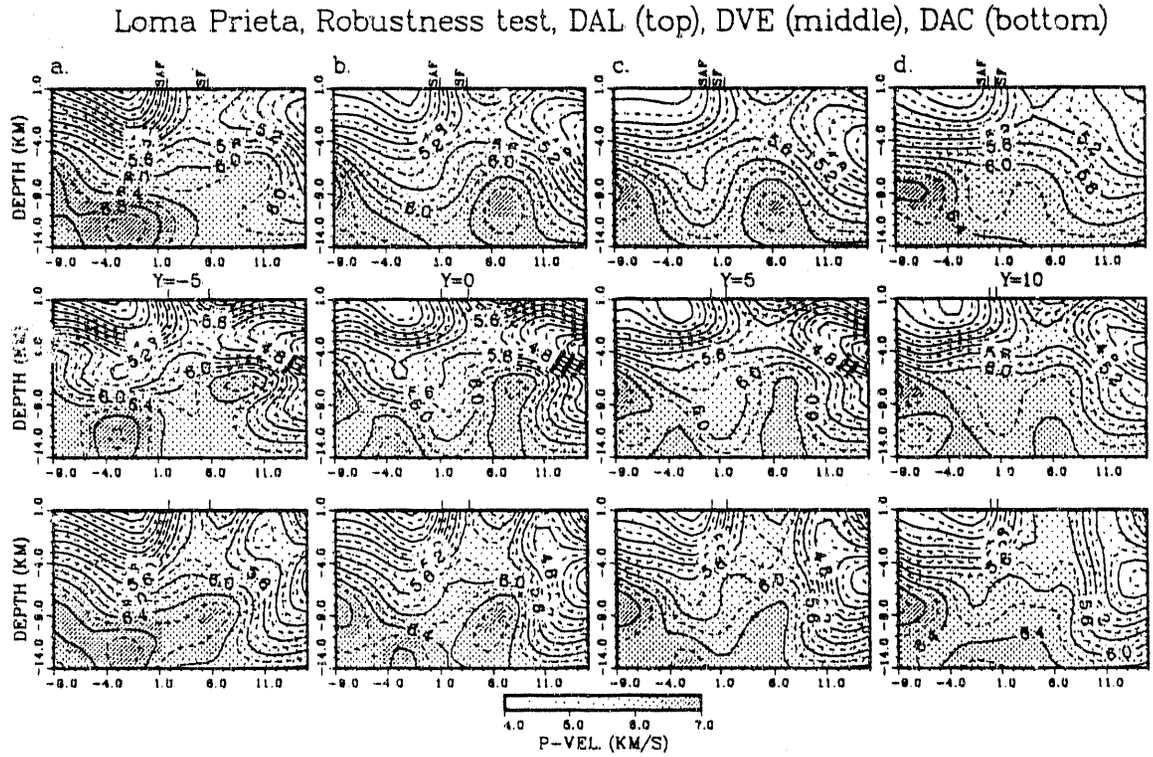

Figure 5.6: Robustness test for the Loma Prieta P-model from $y = -5$ to $y = 10$ km. (See figure 5.4 for explanations).

5.6 Model description

A complete and detailed discussion of the final resolved model and its relationships to background seismicity and the aftershock distribution is given in the study by Foxall, Michelini and McEvilly (1991) which uses a total of more than 700 3-D located earthquakes in the Loma Prieta area. In this section I will describe and discuss the principal features of the velocity model.

The isostatic gravity anomaly map of the study area is shown in figure 5.7. The final model is presented as plan view sections in figure 5.8 and as vertical sections across and along the fault in figures 5.9 to 5.11 and 5.12, respectively. The earthquakes adopted in the inversion are also shown in the model sections as solid circles together with the location of the mainshock as determined using the final model (solid square).

The shallow plan view sections ($z = -2$ and $z = -4$ in figure 5.8) correlate remarkably well with the surface geology and the isostatic gravity map. The imaged model can be subdivided into two domains, northeast and southwest of the SAF. I will describe the two domains separately by proceeding from southeast to northwest and by relating the main features to the mapped geology and previous geophysical studies in the area.

In the southern part of the southwest domain ($-55 \leq y \leq -45$) the resolved structure displays higher velocities ($\approx$ 6 km/sec) that correlate well with the Salinian block that crops out south of the Vergeles fault. The remaining part of the southwest domain at $z = -2$ is characterized by low velocities ($\approx$ 4 km/sec). However, an elongated high velocity body (HVB) appears between $y = -40$ km and $y = -25$. This HVB correlates well with the gabbroic structure that crops out near Logan (Ross, 1970). Maximum velocities in the imaged Logan gabbro are lower than those found in laboratory experiments even at zero pressure for gabbroic compositions. In our model the grid spacing across the SAF is 3 km which is too coarse to image a sliver

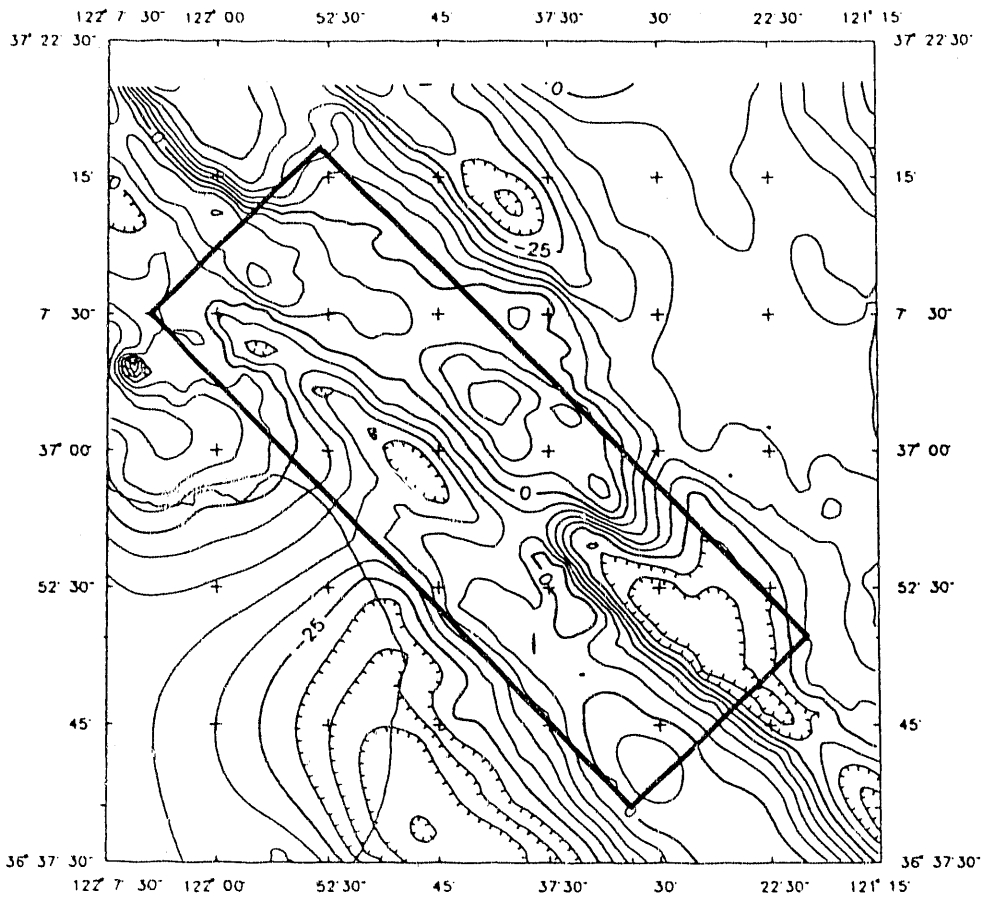

ISO grid from loma grav

Figure 5.7: Loma Prieta isostatic gravity map. The inset rectangular area is the target area of the velocity inversion.

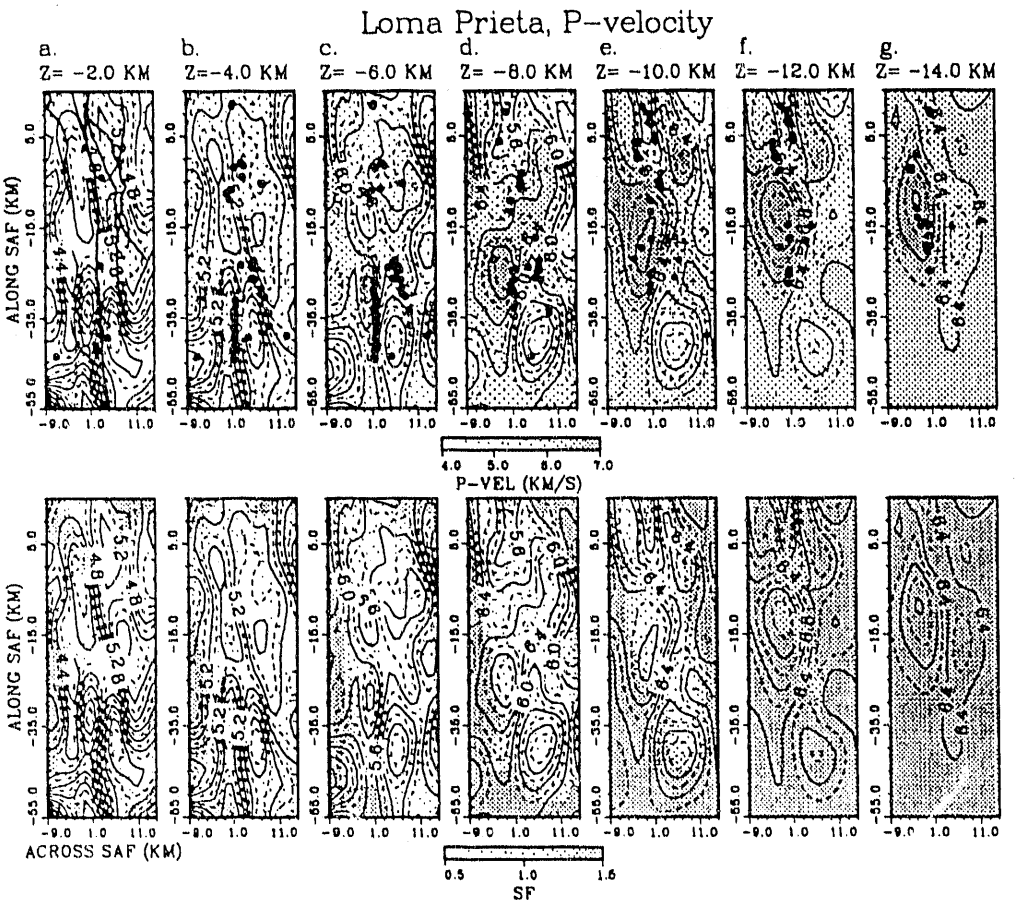

Figure 5.8: Loma Prieta final P-model: plan view sections. Contour lines indicate the resolved velocity values whereas shading indicates velocity values (top row) and the values of the associated spread function (SF) (bottom row). Larger values of the SF indicate less resolution.

of 1 km width as the one mapped at the surface for the Logan gabbro. In practice, the tomographic model recognizes the existence of the shallow high velocity body but is unable to resolve its true velocities at a scale finer than the node separation.

At $z = -4$ km, the broad, shallow low velocity zone (LVZ) imaged on the southwest side ($z = -2$ km) appears to narrow. This narrowed LVZ is bounded on its southwest side by the Zayante-Vergeles tectonic line and by the SAF to the northeast. Other evidence for this fault bounded LVZ comes from gravity modeling (Clark and Rietman, 1973), deep wells northeast and southwest of the Zayante-Vergeles line (see Clark and Rietman, 1973, for a discussion) and by Mooney and Colburn (1985) in the interpretation of a refraction seismic line across the SCM from Watsonville to Gilroy (i.e., approximately the vertical cross-section at $y = -20$, in our model). The interpretation is that the Salinian basement has downdropped between the two faults by approximately 2 to 3 km (Clark and Rietman, 1973) or by about 1.5 km (Mooney and Colburn, 1985). Our results appear to confirm these previous conclusions.

In the northeast domain, between $y = -55$ and $y = -30$ km, the model is characterized by a prominent wedge-like LVZ which is visible in our cross sections to depths of at least 10 km. This LVZ corresponds at the surface to Pliocene marine and non-marine sediments which overlay the Great Valley Sequence. The Great Valley sequence consists of upper Cretaceous sedimentary and volcanic rocks and is in fault contact (Coast Range thrust) with the underlying Franciscan Assemblage (e.g., Irwin, 1990). This LVZ correlates also remarkably well with a pronounced gravity low shown in figure 5.7. Further to the northwest in the northeast domain and at shallow depths ($-4 \leq z \leq -2$), the plan view sections display an elongated HVB that extends from $y = -35$ km to the northwestern edge of the model and is bounded on its southwest side by the Sargent fault to the south and by the SAF for $y \geq -10$ km. This HVB correlates well with the outcropping metamorphic rocks (greenstone, Dibblee, 1973) of the Franciscan assemblage mapped in the same area. In addition, Mooney and

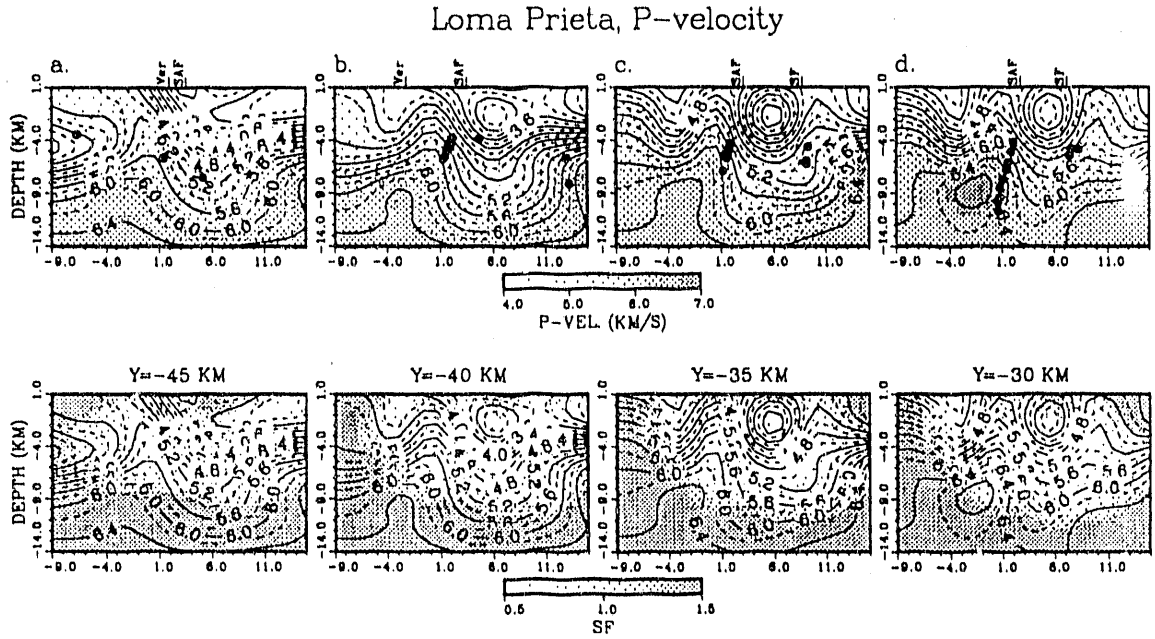

Figure 5.9: Loma Prieta final P-model: vertical sections across the fault from $y = -45$ to $y = -30$ (the view is from the southeast and the format is similar to figure 5.8). The principal structural features of the area are plotted in the top row: San Andreas Fault (SAF), Sargent fault (SF).

Luetgert (1982) interpreted a seismic refraction line which runs near the edge of the northeast side of our model and found high velocities at shallow depth which are consistent with our results and with the gravity data in the area. The refraction profile of Mooney and Colburn (1985) across the SAF also images this HVB, and their model again correlates well with ours. A similar consistency with gravity and refraction data is found at the northeastern edge of our model for $y > -10$ km. The northeastearn boundary of the model displays low velocities that can be correlated with serpentinite slivers outcropping northeast of the Berrocal fault (Mooney and Colburn, 1985).

The earthquakes used in the inversion lie near or on the SAF and the Sargent fault. They separate the southwest and northeast domains, and within the northeast domain they appear to delimit the perimeter of the low-velocity wedge (LVW) which was previously described.

This extremely good correlation between the resolved model and the mapped geology gives us confidence in the interpretation of the deeper parts of the resolved model.

The plan-view section at $z = -6$ km can be considered to be at the transition between the shallow and deep features of the resolved velocity model. For $z \leq -8$ km and southwest of the SAF fault trace, two main velocity anomalies characterize the imaged structure. In the following, we assume the contour at 6.5 km/sec to indicate the shape of imaged high velocity anomalies (see also Foxall et al., 1991). This choice is not arbitrary. It represents velocities substantially higher than average Franciscan and Salinian velocities in this depth range (Stewart and Peselnik, 1977, 1978; Lin and Wang, 1981). An elongated HVB appears between $y = -30$ and $y = -20$ km centered at $x = 1$ km with a width of about 4 km. This HVB appears to broaden and to extend toward the northwest with increasing depth. In the plan-view section at $z = -10$, the maximum velocities of the HVB reach values of approximately 7.2

km/sec and the 6.5 km/sec contour extends from $y = -35$ to approximately $y = -6$ km. The longitudinal extent of this HVB can be appreciated in figure 5.12.

The model resolves well, within the accuracy implicit in the grid discretization, the northeastern boundary of this HVB but, because of the source-receiver geometry and the associated lack of resolution, it does not define its southwestern boundary. An important feature of the HVB is that its well-resolved northeastern side lies approximately 4 km northeast of the vertical projection of the SAF. The velocity range of this HVB suggests a mafic composition (e.g., Lin and Wang, 1981).

The second feature on the deep part of the southwest domain of the resolved model is the pronounced, oblong relatively low-velocity zone that extends northwestward from approximately $y = 0$. The southeastern side of this LVZ bounds the deep HVB previously discussed, and its northeastern side is in contact with another HVB that lies northeast of the SAF. The small scale features of this LVZ can be examined in the across-SAF vertical sections of figure 5.11 between $y = 0$ and $y = 10$ km. These sections reveal two LVZs, a more prominent, vertical one which is intersected between $z = -5$ and $z = -10$ by another less well-resolved LVZ dipping approximately 45° to the southwest. The SW dipping alignment of earthquakes in the section at $y = 10$ km lies at the base of the oblique LVZ and consists exclusively of aftershocks of the LP earthquake. In contrast, the vertical LVZ includes almost exclusively background seismicity earthquakes (i.e., Lake Elsman cluster), which lie near its northeastern boundary (Olson, 1990; Foxall et al., 1991).

The deep structure of the northeast domain is characterized in its southeastern part by the deep extension of the low velocity wedge (LVW) imaged in the shallow structure (sections between $y = -45$ and $y = -30$ km). The range of these velocities appears to be in agreement with velocities determined in laboratory experiments for Franciscan assemblage rocks in the same pressure-range (Stewart and Peselnik, 1977, 1978; Lin and Wang, 1981). Farther to the north, between $y = -25$ and $y = -10$, and

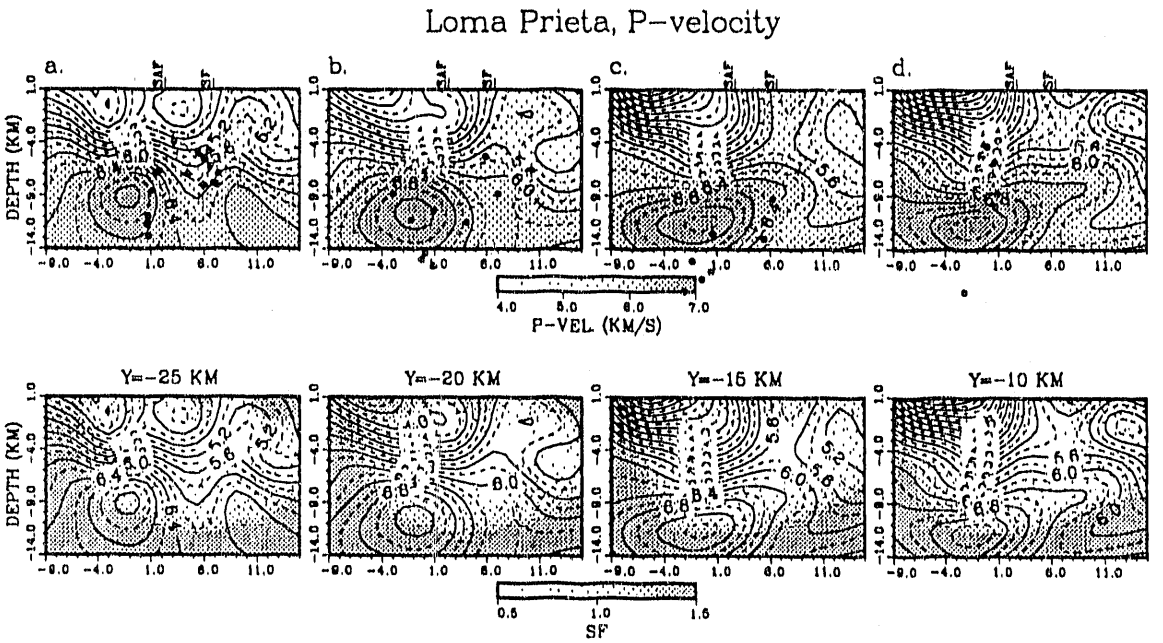

Figure 5.10: Loma Prieta final P-model: vertical sections across the fault from from y=-25 to y=-10 (the view is from the southeast and the figure is similar to figure 5.9).

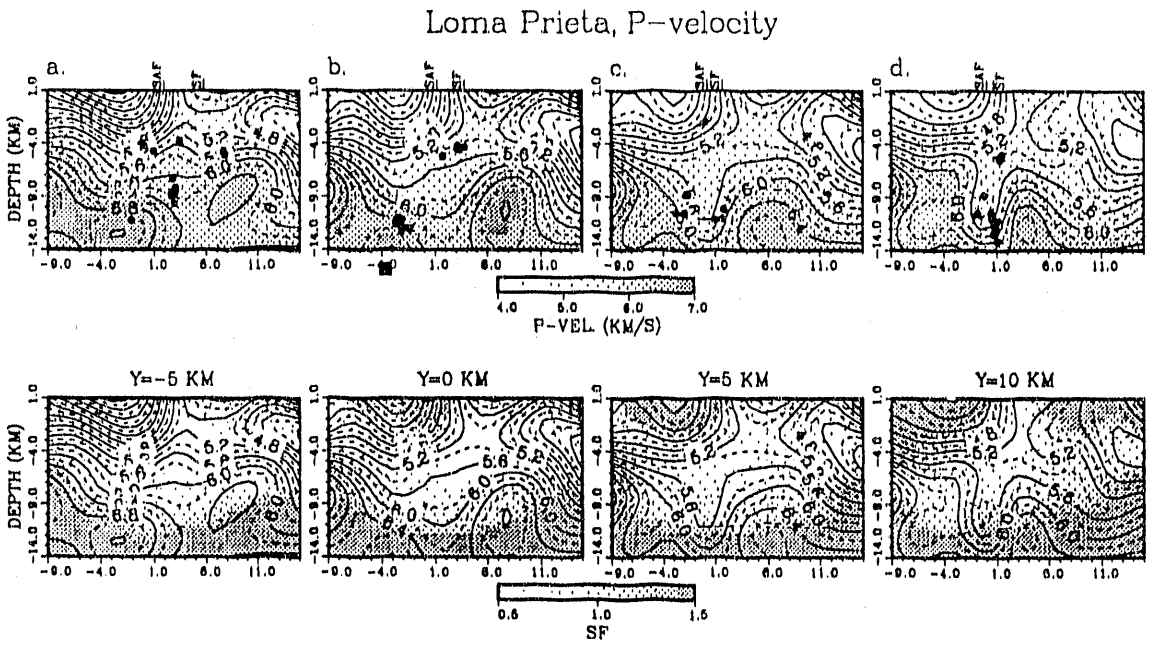

Figure 5.11: Loma Prieta final P-model: vertical sections across the fault from y=-5 to y=10 (the view is from the southeast and the figure is similar to figure 5.9).

apart from the northeastern extension of the deep HVB of the southwest domain which has been already described, velocities are again generally consistent with Franciscan assemblage rocks. Between $y = -30$ and $y = -25$, we image a deep LVZ which could be interpreted as fault-related, but, because it lies beneath the northern extension of the shallow LVW, we prefer to interpret it as being part of the latter.

Finally, in the northwestmost vertical cross-sections, between $y = -5$ and $y = 10$ km, the deep domain on the northeast side of the SAF appears to be characterized by the HVB which bounds the northeast side of the vertical LVZ which was previously mentioned in the description of the deep southwest domain. This deep northeast HVB appears to be in contact at $y = -5$ km with the well-resolved HVB that characterizes the deep southwest side.

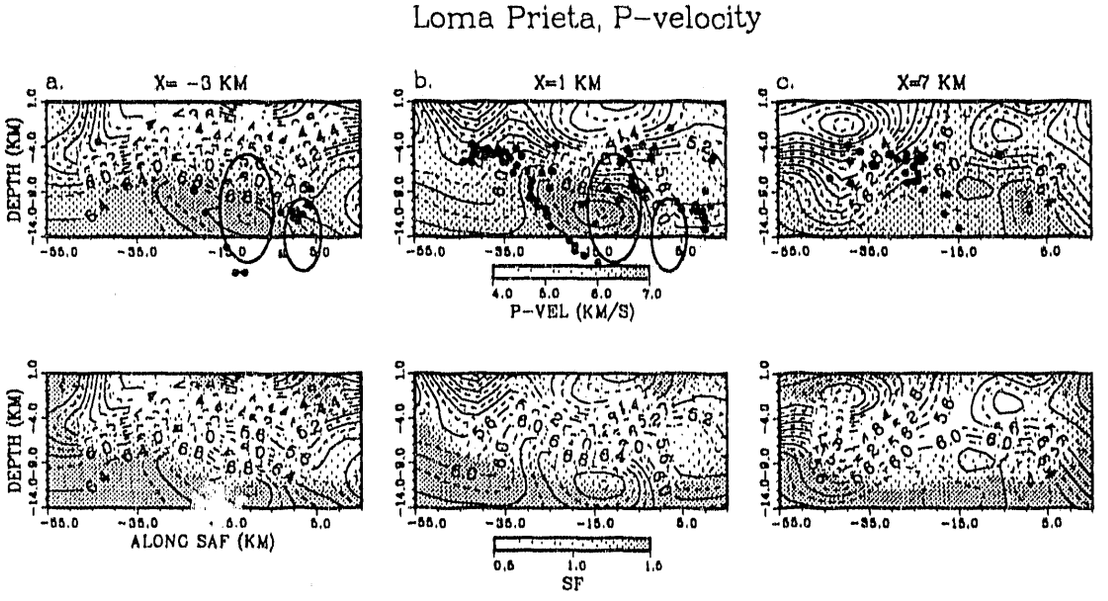

Figure 5.12: Loma Prieta final P-model: vertical sections along the fault (the view is from the northeast and the figure format is similar to figure 5.8). The perimeter of the asperities inferred by Choy and Boatwright, (1990) are plotted and their distortion is due to the vertical exaggeration.

5.7 Discussion and conclusions

The imaged velocity structure in the southern SCM correlates well at shallow depths with the main geologic units outcropping in the area and with previous geophysical studies, particularly gravity data.

At shallow depths, seismicity occurs in most cases at the contact between blocks of different velocities and presumably of different composition (see plan-view sections in figure 5.8). However, we cannot confidently generalize this observation to greater depth.

The most prominent feature of the resolved velocity structure is the deep HVB imaged in the southwest domain. This body reaches maximum velocities of approximately 7.4 km/sec which appear rather high and, in principle, could be caused by the existence of a body with smaller velocities, e.g., 7.0 km/sec, in sharp contact with a neighbouring medium having substantial lower velocities. In this case, the discretization grid would be too coarse to properly model the contact and would result, especially in the areas with poor ray coverage, in some overshooting of the velocities at the nodes near the contact of the HVB. However, there is some independent evidence for the existence of this body. Zandt (1981) used the ACH tomographic technique (Aki et al., 1977) to model teleseismic arrival-time residuals as recorded by the USGS short period stations along the SAF. Although his discretization of the velocity model is coarse (i.e., cubes of 10 km sides in the upper layer and 20 km deeper), he resolved anomalously high velocities across the SAF near San Juan Bautista in the more shallow 30 km of his model. Within the discretization interval used in his study, it appears that we image the same HVB. Zandt's results suggest that the HVB is deep-rooted, a property impossible to define in our model where resolution degrades with depth.

The mainshock hypocenter occurred deep at the northwestern limit of the HVB imaged on the southwest side of the fault. The main release of seismic moment

according to Choy and Boatwright (1990) occurred northwest of the mainshock (34%) and about 7 km southeast and more shallow of the mainshock hypocenter. This second and main moment release (50%) corresponds to the rupture of an asperity having about 6 km in radius (see section $x = 1$ in figure 5.12). The location of Choy and Boatwright main energy release coincides in our model with with the highest velocities of the deep HVB on the southwest side of the SAF and with a zone depleted in aftershock seismicity. Similar results were also found by Beroza (1991) who used near source strong motion data to model the main rupture. This observation is similar to some extent to what was found in chapter 4 for the Parkfield asperity and by Michael and Eberhart-Phillips (1991) for LP and Parkfield. We can find some additional similarities between the rupture pattern observed at Parkfield in 1966 and Loma Prieta in 1989. If we assume that the immediate foreshocks and the mainshock at Parkfield are actually part of the same failure event, we find that both mainshocks nucleate near the perimeter of a HVB and rupture bilaterally in a medium that has lower or average velocities on one front of the propagating rupture and through a body with higher velocities on the other. This observation, attributes a prominent role to high velocity anomalies in rupture dynamics. For example, Aki (1979) noticed the HVB lying across the SAF near San Juan Bautista imaged by Zandt (1981) and speculated that it may have acted as barrier in stopping the rupture of the 1906 San Francisco earthquake. Thatcher and Lisowski (1987) have used geodetic data to model the rupture of the 1906 earthquake. Their data constrained a slip of 2.6 ± 0.2 m, from the surface to 10 km depth, to as far south as 10 km southeast of Loma Prieta peak, where they loose resolution. Loma Prieta peak lies at $x = 4.43$ $y = 0.29$ km in our coordinate system. If we examine the plan view sections in figure 5.8 between $z = -8$ and $z = -12$, the depth range inferred by Thatcher and Lisowski for the rupture in the 1906 earthquake, we note that the 6.5 km/sec contour line which we adopted to delimit the perimeter of the HVB lies approximately at $y = -1$, $y = -6$

and $y = -17$ for $z = -12$, $z = -10$ and $z = -8$, respectively. It follows that our data can support Aki's speculation on the HVB acting as barrier in the 1906 rupture and be consistent with Thatcher and Lisowski analysis. Rupture in 1906 may have "seen" the deep HVB at depths between 8 and 10 km and, consequently, slip decreased and rupture eventually stopped near San Juan Bautista. In this scenario, the HVB does not rupture in 1906-type earthquakes where it acts as a locked patch, but it ruptures in LP-type shocks. This inference is also in agreement with the findings of Segall and Lisowski (1990) that have recently reanalyzed the geodetic data relative to the 1906 earthquake. They found that the pattern of geodetic deformation was different for the 1906 and the 1989 earthquakes.

Another feature of this HVB is that it delimits a deep cluster of earthquakes between the SAF and the Sargent fault that Olson (1990) has interpreted as closing a wedge-like structure between the two faults. However, the HVB imaged in our velocity model does not appear to resemble closely the structure hypothesized by Olson.

Finally, we cannot say if the relatively lower velocities at the northern boundary of the model are fault-related or, more simply, if they reflect only the local juxtaposition of higher velocity bodies in that part of the model.

In summary, these modeling results suggests strongly that structural heterogeneity seem to play a prominent role in the nucleation and rupture of the LP mainshock and that it may have played an important role in details of the 1906 rupture in the SCM. Distribution of aftershocks and background seismicity appear also to be controlled by the heterogeneity. Future studies need to address in detail the relation of the imaged heterogeneities to the crustal deformation of the area. For example, the resolved velocity model could be used as basic structure for finite element modeling of the long-term deformation in the SCM area, or for synthetic-seismogram modeling of the mainshock and its aftershocks by using the ray-method (Cerveny, 1987).

Chapter 6

Summary, Conclusions and Recommendations

The method of joint inversion for hypocenters and velocity structure developed by Thurber (1983) has been modified to determine velocity structures under smoothing constraints of several types. Because the resolving power of the data sets in this type of inversion is generally non-optimal, application of some smoothing appears to be the most efficient way to limit possible instabilities that can arise in tomographic modeling.

In summary, there are three approaches toward smoothing that can be applied at different stages in the inversion procedure. In the first approach, smoothing is applied after the final tomographic model has been determined, i.e., *a posteriori* smoothing, and the smoothed model loses the character provided by the adopted minimization criterion. In the second approach, smoothing can be included after the matrix of the travel-time partial derivatives with respect to the velocity model has been determined. The third approach, developed in this thesis (see also Sambridge, 1990), consists of applying smoothing at the accumulation stage of the partial derivatives. This is achieved by selecting suitable basis functions in the parameterization of the velocity model. Cubic B-splines basis functions were adopted in this study, so that velocities determined within the 3-D grid involve summation over the 64 contiguous basis functions for the inner parts of the model. In addition, the model, everywhere

continuous to the second spatial derivative of velocity, can be used to determine synthetic body-wave seismograms using the ray-method (e.g., Cerveny, 1987).

The inversion formalism developed here includes also the second smoothing approach described above. However, it is found through testing with synthetic cases that use of this type of smoothing can lead the inversion to local minima. Similarly, it is found that use of coarse grid spacing in the initial iterations of the non-linear inversion can also lead to local minima. This problem appears to be caused by the often poor resolving power of the data so that, when the velocity model is more densely resampled and the iterative inversion is continued, this lack of resolving power does not allow sharpening of the smooth features in the previously resolved velocity model.

The inversion code used in this study has the capability to resolve simultaneously both P- and S-wave velocity models (Eberhart-Phillips, 1989). However, S-wave models are generally affected by sparse ray-coverage and by larger errors in phase onset determination. These factors tend to degrade the quality of the S-model by causing instabilities manifested in large fluctuations in the V_P/V_S values. Given the importance of the V_P/V_S ratios in the identification of rock type or of anomalous fluid pressures, I have introduced some coupling (i.e., proportionality, conditioning) between P- and S-wave velocities. This coupling permits solving for models having minimum variations *wrt* to some pre-selected average value. Evaluation of the data misfit (i.e., weighted RMS residual) with various amounts of coupling assesses the significance of the resolved V_P/V_S anomalies. This coupling was exercised in synthetic tests, displaying an overall stabilizing effect on the velocity inversion and permitted retrieval of the correct values of V_P/V_S ratio in most parts of the model. Application of this coupling in the analysis of the Parkfield data set (chapter 4) stabilized the V_P/V_S model, permitting retrieval of the previously hypothesised bend in the alignment of seismicity near the 1966 epicenter. It appears that the method for introduction of V_P/V_S coupling is completely general and can be adapted to other seismic

inversion methods where reliable estimates of V_P/V_S ratio are needed.

In the presence of strong lateral velocity gradients, earthquake hypocenters can be biased toward the regions of higher velocity. The fault-model tests show that with small error added to the data, and with a discretization grid only slightly aliased with respect to that used to calculate the synthetic travel-times, the final weighted RMS residual time does not decrease to values obtained in the calculated travel times, and the earthquake locations tend to be biased toward the fast side of the model. This appears to be caused mainly by the resolving power limitations of the data set which leads the model into a local minimum. The earthquakes relocated using the 3-D model in the Parkfield region are shifted toward the fast side of the model with respect to the vertical projection downward of the SAF trace. One test to verify whether this shift is real would be to constrain the hypocenters to lie on the vertical plane of the SAF and perform the velocity inversion. If the resulting velocity model displayed an improved data misfit then it would suggest that the earthquakes do occur on the SAF.

Two main findings resulted from this analysis of the Parkfield data set. First, a relatively high velocity body was imaged southwest of the SAF and immediately south of the 1966 epicenter at depth larger than 4 km. This HVB contains no background seismicity, and its size and location correlates well with previous determinations of the "Parkfield asperity" from geodetic data (Stuart et al., 1985; Tse et al., 1985; Harris and Segall, 1987; Michael and Eberhart-Phillips, 1991). The second important result is the anomalously high V_P/V_S ratio found in the nucleation zone of the 1966 hypocenter (Michelini and McEvilly, 1991). A possible cause for this anomaly is increased pore-fluid pressure and/or porosity in the nucleation zone.

The inversion for the velocity structure in the Loma Prieta aftershock zone was performed using only P-wave arrival times. The result is an excellent correlation between the shallow velocity structure and the local geology and results of previous

geophysical investigations. The deeper structure in the LP zone is characterized by a deep-rooted anomalously high velocity body that appears to control the mode of deformation in the area. The main release of seismic moment determined for the LP mainshock coincides in location with the highest velocities of this anomalous HVB. Both background seismicity and LP aftershocks appear to be influenced by the extent of this body.

Finally, it must be realized that discretization and parameterization are two rather strong *a priori* constraints in a tomographic inversion. In current studies, both discretization and parameterization are held fixed throughout the various inversion procedures in use, but the earth cannot be assumed to have a certain degree of smoothness or a certain minimum wavelength for its anomalies. It appears to the author that implementation of some type of adaptive parameterization and/or discretization scheme that would take into account the minimum scale length provided by the data but that would be flexible enough to switch from higher to lower order basis functions, or change the sampling interval in the grid of nodes (or both), would probably improve the tomographic modeling estimate. This approach is already in use in finite element modeling for fluid dynamics problems. However, the ubiquitous problem with which most geoscientists grapple is lack of resolving power in the data set, and this must be accounted for in designing any adaptive parameterization/discretization scheme.

Both applications of the technique to high quality data sets have shown that velocity anomalies play prominent roles in the distribution of the seismicity and in the nucleation and extent of the main rupture. These findings appear to put some strong constraints on the geologic structures that control rupture in larger earthquakes and this concept should be pursued in laboratory rock-mechanics studies of failure and in finite element modeling of the long-term deformation in the earthquake cycle in areas of potentially damaging earthquakes.

References

Aki, K. (1979). Characterization of barriers on an earthquake fault, *J. Geophys. Res.*, **84**, 6140-6148.

Aki, K., A. Christoffersson and E.S. Husebye (1977). Determination of the three-dimensional seismic structure of the lithosphere, *J. Geophys. Res.*, **82**, 277-296.

Aki, K. and W.H.K.Lee (1976). Determination of three-dimensional velocity anomalies under a seismic array using first P arrival times from local earthquakes, I, A homogeneous initial model, *J. Geophys. Res.*, **81**, 4381-4399.

Bailey, E.H, M.C.,Jr. Blake, and D.L. Jones (1970). On-land Mesozoic oceanic crust in California Coast Ranges, in *Geological Survey research: U.S. Geological Survey Professional Paper*, **700-C**, p. c70-c81.

Backus, G. (1970). Inference from inadequate and inaccurate data, II, *Proc. Natl. Acad. Sci. U.S.A.*, **65**, 281-287.

Bakun, W.H. and A.G. Lindh (1985). The Parkfield, California, Prediction Experiment, *Earthq. Predict. Res.*, **3**, 285-304.

Bakun, W.H. and T. V. McEvilly (1979). Earthquakes near Parkfield, California: Comparing the 1934 and 1966 sequences, *Science*, **205**, 1375-1377.

Bakun, W.H. and T. V. McEvilly (1981). P-wave spectra for M_L5 foreshocks, aftershocks and isolated earthquakes near Parkfield, California, *Bull. Seism. Soc. Am.*, **71**, 423-436.

Bakun, W.H. and T. V. McEvilly (1984). Recurrence models and Parkfield, California earthquakes, *J. Geophys. Res.*, **89**, 3051-3058.

Bartels, R.H., J.C. Beatty and B.A. Barsky (1987). *An introduction to Splines for use in Computer Graphics and Geometry Modeling*, Morgan Kaufmann Publishers, Inc, Los Altos, California, 476 pp.

Ben-Zion, Y., and K. Aki (1990). Seismic radiation from an SH line source in laterally heterogeneous planar fault zone, *Bull. Seism. Soc. Am.*, **80**, 971-994.

Beroza, G. (1991) Near source modeling of the Loma Prieta earthquake: evidence for heterogeneous slip and implications for earthquake hazard, *submitted to Bull. Seism. Soc. Am.*.

Berry, F.A.F. (1973). High fluid potentials in California Coast Ranges and their tectonic significance, *Amer. Assoc. Petrol. Geol. Bull.*, **57**, 1219-1249.

Berryman, J.G. (1990). Lecture on nonlinear inversion and tomography, *Lawrence Livermore National Laboratory, UCRL-LR-105538*, 75 pp.

Brown, R.D. Jr. and J.G. Vedder (1967) Surface tectonic fractures along the San

Andreas fault, in *The Parkfield-Cholame California, Earthquakes of June-August 1966 - surface geologic effects water-resources aspects, and preliminary seismic data, U.S. Geol. Survey Prof. Paper 579*, 2-23.

Cerveny, V. (1987). Ray tracing algorithms in three-dimensional laterally varying layered structures, in *Seismic Tomography*, G. Nolet, (Editor), D. Reidel Publishing Company, 99-133.

Chou, C.W. and J.R. Booker (1979). A Backus-Gilbert approach to the inversion of travel-time data for three-dimensional velocity structure, *Geophys. J. R. astr. Soc.*, **59**, 324-344.

Choy, G.L. and J. Boatwright (1990). Source characteristics of the Loma Prieta, California, earthquake of October 18, 1989, from global data, *Geophys. Res. Lett.*, **17**, 1183-1186.

Clark, J.C. and J.D. Rietman (1973) Oligocene stratigraphy, tectonics, and paleogeography southwest of the San Andreas fault, Santa Cruz mountains and Galilan range, California Coast Ranges, *U.S. Geological Survey Prof. Paper, 783*, 18 pp.

Clymer, R.W., E. D. Karageorgi and T. V. McEvilly (1989). The Parkfield Monitoring Program: Repeated Illumination of the Nucleation Zone with the S-wave Vibrator, *Seis. Res. Lett.*, **60**, 32.

Christensen, N.I. (1984). Pore pressure and oceanic crustal structure, *Geophys. J. R. astr. Soc.*, **79**, 411-424.

Christensen, N.I. and H.F. Wang (1985). The influence of pore pressure and confining pressure on dynamic elastic properties of Berea sandstone, *Geophysics*, **50**, 207-213.

Crosson, R.S. (1976). Crustal structure modeling of earthquake data, 1, Simultaneous least squares estimation of hypocenter and velocity parameters, *J. Geophys. Res.*, **81**, 3036-3046.

Dibblee, T.W., Jr. (1973). Geological maps of the Morgan Hill, Mt. Madonna, Mt. Sizer, Gilroy Hot Springs and Gilroy quadrangles, California, *U.S. Geol. Surv. Open File Maps*, 1:24000.

Dickinson, W.R. (1966). Structural relationships of San Andreas fault system, *Geol. Soc. Am. Bull.*, **77**, 707-726..

Dietz, L.D. and W.L. Ellsworth, (1990). Loma Prieta, California, earthquake and its aftershocks: geometry of the sequence from high-resolution locations, *Geophys. Res. Lett.*, **17**, 1417-1420.

Eberhart-Phillips, D. (1989) Investigations of crustal structure and active tectonic processes in the Coast Ranges, central California, *Ph.D. thesis, Stanford University*, Stanford, California.

Eaton, J.P., M.E. O'Neill and J.N. Murdock (1970). Aftershocks of the 1966 Parkfield-Cholame, California, earthquake: a detailed study, *Bull. Seism. Soc. Am.*, **60**, 1151-1197.

Eberhart-Phillips, D. and A.J. Michael (1989). Three-dimensional velocity structure in the Parkfield, California region from from inversion of local earthquakes and shot arrival times, *EOS Transactions, Amer. Geophys. Union*, **70**, 1203-1204.

Farra, V. and R. Madariaga (1988). Non-linear reflection tomography, *Geophys. Journ. Int.*, **95**, 135-147.

Feng, R. and T. V. McEvilly (1983). Interpretation of seismic reflection profiling data for the structure of the San Andreas fault zone, *Bull. Seism. Soc. Am.*, **73**, 1701-1720.

Firbas, P (1987). Tomography from seismic profiles, in *Seismic Tomography*, G. Nolet, (Editor), D. Reidel Publishing Company, 189-202.

Foxall, W., A. Michelini and T. V. McEvilly (1989). The Parkfield Monitoring Program: Fault Zone Characteristics Revealed by High-Precision Microearthquake Locations, *Seis. Res. Lett.*, **60**, 32.

Foxall, W., A. Michelini and T. V. McEvilly (1991). 3-D earthquake tomography of the Loma Prieta segment of the San Andreas Fault zone: control of slip behaviour by lithological heterogeneity, *in preparation.*

Harris, R.A. and P. Segall (1987). Detection of a locked zone at depth on the Parkfield segment of the San Andreas fault, *J. Geophys. Res.*, **92**, 7945-7962.

Healy, J.H and L.G. Peake (1975). Seismic velocity structure along a section of the San Andreas fault near Bear Valley, California, *Bull. Seism. Soc. Am.*, **65**, 1177-1197.

Irwin, W.P. (1990) Geology and Plate-Tectonics development, in *The San Andreas fault system, California, U.S. Geol. Survey Professional Paper*, **1515**, 60-80.

Irwin, W.P. and Barnes, I. (1975). Effect of geologic structure and metamorphic fluids on seismic behaviour of the San Andreas fault system in central and northern California, *Geology*, **3**, 713-716.

Jackson, D.D. (1979). The use of *a priori* information to resolve non-uniqueness in linear inversion, *Geophys. J. R. astr. Soc.*, **57**, 137-157.

Kanamori, H. and K. Satake (1990). Broadband study of the 1989 Loma Prieta earthquake, *Geophys. Res. Lett.*, **17**, 1179-1182.

Karageorgi, E.D., R.W. Clymer and T.V. McEvilly (1991). Seismological studies at Parkfield: II. search for temporal variations in wave propagation using vibroseis, *in press Bull. Seism. Soc. Am.*.

Kern, H. and A. Richter (1981). Temperature derivatives of compressional and shear wave velocities in crustal and mantle rocks at 6 kbar confining pressure, *J. Geophysics*, **49**, 47-56.

Lancaster, P. and K. Salkauskas (1986). *Curve and surface fitting, an introduction*, Academic Press, 280 pp.

Lawson, C.L. and R.J. Hanson (1974). *Solving least squares problems*, Prentice-Hall, 340 pp.

Lees, J.M. and R.S. Crosson (1989). Tomographic inversion for three-dimensional velocity structure at Mount St. Helens using earthquake data, *J. Geophys. Res.*, **94**, 5716-5728.

Lees, J.M. and P.E. Malin (1990). Tomographic images of P wave velocity variation at Parkfield, California, *J. Geophys. Res.*, **95**, 21793-21804.

Li, Y.G. and P.C. Leary (1990). Fault zone trapped seismic waves, *Bull. Seism. Soc. Am.*, **80**, 1245-1271.

Lin, W. and C.Y. Wang (1980). P-wave velocities in rocks at high pressure and temperature and the constitution of the central California crust, *Geophys. J. R. astr. Soc.*, **61**, 379-400.

Lindh, A.G. (1983). Preliminary assessment of long-term probabilities for large earthquakes along selected segments of the San Andreas fault system in California, *U.S. Geol. Survey Open File Report 83-63*, 115.

Lindh, A.G. and D.M. Boore (1981). Control of rupture by fault geometry during the 1966 Parkfield earthquake, *Bull. Seism. Soc. Am.*, **71**, 95-116.

Lisowski, M., W.H. Prescott, J.C. Savage and M.J. Johnston (1990). Geodetic estimate of coseismic slip during the 1989 Loma Prieta, California, earthquake, *Geophys. Res. Lett.*, **17**, 1437-1440.

Louie, J.N., R.W. Clayton and R.J. LeBras (1988). Three-dimensional imaging of steeply dipping structure near the San Andreas fault, Parkfield, California, *Geophysics*, **53**, 176-185.

Malin, P.E., S.N. Blakeslee, M.G. Alvarez and A.J. Martin (1989). Microearthquake imaging of the Parkfield asperity, *Science*, **244**, 557-559.

Marquardt, D.W. (1963). An algorithm for least squares estimation of non-linear parameters, *SIAM J.*, **11**, 431-441.

Marquardt, D.W. (1970). Generalized invverses, ridge regression, biased linear estimation of non-linear parameters, *Technometrics*, **12**, 591-612.

McBride, J.H. and L.D. Brown (1986). Reanalysis of the COCORP deep seismic reflection profile across the San Andreas fault, Parkfield, California, *Bull. Seism. Soc. Amer.*, **76**, 1668-1686.

McEvilly, T.V., W.H. Bakun and K.B. Casaday (1967). The Parkfield, California earthquakes of 1966, *Bull. Seism. Soc. Amer.*, **57**, 1221-1244.

McLaughlin, R.J., J.C. Clark, and E.E. Brabb (1988). Geologic map and structure sections of the Loma Prieta 7 1/2' quadrangle, Santa Clara and Santa Cruz counties, California, *U.S. Geological Survey Open-File Report 88-752*, 31 pp.

Menke, W. (1984). *Geophysical data analysis: discrete inverse theory*, Academic Press, Inc., 260 pp.

Michael, A.J. and D. Eberhart-Phillips (1991). Relations among fault behaviour, subsurface geology, and three-dimensional velocity models, *Science*, **253**, 651-654.

Michelini, A., W. Foxall and T.V. McEvilly (1989). The Parkfield monitoring program: joint hypocentral and velocity inversion for three-dimensional structure, *Seis. Res. Lett.*, **60**, 31-32.

Michelini, A. and T.V. McEvilly (1991). Seismological Studies at Parkfield: I. simultaneous inversions for velocity structure and hypocenters using cubic B-splines paramemeterization, *Bull. Seism. Soc. Amer.*, **81**, 524-552.

Mooney, W.D. and J.H. Luetgert (1982). A seismic refraction study of the Santa Clara valley and southern Santa Cruz mountains, west-central California, *Bull. Seism. Soc. Amer.*, **72**, 901-909.

Mooney, W.D. and R.H. Colburn (1985). A seismic refraction profile across the San Andreas, Sargent and Calaveras faults, west-central California, *Bull. Seism. Soc. Amer.*, **75**, 175-191.

Mooney, W.D. and A. Ginzburg (1986). Seismic measurements of internal properties of fault zones, *Pageoph.*, **124**, 141-157.

Moos, D. and M.D. Zoback (1983). In situ studies of velocity in fractured crystalline rocks, *J. Geophys. Res.*, **88**, 2345-2358.

Nishioka, G. and A.J. Michael (1990). A detailed seismicity study of the Middle Mountain zone at Parkfield, California, *Bull. Seism. Soc. Amer.*, **80**, 577-588.

Nolet, G. (1987). Seismic wave propagation and seismic tomography, in *Seismic Tomography*, G. Nolet, (Editor), D. Reidel Publishing Company, 1-23.

Nur, A. and G. Simmons (1969). The effect of saturation on velocity in low porosity rocks, *Earth Planetary Science Lett.*, **7**, 183-193.

O'Connell, D.R. (1986). Seismic velocity structure and Microearthquake source properties at the Geysers, California, geothermal area, *Ph.D. Thesis*, University of California, Berkeley, 204 pp.

O'Connell, D.R. and L.R. Johnson (1991). Progressive inversion for hypocenters and P wave and S wave structure: application to the Geysers, California, Geothermat field, *J. Geophys. Res.*, **96**, 6223-6236.

O'Connell, R.J. and B. Budiansky (1974).. Seismic velocities in dry and saturated cracked solids, *J. Geophys. Res.*, **79**, 5412-5426.

Olson, J.A. (1990). Seismicity in the twenty years preceding the Loma Prieta, California, earthquake, *Geophys. Res. Lett.*, **17**, 1429-1432.

O'Neill, M.E. (1984). Source dimensions and stress drops of small earthquakes near Parkfield, California, *Bull. Seism. Soc. Am.*, **74**, 27-40.

Oppenheimer, D.H. (1990). Aftershock slip behaviour of the 1989 Loma Prieta, California earthquake, *Geophys. Res. Lett.*, **17**, 1199-1202.

Pavlis, G.L. and J.R. Booker (1980). The Mixed Discrete-Continuous Inverse Problem: Application to the Simultaneous Determination of Earthquake Hypocenters and Velocity Structure, *J. Geophys. Res.*, **85**, 4801-4810.

Poley, C.M., A.G. Lindh, W.H. Bakun and S.S. Schulz (1987). Temporal changes in microseismicity and creep near Parkfield, California, *Nature*, **327**, 134-137.

Prothero, W. A., W.J. Taylor and J.A. Eickemeyer (1988). A fast two-point, three-dimensional raytracing algorithm using a single step search method, *Bull. Seism. Soc. Am.*, **78**, 1190-1198.

Pulliam, R.J. (1991). Imaging Earth's interior: tomographic inversions for mantle P-wave velocity structure, *Ph.D. Thesis*, University of California, Berkeley, 266 pp.

Rodi, W.L., T.H. Jordan, J.F. Masso and J.M. Savino (1980). Determination of the three-dimensional structure of eastern Washington from the joint inversion of gravity and earthquake data, *Rep. SSS-R-80-4516, Systems Science and Software*, La Jolla.

Roecker, S.W. (1982). Velocity structure of the Pamir-Hindu Kush region: possible evidence of subducted crust, *J. Geophys. Res.*, **87**, 945-959.

Ross, D.C. (1970). Quartz gabbro and anorthositic gabbro: markers of offset along the San Andreas fault in the California Coast Ranges, *Geol. Soc. America Bull.*, **81**, 3647-3662.

Sambridge, M.S. (1990). Non-linear arrival time inversion: constraining velocity animalies by seeking smooth models in 3-D, *Geophys. Journ. Int.*, **102**, 653-677.

Scholz, C.H. (1985). The Black mountain asperity: seismic hazard of the southern San Francisco peninsula, California, *Geophys. Res. Lett.*, **12**, 717-719.

Schwartz, S.Y., D.L. Orange and R.S. Anderson (1990). Complex fault interactions in a restraining bend on the San Andreas fault, southern Santa Cruz mountains, California, *Geophys. Res. Lett.*, **17**, 1207-1210.

Segall, P. and R. Harris (1987). Earthquake deformation cycle on the San Andreas fault near Parkfield, California, *J. Geophys. Res.*, **92**, 10511-10525.

Segall, P. and M. Lisowski (1990). Surface displacement in the 1906 San Francisco and 1989 Loma Prieta earthquakes, *Science*, **250**, 1241-1244.

Sibson, R.H. (1982). Fault zone models, heat flow, and the depth distribution of earthquakes in the continental crust of the United States, *Bull. Seism. Soc. Am.*, **72**, 151-163.

Sieh, K.E. (1978). Central California forshocks of the great 1857 earthquake, *Bull. Seism. Soc. Am.*, **68**, 1731-1749.

Sims, J.D. (1988). Geologic map of the San Andreas Fault zone in the Cholame valley and Cholame hills quadrangles, San Luis Obispo and Monterey counties, California, Miscellaneous Field Studies Map, U.S. Geological Survey.

Sims, J.D. (1990). Geologic map of the San Andreas Fault in the Parkfield 7.5-minute quadrangle, Monterey and Fresno counties, California, Miscellaneous Field Studies Map, U.S. Geological Survey.

Spakman, W. and G. Nolet (1988). Imaging algorithms, accuracy and resolution in delay time tomography, in *Mathematical Geophysics*, N.J. Vlaar, G. Nolet, M.J.R. Wortel and S.A.P.L. Cloetingh, (Editor), D. Reidel Publishing Company, 155-187.

Spencer, C. (1985). The use of partitioned matrices in geophysical inversion problems, *Geophys. J. R. astr. Soc.*, **80**, 619-629.

Spencer, C., and D. Gubbins (1980). Travel time inversion for simultaneous earthquake location and velocity structure determination in laterally varying media, *Geophys. J. R. astr. Soc.*, **63**, 95-116.

Stewart, R. and L. Peselnik (1977). Velocity of compressional waves in dry Franciscan rocks to 8 kilobars and 300°C, *J. Geophys. Res.*, **82**, 2027-2039.

Stewart, R. and L. Peselnik (1978). Systematic behaviours of compressional velocity in Franciscan rocks at high pressure and temperature, *J. Geophys. Res.*, **83**, 831-839.

Strang, G. (1976). *Linear algebra and its applications*, Academic Press, Inc, 414 pp.

Stuart, W.D., R.J. Archuleta and A.G. Lindh (1985). Forecast models for moderate earthquakes near Parkfield, California, *J. Geophys. Res.*, **90**, 592-604.

Sykes, L.R. and S. Nishenko (1984). Probabilities of occurrence of large plate rupturing earthquakes for the San Andreas, San Jacinto, and Imperial faults, California, 1983-2003, *J. Geophys. Res.*, **89**, 5905-5927.

Tarantola, A. and B. Valette (1982). Inverse problems = quest for information, *J. Geophys.*, **50**, 159-170.

Thatcher, W. and M. Lisowski (1987). Long-term seismic potential of the San Andreas fault southeast of San Francisco, California, *J. Geophys. Res.*, **92**, 4771-4784.

Thomson, C.J. and D. Gubbins (1982). Three-dimensional lithospheric modelling at NORSAR linearity of the method and amplitude variations from anomalies, *Geophys. J. R. astr. Soc.*, **71**, 1-36 and microfiche GJ71/1.

Thurber, C.H. (1983). Earthquake locations and three-dimensional crustal structure in the Coyote Lake area, Central California, *J. Geophys. Res.*, **88**, 8226- 8236.

Toomey, D.R. and G.R. Foulger (1989). Tomographic inversion for local earthquake data from the Hengill-Grensdalur central volcano complex, Iceland, *J. Geophys. Res.*, **94**, 17497-17511.

Tse, S.T., R. Dmowska, and J.R. Rice (1985). Stressing locked patches along a creeping fault, *Bull. Seism. Soc. Am.*, **75**, 709-736.

Um, J. and C. H. Thurber (1987). Rapid solution of ray tracing problems in heterogeneous media, *Bull. Seism. Soc. Am.*, **77**, 972-986.

U.S. Geological Survey Staff (1990). The Loma Prieta, California earthquake: an anticipated event, *Science*, **247**, 286-293.

Woodhouse, J.H. and A.M. Dziewonski (1984). Mapping the upper mantle: three-dimensional modelling of Earth structure by inversion of seismic waveform, *J. Geophys. Res.*, **89**, 5953-5986.

Working Group on California Earthquake Probabilities (1988) Probabilities of large earthquakes occurring in California on the San Andreas fault, *U.S. Geological Survey Open File Report, 88-398*, 51 pp.

Zandt, G. (1981). Seismic images of the deep structure of the San Andreas fault system, Central Coast Ranges, California, *J. Geophys. Res.*, **86**, 5039-5052.

Zhang, J. and T. Lay (1990). Source parameters of the 1989 Loma Prieta earthquake determined from long-period Rayleigh waves, *Geophys. Res. Lett.*, **17**, 1195-1198.

END

DATE FILMED

5/8/92